

**Tethyan evolution of the Black Sea region since the Paleozoic:
a paleomagnetic approach**

Maud Meijers

Members of the dissertation committee:

Dr. G. Muttoni
University of Milan

Prof. dr. A.I. Okay
Istanbul Technical University

Prof. dr. T.H. Torsvik
University of Oslo

Prof. dr. R.L.M. Vissers
Utrecht University

Prof. dr. M.J.R. Wortel
Utrecht University

The research of this thesis was carried out at:

Paleomagnetic Laboratory 'Fort Hoofddijk'
Department of Earth Sciences
Faculty of Geosciences
Utrecht University
Budapestlaan 17
3584 CD Utrecht
The Netherlands

2

and at:

Department of Tectonics and Structural Geology
Faculty of Earth and Life Sciences
VU University Amsterdam
De Boelelaan 1085
1081 HV Amsterdam
The Netherlands

ISBN: 978-90-5744-180-6

Tethyan evolution of the Black Sea region since the Paleozoic: a paleomagnetic approach

*Tethys evolutie in het Zwarte Zee gebied sinds het Paleozoïcum:
een paleomagnetische benadering*

(met een samenvatting in het Nederlands)

PROEFSCHRIFT

ter verkrijging van de graad van doctor aan de Universiteit Utrecht
op gezag van de rector magnificus, prof. dr. J.C. Stoof, ingevolge het besluit van het
college voor promoties in het openbaar te verdedigen op
woensdag 24 maart 2010 des middags te 2.30 uur

door
Mathilde Joseph Maria Meijers

geboren op 24 juli 1981
te Schinveld

Promotoren: Prof. dr. C.G. Langereis
Prof. dr. S.A.P.L. Cloetingh
Co-promotoren: Dr. R.A. Stephenson
Dr. D.J.J. van Hinsbergen

This thesis was accomplished with financial support from the Netherlands Research Centre for Integrated Solid Earth Sciences (ISES), the Netherlands Geosciences Foundation (ALW), the Netherlands Organization for Scientific Research (NWO). The research was carried out under the program of the Vening Meinesz Research School of Geodynamics (VMSG).

Contents

<i>Bibliography</i>	11
<i>Introductie en samenvatting (in Dutch)</i>	13
<i>Introduction and synopsis</i>	19
<i>Chapter 1</i>	
New late Paleozoic paleopoles from the Donbas Foldbelt (Ukraine): implications for the Pangea A vs. B controversy	25
<i>Chapter 2</i>	
Jurassic-Cretaceous low paleolatitudes from the circum-Black Sea region (Crimea and Pontides) due to True Polar Wander	51
<i>Chapter 3</i>	
Jurassic arc volcanism on Crimea (Ukraine): implications for the paleo-subduction zone configuration of the Black Sea region	85
<i>Chapter 4</i>	
Late Cretaceous to Paleocene oroclinal bending in the central Pontides (Turkey)	119
<i>Chapter 5</i>	
Pervasive Paleogene remagnetization of the central Taurides fold-and-thrust belt (southern Turkey) and implications for rotations in the Isparta Angle	147
<i>References</i>	185
<i>Acknowledgements</i>	211
<i>Curriculum Vitae</i>	215
<i>Appendices</i>	217

Bibliography

Chapter 1

Meijers, M.J.M., Hamers, M.F., van Hinsbergen, D.J.J., van der Meer, D.G., Kitchka, A., Langereis, C.G. and Stephenson, R.A., in review, New late Paleozoic paleopoles from the Donbas Foldbelt (Ukraine): implications for the Pangea A vs. B controversy, *Earth and Planetary Science Letters*

Chapter 2

Meijers, M.J.M., Langereis, C.G., van Hinsbergen, D.J.J., Kaymakci, N., Stephenson, R.A., and Altiner, D., in revision, Jurassic-Cretaceous low paleolatitudes from the circum-Black Sea region (Crimea and Pontides) due to True Polar Wander, *Earth and Planetary Science Letters*

Chapter 3

Meijers, M.J.M., Vrouwe, B., van Hinsbergen, D.J.J., Kuiper, K.F., Wijbrans, J., Davies, G.R., Stephenson, R.A., Kaymakci, N., Matenco, L. and Saintot, A., submitted, Jurassic arc volcanism on Crimea (Ukraine): implications for the paleo-subduction zone configuration of the Black Sea region, *Lithos*

Chapter 4

Meijers, M.J.M., Kaymakci, N., van Hinsbergen, D.J.J., Langereis, C.G., Stephenson, R.A. and Hippolyte, J.-C., in revision, Late Cretaceous to Paleocene oroclinal bending in the central Pontides (Turkey), *Tectonics*

Chapter 5

Meijers, M.J.M., van Hinsbergen, D.J.J., Dekkers, M.J., Altiner, D., Kaymakci, N. and Langereis, C.G., submitted, Pervasive Paleogene remagnetization of the central Taurides fold-and-thrust belt (southern Turkey) and implications for rotations in the Isparta Angle, *Geophysical Journal International*

M.J.M. Meijers contributed to:

Dupont-Nivet, G., Lippert, P.C., van Hinsbergen, D.J.J., Meijers, M.J.M. and Kapp, P., in review, Paleolatitude and age of the Indo-Asia collision, *Geology*

Introductie en samenvatting

Sinds Wegener's (1915) ontdekking van het supercontinent Pangea dat ontstond in het Paleozoïcum is er grote vooruitgang geboekt op het terrein van de plaat tektonische reconstructies. Sinds de late jaren '50 heeft paleomagnetisme bewezen een krachtige techniek te zijn om de positie van de continenten op Aarde door de tijd te reconstrueren. De ontdekking van Vine en Matthews (1963) dat de magnetische anomalieën op de zeebodem die parallel zijn aan de mid-oceanische ruggen het gevolg zijn van omkeringen van het aardmagneetveld, leidde tot de ontwikkeling van het concept van de plaattektoniek (McKenzie, 1966; McKenzie en Parker, 1967).

De continentconfiguratie van de Aarde in het Carboon en Perm echter, is al decennia een onderwerp van discussie. De Wegeneriaanse plaatsing van de noordelijke continenten (Laurussia) ten op zichte van de zuidelijke continenten (Gondwana), genaamd Pangea A, leidt in meerdere reconstructies tot een overlap van de continenten in equatoriale gebieden in het Carboon en Perm. Daarom stelde Irving (1977) voor om Laurussia ~3500 km naar het westen te plaatsen ten opzichte van Gondwana. Deze configuratie is bekend als Pangea B. Momenteel is er een algemene consensus dat tegen het eind van het Trias, een Pangea A configuratie was ontstaan. In deze configuratie worden de noordelijke en zuidelijke continenten gescheiden door een grote, driehoekvormige oceaan: de Tethys oceaan. Subductie van de Tethys oceaan onder Eurazië en de opening van een nieuwe oceaan ten zuiden van een serie langgerekte continenten die afkomstig zijn van de Afrikaanse continentrand leidde tot de vernieuwing van de oceaanorst die de twee continenten scheidde. Het opbreken van Pangea sinds het vroeg Jura had de convergentie van Afrika en Eurazië sinds het laat Krijt tot gevolg.

Analyse van de paleolatitute en de timing van collisie van de langgerekte continenten die van Afrika naar Eurazië bewogen, kan randvoorwaarden geven voor de evolutie van de Tethys oceaan, die inmiddels grotendeels verdwenen is door subductie onder Eurazië. Eén van de gebieden waar we het proces van Tethys subductie en accretie van continentale terreinen aan de zuidelijke Euraziatische continentrand kunnen bestuderen, samen met gerelateerde processen zoals *back-arc* opening en sluiting is het gebied rondom de Zwarte Zee.

Om onderscheid te kunnen maken tussen verschillende modellen die de evolutie van het Zwarte Zeegebied sinds het Paleozoïcum beschrijven hebben we een paleomagnetische studie uitgevoerd in dit gebied. Het is van belang hier dat bewegingen in het onderzoeksgebied grofweg noord-zuid gericht waren, waardoor de paleolatitute bepalingen die we verkrijgen uit paleomagnetische randvoorwaarden geven voor de verschillende modellen. De positie van de langgerekte keten van continenten ten opzichte van de Afrikaanse en Euraziatische continentranden kan worden bepaald door de verworven paleomagnetische data te vergelijken met de *apparent polar wander paden* (schijnbare poolbewegingspaden) die de beweging van de grote continenten door de tijd beschrijven. Rotatiedata van paleomagnetische data kunnen

informatie geven over plaatbotsingen die zich voordeden in het onderzoeksgebied. Om het geologisch verleden van de zuidelijke Euraziatische continentrand verder te reconstrueren, hebben we isotopische $^{40}\text{Ar}/^{39}\text{Ar}$ dateringen en geochemische analyses uitgevoerd waarmee we de ouderdommen en karakteristieken van het vulkanisch gesteente exact kunnen bepalen. De gesteenten werden tot nu toe een midden Jura ouderdom toegeschreven.

In een noord-zuid doorsnede door het Zwarte Zeegebied, komen we de volgende tectonische eenheden tegen: het Oost Europese Platform met een verdunde continentrand, genaamd het Scytische Platform, de Zwarte Zee, de Pontiden en het Anatolide-Tauride Blok. De eerste twee zijn, in ieder geval gedeeltelijk, onderdeel van de Oekraïne. De laatste drie zijn onderdeel van Turkije. De Tauriden waren onderdeel van het Afrikaanse continent, waarschijnlijk op zijn minst to het vroeg Trias, en hebben een kristallijn *basement* van Pan-Afrikaanse affiniteit. Scheiding van het continentale Tauriden platform van Afrika leidde tot haar beweging in de richting van de Euraziatische continentrand en de opening van de zuidelijke Neo-Tethys (ook wel İzmir-Ankara oceaan genoemd). Botsing van de Tauriden met de zuidelijke Euraziatische continentrand in het laat Paleoceen tot Eoceen resulteerde in de formatie van de Tauriden *fold-and-thrust* belt. Gedeeltelijk tegelijkertijd en vanaf het vroege Krijt, begon de Zwarte Zee zich te openen, meest waarschijnlijk als een *back-arc* bekken. Dit leidde tot een zuidwaartse beweging van de Pontiden ten op zichte van Eurazië en de Krim.

In **Hoofdstuk 1** van dit proefschrift presenteren we vroeg Carboon paleolatitudes data uit drie tijd intervallen en drie laat Carboon tot vroeg Perm paleopolen voor de Donbas Foldbelt (Oekraïne). Met name het Carboon *apparent polar wander* (APW) pad is slecht bepaald, waardoor meer betrouwbare data gewenst zijn (Torsvik en Cocks, 2005; Torsvik et al., 2008). De Donbas Foldbelt is een oorspronkelijk laat Devoon rift bekken dat later onder compressieve spanning heeft gestaan in het zuidelijke deel van het Oost Europese Platform. Het Oost Europese Platform was onderdeel van Baltica, dat op zijn beurt deel uit maakte van stabiel Laurussia in het Carboon en Perm. De gemonsterde Carboon sedimenten werden allemaal gecorrigeerd voor de inclinatie-verlaging met een model benadering: de elongatie/inclinatie (E/I) methode die gebaseerd is op het seculaire variatie model TK03.GAD van Tauxe en Kent (2004). Inclinatie-verlaging treedt op als gevolg van compactie tijdens begraving en resulteert in te lage latitudes. Het is een welbekend probleem in paleomagnetische data verkregen uit sedimenten. Onze paleomagnetische data van de Carboon kalkgesteenten en de Permische rode silt-en zandstenen laten een algehele noordwaartse beweging zien van de Donbas, van van latitudes net ten noorden van de evenaar tot $\sim 16^\circ\text{N}$. Deze latitudes zijn goed in overeenstemming of net iets hoger dan voorspeld vanuit de APW paden van de grote continenten. We moeten hierbij de kanttekening plaatsen dat er geen polen van Baltica (exclusief degenen afkomstig van Scandinavië) zijn opgenomen

in het Carboon APW pad. Voor het laat Carboon en vroeg Perm zijn de declinatie patronen in overeenstemming met het APW pad, maar de vroeg Carboon data laten een rechtsomdraaiende afwijking van het APW pad zien. De drie vroeg Carboon monster-locaties zijn gelegen in het meest zuidelijke deel van de Donbas Foldbelt, een gebied dat een afwijkende structurele trend laat zien ten op zichte van de rest van de *foldbelt*. Daarom gaan we er van uit dat deze afwijkende declinaties het gevolg zijn van strekkingsverschillen van de scheve gelaagdheid en plooiassen, en kunnen de data van onze oudste drie locaties alleen paleolatitudes geven en geen paleopolen. Onze laat Carboon en vroeg Perm paleopolen zijn zeer relevant voor de Pangea A versus Pangea B discussie. De reconstructie van Laurussia gebaseerd op deze drie polen laat geen overlap zien met Gondwana, waardoor een Pangea B configuratie niet vereist is. Recente studies die Laurentia (gesitueerd op het zuidelijk halfrond in het Carboon en onderdeel van Laurasia) polen presenteerden die voor inclinatie gecorrigeerd werden laten opmerkelijk genoeg het tegenovergestelde van onze bevindingen zien. Dit toont dat de Pangea A versus B controversie schijnbaar even levendig is dan 30 jaar terug, na de eerste introductie (Irving, 1977).

In **Hoofdstuk 2** presenteren we nieuwe paleolatitude data gecombineerd met literatuurdata van Jura en het Krijt sedimenten uit de Krim en de Pontiden, om de positie van de Euraziatische continentrand in het Mesozoïcum te bepalen. Op basis van betrouwbaarheidscriteria hebben we een groot deel van de data verworpen voor paleolatitude analyse. Om te corrigeren voor de inclinatie-fout hebben we op voldoende grote datasets de E/I methode toegepast (Tauxe en Kent, 2004). De beschikbare paleolatitude data laten een positie van de Krim en de Pontiden aan de Euraziatische continentrand zien in het vroeg Jura en laat Krijt, bij vergelijking met de APW paden (Besse en Courtillot, 2002; Torsvik et al., 2008). Echter, onze data die paleolatitude-randvoorwaarden geven voor het laat Jura en het vroegste Krijt, laten een positie zien die opvallend veel lager is dan verwacht kan worden van de APW paden; ~1600 km zuidelijker. Muttoni et al. (2005) hebben een vergelijkbare zuidelijke positie laten zien voor de Adria plaat (een onderdeel van stabiel Afrika) in het exact hetzelfde tijdsinterval. Op basis hiervan concludeerde Muttoni et al. (2005) dat deze zuidwaartse beweging onderschat wordt in de APW paden. Wij zijn het eens met deze observatie, maar wij beweren dat het niet waarschijnlijk is dat deze beweging het gevolg is van een werkelijke verplaatsing van de Afrikaanse en Euraziatisch platen ten op zichte van de aardmantel. Deze periode werd namelijk gekenmerkt door grote subductiezones die de Afrikaanse en Euraziatische platen omringden en scheidden en fungeerden als een anker in de aardmantel. Recentelijk kwantificeerden Steinberger en Torsvik (2008) een mechanisme dat verantwoordelijk is voor de verplaatsing van continenten, zonder de continenten te bewegen ten op zichte van de aardmantel: *true polar wander* (TPW; of werkelijke poolbeweging). Tijdens periodes van TPW roteren de gehele korst en mantel van de Aarde ten op zichte van de draaias van de Aarde (en daardoor

het magnetische veld) rond een Euler pool die gepositioneerd is op de evenaar. TPW is het gevolg van dichtheidsherverdelingen in de mantel, die het gevolg kunnen zijn van het zinken van relatief koude oceanische lithosfeer in de mantel of het rijzen van mantelpluimen. Het laat Jura poolpad is een periode waarin TPW lage latitudes zou veroorzaken in het huidige Oostelijk Middellandse Zeegebied. Op basis hiervan concluderen wij dat de zuidwaartse beweging het gevolg is van TPW.

Het onderzoek in **Hoofdstuk 3** is gebaseerd op isotopische $^{40}\text{Ar}/^{39}\text{Ar}$ dateringen en geochemische röntgenstraling fluorescentie (XRF; *X-ray fluorescence*) analyses die werden uitgevoerd op magmatische gesteenten van het Krim schiereiland. We hebben deze studie uitgevoerd om de ouderdom en eigenschappen van magmatische gesteenten vast te stellen die voorheen een midden Jura ouderdom toegeschreven werden. Sinds het Trias wordt het onderzoeksgebied gekarakteriseerd door opening van de Neo-Tethys oceaan. Omdat convergentie van de Afrikaanse en Euraziatische continenten pas aanving in het laat Krijt, werd rifting (ook wel spreiding genoemd) geacomodeerd door subductie onder de zuidelijke Euraziatische continentrand. In de Turkse Pontiden kunnen overblijfselen van Trias en Krijt subductie gevonden worden. Echter, de Jurassische Tethys subductie geschiedenis is veel minder goed bekend. De midden Jura ouderdommen die voorheen aan de magmatische gesteenten werden toegeschreven, zijn gebaseerd op onderlinge relaties en contacten tussen gesteenten van verschillende ouderdommen en op biostratigrafische gegevens. Onze resultaten laten zien dat de magmatische gesteenten die gemonsterd werden in het westelijke deel van het schiereiland inderdaad midden Jura ouderdommen hebben. De monsters van het magmatische Karadag complex in het centrale deel van het schiereiland hebben echter vroegste Krijt ouderdommen. Beide ouderdomsgroepen laten de eigenschappen zien van een vulkanische arc, die subductie onder de Krim getuigt. Op basis van onze data en gepubliceerde data stellen wij noordwaartse subductie onder de Krim en Pontiden voor in de onderzochte periode. Paleogeografische reconstructies van het laat Jura (Dercourt et al. 2000; Barrier en Vrielynck, 2008) vereisen grote afstanden tussen de subductietrog en de vulkanische arc, en daarom stellen wij voor dat de hoek tussen de subducerende plaat en het aardoppervlak laag was.

In **Hoofdstuk 4** verlaten we het Jura tijperk en gaan we naar de Krijt tot Eocene geschiedenis van het Zwarte Zeegebied. De centrale Pontiden zijn gekenmerkt door een opvallende noordwaartse bolvormige geometrie die terug te vinden is in de structurele trend, d.w.z. de strekking van de lagen, plooiassen en breuken. Deze geometrie zou een oorspronkelijk kenmerk kunnen zijn dat het gevolg is van initiële dekbladstapel vorming, maar het zou ook een jongere fase van deformatie kunnen representeren, die resulteerde in zogenaamde oroclinale buiging. Oroclinale buiging zou een belangrijke, regionale deformatie fase vereisen van de bestaande oost-west georiënteerde *fold-and-thrust belt*. Om na te gaan of deze geometrie het gevolg kan zijn van oroclinale buig-

ing, hebben we een paleomagnetische studie uitgevoerd op Krijt tot Eocene gesteenten uit de centrale en oostelijke Pontiden om de rotatiegeschiedenis van het gebied te bepalen. We hebben onze data met data van eerdere studies gecombineerd en daarop strikte betrouwbaarheidscriteria toegepast. De laat Krijt rotatiepatronen laten rotaties zien die ongeveer loodrecht op de structurele trend staan, terwijl laat Paleoceen tot Eoceen datasets geen rotaties laten zien. Daarom concluderen we dat orocline vorming gebeurde tijdens het laatstmogelijke Krijt tot vroege Paleoceen. We bediscussieren drie mogelijke mechanismen die oroclinale buiging veroorzaakt kunnen hebben: botsing van het microcontinent Kargı met de Euraziatische continentrand, opening van de Zwarte Zeebekkens en botsing van het Anatolide-Tauride block met de Pontiden. Grotendeels gebaseerd op tijdsargumenten, beweren wij dat het laatstgenoemde mechanisme het meest waarschijnlijk oroclinale buiging heeft veroorzaakt.

In het laatste deel van dit proefschrift, **Hoofdstuk 5**, presenteren we paleomagnetische data uit de centrale Tauriden, een continentaal blok ten zuiden van de İzmir-Ankara-Erzincan sutuur. Het doel van dit onderzoek was het reconstrueren van een poolpad van dit continentale blok, dat van de Afrikaanse naar de Euraziatische continentrand bewoog in het Trias tot laat Krijt. Daarvoor hebben we gesteente gemonsterd in drie secties/locaties in de relatief autochtone Geyikdağ en Aladağ eenheden, die in ouderdom variëren van vroeg Carboon tot Paleoceen. De opvallend gelijkende paleolatitudes-resultaten in de lange tijdsperiode en omgekeerde polariteiten in gesteenten die werden afgezet tijdens het Krijt Nomaal Superchron, leidden ons tot de gedachte dat een remagnetisatie gebeurtenis heeft opgetreden in dit gebied. Om de mogelijkheid remagnetisatie verder te onderzoeken hebben we een nieuwe *end-member* model benadering gebruikt op isotherme remanente remagnetisatie (IRM) acquisitie curves. De modelresultaten van het preferente drie *end-member* model bevestigen de geremagnetiseerde aard van de gemonsterde gesteenten. De declinatie trends in de centrale Tauriden zijn in overeenstemming met resultaten van eerdere studies (e.g. Kissel et al., 1993). Een vergelijking van onze data met eerder gepubliceerde data uit de Isparta Angle zaait twijfel over de voorheen gerapporteerde vroeg tot midden Mioceen remagnetisatie gebeurtenis uit een studie van Morris en Robertson (1993). Hun Trias data uit de zuidwestelijke Antalya dekbladstapel na correctie voor scheve gelaagdheid zijn in goede overeenstemming met de primaire magnetisaties van magnetostratigrafische studies van Gallet et al. (1992; 1994; 2000), die de Tauriden aan de Afrikaanse continentrand plaatsen in deze tijd. Rotaties van deze studies impliceren dat we een rechtsomdraaiende rotatie documenteren voor de zuidwestelijke Antalya dekbladstapel sinds het Trias. Dit is vrij opzienbarend, omdat het vrijwel gelijk is aan de post-Eocene ($\sim 40^\circ$) rotaties in de centrale Tauriden. Voor de resultaten van Morris en Robertson (1993) die duidelijk geremagnetiseerd zijn beargumenteren we dat remagnetisatie eerder plaatsvond, in het Paleoceen tot Eoceen in plaats van in het vroeg tot midden Mioceen.

Introduction and synopsis

Since Wegeners (1915) recognition of the supercontinent Pangea that assembled in the Paleozoic, large advances in plate tectonic reconstructions have been made. Since the late 1950s, paleomagnetism has proven a powerful tool to reconstruct the positions of the Earth's continents through time. Vine and Matthews (1963) discovery that the magnetic anomalies on the sea floor that are parallel to mid-ocean ridges resulted from reversals of the Earth's magnetic field, led to the development of the concept of plate tectonics (McKenzie, 1966; McKenzie and Parker, 1967).

The Carboniferous and Permian configuration of the Earth's continents however, is already a matter of a debate for decades. The Wegenerian placement of the northern continents (Laurussia) with respect to the southern continents (Gondwana), named Pangea A, leads in several reconstructions to an overlap of the continents in the equatorial realm in the Carboniferous and Permian. Therefore, Irving (1977) proposed the positioning of Laurussia ~3500 km west with respect to Gondwana, a configuration known as Pangea B. At present, there is a general consensus that by the Triassic, a Pangea A configuration of the continents had been reached. In this configuration, the northern and southern continents were separated by a large, triangular-shaped ocean: the Tethys ocean. Subduction of the Tethys ocean below Eurasia and the opening of a new ocean behind a series of ribbon-continents that rifted of the African margin, led to the renewal of the oceanic crust separating the two continents. The break-up of Pangea since the early Jurassic resulted in the convergence between Africa and Eurasia since the late Cretaceous.

Paleolatitude analysis and timing of collision of the continental terranes that moved from the African to the Eurasian margin, can give constraints on the evolution of the Tethys oceans that largely subducted below Eurasia. One of the regions where we can study the process of Tethyan subduction and the accretion of continental terranes to the southern Eurasian margin, together with related processes such as back-arc opening and closure is the circum-Black Sea region.

To distinguish between varying models on the evolution of the circum-Black Sea region since the Paleozoic, we conducted a paleomagnetic study in this area, since motions in the Tethyan realm were roughly north-south directed and paleomagnetism can constrain paleolatitude. The position of continental terranes with respect to the African and Eurasian margins can be determined by comparing the acquired paleomagnetic data to the apparent polar wander paths that describe the motion of the Earth's major continents through time. Rotational data from paleomagnetic data can give information on collisional events that occurred in the region. Furthermore, we carried out isotopic $^{40}\text{Ar}/^{39}\text{Ar}$ dating and geochemical analysis to exactly date and characterize supposedly middle Jurassic volcanics on Crimea, in order to reconstruct part of the geological history of the southern Eurasian margin.

In a north-south transect through the Black Sea area, the following tectonic

blocks can be found: the East European Platform (EEP) with its thinned margin – the Scythian Platform, the Black Sea, the Pontides and the Anatolide-Tauride Block. The first two blocks are, at least partly, located in Ukraine, the latter three in Turkey. The Taurides were part of Africa, probably at least until the early Triassic, and have a basement of Pan-African affinity. Separation of the continental Tauride platform from Africa led to its motion towards the Eurasian margin, and to opening of the southern Neo-Tethys (or İzmir-Ankara ocean). Collision of the Taurides with the southern Eurasian margin in the late Paleocene to Eocene led to the formation of the Taurides fold-and-thrust belt. Partly simultaneous, and from early Cretaceous times onwards, the Black Sea started to develop, likely as a back-arc basin, leading to the motion of the Pontides away from the Eurasian margin and Crimea.

In **Chapter 1** of this thesis, we present early Carboniferous paleolatitude constraints from three time intervals and three late Carboniferous to early Permian paleopoles for the Donbas Foldbelt (Ukraine). Especially the Carboniferous apparent polar wander (APW) path is poorly constrained, and therefore requires more reliable data (Torsvik and Cocks, 2005; Torsvik et al., 2008a). The Donbas Foldbelt is an inverted late Devonian rift basin on the southern East European Platform that was part of Baltica, which in turn was part of stable Laurussia in the Carboniferous and Permian. The sampled Carboniferous sediments were all corrected for inclination shallowing with a model approach: the elongation/inclination (E/I) method, based on the secular variation model TK03.GAD of Tauxe and Kent (2004). Inclination shallowing as a result of compaction during burial is a well-known problem in paleomagnetic data from sediments, and it results in too low latitudes. The paleomagnetic data of the Carboniferous limestones and Permian red beds show a general northward motion of the Donbas, from latitudes just north of the equator to $\sim 16^\circ\text{N}$. They are in good agreement or slightly higher than predicted by the APW paths of the major continents. It must be mentioned here that no Baltica poles (excluding those from Scandinavia) are incorporated in the Carboniferous APW paths. Declination patterns agree well with the late Carboniferous and early Permian APW path, but show a clockwise deviation from the APW path in the three oldest, early Carboniferous sites. The three early Carboniferous sites were sampled in the southernmost part of the Donbas Foldbelt, a region that shows a diverging structural trend from the rest of the foldbelt, and we consider that the deviating declinations are resulting from the strike-differences of strata and fold-axes. Therefore, our oldest three sites can only provide paleolatitude constraints and no paleopoles. Our late Carboniferous and early Permian paleopoles are very relevant for the Pangea A versus B discussion. The reconstruction of Laurussia on the basis of our three poles shows that there is no overlap with Gondwana. Based on our data, a Pangea B configuration is therefore not required. Recent studies that showed inclination-error corrected poles for Laurentia (situated at the southern hemisphere in the Carboniferous as a part of Laurussia), however, show exactly the

opposite. Therefore, the Pangea A versus B controversy is seemingly as lively as it was more than 30 years ago, when it was first introduced (Irving, 1977).

In **Chapter 2** we present Jurassic and Cretaceous paleolatitude data from sediments from Crimea and the Pontides, combined with data from the literature, to constrain the position of the Eurasian margin in the Mesozoic. On the basis of reliability criteria, we rejected many datasets for paleolatitude analysis. To correct for inclination error, we used the E/I method (Tauxe and Kent, 2004), provided that the number of samples was large enough. The available paleolatitude constraints show a position of Crimea and the Pontides at the Eurasian margin in the early Jurassic and late Cretaceous with respect to the APW paths (Besse and Courtillot, 2002; Torsvik et al., 2008a). Our data that provide constraints for the late Jurassic and earliest Cretaceous, however, show remarkably lower paleolatitudes than can be expected from the APW paths; ~1600 km more south. Muttoni et al. (2005) have shown a similar southerly position for the Adria plate (as part of stable Africa) in exactly the same time span, which led Muttoni et al. (2005) to conclude that the southward motion of the plates is underestimated in the APW paths. We agree with this observation, but we argue it is unlikely that this motion resulted from actual movement of the African and Eurasian plates with respect to the mantle. This period was characterized by major subduction zones that surrounded and separated the African and Eurasian continents, and likely functioned as an anchor in mantle. Recently, Steinberger and Torsvik (2008) quantified a mechanism that is responsible for the motion of continents, without moving continents with respect to the mantle: true polar wander (TPW). During periods of TPW, the entire crust and mantle of the Earth rotate with respect to its spin axis (and therefore magnetic field) around an Euler pole positioned at the equator, as a result of density redistributions in the mantle. The late Jurassic is such a period of TPW, which would cause low paleolatitudes in the present-day eastern Mediterranean area. Therefore, we conclude that the southward motion is resulting from TPW.

The research in **Chapter 3** is based on isotopic $^{40}\text{Ar}/^{39}\text{Ar}$ dating and geochemical X-ray fluorescence (XRF) analysis of magmatic rocks from the Crimean peninsula. We carried out this study to precisely date and characterize the supposedly middle Jurassic magmatics in Crimea. Since the Triassic period, the area is characterized by opening of the Neo-Tethys ocean. Because convergence of the African and Eurasian continents did not initiate until the late Cretaceous, rifting should have been accommodated by subduction below the southern Eurasian margin. In the Turkish Pontides remnants of Triassic and Cretaceous Tethys subduction can be found. The Jurassic history of Tethys subduction, however, is much less well constrained. The middle Jurassic ages that were previously assigned to the magmatic rocks, are based on cross-cutting relationships and biostratigraphy. Our results show that the magmatic rocks that were sampled in the western part of the peninsula, yield middle Jurassic ages.

The samples from the magmatic Karadag complex in the central part of the peninsula however, yield mostly earliest Cretaceous ages. Both age groups show the geochemical characteristics of a volcanic arc, evidencing subduction below Crimea. On the basis of our data and published data, we propose northward subduction below Crimea and the Pontides in the researched time span. Paleogeographic reconstructions from the late Jurassic (Dercourt et al., 2000; Barrier and Vrielynck, 2008) would require large trench-arc distances, and therefore we propose flat-slab subduction in this time span.

In **Chapter 4**, we leave the Jurassic period and move to the Cretaceous to Eocene history of the Black Sea region. The central Pontides are characterized by a peculiar northward convex geometry that is reflected in the structural trend, i.e. bedding strike, fold axes and faults. This geometry could be an original feature that developed during initial nappe stacking, but it may represent a younger phase of deformation, resulting in oroclinal bending. Oroclinal bending would require major, regional deformation of the pre-existing east-west striking fold-and-thrust belt. To check whether the geometry could result from oroclinal bending, we carried out a paleomagnetic study on Cretaceous to Eocene rocks from the central and eastern Pontides to determine the rotational history of the area. We combined our data with data from previous studies, and applied strict reliability criteria to all data sets. The late Cretaceous rotation pattern shows rotations that are approximately perpendicular to the structural trend, whereas the late Paleocene to Eocene data sets yield no rotation. Therefore, we conclude that orocline formation occurred during the latest Cretaceous to early Paleocene. We discuss three possible mechanisms that could have caused oroclinal bending: accretion of the Kargı microcontinent to the Eurasian margin, opening of the Black Sea basins and collision of the Anatolide-Tauride block with the Pontides. Mainly on the basis of timing, we argue that the latter mechanism is the most likely cause of oroclinal bending.

In the last part of this thesis, **Chapter 5**, we present paleomagnetic data from the central Taurides, situated south of the İzmir-Ankara-Erzincan suture. We attempted to construct a pole path for this continental block that moved from the African to the Eurasian margin in the Triassic to late Cretaceous. Therefore, we sampled three sections/localities ranging in age from early Carboniferous to Paleocene, in the relatively autochthonous Geyikdağ and Aladağ units. The remarkably similar paleolatitudes in this very long time span, and reversed polarities in rocks that were deposited during the Cretaceous Normal Superchron, lead us to suspect a remagnetization event in the area. To further research the possibility of remagnetization, we used a novel end-member modeling approach on isothermal remanent magnetization (IRM) acquisition curves. The modeling results of the preferred three end-member model confirm the remagnetized nature of the sampled rocks. The declination trends in the central Taurides are in agreement with results from previous studies (e.g. Kissel et al., 1993).

A comparison of our data with previously published data from the Isparta Angle casts doubt on the earlier reported early to middle Miocene remagnetization event in a study by Morris and Robertson (1993). Their Triassic data from the southwestern Antalya nappes after tilt correction are in good agreement with the primary magnetizations from magnetostratigraphic studies by Gallet et al. (1992; 1994; 2000), positioning the Taurides at the African margin. Rotations from these studies imply that we document a clockwise rotation for the southwestern Antalya Nappes since the Triassic. This is rather remarkable, because it is similar to the post-Eocene ($\sim 40^\circ$) rotation of the central Taurides. For those results from Morris and Robertson (1993) that are clearly remagnetized, we argue that remagnetization has occurred earlier, in the Paleocene to Eocene rather than the early to middle Miocene.



Horse rider in the Donbas region

CHAPTER 1

New late Paleozoic paleopoles from the Donbas Foldbelt (Ukraine): implications for the Pangea A vs. B controversy

The Carboniferous to early Permian apparent polar wander (APW) path for Eurasia is not well constrained, because of the paucity of reliable paleomagnetic poles. This is at least partly responsible for the Pangea A vs. Pangea B controversy in the early Permian: is the overlap between the northern and southern continents during the early Permian caused by a lack of reliable paleomagnetic data (Pangea A) or must a large displacement along a mega-shearzone be invoked (Pangea B)?

Here, we present results from six paleomagnetic sampling sites ranging in age from the early Carboniferous to the early Permian from sedimentary rocks in the Donbas Foldbelt (Ukraine) to improve the Carboniferous – early Permian APW path for Eurasia and to contribute to solving the Pangea A vs. Pangea B controversy. Six time intervals were sampled in the Donbas Foldbelt (eastern Ukraine), which was filled with sediments and volcanic units during the late Devonian to Permian syn- and post-rift subsidence phases. We present results from sediments that were corrected for inclination shallowing with the elongation/inclination (E/I) method.

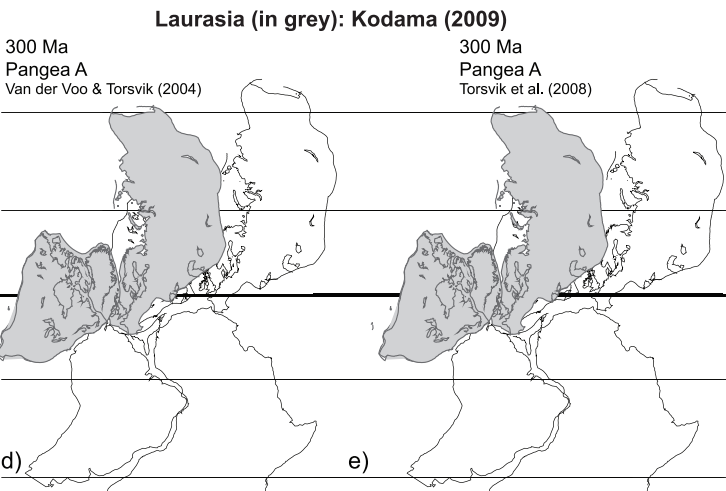
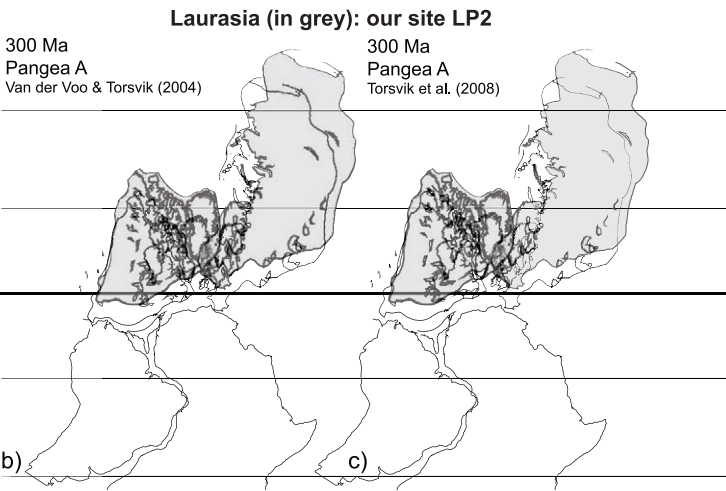
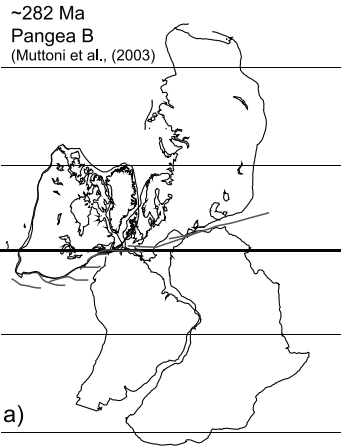
We conclude that there is a general northward movement of the Donbas Foldbelt: the resulting paleolatitudes are slightly but generally significantly higher than expected from existing APW paths. The late Carboniferous to early Permian data provide three new reliable paleopoles for Eurasia. The early Permian pole does not necessarily require a Pangea B reconstruction. It results in higher paleolatitudes for Laurussia in the early Permian and removes the overlap between Gondwana and Pangea. We also reconstructed the position of Laurussia based on Carboniferous Laurentian poles recently corrected for inclination shallowing, which clearly favours a Pangea B configuration. It seems that the Pangea A versus B debate is as lively as before. The three early Carboniferous paleopoles give reliable paleolatitudes, but declinations significantly deviate from the expected directions. We argue that the southernmost part of the Donbas Foldbelt underwent a counterclockwise rotation, related to Mesozoic compressional events that are recognized in paleostress analyses.

1. Introduction

Pangea is the youngest in a series of postulated supercontinents that assembled most of the Earth's continents. The reconstruction of Pangea stems from Wegener's recognition (1915) that the modern Atlantic margins may once have fit together. Subsequently, this assemblage was further constrained by linking similar paleontological and lithostratigraphical paleogeographic domains (Köppen and Wegener, 1924; Du Toit, 1937). The identification of Pangea formed a crucial basis for the concept of plate tectonics, one of the most fundamental discoveries in Earth Sciences. Pangea existed from the late Paleozoic to early Mesozoic, and broke up since the Jurassic, finally leading to the present-day configuration of oceans and continents. For the break-up history an array of geological and geophysical techniques is available, including reconstruction of sea floor spreading through marine magnetic anomalies (Heezen, 1960; Dietz, 1961), hotspot tracks (Richards et al., 1989; Müller et al., 1993; Norton, 2000) and paleomagnetically constrained apparent polar wander (APW) paths (Creer et al., 1954; Besse and Courtillot, 2002; Torsvik et al., 2008a).

The history of assembly as well as the final configuration and subsequent break-up of Pangea is essential to constrain the starting point of our present-day plate tectonic configuration and to define rates and dimensions of plate tectonic motion. The break-up history can well be constrained through the record of marine magnetic anomalies, but constraining of Pangea's assembly largely relies on APW path reconstructions. Hence, we need more reliable and accurate paleomagnetic poles, because their scarcity leaves room for the ongoing controversy on the position of northern Pangea (Laurussia) with respect to southern Pangea (Gondwana) during the Permo-Carboniferous. In particular, paleomagnetic data provide paleolatitudes and rotations of continents, but no paleolongitude constraints. Depending on the selection of paleomagnetic data, a paleolatitudinal overlap exists between the northern and southern continents in the equatorial realm during the late Carboniferous and Permian, that can be as large as 15° (or ~1650 km). The first recognition of this overlap by Irving (1977) led him to propose a so-called Pangea B configuration (Fig. 1.1a), in which a shear zone with a mainly longitudinal displacement of ~3500 kilometres during the Permo-Triassic places Gondwana east of Laurussia in the early Permian. On the

Figure 1.1 Pangea reconstructions (in white) at a) 282 Ma after Muttoni et al. (2003), where the overlap between the northern and southern continents is removed by introducing a large shear zone, b) and d) in white, reconstruction at 300 Ma following Torsvik and Van der Voo (2002); c) and e) in white, reconstruction at 300 Ma following Torsvik et al. (2008a). In the b) and c) there is no overlap between the northern and southern continents. b) and c) in grey: Laurussia reconstruction on the basis of our site LP2 (299 Ma); d) and e) in grey: Laurussia reconstruction on the basis of the inclination shallowing corrected pole for the Glenshaw Formation of Kodama (2009). Eurasian (Laurussian) poles are calculated from Laurentian (Eurasian) poles using a Bullard fit (Bullard et al., 1965), with an Euler pole at 88°N, 27°E (angle= 38°). Iberia was not included in the reconstructions. On the basis of our site LP2, a Pangea B reconstruction is not required. The corrected Glenshaw pole however, results in a large overlap between Laurussia and Gondwana in both reconstructions, clearly requiring a Pangea B type configuration.



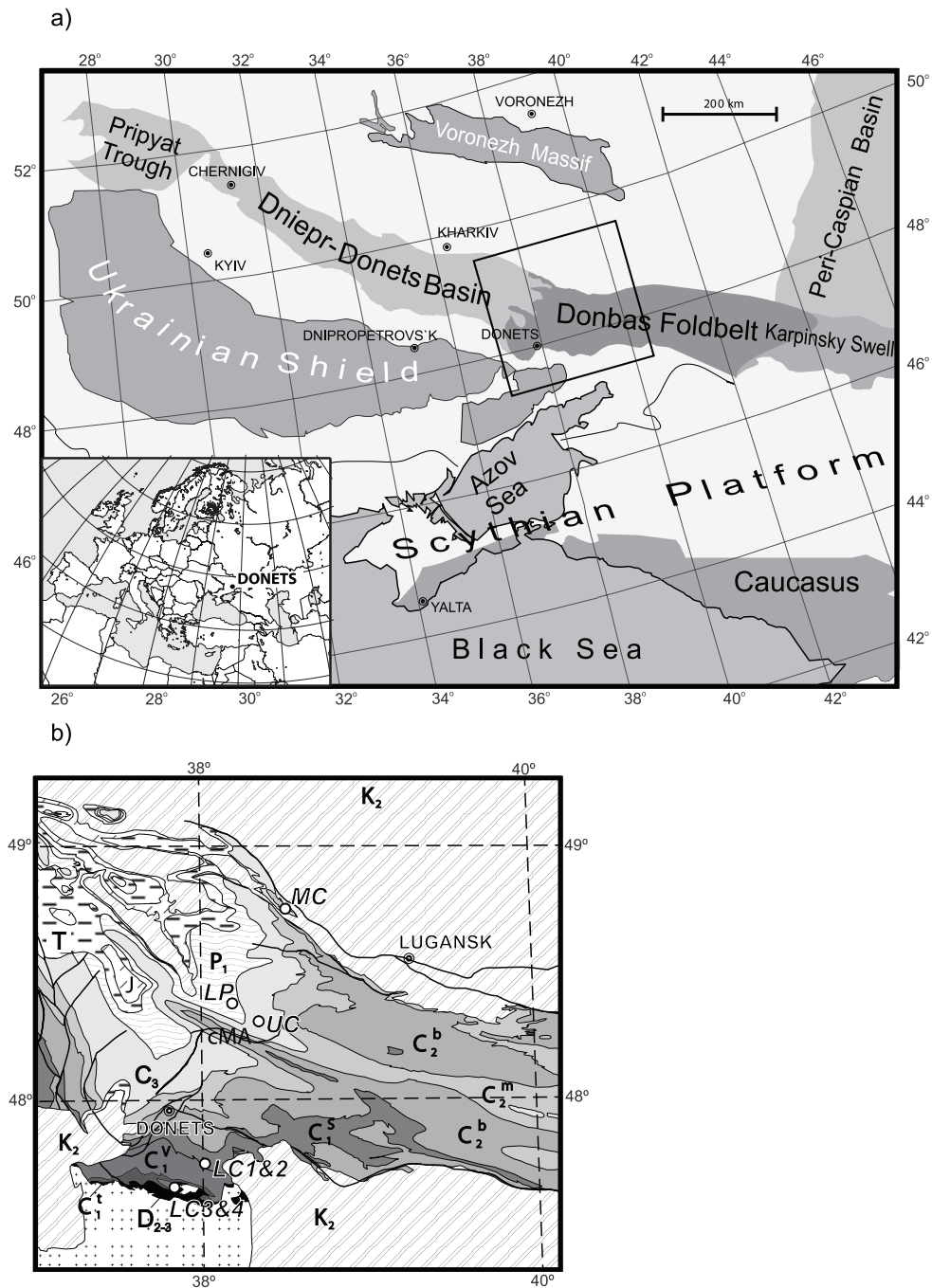


Figure 1.2 a) Tectonic map of the southern part of the East European Craton, showing the Late Devonian Pripjat-Dniepr-Donets rift basin, and the inverted Donbas Foldbelt. Rectangle indicates the location of Fig. 1.2 b. b) Cenozoic subcrop map of the Donbas Foldbelt around Donetsk (modified after Stovba and Stephenson, 1999), indicating the paleomagnetic sampling sites (LC3&4, LC1&2, MC, UC and LP). D₂₋₃, Middle Devonian–Upper Devonian; C₁^t, Tournaisian; C₁^v, Viséan; C₁^s, Serpukhovian; C₂^b, Bashkirian; C₂^m, Moscovian; C₃, Kasimovian-Gzhelian; P₁^{as}, Asselian; P₁^s, Sakmarian; T, Triassic; J, Jurassic; K₂, Upper Cretaceous; cMA, central Main Anticline.

basis of a new compilation of paleomagnetic data, Morel and Irving (1981) propose a transition from Pangea B to Pangea A to occur mainly in the Permian and Triassic, whereas Torcq et al. (1997) suggest a Triassic transformation. More recently, Muttoni et al. (1996; 2003; 2009) argued for the necessity of a Pangea B type reconstruction on the basis of paleomagnetic data from Adria, as a part of the African plate (Fig. 1.1a) and propose a transition from Pangea B to Pangea A in the Permian. The Triassic overlap between the northern and southern continents has disappeared, since more paleomagnetic data have become available. Other authors, however, question the necessity for Pangea B, and suggest that the overlap is caused by a lack of sufficient high quality paleomagnetic data (e.g. inclination shallowing due to compaction) (Rochette and Vandamme, 2001; Van der Voo and Torsvik, 2004) or to an octupolar contribution to the Earth's magnetic field (Kent and Smethurst, 1998; Van der Voo and Torsvik, 2001; Torsvik and Cocks, 2004). Most studies (e.g. Van der Voo and Torsvik (2004)) also question the quality of assigned ages.

Numerous authors have attempted solving the Pangea controversy that was identified in paleomagnetic data, by researching independent lines of evidence. Evidence for a shear zone that may have accommodated the Pangea B to Pangea A transformation was first proposed in the late-70's by Arthaud and Matte (1977). Based on their data review on rifts that extend from the Appalachians to the Urals, they conclude that the Pangea transformation occurred in the in the late Paleozoic. Later studies, by e.g. Schaltegger and Brack (2007) on magmatism related to shearing, seem to confirm the scenario of a Permian Pangea B to A transition. However, a number of rift basins that are possibly associated with Pangea transformation, have been explained differently by Gutierrez-Alonso et al. (2008). They explain the shear zone in the central part of a Pangea A world and rift basins that are radially positioned in the outer part of Pangea by introducing a novel model of 'self-subduction' of the Pangean plate.

Lines of evidences from climatic reconstructions, based on palynology were investigated by e.g. Angiolini et al. (2007). By coupling palynology, ocean circulation patterns and paleomagnetic data, they reconstruct the early Permian landmasses to a Pangea B configuration. Geophysical data were used by Torsvik et al. (2008b) to develop a hybrid plate motion reference frame that places reconstructed large igneous provinces of the past 300 Myr above the edges of large low shear wave velocity provinces, enabling correlation of surface processes to the deep mantle. In their reconstructions, a Pangea A assemblage of the continents is favored. Recently, van der Meer et al. (2010) have shown that tomography constrains the paleolongitude of subducted slabs, but unfortunately only has the required resolution until the late Permian (260 Ma), showing a Pangea A configuration at that time. Decades after introduction of the Pangea B configuration, the Pangea controversy remains a matter of debate. The solution could come from enlarging the paleomagnetic database, by supplying well-dated paleomagnetic data from the stable continents.

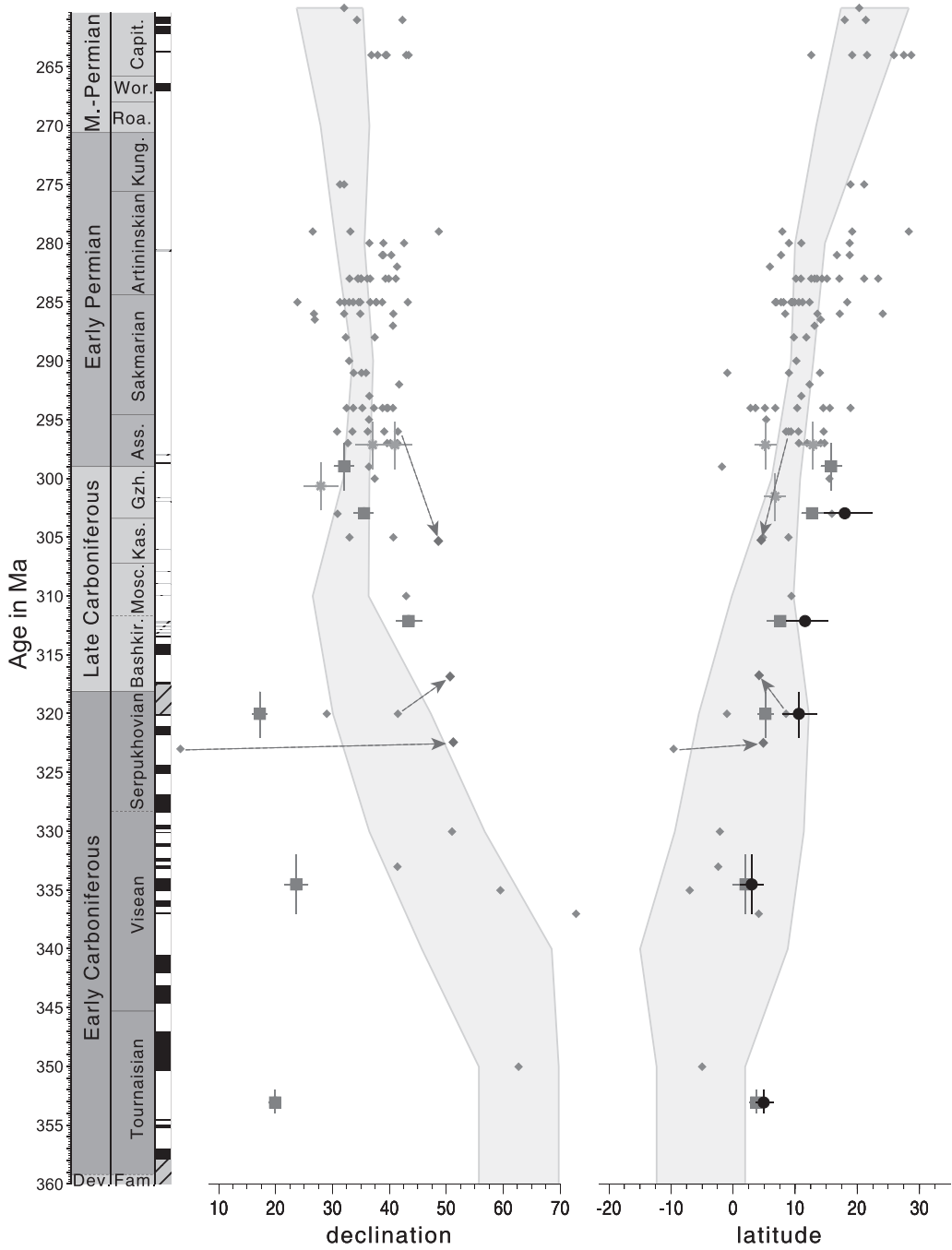
Only very few Carboniferous paleomagnetic poles exist for Laurussia, which formed the major constituent of northern Pangea. Laurussia included the late Devonian and younger Dniepr-Donets basin in present-day Ukraine (Fig. 1.2). Here, we present paleomagnetic results of six age intervals from lower Carboniferous to lower Permian sediments in the Donbas foldbelt, a mildly compressively deformed segment of the Dniepr-Donets basin, and we discuss the results within the context of the Pangea A versus B controversy.

2. Geological setting

The Donbas Foldbelt is the inverted southeasternmost segment of the NW-SE trending Pripjat-Dniepr-Donets Basin (DDB), which formed since the middle-late Devonian (Stephenson et al., 2006). It is located in the southern part of the East European Craton (EEC) (Fig. 1.2). The EEC was part of Baltica until the early Paleozoic, after which it amalgamated with Laurentia to form Laurussia. The DDB extends from Belarus to southern Russia, linking with the Karpinsky Swell further to the southeast (Fig. 1.2). To the north it is bounded by the (Archean-) Paleoproterozoic Voronezh Massif, to the south by the Ukrainian Shield, also of (Archean-) Paleoproterozoic age. The DDB deepens towards the southeast, with sediments having a maximum thickness of ~2 km in the Pripjat Through in the northwest and ~22 km in the Donbas Foldbelt (Chekunov et al., 1993; Stovba et al., 1996). In middle-late Devonian times pre- and syn-rift sedimentary and volcanic units were deposited on top of the crystalline basement of the EEC followed by the deposition of Carboniferous and Permian post-rift sequences as a result of thermal subsidence in the Permo-Carboniferous (Van Wees et al., 1996). Relatively thin units of Tournaisian and lower Viséan carbonates and thick upper Viséan to upper Carboniferous successions of dominantly paralic clastic sediments were deposited unconformably on top of the basement and the Devonian sediments (Stovba et al., 1996). Permian sediments are scarce in the Donbas Foldbelt,

Figure 1.3 Paleomagnetic directions, correlated to the GTS 2008 (Ogg et al., 2008), see section 3.1 for explanation. Vertical bars denote age errors. Blue closed squares indicate the mean formation directions (declination, latitude) and their errors (blue horizontal bars, ΔD_x , $\Delta \lambda$ (calculated from ΔI_x)) from the present study (Table 1.1). Black closed circles in the right panel indicate paleolatitude resulting from inclination correction with the TK03.GAD model (Tauxe and Kent, 2004), horizontal bars shows the 95% bootstrap error range. Green star indicates data points from Iosifidi et al. (submitted) (one late Carboniferous and two Permian data points). Grey shaded area shows the ΔD_x , $\Delta \lambda$ error envelope of the Eurasian APW path from Torsvik et al. (2008a) for 310-260 Ma and the Laurussia polepath from Torsvik and Cocks (2005) for 360-320 Ma, calculated for the city of Donets (48°N, 37.8°E). Red diamonds are the raw data entries from Eurasia and North America used to construct these APW paths. Purple arrows and diamonds shows the effect of correction for inclination error and improvement of dating of North American poles by Kodama (2009) and Bilardello and Kodama (2009) on the declination/latitude calculations for the Donbas. Dev.= Devonian, Fam.= Famennian, Bashkir.= Bashkirian, Mosc.= Moscovian, Kas.= Kasimovian, Gzh.= Gzhelian, Ass.= Asselian, Kung.=Kungurian, Roa.= Roadian, Wor.= Wordian, Capit.= Capitanian, GPTS= geomagnetic polarity time scale. See Appendix 1

Donets - ChRM directions
48°N , 37.8°E



and confined to the north of the basin (Stovba and Stephenson, 1999). Reactivation of the rift occurred during the end of the late Viséan and during latest Carboniferous-earliest Permian times (Stovba et al., 2003; Stephenson et al., 2006).

After the Paleozoic, the Donbas basin was deformed by large-scale WNW to ESE striking faults and folds, of which the central Main Anticline is the most dominant feature (Fig. 1.2b). The origin of these folds and faults was formerly ascribed to a compressional period in the Permian, but recently (Stephenson et al., 2006) argued that subtle deformation of Permian age was caused by salt tectonics in a transtensional setting. Saintot et al. (2003a) and Stovba & Stephenson (1999) propose two post-Paleozoic compressional phases that caused basin inversion: a latest Triassic-earliest Jurassic Cimmerian phase and a latest Cretaceous-earliest Paleogene Alpine phase, leading to erosion and exposure of the basin's stratigraphy.

3. Paleomagnetic sampling, methods and results

3.1 Sampling procedure and age of sampled formations

For the purpose of constructing a late Paleozoic APW path from the Donbas Foldbelt, we collected 724 samples from eleven sites at five localities, covering six time intervals, north and south of the city of Donetsk (Table 1.1, Fig. 1.2b). The Carboniferous lithostratigraphy of the Donbas Foldbelt is in the former Soviet Union traditionally subdivided into suites (Popov, 1965). These suites have been correlated to the regional stratigraphic substages and to the global stratigraphic scales; for the most recent overview and compilation we refer to Menning et al. (2006). Recently, Davydov et al. (2010) have provided new results on U-Pb ages and Milankovitch cyclicity in the Donetsk Basin, and calibrated the regional time scale to the global time scale, essentially confirming the earlier correlation of Menning et al. (2006). We indicated the ages of the sampled marker limestones and horizons, according to Menning et al. (2006) and Davydov et al. (2010) in Table 1.1. To allow comparison of our data to the APW paths, we correlated the regional substages to the latest version of the Geologic Time Scale, GTS2008 (Ogg et al., 2008). Those ages are indicated in Table 1.1 and Figure 1.3.

The oldest sampled rocks have a Tournaisian (early Carboniferous) age, the sites with the youngest rocks represent the Gzhelian (latest Carboniferous) to Asselian (early Permian). All Carboniferous samples were collected from limestones, except for one upper Carboniferous site (MC2) that was drilled in claystones. The upper Carboniferous to lower Permian sites (LP1, LP2 and LP3) were sampled in sandy red beds. We sampled the rocks by drilling standard paleomagnetic cores, using a gasoline powered motor drill or an electric drill with generator. Most sites consist of 50-100 cores, the majority of which were long enough to provide two or more specimens. In total, 749 cores were drilled. Sample orientations were measured with a magnetic compass; we corrected the sample orientations and measured bedding planes for the present-day 007°E declination. The samples we collected were mostly large enough to

provide two or more specimens, and 907 specimens were demagnetized.

3.2 Methods

Thermomagnetic runs to determine magnetic carriers were carried out in air, using a modified horizontal translation type Curie balance, with a sensitivity of $\sim 5 \times 10^{-9}$ Am² (Mullender et al., 1993). Approximately 30-65 mg of powdered rock samples was put into a quartz glass sample holder and was held in place by quartz wool. Heating and cooling rates were 10°C/min. Temperatures were increased to a maximum of 700°C.

The anisotropy of magnetic susceptibility (AMS) was measured to determine the magnetic fabric of the sediments and to assess whether they have a mainly sedimentary fabric or a tectonic fabric that may be indicative of the amount of strain that the rocks underwent since their deformation (Hrouda, 1982). During deformation, the maximum axis of the AMS tensor (k_{max}) will gradually align with the direction of maximum extension and become perpendicular to the direction of maximum compression. For calculations Jelinek (Jelinek, 1981, 1984) statistics were used. The samples were demagnetized using alternating field (AF) and thermal (TH) progressive stepwise demagnetisation. Samples were thermally demagnetized in a magnetically shielded oven, with steps of 10°C-100°C up to a maximum of 645°C. The AF demagnetisation was carried out with increments of 3-20 mT, up to a maximum of 80 or 100 mT. The natural remanent magnetisation (NRM) of all samples was measured on a 2G Enterprises horizontal 2G DC SQUID cryogenic magnetometer (noise level 3×10^{-12} Am²). For AF demagnetisation, we used an in-house developed robot assisted and fully automated 2G DC SQUID cryogenic magnetometer.

Demagnetisation diagrams of the NRM were plotted as orthogonal vector diagrams (Zijderveld, 1967) (Fig. 1.5). To determine characteristic remanent magnetization (ChRM) directions, results from generally five to eight successive temperature or AF steps were analysed by principal component analysis (Kirschvink, 1980). In several cases, samples with a direction that deviated from the general NRM behavior were analysed using the great-circle approach (McFadden and McElhinny, 1988) (Fig. 1.5c). This method was developed to identify the direction on the great circle that lies closest to the average direction obtained from well-determined NRM directions. Samples yielding maximum angular deviation (MAD) $> 15^\circ$ were rejected from further analysis. A total of 907 specimens was demagnetized, from 749 samples. Of these, the results of 503 demagnetisations were used to calculate the final paleomagnetic poles (Table 1.1).

Fisher statistics (Fisher, 1953) were used to calculate site-means and virtual geomagnetic pole (VGP) means. Because scatter of paleomagnetic directions induced by secular variation of the Earth's magnetic field is circular at the poles, but gradually becomes more ellipsoid towards the equator (Tauxe and Kent, 2004), we calculated the VGPs from all directions. Successively, a variable cut-off (Vandamme, 1994) was

applied and the error in declination (ΔD_x) and the error in inclination (ΔI_x) of the site were calculated following Butler (1992).

To determine whether two distributions have a common true mean direction (ctmd), we used the reversal test developed by McFadden and McElhinny (1990) and their classifications (A, B, C, indeterminate). The classifications are based on the critical angle γ_c and the angle γ between the means. Because we use their test with simulation, the test is equivalent to using the V_w statistical parameter of Watson (1983). To correct for a possible shallowing of inclination in sediments caused by compaction during burial, we used the elongation/inclination (E/I) method of Tauxe and Kent (2004). A large number of individual directions is required to apply the model suc-

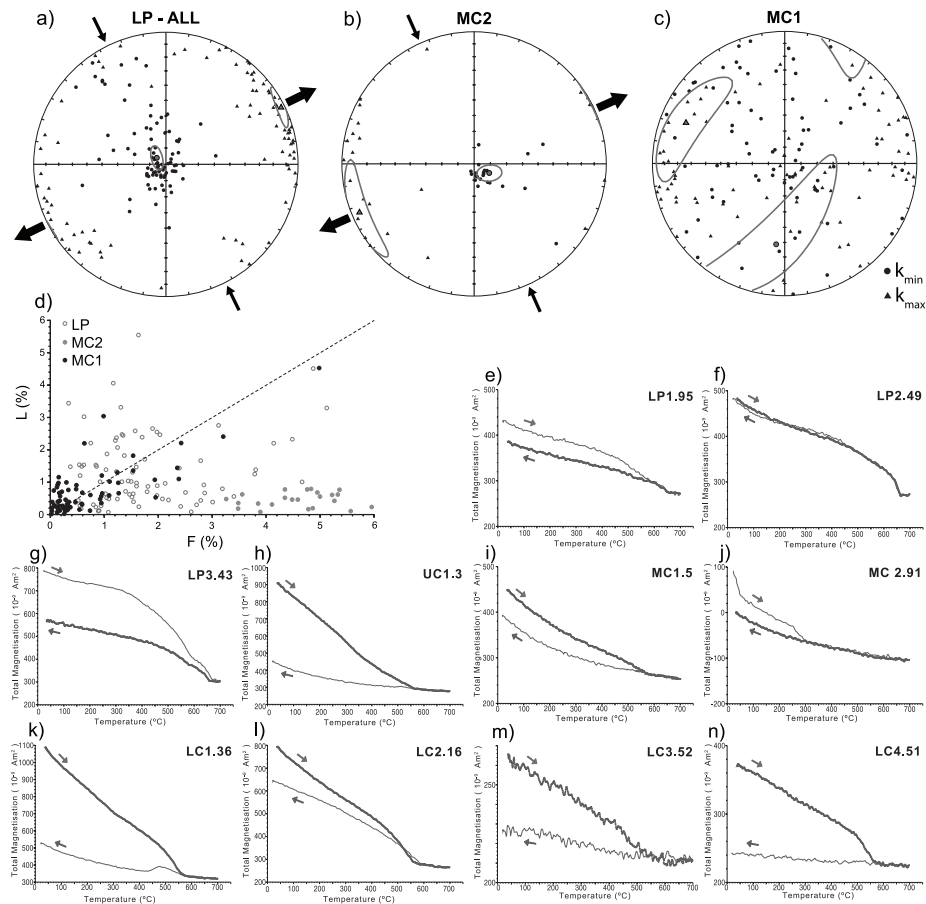


Figure 1.4 a, b) and c) Equal-area projections of the AMS (anisotropy of the magnetic susceptibility) for characteristic sites in tilt corrected coordinates. Grey, large symbols indicate the mean of the individual directions and their error ellipses (Jelinek, 1981). Thick (thin) arrows represent inferred extension (compression) directions. d) Flinn diagram for AMS measurements of sites LP, MC2 and MC1. $L (%) > F (%)$ denotes a prolate magnetic fabric, $F (%) > L (%)$ an oblate fabric. e-n) Thermomagnetic curves measured on a Curie balance (Mullender et al., 1993) for characteristic samples of each site. Arrows indicate heating (red) and cooling (blue) curves. See Appendix 2

cessfully (preferably $N > 100$). Since the number of individual directions from our sites varies from 50-118, we will discuss the validity of using this correction per locality.

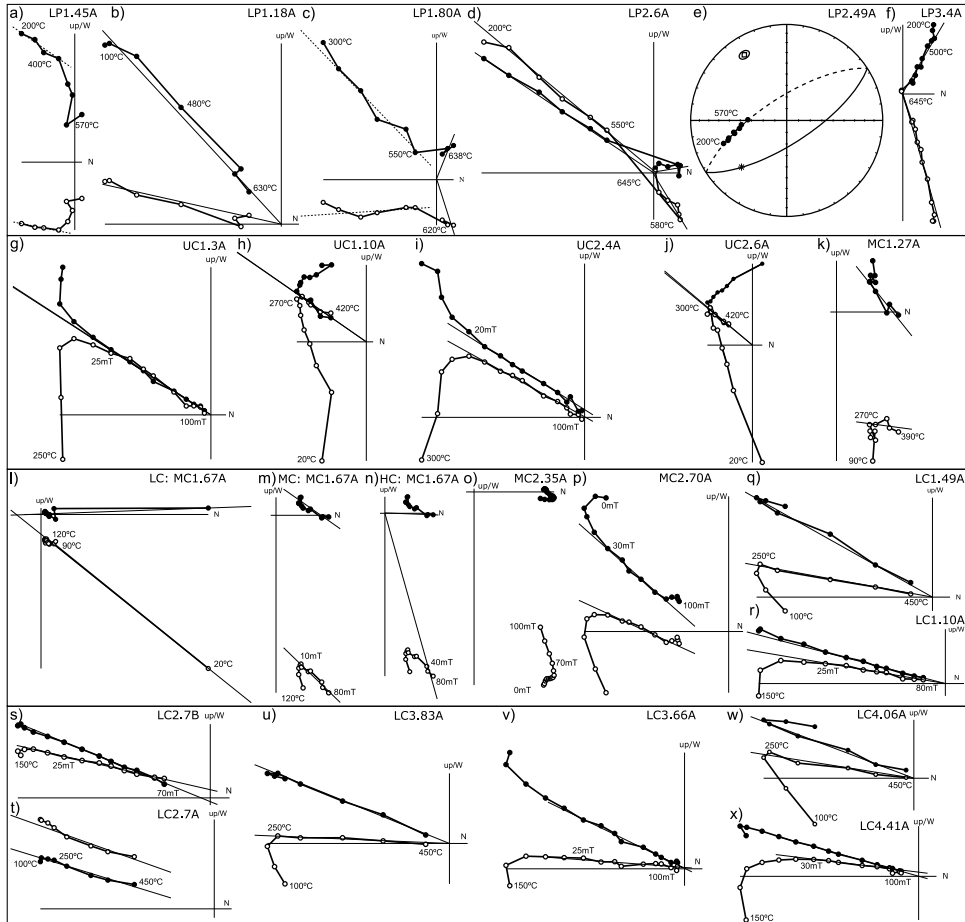


Figure 1.5 Orthogonal vector diagrams (Zijderveld, 1967), showing characteristic demagnetisation diagrams for all sampled sites in tilt corrected coordinates. Closed (open) circles indicate the projection on the horizontal (vertical) plane. Dashed lines in a) and c) indicate the steps that were used for great circle analysis (McFadden and McElhinny, 1988). In Figs. 1.5 c), k), n), o) and t), the remaining magnetisation after thermal or AF demagnetisation can be seen. These components are also displayed in Fig. 1.6 b)-d). l)-n) show the same demagnetisation diagram, that carries three distinct directions: l) the low temperature component (LC) that resembles the present-day GAD direction, m) the medium coercive force component (MC, interpreted as the primary ChRM) and n) the remaining high coercive force component (HC) after full AF demagnetisation, that is close to the present-day GAD direction. o) is shown in more detail in Figure 1.8 c). c) equal area plot of a demagnetisation diagram that was interpreted using great circle analysis: dashed (solid) line denotes projection on lower (upper) hemisphere. f) and g) are typical examples of orthogonal vector diagrams that were rejected (o) or accepted (p) after analysing their decay-curves (Fig. 1.8).

3.3 Paleomagnetic results

The AMS measurements of sites LP and MC 2 (Fig. 1.4a and b) show an alignment of the k_{max} axis, which may have been caused by an ENE-WSW extensional or a NNW-SSE compressional episode, or by transport current directions during the time of deposition. The AMS measurements of all other sites revealed random directions, with very large error ellipses (e.g. Fig. 1.4c) (Jelinek, 1981, 1984), and cannot be interpreted in terms of an AMS fabric. Flinn diagrams of the AMS measurements (Fig. 1.4d) show that MC2 is strongly oblate, likely because of more compaction of these clays than of the limestones, while the reds of site LP show a mixture of oblate and prolate fabrics. The dominant prolate fabric of site MC1 has little meaning of a random AMS fabric (Fig. 1.4c), likely caused by the low intensities of the limestones and a relatively large diagenetic contribution.

From all sites, test sets of samples were demagnetized both thermally and using AF demagnetisation, to allow comparison of both techniques (Fig. 1.5), similar to the procedures in Gong et al. (2008b). This implies that all AF demagnetized samples were first heated to 150°C to remove possible stress in magnetite grains caused by surface oxidation at low temperatures (Van Velzen and Zijdeveld, 1995), except for the clays of site MC2. Our tests showed that the limestones of site UC should be pre-heated to higher temperatures, until 250°C or 300°C before AF demagnetisation. In general, this pre-heating technique appeared very successful, since the overprint direction could already be removed at significantly lower AF fields. The lower Permian (LP) sites were not demagnetized using AF treatment, since the maximum applicable alternating field (100 mT) was not high enough to fully demagnetize the hematite-bearing samples.

From most sites, a low temperature/low coercive force component (LT/LC) could be isolated, that is indistinguishable from the GAD field at the present latitude (Fig. 1.6a) and is therefore a recent overprint. Only in site LP, we did not observe this LT GAD field, because nearly all samples were pre-heated until 200°C.

In samples from sites LP, we observed a high temperature component between 580°C and ~640°C (Fig. 1.5c and d). This component, although not very often observed, yields a direction that seems to be resulting from a present-day overprint (Fig. 1.6b). Samples from sites MC1, MC2 and LC1_2 could in ~40% of the samples not be demagnetized to the origin using AF demagnetisation techniques (Figs. 5 n, o, p and s). Using thermal demagnetisation techniques, we could not isolate this component (e.g. Fig. 1.5 k and t), because of magnetite generation and random natural remanent magnetization (NRM) behavior at temperatures above ~400-450°C. This indicates that there is a remaining hematite component in the samples. When interpreting this remaining component towards the origin, it is indistinguishable from the GAD field for sites MC1 and LC1_2 (Fig. 1.6 c and d). This component has both normal and reversed polarities in site LC1_2, which indicates that it results from a recent overprint that at least in part predates the Brunhes Chron.

In site MC, this component is more disperse (Fig. 1.6c), particularly in the clays of MC2, but most directions of the limestones of MC1 are close to the present-day GAD field. This may indicate that the remagnetisation is of chemical origin, possibly resulting from circulating fluids. In this case, clays would function as an aquitard, being more resistant to fluid circulation than the directly underlying limestones (MC1). A similar process has then likely occurred in the limestones of sites LC1_2. The fluids likely derive from burial and pressure dissolution of calcite, with the lithological effect that limestones are more prone to remagnetization than marls. It is less likely that externally derived fluids have played an important role (Gong et al., 2008a).

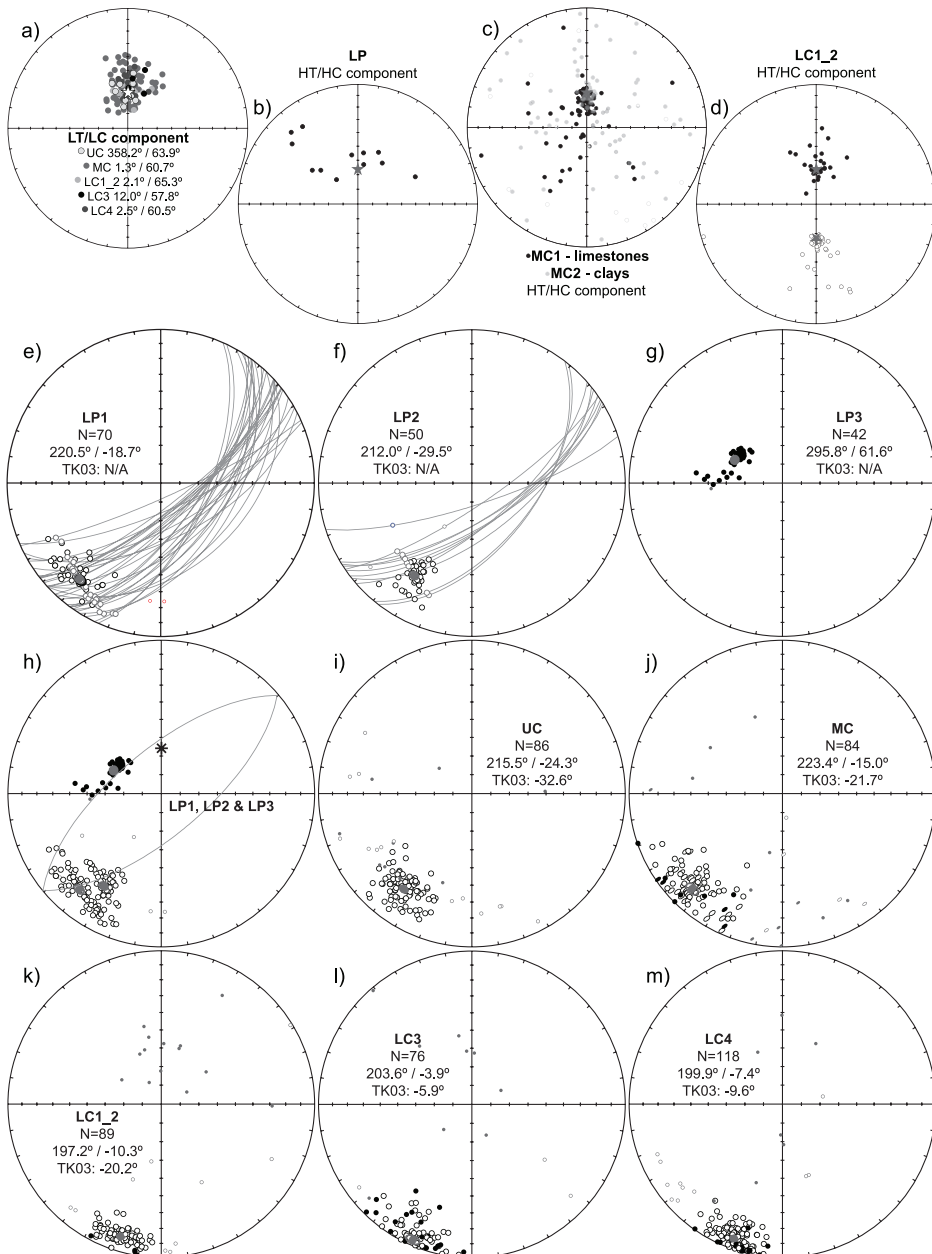
Tournaisian

Site LC4 was sampled in lower Carboniferous (Tournaisian B) limestones. The stratigraphic thickness of the sampled interval is 23 meters. It comprises 139 demagnetized specimens, from which 8 were demagnetized thermally and 131 using combined thermal and AF demagnetisation (Fig. 1.5w and x). Initial intensities range from ~50 to 500 $\mu\text{A}/\text{m}$. Curie temperatures are 570°C-580°C (Fig. 1.4m), indicating that the magnetic carrier in the samples is magnetite. After application of our criteria, the ChRM corrected for bedding tilt for this site (N= 118) is D= 199.9, I= -7.4 (Table 1.1, Fig. 1.6m). Correction for inclination shallowing results in a slight and is not significant, within the 95% bootstrap errors, changing the inclination to I= -9.7 (Fig. 1.7; Table 1.1).

Figure 1.6 a-d) in situ: a) Low temperature/low coercive force (LT/LC) component of sites UC, MC, LC1_2, LC3 and LC4. See section 3.3.2 for explanation. Color coding according to the colors in the figure. White star indicates the GAD field direction at the current latitude. b)-d) High temperature high / coercive force (HT/HC) component. We interpreted the remaining magnetization after AF or thermal demagnetization towards the origin. The remaining magnetization clearly represents a recent field direction (red star denotes present-day GAD field). In the clays of site MC2 the directions are more random, see text for explanation. e)-m) tilt corrected: Equal area projections of the ChRM directions of all sites (Table 1.1). Open (down) and closed (up) circles indicate the individual directions. Blue symbols indicate respectively the mean directions and their cone of confidence (α_{95} ; not always visible). Red (small) circles indicate the individual directions rejected by the Vandamme cut-off angle (Vandamme, 1994). Solid (open) symbols are lower (upper) hemisphere projections. Number of individual directions after applying the Vandamme cut-off (N), declination, inclination and inclination after E/I correction are indicated. In e) and f) black lines indicate the great circles that were used to calculate the best fitting ChRM directions (McFadden and McElhinny, 1988), the corresponding directions are indicated in blue. h) Equal area projection of all Permian (Asselian) sites, with their individual site-mean direction. Black star indicates the present-day geo-axial dipole (GAD) position in the Donbas Foldbelt. Great circle (best fitting) through LP1, LP2, LP3 and the GAD indicates the transition from an Asselian direction in LP2 increasingly toward the present-day GAD overprint directions of LP1 and LP3. j) Equal area projections of the ChRM directions of site MC. Individual directions of MC1 (limestones) are represented by circles, individual directions of MC2 (claystones) are represented by ovals. See Appendix 3

Visean

The samples of site LC3 were taken from lower Carboniferous (Visean) limestones and were sampled in 16.5 meters of stratigraphy. Site LC3 consists of 127 demagnetized specimens, from which five were demagnetized thermally and the remaining specimens by combined thermal and AF demagnetisation (Fig. 1.5u and v). Initial intensities range from ~ 50 to $500 \mu\text{A/m}$. Curie temperatures are between 520°C and



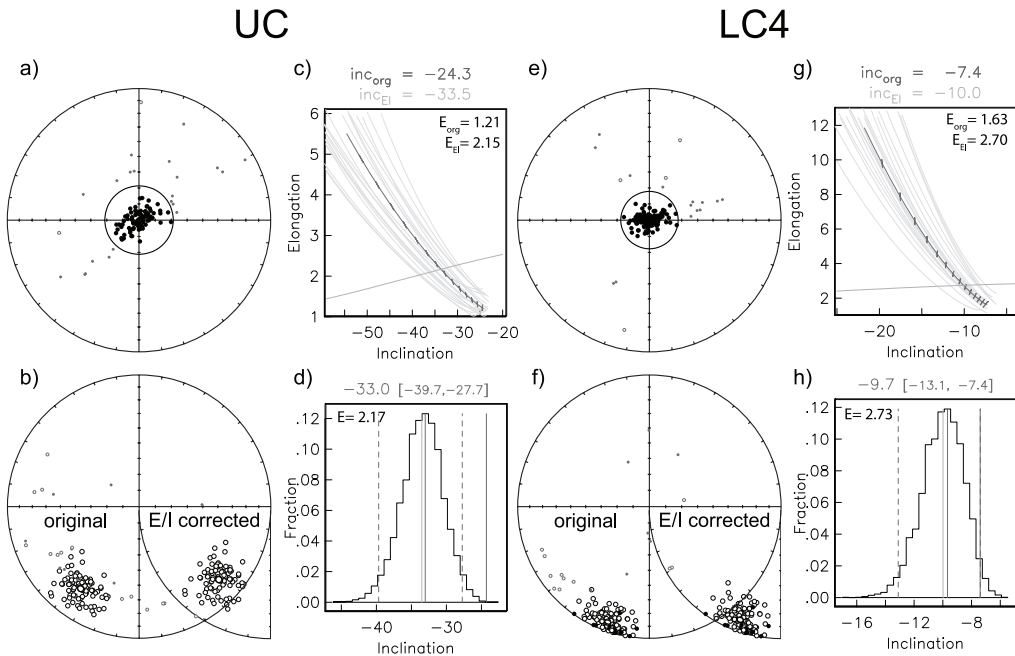


Figure 1.7 Equal-area projections of the individual VGP directions before E/I correction (a and e) and equal-area projections of the individual ChRM directions before (b and f, left side) and after (b and f, right side) E/I correction (symbols as in Figure 1.6) (Tauxe and Kent, 2004) with corresponding elongation vs. inclination (c and g) and fraction (of 5000 bootstraps) vs. inclination plots (d and h) for UC (a-d) and LC4 (e-h). In the elongation vs. inclination plots the E/I for the TK03.GAD model (green dashed line) and for the datasets (red barbed line) for different degrees of flattening are plotted. The red barbs indicate the direction of elongation (horizontal is E–W and vertical is N–S). Also shown are examples (yellow lines) from 20 (out of 5000) bootstrapped data sets. The crossing points (if the dataset intersects the model) represent the inclination/elongation pair most consistent with the TK03.GAD model, given as inc_{EI} and E_{EI} (in green) above the panel; inc_{org} = original inclination, E_{org} = original elongation of the dataset. In the fraction/inclination plot, a histogram of crossing points from 5000 bootstrapped data sets is shown. The most frequent inclination (solid red vertical line; dashed red vertical lines denote the 95% bootstrap errors) is given as value (and error range) on top of the panel; the inclinations of the original distribution (blue vertical line) or the intersection with the model (green vertical line) are indicated; E = the elongation resulting from the bootstrapped data sets. See *Appendix 4*

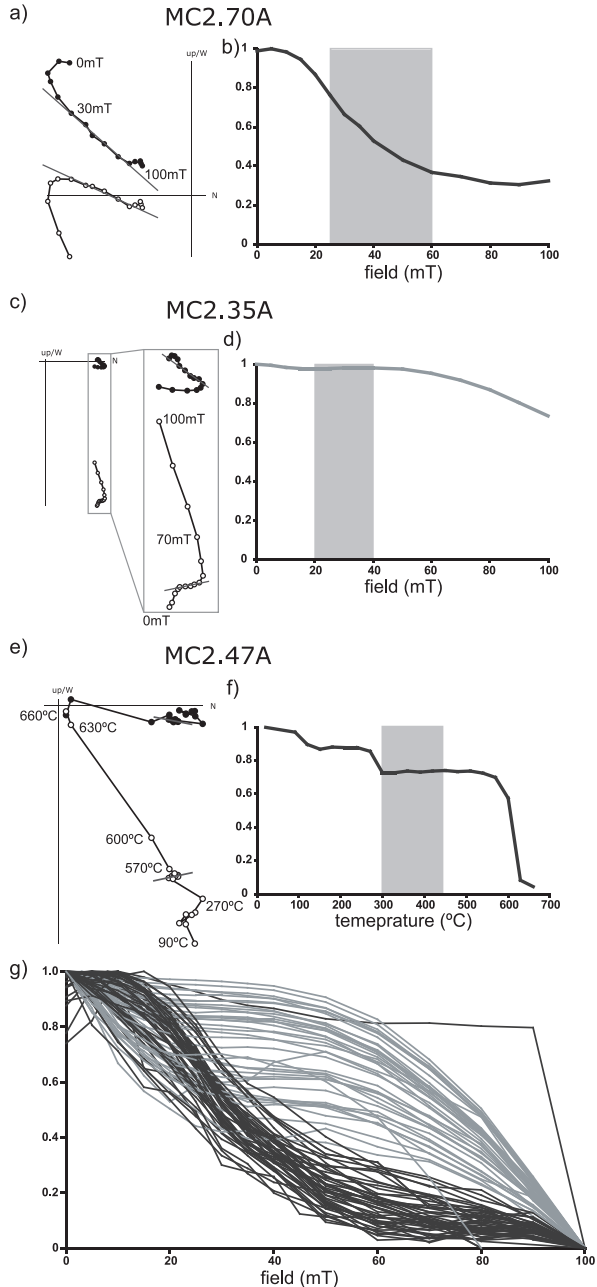
580°C (Fig. 1.41), indicating that the main magnetic carrier is (Ti-poor) magnetite. For many specimens, we could not reliably determine the ChRM, caused by very low intensities between 550°C and 600°C. The resulting mean ChRM ($N=76$), corrected for bedding tilt is $D=203.6$, $I=-3.9$ (Table 1.1, Fig. 1.61). Correction for inclination shallowing yields again a not significant correction to $I=-5.9$.

Serphukovian

The fossiliferous and locally sandy limestones of the combined sites LC1_2 are early

Carboniferous (late Serpukhovian) in age. The stratigraphic thickness of the sampled interval is several meters thick. Site LC1_2 consists of 118 demagnetized specimens, of which 12 specimens were demagnetized thermally, 106 using combined thermal and AF demagnetisation (Fig. 1.5q-t). Initial intensities range from ~ 1 to 5 mA/m. Curie temperatures are 560°C - 570°C (Fig. 1.4k). In some samples, an inflection around 300°C may indicate an inversion of maghemite (Fig. 1.4j). The resulting

Figure 1.8 a), c) and e) demagnetisation diagrams of characteristic samples of the claystones of site MC. b), d) and f) NRM intensity upon AF demagnetisation normalized by initial NRM intensity. Grey rectangle indicates AF / temperature steps that were used for calculation of the ChRM directions. g) NRM intensity upon AF demagnetisation normalized by initial NRM intensity of all individual samples of site MC2 normalized (total intensity). Highest AF / temperature step intensity was set to zero for display purposes. Grey (light-colored) curves indicate the curves of the samples that were rejected and blue (dark-colored) curves indicate the samples that were used for calculation of the mean ChRM direction of site MC. The ChRM directions belonging to the grey (light-colored) curves were typically affected by a later acquired NRM component. See Appendix 5



ChRM ($N=89$) after correction for bedding tilt is $D=197.2$, $I=-10.3$ (Fig. 1.6k). The correction for inclination shallowing is statistically significant ($I=-20.5$), although the number of samples is quite low ($N<100$).

Bashkirian

The samples of the combined sites MC 1 and MC2 (sampled stratigraphy interval ~ 1 and 1.5 m, respectively) were taken from upper Carboniferous (Bashkirian) limestones and claystones. Locality MC provided 193 demagnetized specimens; 17 specimens were fully demagnetized thermally and 176 using AF demagnetisation (the clays) or combined thermal and AF demagnetisation (the limestones) (Fig. 1.5k-p). Initial intensities of the limestone specimens (MC1) range from 10 - $200 \mu\text{A/m}$, with some exceptions that have initial intensities up to $15,000 \mu\text{A/m}$. Curie temperatures for the limestone samples are 570°C - 580°C (Fig. 1.4h), so the magnetic carrier in the samples is magnetite. Thermal and AF demagnetisation yield identical results. Initial intensities of the claystones (MC2) range 200 - $5,000 \mu\text{A/m}$. Thermomagnetic treatment shows a mainly paramagnetic decay (Fig. 1.4i), but a drop in intensity around 300°C suggests either an iron sulfide as main carrier, or points to an inversion of maghemite.

The medium temperature/medium coercivity (MT/MC) component in specimens from site MC1 was interpreted as the ChRM direction (Fig. 1.5k and m and Fig. 1.6j). Thermal demagnetisation of the claystone specimens of MC2 gave three components: a low temperature ($\sim 20^\circ\text{C}$ - 270°C) direction (Fig. 1.6c), a high temperature ($> 400^\circ\text{C}$) and high coercive force component (> 100 mT) direction that yields the present day geocentric axial dipole (GAD) direction (Fig. 1.6a), and a medium temperature component ($\sim 300^\circ\text{C}$ - 400°C) that yields directions similar to those obtained in the AF demagnetized claystone and limestone samples (Fig. 1.5k-p, Fig. 1.6j and Fig. 1.8e-f). Because this medium temperature component was largely overprinted by the high temperature component (Fig. 1.6c), these results could not be used for further analysis.

AF demagnetisation diagrams of the claystones of MC2 yield three components: a low coercive force component (~ 0 - 20 mT) (Fig. 1.6a), a medium coercive force component (MC) (~ 20 - 60 mT) (Fig. 1.6j) and a high coercive force component (HC) (> 60 mT) (Fig. 1.6c), that in general do not trend towards the origin, with some exceptions of the MC component. This MC component is similar to the directions in the other Carboniferous sites, although in a part of the samples it is heavily affected by a HC component (> 60 mT) (Fig. 1.8a-d). To discriminate between samples that were heavily affected by this HC component and samples that could be used for determining ChRM directions, decay curves of the specimens were plotted and compared (Fig. 1.8b, d and g). In Figure 1.8g, a clear difference between the samples that were significantly affected by the HC component and samples that still yield a Carboniferous direction is clearly visible. The former were rejected from further analysis.

The mean directions of the limestones (MC1) and claystones (MC2) have a common true mean direction (ctmd) ($\gamma = 4.0 < \gamma_c = 5.6$, classification B). The mean ChRM direction for MC1 and MC2 (corrected for tilt, $N=84$) is: $D = 223.4$, $I = -15.0$ (Table 1.1, Fig. 1.6j). Correction for inclination error is significant and results in a steeper inclination of $I = -22.4$.

Kasimovian/Gzelian

Site UC was drilled in upper Carboniferous limestones (upper Kasimovian or lower Gzelian, marker limestone O-6-1 of Popov (1965)). The marker limestone was sampled at two locations (several tens of meters apart), each in ~ 2 meters of stratigraphy, covering the entire thickness of the limestone bed (see Table 1.1). The total number of demagnetized specimens is 114, out of which 18 specimens were demagnetized thermally (Fig. 1.5g-j). The remaining specimens were demagnetized using AF treatment, after thermal treatment until 250°C or 300°C . Initial intensities range from ~ 100 to $600 \mu\text{A/m}$. We found a Curie temperature of 570°C (Fig. 1.4g), indicating that the magnetic carrier is magnetite. An additional inflection point between ~ 300 - 350°C could indicate an inversion of some maghemite. The ChRM direction that was corrected for bedding tilt ($N=86$) is: $D = 215.5$, $I = -24.3$ (Table 1.1, Fig. 1.6i). Correction for inclination error yields $I = -33.0$, which is statistically significant (Fig. 1.7, Table 1.1).

Asselian

Sites LP1, LP2 and LP3 were drilled in lower Permian (Asselian) red beds, only several tens of metres apart. The red beds in site LP3 are coarser than the red beds of sites LP1 and LP2. Each of the three sites was sampled within ~ 2 stratigraphic metres: the total stratigraphic thickness of the sites together is ~ 6 m. The total number of thermally demagnetized specimens is 208. Initial intensities range from ~ 3 to 7 mA/m in LP1 and LP2, and from ~ 7 to 10 mA/m in LP3). Néel temperatures of 660° - 675°C (Fig. 1.4d-1.4f), and additional inflections in the thermomagnetic curves of LP1 and LP3 (Fig. 1.4d and 1.4f) representing Curie temperatures of 580°C suggest that both hematite and magnetite are the magnetic carriers. We interpreted the magnetite component as the ChRM direction (Fig. 1.5a-f).

Since LP1, LP2 and LP3 were sampled from similar lithologies and within the same formation, and only several tens of metres apart, similar ChRM directions were expected. However, LP3 yields a direction very different from LP1 and LP2 (Table 1.1). Because the mean direction of LP3 plots on a great circle between the mean directions of LP1 and LP2 and the GAD field in the Donbas area (Fig. 1.6e-h), we interpret this as a remagnetization that is transitional direction between the primary, early Permian direction and the GAD field. This is likely related to the slightly coarser nature of the LP3 sediments, and we therefore exclude LP3 from further analysis. The ChRM directions of LP1 and LP2 do not pass a ctmd test (McFadden and Lowes,

1981). From Figure 1.6h, it can be seen that LP1 was also partly influenced by a later overprint. Only LP2 is used for further analysis.

Out of the 50 specimens from LP2 that were used for final calculation of the ChRM, 10 specimens have a ChRM direction derived from great-circle analysis (McFadden and McElhinny, 1988). The mean ChRM direction (bedding tilt corrected) is $D=212.0$, $I=-29.5$ (Table 1.1, Fig 6f). If directions using great-circle analysis are excluded from analysis, the resulting ChRM is identical the same within error: $D=211.0$, $I=-29.0$. Correction for inclination error was not applied, since the number of specimens does not approach the minimum required number ($N>100$).

4. Discussion and conclusions

The ChRM directions from the lower Carboniferous to lower Permian limestones, claystones and red beds presented here are very consistent within each site (Fig. 1.6), they differ significantly per site, and all sites recorded reversed polarities. A fold test could not be applied to our datasets since we sampled the different time intervals at a single location, with only a small variation in bedding tilt. Iosifidi and Khramov (2002) did apply a fold test with a positive result to their lower Permian samples from the Donbas basin, which were collected from the same formation as our lower Permian samples.

The reversed polarity of the ChRM directions is in line with the age of MC, UC and LP, which were sampled within rocks that were deposited during the Permian-Carboniferous Reversed Superchron (PCRS), which lasted from ~ 317 to ~ 265 Ma (Opdyke et al., 2000; Menning et al., 2006). During the Carboniferous period preceding the PCRS, several normal polarity chrons are known (Davydov et al., 2004). Although the Carboniferous polarity time scale is not well determined, the normal polarity chrons reported by Davydov et al. (2004) in the time scale of Gradstein et al. (2004) cover only $\sim 31\%$ of the period preceding the PCRS. This implies that in the age range of our sites the probability is 70% that we sampled reversed polarity intervals. A Permian thermal event, recognized in fission track analysis and vitrinite-reflectance studies (Sachsenhofer et al., 2002; Spiegel et al., 2004), possibly related to a magmatic episode in the Donbas Foldbelt during the early Permian (Alexandre et al., 2004), could have caused a partial reversed polarity remagnetisation of the magnetic signal. However, the low inclinations we find here show a trend toward steeper inclinations with time, which is inconsistent with a remagnetisation event influencing our sites (Fig. 1.3). Indeed, several sites, recorded a present-day or recent GAD field direction (Fig. 1.6a-d), but it is clearly distinct from the component that we interpret as a ChRM. The statistically significant directional difference between the sites of different age intervals also implies that the ChRM in all sites older than Permian cannot represent a Permian remagnetisation. We therefore believe that our ChRM directions represent an original magnetization acquired at the time the rocks were formed.

The E/I method gives a significant change in inclination for sites LC1_2, MC

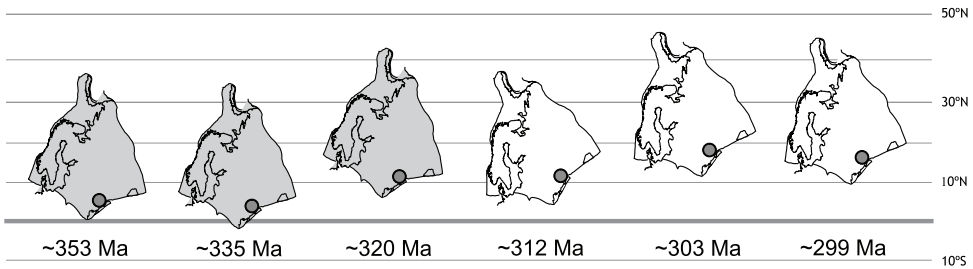


Figure 1.9 Reconstruction of Baltica from the Carboniferous-early Permian using the data of this study. Circle indicates location of Donets. The oldest three reconstructions are displayed in grey, because of the uncertainty in their rotation.

and UC. This is an indication that the NRM was acquired before compaction. Correction with the E/I model for sites LC3 and LC4 produces a small but not significant change. There are several possible explanations for this. It may imply that NRM acquisition was slightly delayed, and acquired after early dewatering and compaction of the sediments, possibly during early diagenesis (e.g. Van Hoof and Langereis (1991)). A more likely explanation is that, because the sediments of sites LC3 and LC4 were deposited nearest to the equator, inclination shallowing is not significant, because of the low magnetic field inclination.

Therefore, we conclude that the observed inclination/paleolatitude and declination trends of the sampled time interval (Table 1.1, Fig. 1.3) are the result of plate tectonics and/or local tectonic rotations. We must now consider whether the Donbas region formed part of stable Europe, so that corresponding paleopoles can be used for the APW path for this time interval.

The only AMS results that did not give random directions are from sites LP and MC2. Those results (Fig. 1.4) either reflect NNW-SSE compression or the direction of currents during deposition of the sediments. Paleoflow direction measurements from Abels et al. (submitted), indicate southeast flow directions in the middle Carboniferous, so coeval with the sediment deposition of site MC. The AMS measurements of site MC2 do not agree with those directions. Therefore, the AMS data of site MC2 cannot be the result of paleoflow directions, which is also in agreement with the lithology of MC2: a paleocurrent AMS fabric is only recorded in a high-energy and coarser grained sedimentary environment. The coarser lithology of the red beds from LP have the same sedimentary-tectonic fabric as MC2. The AMS orientation of both sites reflect NNW-SSE compression, which is in very good agreement with paleostress data from Saintot et al. (2003a). These data indicate an Eo-Alpine strike-slip regime with NNW-SSE trending σ_1 .

Outside Scandinavia, there are no Carboniferous and early Permian datasets from Baltica that are incorporated into the APW paths (Torsvik and Cocks, 2005; Torsvik

et al., 2008a). To discuss our data in the large-scale framework of global plate movements, the A95 error envelope of the APW paths of Torsvik et al. (2008a) (310-0 Ma) and Torsvik and Cocks (2005) (360-310 Ma) are plotted in Figure 1.3, recalculated to the city of Donetsk (48°N, 37.8°E). The APW path of Laurussia at 350 and 360 Ma (Torsvik and Cocks, 2005) however, is constructed on the basis of a single pole entry and is therefore very poorly constrained.

Our datasets without correction for inclination shallowing with the E/I model (Tauxe and Kent, 2004) show that in general, the paleolatitudes agree very well with those of the Eurasian polepaths (Fig. 1.1), although our oldest pole (LC4) and our two youngest poles (UC and LP2) yield slightly higher paleolatitudes. Applying the E/I correction slightly increases the paleolatitudes (Fig. 1.1). In published APW paths, the paleolatitude may be underestimated because of unrecognized or uncorrected inclination shallowing in sediments (Torsvik and Cocks, 2005; Torsvik et al., 2008a), although the majority of the data points used to construct the APW path between 360 Ma and 290 Ma is based on volcanic rocks (25 out of 38 entries). In Fig. 1.9, the position of Baltica with E/I correction is shown, showing its gradual northward motion.

Our data from the lower Permian red beds (LP2), yield nearly-identical results to data from time-equivalent red beds in the Donbas Foldbelt studied by Iosifidi and Khramov (2002) and Iosifidi et al. (submitted) (Fig. 1.3, green stars). Their positive fold tests on the data from lower Permian and upper Carboniferous rocks (McFadden and Jones, 1981; Watson and Enkin, 1993), confirm our confidence in the primary origin of the directions obtained from our sites. The lower Permian results of Iosifidi et al. (submitted) supersede those of Iosifidi and Khramov (2002), since they are from the same formation, but with more samples; the difference is negligible. Their upper Carboniferous data are new. Iosifidi et al. (submitted) isolated a component mainly residing in pigmentary hematite in the red beds, yielding a higher inclination than the component residing in detrital, specular hematite. Since pigmentary hematite is formed after deposition, they argue that these components have no significant inclination error. This was also observed in redeposition experiments of the Kartamysh Formation, performed by Khramov et al. (1987).

Comparing the declinations of our three youngest sites (MC, UC and LP2) with the published APW paths (Fig. 1.3), they plot reasonably well within the error. The oldest three sites (LC4, LC3 and LC1_2), have a consistently different declination both compared to the APW paths and to the youngest three sites. The sites are in the region where Arthaud and Matte (1977) proposed the shear zone that accommodated Pangea-transformation. The shear zone however, would cause clockwise rotations, which is opposite to the counterclockwise (CCW) rotations of our oldest three sites. The geological map (Fig. 1.2b) shows that the oldest sites were sampled in the southern part of the Donbas Foldbelt, which has a diverging strike from the general trend in the belt. This strike difference, corresponds both in sense and magnitude

to the declination deviation of our oldest sites from the published APW paths. We therefore suggest that the deviation is the result of local CCW vertical-axis rotations in the southern part. Anomalous N-S trending thrusts and folds in the sampling area of LC4 and LC3 were recognized by Saintot et al. (2003b), which they ascribed to the Cimmerian (late Triassic to Jurassic) and Alpine (Cretaceous/Tertiary boundary) reactivation of shallow inherited structures at the southern margin of the basin. Numerical models in their study that calculate stress axis trends, predict a counterclockwise rotation of $\sim 15^\circ$ with respect to the surrounding area. This is in very good agreement with our relative paleomagnetic rotations. This implies that we cannot use the directions of these sites for determining pole positions for further analysis of the APW path.

In Figure 1.1 b-c), we compare a continent reconstruction at 300 Ma based on our data from LP2, with those of Torsvik et al. (2008a) and Van der Voo and Torsvik (2004) at 300 Ma. Laurussia is displayed in grey, according to the pole from site LP2. Because Laurentia and Eurasia were part of the same tectonic plate (called Laurussia) in Pangean times, usage of Laurentian poles is allowed for Laurentia. Comparing our data to the Gondwana reconstructions, there is no overlap between the northern and southern continents. The same holds for a reconstruction using the latest Carboniferous pole UC (not displayed here). Therefore, these two datasets would not require a Pangea B type reconstruction. As mentioned above, Van der Voo and Torsvik (2004) partly solve the overlap problem in the early Permian by considering only the highest quality European poles. They selected these on the basis of paleomagnetic quality, age control and also rock type (volcanics) to avoid the possibility of inclination shallowing in sediments (Van der Voo, 1990). In this way, Eurasia is located almost 10° further north at 280 Ma. If we compare our Permian data to Van der Voo and Torsvik's (2004) presented polepath at 300 Ma, our data plot even $\sim 5^\circ$ further to the north (Fig. 1.1b). Moreover, our Carboniferous data points (Fig. 1.3) show a very general and gentle northward motion of Laurussia (at Donets) from near-equatorial position ($3\text{--}5^\circ\text{N}$) to $\sim 18^\circ\text{N}$, which strengthens the interpretation of a more northerly position of Laurussia during Pangean times, in line with Van der Voo and Torsvik (2004). Because of the juxtaposition of Laurentia and Eurasia, this means that, in the early Permian, our data from the Donbas Foldbelt would place Laurussia at a more northerly position, explaining the Pangea misfit without a need to introduce an octupole contribution to the Earth's magnetic field (e.g. Torsvik and Cocks, 2004). Interestingly, Kodama (2009) and Bilardello and Kodama (2009), very recently reassessed ages and corrected Carboniferous poles from present-day North America for inclination error, using the method developed by Tan and Kodama (2003). The sampling region of those studies is located in the southern hemisphere in Carboniferous times, so the effect of correcting (i.e. steepening) the inclination for Laurentian on the Laurussian polepath is inverse: Laurussia moves southward whereas steeper inclinations in Eurasia would move Laurussia northward. We illustrated this effect in Fig. 1.3 for the corrected results from the Glenshaw, Shepody and Maringouin Formations: the overlap

of Gondwana and Laurussia is significantly increased, clearly requiring a Pangea B configuration (d and e). The strongly contrasting results of our study and those of Bilardello and Kodama (2009) and Kodama (2009) show that the Carboniferous pole paths are still too poorly constrained to solve the Pangea controversy. Furthermore, data should cover and be representative for an entire continent, which is not the case for the Carboniferous and early Permian Eurasian polepaths, since no reliable eastern European and Asian data entries are available. In the late Permian pole path, many poles from southern France have been included, mainly from sediments (red beds). It was recently pointed out by Bazhenov and Shatsillo (2010) that at least during the late Permian, the French group of poles shows a significant deviation with respect to the late Permian poles of the remaining part of the continent. The authors suggest that this is caused by a hitherto unrecognized rotation of southern France. A similar effect of Carboniferous and early Permian groups of poles on the Eurasian polepath, would obviously have large implications for Pangea reconstructions and the Pangea A versus B controversy. It appears that the Pangea controversy cannot yet be unambiguously resolved by paleomagnetic data.

Summarising, we present new Eurasian Carboniferous and early Permian sedimentary paleomagnetic datasets from sediments, and the only ones that are large enough to enable E/I correction for inclination shallowing in sediments (Tauxe and Kent, 2004), thereby improving the quality of these paleopoles. This allows us to constrain the Permo-Carboniferous paleolatitude of Laurussia at the position of the Donbas Foldbelt. In general, our results yield similar or higher values for paleolatitude than those previously used to construct the APW path. Unfortunately, our lower and middle Carboniferous poles are most likely affected by a tectonic rotation, and therefore can only indicate reliable paleolatitudes. Our upper Carboniferous and lower Permian data do not require a Pangea B type reconstruction. The paleolatitudes of Laurussia calculated from our poles enable a Pangea A reconstruction, and do not require an overlap of northern and southern Pangea terranes. However, a recent correction and reassessment of North American (Laurentian) paleomagnetic data from recent studies pointed out quite the opposite. Therefore, the Pangea A versus B controversy is as lively as during the past 30+ years, since Irving (1977).

5. Acknowledgements

The authors would like to thank Hemmo Abels, Flora Boekhout, Wolter Bosch and Constantin Pechnikov for their field assistance. We thank Shell International Exploration and Production, Rijswijk, the Netherlands, and Shell Ukraine, for logistical and financial support; Calum MacDonald, Mark Geluk and Maxim Vityk, as well as Sergiy Stovba from NAUKA Ukraine are thanked for discussion. An earlier version of this manuscript benefited from the comments of Sacha Iosifidi and three anonymous reviewers. M.J.M.M. acknowledges the Netherlands Research Centre for Integrated

Solid Earth Sciences (ISES) and the Netherlands Organization for Scientific Research (NWO) for financial support.



Sümela monastery (Maçka, Trabzon province)

CHAPTER 2

Jurassic-Cretaceous low paleolatitudes from the circum-Black Sea region (Crimea and Pontides) due to True Polar Wander

In a recent study, paleomagnetic and paleoenvironmental data from Adria (as part of the African plate) suggest much lower ($\sim 15^\circ$) African latitudes from early Jurassic to earliest Cretaceous at the position of Adria. A smoothing of the apparent polar wander (APW) path is suggested to explain the low latitudes. In this study, we test if the low paleolatitudes in the Jurassic to early Cretaceous can also be found in Eurasia, i.e. Crimea (Ukraine) and the Pontides (Turkey) that are situated in the present-day Black Sea region. Our Eurasian data suggest the same low late Jurassic to early Cretaceous paleolatitudes as shown for Africa. This time span is characterized in the Mediterranean realm by Tethys subduction and these subduction zones likely functioned as an anchor in the mantle. Therefore, we regard it unlikely that both the African and Eurasian plates moved by >1500 km south and subsequently north with respect to the mantle, as suggested by the paleomagnetic results. True polar wander (TPW) provides a mechanism that rotates the Earth's crust and mantle with respect to its core, and it was recently quantified. The period from 195-135 Ma (early Jurassic to earliest Cretaceous) is subject to clockwise TPW, which could well explain our results. We conclude that TPW rather than plate tectonics is the cause of low late Jurassic to early Cretaceous African and Eurasian paleolatitudes in the eastern Mediterranean area.

1. Introduction

A recent paleomagnetic study on the Adria terrane, as part of the African continent in the Mesozoic, identified a rapid southward-then-northward movement of Adria within ~50 Myr, from the early Jurassic to earliest Cretaceous (Muttoni et al., 2005). These authors suggested that this middle-late Jurassic cusp in the African paleolatitudinal motion is underestimated in the apparent polar wander (APW) path of Besse and Courtillot (2002), as a result of smoothing due to the application of a moving average. In terms of displacement, Africa would move approximately 1600 km further southward at the position of Adria than is expected from the APW path of Besse and Courtillot (2002). The conclusion of Muttoni et al. (2005) was based on new data from Adria and published data from African and North American magmatic rocks that were rotated to northwest African coordinates using the Atlantic plate circuit. The movement towards and away from equatorial latitudes was supported by a corresponding change in latitude suggested by the nature of deep marine sediments in Adria, changing from lower Jurassic carbonate facies at tropical latitudes to middle to upper Jurassic radiolarites at equatorial latitudes, and back again to carbonate facies at tropical latitudes in the Cretaceous. Muttoni et al. (2005) concluded that the underestimated motion of Africa is the result of statistical procedures in the construction of APW paths, and that their revised pole path represents the true motion of the African plate to southerly latitudes in middle-late Jurassic times. However, they did not explore the possible reasons for this strong paleolatitudinal shift.

Plate kinematic reconstructions for the period following the break-up of Pangea are based on the constructions of plate circuits from the marine magnetic anomaly record. The placing of the continents with respect to the Earth's magnetic field, which is aligned with the spin axis, is reconstructed using paleomagnetic data. The position of continents with respect to the mantle in the period after 130 Ma is further constrained using hotspot reference frames (Müller et al., 1993; Steinberger and O'Connell, 1998; O'Neill et al., 2005; Torsvik et al., 2008a). To filter out or reduce paleomagnetic and geochronologic errors, APW paths are constructed using sliding windows. Consequently, fast motions of the continents are underestimated in APW paths.

However, the movement of a plate recorded in an APW path, is not necessarily entirely unique for that plate, but may share a motion component with all other plates. There are several episodes wherein the entire mantle and crust rotated with respect to the Earth's spin axis. These episodes are known as periods of true polar wander (TPW) and have already been reported since the 1950s (Gold, 1955; Goldreich and Toomre, 1969; Besse and Courtillot, 1991; Besse and Courtillot, 2002; Evans, 2003; Torsvik et al., 2008a). TPW results from a redistribution of density inhomogeneities in the mantle, for example caused by the rise of mantle plumes or the subduction of plates (Steinberger and Torsvik, submitted). Since TPW represents a true rotation of the mantle and crust with respect to the Earth's spin axis, it is also recorded

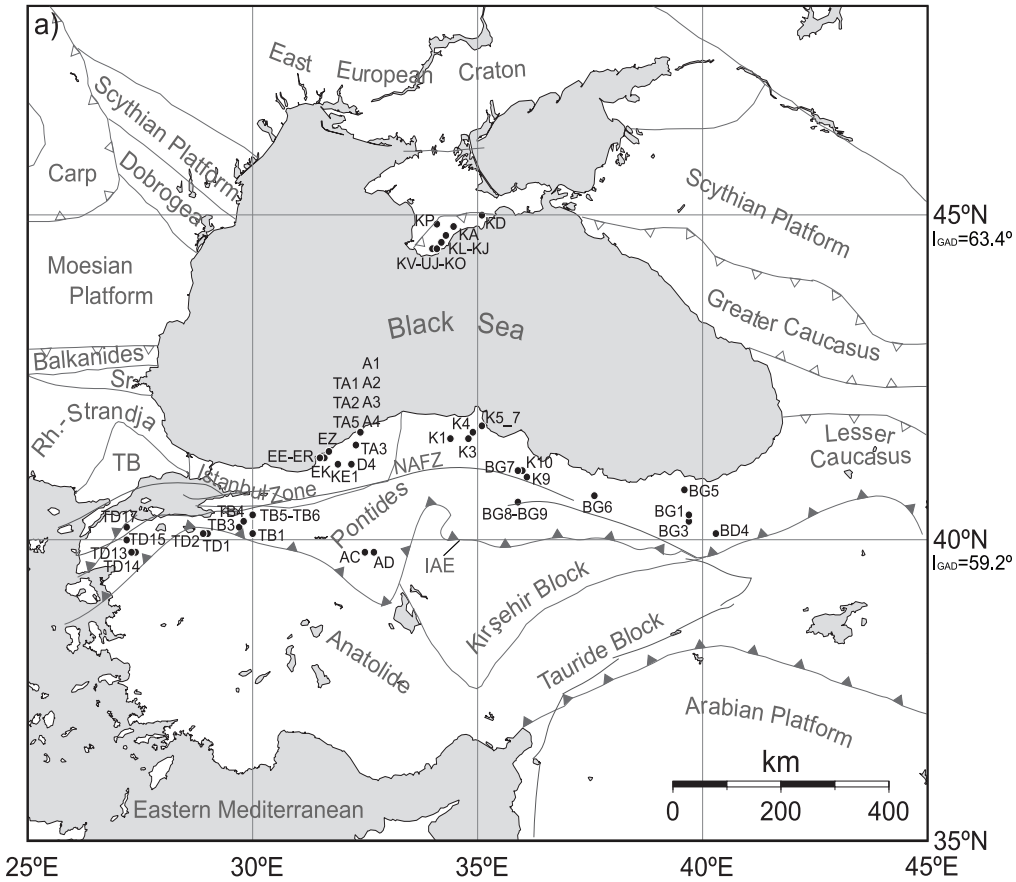


Figure 2.1 a) Map of the circum-Black Sea area indicating the sampled sites, the Izmir-Ankara-Erzincan suture (IAE), the North Anatolian Fault Zone (NAFZ), and the regional structural framework. TB=Thrace Basin; Rh.-Strandja=Rhodope-Strandja Massif; Carp=Carpathians.

in the sedimentary record, through climate controlled facies changes, and flora and fauna variations. Several post-Permian episodes of TPW were recently quantified by Steinberger and Torsvik (2008). One of the proposed intervals of TPW (between 195 and 135 Ma) coincides with the proposed southward movement of Africa of Muttoni et al. (2005). Therefore, there are two possibilities to explain the rapid motion of Africa to southerly latitudes in the late Jurassic: 1) the African plate moved with respect to the surrounding plates (with major tectonic implications), or 2) all continents move with respect to the spin axis, and therefore there is no relative motion between the continents other than that expected from plate kinematics. If this rapid motion of Africa is (mainly) caused by TPW, we should find a similar southward motion in the Eurasian plate at longitudes comparable to the Adrian paleolongitude, i.e. with respect to the Euler pole (positioned at the equator) that describes the Jurassic TPW event (Steinberger and Torsvik, 2008). The distance away from this Euler pole determines the paleolatitudinal effect of TPW.



Figure 2.1 b) Early Kimmeridgian paleogeographic reconstruction after Dercourt et al. (2000), indicating the position of the main tectonic blocks in the western Tethyan realm, and their proposed position with respect to the plate boundaries. A=Apulia; Adr=Adria; As=Asteroussia=BD=Bey Dağları; DM=Dalmatia; EP=eastern Pontides; ET=eastern Tau-rides; Fr=Friuli; G=Gavrovo; GCT=Greater Caucasus Through; Ks=Kırşehir Massif; Me=Menderes Massif; NTC=Northern Transcaucasus; P=Parnassos; Rh=Rhodes; SCrT=South Crimean Through; Se=Severin; SP=Serbo-Pelagonian; Str=Strandja; TP=Tisza Plate; WP=western Pontides. Adria is part of the African plate, whereas the Pontides and Crimea are part of the Eurasian plate. Note that we correlated the early Kimmeridgian to the GTS2004 timescale (Ogg, 2004). See Appendix 6

In this study, we test if the middle to late Jurassic southward cusp is limited to the African plate, or if the same event can be recognized for the Eurasian plate. To this end, we aimed to determine the paleolatitudinal position of the southern Eurasian margin at the location of the Pontides (Turkey) and Crimea (Ukraine). We have sampled rocks ranging from the lower Jurassic (syn-APW path cusp) to Cretaceous (post-APW path cusp). In total, we analyze the results of 27 new sites and combine them with our 13 Cretaceous sites from the Pontides (Fig. 2.1a) (Meijers et al., in review) and with 43 previously published datasets. We corrected, where possible, for the inclination shallowing in sediments with the E/I method (Tauxe and Kent, 2004).

2. Geological setting

The southern Eurasian margin was affected by the subduction of the Paleo-Tethys and Neo-Tethys oceans since the Paleozoic. The Neo-Tethys opened in the Permian, and sediments attributed to this event are widely distributed in the present-day Mediterranean area (Dercourt et al., 2000; Besse and Courtillot, 2002; Stampfli and Borel, 2002; Gutierrez-Alonso et al., 2008; Torsvik et al., 2008a). The Paleo- and Neo-Tethyan domains were separated by a series of presently east-west distributed 'Cimmerian continents' that rifted away from the African margin upon opening of the Neo-Tethys. Following Paleo-Tethys closure, northward subduction of the Neo-Tethys ocean (Fig. 2.1b) controlled the development of the Eurasian continental margin and led to the formation of several back-arc basins on the overriding plate, of which the Cretaceous-Eocene Black Sea basin is a prominent example. The absence of the Black Sea, before middle to late Cretaceous times (Okay et al., 1994b), implies that Jurassic and lower Cretaceous rocks from both sides of the present-day Black Sea were deposited at comparable latitudes. Opening of the Black Sea accommodated only $\sim 100\text{-}150$ km ($\sim 1\text{-}1.5^\circ$ inclination) of extension (Cloetingh et al., 2003; Starostenko et al., 2004; Shillington et al., 2008), which is well within paleomagnetic errors and an order of magnitude smaller than the African cusp. Therefore, the opening of the Black Sea is not expected to be significantly reflected in paleomagnetic results from the Pontides. Some authors suggested the presence of a small oceanic basin between the Pontides and Crimea in Triassic to Jurassic times (Küre ocean) (Şengör and Yilmaz, 1981; Robertson and Dixon, 1984; Stampfli and Borel, 2002; Moix et al., 2008), although the oceanic nature of this basin was challenged by others (Dercourt et al., 2000; Barrier and Vrielynck, 2008). We will explore the possible implications of this suggested oceanic basin further in this paper.

The Paleozoic and/or older Crimean basement is formed by the thinned margin of the East European Craton (EEC): the Scythian Platform (Fig. 2.1a) (Stephenson et al., 2004; Saintot et al., 2006b). Crimea is part of a deformed belt running from North Dobrogea in Romania in the west, over Crimea to the Greater Caucasus in the east (Saintot et al., 2006b) (Fig. 2.1). The Crimean basement is almost entirely covered by Mesozoic-Cenozoic volcano-sedimentary units (Nikishin et al., 2001).

They comprise: 1) a lower unit of Triassic to middle Jurassic (Bathonian) intensely deformed series of turbidites and shales, olistostromes, calc-alkaline volcanics and continental clastics, 2) a middle unit of upper Jurassic to lower Cretaceous (Berriasian) platform carbonates that changes eastward into conglomerates and turbidites. The upper Jurassic platform carbonates are allochthonous thrust slices according to Mileyev et al. (1996). Furthermore, an episode of folding and thrusting occurred in intra-Berriasian times (~145-140 Ma), 3) an upper unit of lower Cretaceous (upper Berriasian) to Eocene platform carbonates, shales, conglomerates, marls and calarenites were deposited. The upper unit experienced little deformation, compared to the lower two units (Mileyev et al., 1996; Mileyev et al., 1997; Saintot et al., 1999). The upper unit developed as a rift-related sequence (Zonenshain and Le Pichon, 1986), probably resulting from back-arc spreading in the hanging wall of the northward subducting Neo-Tethyan crust (Okay et al., 1994b; Banks et al., 1997).

The Pontides constitute the region between the Black Sea in the north and the İzmir-Ankara-Erzincan suture zone in the south, which demarcates the (northern) Neo-Tethyan ocean in Turkey (Şengör and Yilmaz, 1981). In the studied area, the Pontides consist of two different tectonic blocks: the İstanbul and Sakarya Zones (Fig. 2.1a) (Şengör and Yilmaz, 1981). The age of amalgamation of the İstanbul and Sakarya Zones has been a matter of debate, and proposed ages range from early Jurassic (Şengör et al., 1980) to early late Cretaceous (Tüysüz, 1999). In the case of early late Cretaceous amalgamation, it was thought to result from closure of the so-called 'Intra-Pontide ocean', a narrow (~300 km) oceanic basin, that separated the İstanbul Zone from Sakarya (Okay et al., 1994b; Robertson and Ustaömer, 2004). Recent studies by Bozkurt et al. (2008) and Okay et al. (2008) revealed, however, that the İstanbul and Sakarya Zones amalgamated with Eurasia during the Paleozoic, with possibly some post-Triassic reactivation (Okay et al., 2008).

The Sakarya Zone constitutes an intensely deformed Variscan (i.e. Eurasian) basement and the locally metamorphosed pre-Jurassic Karakaya Complex (Tekeli, 1981; Okay et al., 1991). The Karakaya complex is interpreted either as an inverted rift basin, or as a mid to late Triassic subduction-accretion complex (Genç and Yilmaz, 1995; Okay and Göncüoğlu, 2004; Pickett and Robertson, 2004). The İstanbul Zone comprises a non-metamorphic Ordovician to Carboniferous sedimentary sequence that experienced mild deformation during the Permo-Carboniferous, overlain by Triassic sediments. Its stratigraphy is generally correlated to the Moesian Platform in Bulgaria, from which it separated during western Black Sea opening in the early Cretaceous (Görür, 1988; Okay et al., 1994b).

The post-Triassic volcano-sedimentary cover of the Sakarya and İstanbul Zones is similar. The lower Jurassic consists of shallow marine clastics, and includes some ammonitico-rosso levels (Altuner et al., 1991). In the eastern part of the Sakarya Zone, the lower to middle Jurassic sequences include volcanics and volcanoclastics (Yilmaz et al., 2003; Yilmaz and Kandemir, 2006). The middle Jurassic (Callovian) to

lower Cretaceous deposits consist of platform carbonates (İnaltı Formation). Like on Crimea, the entire lower Cretaceous (Hauterivian) to Eocene is covered by rift-related deposits, which are related to opening of the Black Sea (Görür, 1997).

It is of importance here that Africa and Europe were separated in the Jurassic by a subduction zone in the present-day eastern Mediterranean (Ricou et al., 1998; Dercourt et al., 2000; Stampfli and Borel, 2004; van Hinsbergen et al., 2005; Barrier and Vrielynck, 2008). Further to the east, in the Pontides (Turkey), Crimea (Ukraine) and the Greater Caucasus (Russia) (Fig. 2.1a), early and middle Jurassic rift basin development probably took place in a back-arc setting, driven by the northward subduction of the Neo-Tethys south of the Pontides. This is evidenced by the large amount of volcanogenic sediments in Crimea and the eastern Pontides, and the dominantly volcanic Bathonian-Bajocian interval in the Greater Caucasus (Robinson et al., 1995b; Banks and Robinson, 1997; Nikishin et al., 2001; Saintot et al., 2006a; Saintot et al., 2006b). The subduction zones in the Jurassic Tethyan realm must have acted as an anchor in the mantle, and therefore relatively fast motion of both the African and Eurasian continents with respect to the mantle is unlikely.

3. True Polar Wander

True Polar Wander (TPW) events during the last 200 Myrs were quantified in several studies (Besse and Courtillot, 1991; Prevot et al., 2000; Besse and Courtillot, 2002). Recently, Steinberger and Torsvik (2008) calculated TPW over the last 320 Myr, by assessing the APW paths of all continents. For periods younger than 130 Ma, the paths were compared to a moving hotspot reference frame. By definition, a TPW event has an equatorial Euler pole. The paleomagnetic expression of TPW is dependent on the position of the sampling site with respect to the Euler pole during TPW, because it determines the sense of motion a location would experience during TPW.

Four intervals of TPW were identified by Steinberger & Torsvik (2008). In the period from 250-220 Ma a counterclockwise TPW (18°) around an equatorial Euler pole at 15°W would cause large northward movements in the present-day circum-Black Sea region, located at the southern margin of Eurasia. The effect of TPW was compensated in the period of 195-145 Ma with a clockwise movement around the same Euler pole. This was followed by dominantly east-west movements from 145-135 Ma, caused by 10° clockwise rotation around an equatorial Euler pole located at 37.5°E , compensated by a next period of counterclockwise TPW from 110-100 Ma that would have resulted in northward movement of the circum-Black Sea area. Therefore, in the case that TPW has been the (main) mechanism to transport Adria to low latitudes, the present-day circum-Black Sea region should have experienced a similar, and even more pronounced movement. So far, the possibility of a period of TPW causing low latitudes remains to be tested.

4. Paleomagnetic sampling, analysis and reliability criteria

4.1 Paleomagnetic sampling and analysis

Sampled lithologies vary from limestones to sandstones, siltstones, shales, marls, clays, calcarenites and volcanoclastics (see Table 2.1 and Supplementary data). Cores were collected using a motor drill. Sample orientations were measured with a magnetic compass and corrected for the present-day declination. In most cases, cores were long enough to provide multiple specimens from a single core. Therefore, the number of demagnetized specimens is sometimes higher than the number of sampled cores (Table 2.1). For absolute ages, we correlate biostratigraphic ages to the GTS2004 timescale (Ogg, 2004; Ogg et al., 2004). For several sampled sites, new biostratigraphic ages from limestones were determined by D. Altiner. Ages for all sites can be found in the Supplementary information and in Table 2.1.

Magnetic carriers were determined by performing thermomagnetic runs and isothermal remanent magnetization (IRM) curves. IRM acquisition curves were performed on samples that had been heated already until 150°C and used for AF demagnetization (Fig. 2.2a-f). Before IRM acquisition curves determination, all specimens were first demagnetized until 300 mT in three orthogonal directions, to minimize the influence of magnetic interaction and thermal activation (Heslop et al., 2004). The IRM was acquired 57 steps until 700 mT, with an in-home developed robot assisted and fully automated 2G DC SQUID cryogenic magnetometer (noise level 10^{-12} Am²). IRM measurements were analyzed using the cumulative log-Gaussian approach to identify the different coercivity components with the method developed by Kruiver et al. (2001). The diagrams were interpreted with either two or three magnetic components, overlapping in coercivity spectrum, to provide a best-fit to the IRM curves. The low intensity and low coercivity component that is usually observed using this method results from a skewed data distribution and has no physical meaning (Heslop et al., 2004). The magnetic components can be characterized by the saturation isothermal remnant magnetization (SIRM), the peak field, at which half of the SIRM is reached ($B_{1/2}$) and the dispersion of its corresponding cumulative log-normal distribution (DP) (Kruiver et al., 2001). The thermomagnetic runs were carried out in air, using a modified horizontal translation type Curie balance, with a sensitivity of $\sim 5 \times 10^{-9}$ Am² (Mullender et al., 1993) (Fig. 2.2g-i). Approximately 40 mg of powdered rock samples were put into a quartz glass sample holder and were held in place by quartz wool. Heating and cooling rates were 10°C/min. Temperatures were increased to a maximum of 700°C.

Samples were demagnetized using thermal and alternating field (AF) demagnetization methods, or a combination of both methods. Thermal demagnetization was carried out in a magnetically shielded oven, with steps of 30°C-50°C up to a maximum of 540°C. AF demagnetization up to a maximum of 90 mT was carried out with steps of 3-20 mT. A 2G Enterprises horizontal 2G DC SQUID cryogenic

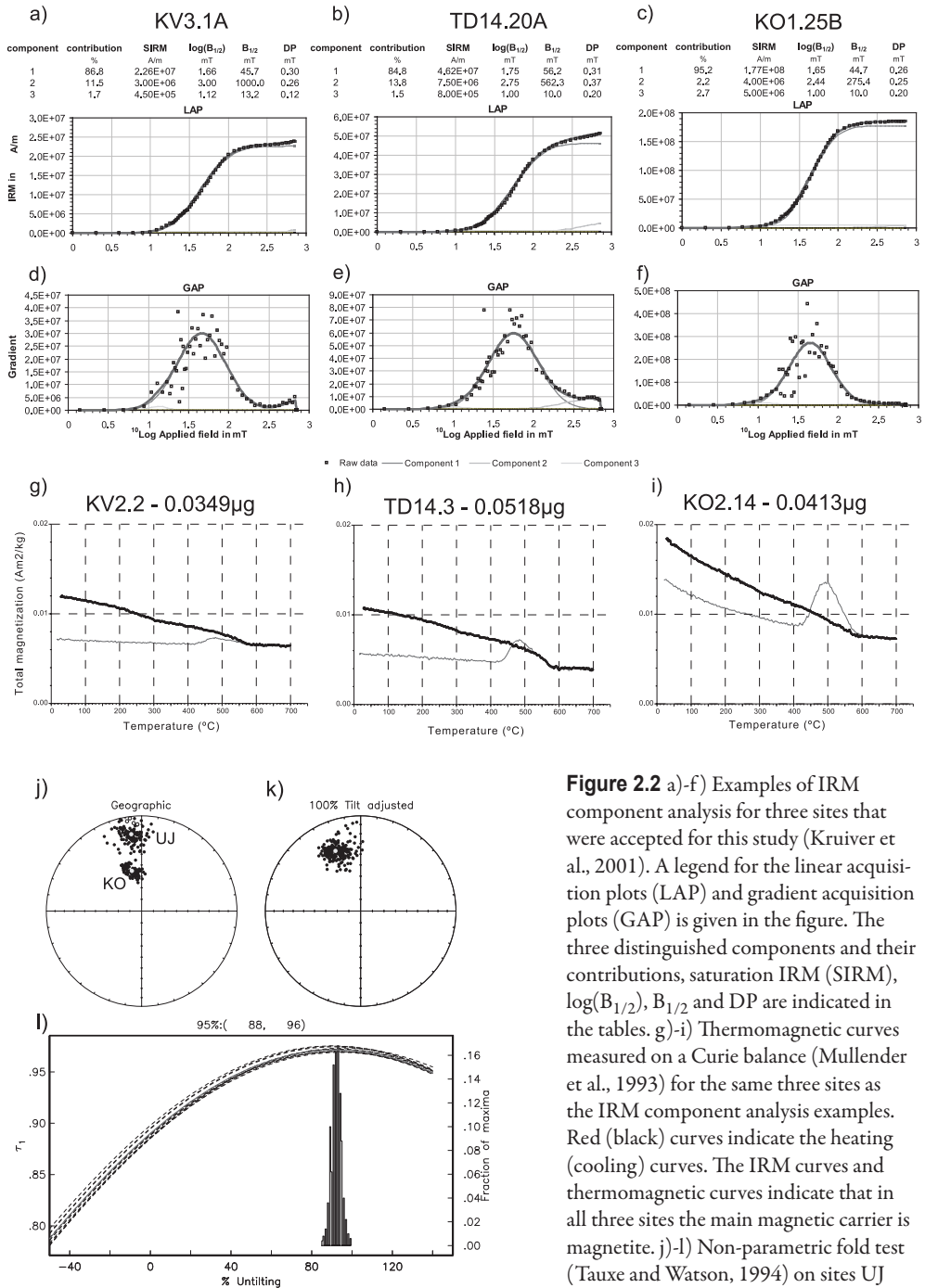


Figure 2.2 a)-f) Examples of IRM component analysis for three sites that were accepted for this study (Kruiver et al., 2001). A legend for the linear acquisition plots (LAP) and gradient acquisition plots (GAP) is given in the figure. The three distinguished components and their contributions, saturation IRM (SIRM), $\log(B_{1/2})$, $B_{1/2}$ and DP are indicated in the tables. g)-i) Thermomagnetic curves measured on a Curie balance (Mullender et al., 1993) for the same three sites as the IRM component analysis examples. Red (black) curves indicate the heating (cooling) curves. The IRM curves and thermomagnetic curves indicate that in all three sites the main magnetic carrier is magnetite. j)-l) Non-parametric fold test (Tauxe and Watson, 1994) on sites UJ and KO. j) Equal area plots of the ChRM before correction for bedding tilt (geographic coordinates), and k) after correction for bedding tilt. Results of the fold test l) as 500 bootstrapped examples of the first eigenvalues (τ_1) upon progressive untilting. Above the diagram the 95% bootstrap error is given. See Appendix 7

magnetometer with a noise level of $3 \times 10^{-12} \text{Am}^2$ was used to measure the natural remanent magnetization (NRM) of all samples. The AF demagnetization procedure and measurement of the samples was performed with an in-home developed robot assisted and fully automated 2G DC SQUID cryogenic magnetometer.

Test sets of samples were demagnetized both thermally and by alternating field, to allow comparison of both applied techniques (e.g. Gong et al. (2008b)). To remove possible stress in magnetite grains caused by surface oxidation at low temperatures (Van Velzen and Zijdeveld, 1995), most AF demagnetized samples were heated to 150°C before demagnetization (see procedures in Gong et al. (2008b)). Several samples of site UJ that were AF demagnetized were heated until 210°C before

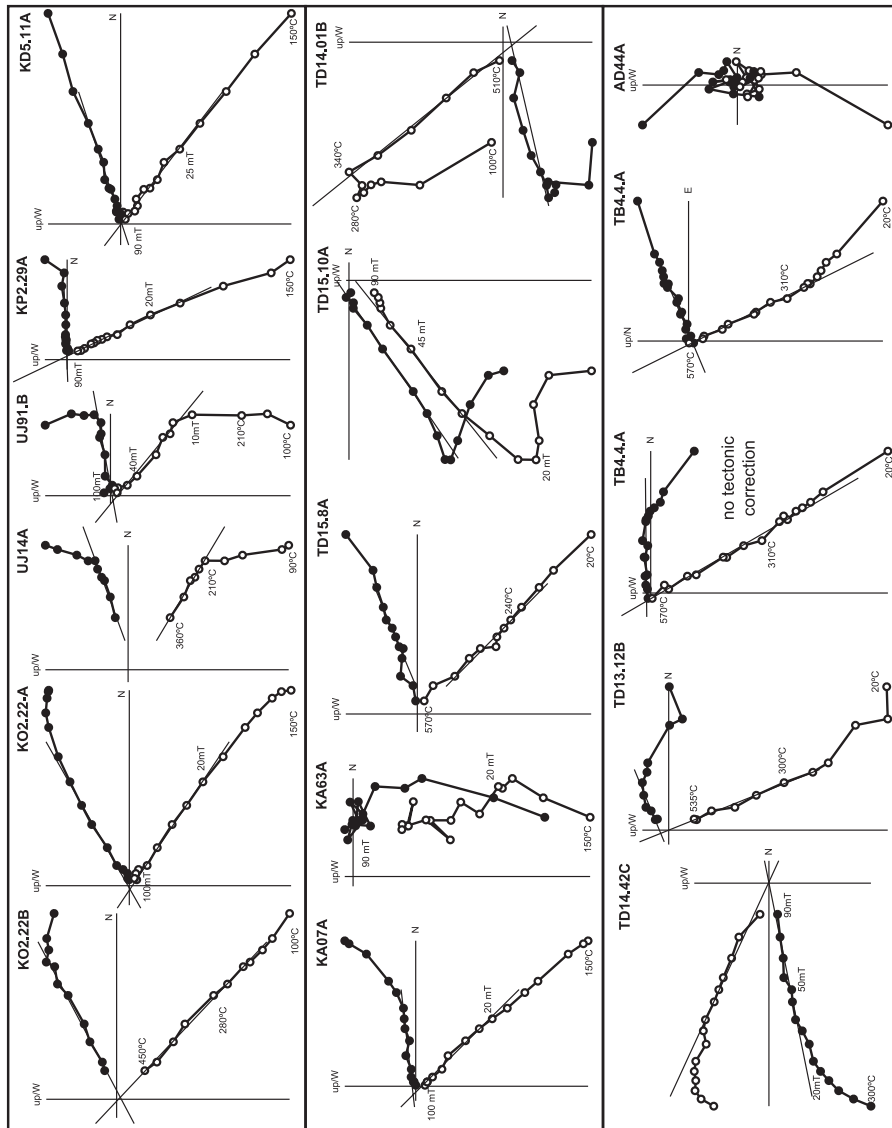


Figure 2.3 Orthogonal vector diagrams (Zijdeveld, 1967), showing characteristic demagnetization diagrams for sampled sites. Closed (open) circles indicate the projection on the horizontal (vertical) plane. Alternating field and thermal demagnetization steps are indicated. All diagrams (except for TB4.4A note) are displayed after correction for bedding orientation.

AF demagnetization, while part of the samples of site of site TD14 were heated until 300°C before demagnetization, the temperatures at which a secondary component was generally removed.

Demagnetization diagrams of the natural remanent magnetization (NRM) were plotted as orthogonal vector diagrams (Zijderveld, 1967) (Fig. 2.3). Results from generally five to eight successive temperature or AF steps were analyzed by principal component analysis (Kirschvink, 1980) to determine the characteristic remanent magnetization (ChRM) in the samples (Table 2.1).

Fisher statistics (Fisher, 1953) were used to calculate directional and virtual geomagnetic pole (VGP) means (Fig. 2.4). Because secular variation of the Earth's magnetic field induces scatter in paleomagnetic directions, which is near-Fisherian at the poles, but gradually becomes more ellipsoidal towards the equator (Creer et al., 1959; Tauxe and Kent, 2004), we calculated the VGPs from all directions. Subsequently, a variable cut-off (Vandamme, 1994) was applied to remove outliers from the datasets (e.g. from excursions, reversal transitions or other outliers) and the errors in declination (ΔD_x) and inclination (ΔI_x) were calculated following Butler (1992) (Table 2.1).

Since we sampled sedimentary rocks, we corrected sufficiently large datasets for a possible shallowing of inclination in sediments caused by compaction during burial with the elongation/inclination (E/I) method of (Tauxe and Kent, 2004), which is based on the field model TK03.GAD (Fig. 2.5, Table 2.1). The model is based on the assumption that the field averaged over sufficient time resembles that of a geocentric axial dipole (GAD). A large number (preferably $N > 100$) of individual directions is required to apply the model successfully. We ran the model for each dataset twice: once without applying a cut-off before running the model, and once applying a variable cut-off (Vandamme, 1994) before applying the model to remove outliers. The difference between both runs was not significant (Table 2.1).

Our data were compared to the paleolatitudes calculated from the APW paths of Torsvik et al. (2008a) and Besse and Courtillot (2002) (Fig. 2.6), that are very comparable for periods younger than 160 Ma. We discuss results in more detail (per site) in the Supplementary Information.

4.2 Reliability criteria

To guarantee the quality of both published and new datasets and to reliably reconstruct the paleolatitude of Crimea and the Pontides throughout the Jurassic and Cretaceous we applied a number of reliability criteria. The datasets and, if applicable, the reason of exclusion from further analysis is indicated in Tables 2.1 and 2.2. More detailed information of each site is given in the Supplementary Information.

The following reliability criteria were applied:

- 1) Samples that were demagnetized using bulk demagnetization were excluded, for

- example sites G1-G5 and O1-O2 in the study of Orbay and Bayburdi (1979),
- 2) sites that have a mean ChRM direction in geographic coordinates that is indistinguishable from the present-day geocentric axial dipole (GAD) field at the sampling location were excluded,
 - 3) datasets with suspect directions (e.g. N/up or S/down directions) that may result from an insufficiently removed (partial) overprint, datasets with an unresolved component and datasets from sites with samples that were too weak for proper demagnetization

Table 2.1
(caption see p. 64)

Site	Rej.	Rocktype	Site lat.	Site long.	Age	Δ Age	Ns/Nm	NI/NvD	D	Δ Dx	I	Δ Ix	k	α_{95}
Crimea														
KV		limestone	44.5	34.0	142.8	2.7	42/44	29/28	355.4	7.2	52.7	6.3	30.5	5.0
KO		limestone	44.5	34.1	153.3	7.8	78/107	107/105	346.2	1.5	54.2	1.2	184.4	1.0
UJ		limestone	44.5	34.1	153.3	2.5	101/129	124/115	352.2	1.4	19.7	2.5	53.7	1.8
KP		clays	44.9	34.1	112.3	12.7	128/113	84/79	2.9	3.0	52.2	2.7	46.8	2.4
KL	3,5,6,7	siltstones	44.6	34.2	169.7	2.0	17/08	08/07	108.2	8.4	1.3	16.9	19.0	13.0
KJ	5,6,7	siltstones	44.6	34.2	169.7	2.0	33/25	24/19	51.6	9.1	43.3	10.6	20.3	7.6
KA		limestone	44.7	34.3	148.1	2.7	118/147	91/82	30.5	4.9	61.7	3.0	35.9	2.6
KH	3	calcareous and clays	44.8	35.1	163.0	1.8	97/36	0/0						
KD	7	calcareous silt/sandstones and clayey marls	45.0	35.1	135.1	5.1	87/87	119/110	0.3	7.8	74.7	2.2	38.0	2.2
KE	3	calcareous and clays	45.0	35.4	148.2	2.7	97/114	0/0						
Pontides														
TD17	6	red carbonates	40.2	27.2	63.2	7.4	15/14	10/10	312.7	10.5	59.9	7.0	66.9	6.0
TD15	2?,3	calc-arenites and siltstones	40.0	27.2	186.3	3.3	10/17	12/12	353.7	5.5	55.4	4.3	124.3	3.9
TD14		limestones	39.8	27.4	160.2	4.5	59/108	95/92	155.2	1.6	-21.4	2.9	50.7	2.1
TD13		limestones	39.8	27.4	112.3	12.7	70/83	80/70	308.5	2.7	30.3	4.2	40.6	2.7
TD2		limestones	40.1	28.9	160.2	4.5	36/46	29/29	333.0	8.6	64.5	4.6	41.6	4.2
TD1	2?,6	sandstones	40.1	29.0	186.3	3.3	12/12	11/11	350.2	6.5	55.8	5.1	119.5	4.2
TB3	3,5,6	pink limestones	40.2	29.7	163.0	1.8	103/29	21/21	111.0	6.8	-18.7	12.4	11.1	10.0
TB4	2?,3,4,6	limestones	40.3	29.8	130.4	3.0	15/15	13/13	11.7	15.3	59.3	10.4	22.7	8.9
TB5	5,6	red limestones	40.4	30.0	186.3	3.3	73/27	20/23	330.6	5.0	-3.0	10.0	24.4	6.7
TB6	6	siltstones	40.4	30.0	186.3	3.3	26/10	10/10	312.5	5.8	-13.5	11.0	36.9	8.1
TB1	3	limestones	40.1	30.0	163.0	1.8	15/13	0/0						
TA3	2?,3,4,5,6	limestones	41.5	32.3	130.4	3.0	15/9	8/8	14.6	30.6	60.7	19.2	13.4	15.7
TA1	3,4,5,6	limestones	41.7	32.4	130.4	3.0	24/15	10/10	35.8	99.9	61.6	83.9	1.0	99.9
AC	5,6	limestones	39.8	32.5	144.5	2.5	43/20	19/19	272.6	17.6	62.7	10.2	15.0	9.0
AD	3	limestones	39.8	32.7	142.5	12.5	60/30	0/0						
BG8	5,6	limestones/dolomites	40.6	35.9	163.0	1.8	56/10	8/8	318.7	7.9	39.4	10.2	56.4	7.4
BG9	5,6	grainstones	40.6	35.9	150.6	14.1	62/15	14/11	173.0	11.1	-41.3	13.7	25.7	9.2
BG3	2?,5,6	red siltstones	40.3	39.7	187.6	12.0	82/16	11/11	9.0	19.0	67.5	8.6	31.7	8.2
Pontides - previous study														
ER	5,6	clays/volcanoclastics	41.3	31.5	86.4	2.9	16/14	14/14	331.5	8.2	40.3	10.3	24.2	8.3
EE	6	red pelagic limestones	41.3	31.5	86.4	2.9	15/13	13/12	169.2	6.4	-44.6	7.3	56.7	5.8
EK	6	red pelagic limestones	41.3	31.6	86.4	2.9	19/14	14/14	328.6	3.2	36.6	4.4	141.0	3.4
A4	6	red pelagic limestones	41.7	32.4	86.4	2.9	10/7	7/7	210.5	9.9	-44.2	11.3	28.5	11.5
A1	5,6	shales	41.7	32.4	121.0	9.0	14/14	14/14	21.3	12.3	19.2	22.2	9.9	13.3
A3	5,6	shales	41.7	32.4	121.0	9.0	14/14	7/7	45.1	11.5	31.9	17.3	27.9	11.6
TA2	5,6	red pelagic limestones	41.7	32.4	86.4	2.9	149/124	89/86	336.5	2.4	42.2	2.9	47.2	2.3
TA5	5,6	volcanoclastics	41.7	32.4	84.7	1.2	68/121	117/115	186.4	1.9	-46.1	2.1	64.5	1.7
K3	4,5,6	shales	41.6	34.8	114.8	15.2	12/14	14/13	188.0	17.3	44.0	19.7	7.1	16.7
K5_7	5,6	limestones/marls	41.8	35.1	74.5	9.0	19/21	11/11	212.9	11.1	-16.6	20.7	11.4	14.1
BG7	6	red pelagic limestones	41.1	35.9	86.4	2.9	43/27	17/17	85.3	4.2	35.4	6.0	78.9	4.0
K10	6	red pelagic limestones	41.1	36.0	86.4	2.9	7/13	13/13	77.0	2.2	37.4	3.0	324.6	2.3
K9	5,6	red pelagic limestones	41.0	36.1	86.4	2.9	13/14	14/9	31.3	2.9	6.0	5.7	326.0	4.6

zation resulting in erratic behavior (e.g. TB1), were excluded from further analysis. An example is site TB5, where a temporary problem with the oven that was used for demagnetizing the samples resulted in the acquisition of a spurious component in the samples at higher temperatures (>300°C). Another example is site TD15 which gave completely different and unexplainable (but consistent) results using AF and thermal demagnetization.

- 4) datasets with age uncertainties larger than 15 Myrs were excluded,
- 5) datasets that have an error in latitude (using ΔI_x calculated from A95) that is larger than 7° (averaged over ΔI_x^+ and ΔI_x^-) were excluded, because this gives us the resolution to compare the dataset with the APW path,
- 6) datasets that do not reach the minimum amount of samples ($N > 24$) to allow reliable calculation of the paleolatitude (Van der Voo, 1990) were not taken into account. In the case that volcanic rocks were sampled, the minimum required number of flows/sites (with a minimum of demagnetized specimens per lava flow ≥ 5) that constitute one locality is 5,
- 7) datasets that do not pass the fold test were excluded. An example of this is site KD,

Table 2.1 (continued, caption see p. 64)

Site	ChRM directions - tilt corrected					VGPs - tilt corrected						
	Ni/NVD	D	ADx	I	ΔI_x	Paleolatitude	k	α_{95}	λ	ϕ	K	A95
Crimea												
KV	29/28	344.0	4.7	27.0	7.7	14.3	30.5	5.0	56.9	-116.8	36.7	4.6
KO	107/105	332.0	0.7	30.3	1.0	16.3	305.2	0.8	53.2	-97.1	470.7	0.6
UJ	124/115	342.7	1.6	33.8	2.3	18.5	53.7	1.8	60.3	-111.3	76.5	1.5
KP	84/81	353.6	3.8	58.6	2.6	39.3	44.2	2.4	82.7	-103.3	30.3	2.9
KL	08/07	110.5	10.9	28.0	17.6	14.9	19.0	13.0	-3.5	99.3	28.5	10.6
KJ	24/22	19.8	10.5	49.1	10.4	30.0	15.6	8.1	68.6	160.6	12.6	9.1
KA	91/82	331.3	3.3	50.9	3.1	31.6	36.8	2.6	64.1	-76.2	31.1	2.8
KH	0/0											
KD	119/113	350.9	2.3	33.8	3.4	18.5	28.5	2.5	62.4	-126.0	36.9	2.2
KF	0/0											
Pontides												
TD17	10/10	2.2	6.5	39.8	8.2	22.6	66.8	6.0	72.3	-159.5	66.9	6.0
TD15	12/12	346.7	4.1	42.7	4.8	24.8	124.0	3.9	71.1	-112.6	139.0	3.7
TD14	95/92	166.1	1.8	29.9	2.9	16.0	48.9	2.1	63.3	58.4	70.5	1.8
TD13	80/75	305.5	5.1	64.8	2.7	46.7	43.3	2.5	50.5	-34.0	23.0	3.5
TD2	29/29	24.5	4.8	44.9	5.3	26.4	41.5	4.2	65.5	145.2	40.5	4.3
TD1	11/11	13.0	4.2	29.7	6.5	15.9	119.7	4.2	63.3	-179.8	131.6	4.0
TB3	21/21	85.3	17.4	58.3	12.3	39.0	11.1	10.0	27.1	90.1	6.5	13.5
TB4	12/10	78.3	8.9	64.7	4.7	46.6	121.4	4.4	35.2	85.2	63.1	6.1
TB5	23/23	250.2	9.1	35.0	13.0	19.3	11.0	9.5	-27.2	-62.9	13.4	8.6
TB6	10/10	299.8	6.9	-30.5	10.7	16.4	36.9	8.1	10.4	-92.2	54.0	6.6
TB1	0/0											
TA3	8/8	324.6	99.9	78.9	14.9	68.8	12.4	15.7	57.1	9.4	5.2	26.8
TA1	10/10	329.4	99.9	61.3	84.6	42.4	1.0	99.9	67.4	-45.5	1.0	99.9
AC	19/18	315.7	8.9	35.9	12.4	19.9	18.5	8.3	47.3	-72.0	18.1	8.4
AD	0/0											
BG8	8/8	13.0	19.1	63.9	10.4	45.6	33.8	9.7	79.3	83.9	18.5	13.2
BG9	14/11	175.8	12.3	-46.6	13.1	27.9	25.7	9.2	-76.8	52.4	18.7	10.8
BG3	11/11	18.3	40.1	71.4	13.8	56.0	11.7	13.9	70.2	70.9	5.6	21.1
Pontides - previous study												
ER	14/14	320.2	9.0	48.2	9.1	29.2	24.1	8.3	55.7	-66.2	26.7	7.8
EE	13/12	170.0	5.9	-39.7	7.5	22.5	56.7	5.8	-69.5	58.7	65.1	5.4
EK	14/14	322.6	3.9	47.9	4.0	29.0	138.1	3.4	57.3	-68.5	136.9	3.4
A4	7/7	213.3	9.7	-41.5	11.9	15.0	10.4	12.9	-57.1	-35.3	47.2	8.9
A1	14/14	18.9	12.2	28.1	19.6	15.0	10.4	12.9	58.7	175.4	12.4	11.8
A3	7/7	33.1	18.7	53.6	15.9	34.1	27.9	11.6	63.0	127.7	16.3	15.4
TA2	89/86	325.3	2.6	48.8	2.6	29.7	53.4	2.1	59.7	-69.6	47.0	2.3
TA5	117/115	169.6	1.4	-43.9	1.6	25.7	112.1	1.2	71.8	63.9	113.6	1.2
K3	14/12	186.2	14.9	-43.6	17.2	25.5	12.2	12.9	-73.1	15.2	11.4	13.4
K5_7	11/11	206.3	7.7	-30.2	12.0	16.2	41.5	7.2	-54.7	-16.9	39.2	7.4
BG7	17/17	74.7	4.1	43.1	4.8	25.1	114.2	3.4	27.3	115.4	95.1	3.7
K10	13/13	55.9	2.7	43.0	3.2	25.0	324.4	2.3	41.4	127.2	284.4	2.5
K9	14/11	36.8	11.8	42.9	13.9	24.9	12.1	13.7	55.5	142.4	19.3	10.7

TK03 corrected datasets

Site	Age	no cut-off													Vandamme cut-off												
		D	I	I ₉₅	I ₁	I _u	λ	λ _u	K	A95	ΔD _x	ΔI _x	D	I	I ₉₅	I ₁	I _u	λ	λ _u	K	A95	ΔD _x	ΔI _x				
KO	153.3	7.8	332.0	30.2	32.4	30.3	32.0	41.0	16.3	17.4	23.5	365.4	0.7	0.7	1.1	332.0	30.3	30.0	30.9	35.9	16.1	16.7	19.9	454.2	0.6	0.7	1.0
UJ	153.3	2.5	342.8	32.7	31.2	33.8	36.4	16.8	18.5	20.2	27.2	2.5	2.6	3.8	342.7	33.8	32.8	35.4	41.1	17.9	19.6	23.6	75.1	1.5	1.6	2.3	
KP	112.3	12.7	351.5	58.6	64.2	58.2	61.2	78.3	38.9	42.3	67.5	24.9	3.2	4.2	2.8	353.6	58.6	57.9	60.1	71.6	38.6	41.0	56.4	30.4	2.9	3.8	2.6
KA	148.1	2.7	335.1	51.1	50.9	53.8	71.6	31.6	34.3	56.4	13.0	4.3	5.2	4.2	331.3	50.9	49.8	52.1	59.6	30.6	32.7	40.4	31.1	2.8	3.4	3.1	
TD14	160.2	4.5	166.6	-29.8	-39.5	-31.0	-38.5	-50.2	16.7	21.7	31.0	47.0	2.1	2.3	2.7	166.1	-29.9	-29.1	-32.0	-39.4	15.6	17.4	22.3	65.9	1.8	1.9	2.8
TA2	86.4	2.9	324.4	49.2	54.8	49.8	55.0	68.7	30.6	35.5	52.1	40.5	2.4	3.0	2.2	325.3	48.8	48.2	50.6	59.4	29.2	31.3	40.2	46.8	2.3	2.7	2.4
TA5	84.7	1.2	170.1	-44.0	-48.5	-44.2	-46.3	-65.2	25.9	27.6	47.3	92.6	1.4	1.6	1.6	169.6	-43.9	-43.6	-45.0	-54.5	25.5	26.6	35.0	112.0	1.2	1.4	1.5

Table 2.1 (continued) Table showing all data from our study. First and second table: Site number bold; accepted site. Rej.=rejection criterium (see section 4.2), Site lat.=site latitude; Site long.=site longitude; Age=age assigned according to Ogg (2004) and Ogg et al. (2004); Δ Age=age error; Ns/Ns=number of sampled cores/number of measured specimens; Ni/NvD=number of interpreted directions/number of directions that are remaining after applying a variable cut-off (Vandamme, 1994); D=declination; ΔD_x=declination error; I=inclination; ΔI_x=inclination error; k=estimate of the precision parameter determined from the ChRM directions; a95=cone of confidence determined from the ChRM directions. All values are given before and after correction for bedding tilt; λ=pole latitude; φ=pole longitude; K=precision parameter determined from the mean virtual geomagnetic pole (VGP) direction; A95=cone of confidence determined from the mean VGP direction. Third table: The inclination after correction for inclination (I) error results from 5000 bootstraps of TK03.GAD, with 95% lower and upper bounds (I_l, I_u), while I_p is the inclination resulting from intersection of the distribution with TK03.GAD (Tauxe and Kent, 2004). λ is the corresponding corrected latitude, with 95% lower and upper bounds (λ_l, λ_u), ΔD_x, ΔI_x, K and A95 are as mentioned above for the unflattened datasets. * Site TD13 was rejected for reasons discussed in the text.

because the six subsets with different bedding orientation do not pass the fold test (of Tauxe and Watson, 1994 (see Supplementary data). The tightest grouping of data occurs at 40% unfolding. We also determined the paleofield direction from a synfolding remanence of site KD using the small circle intersection (SCI) method of Shipunov (1997), modified by Waldh or and Appel (2006) (see Supplementary data). The directions from the foldtest and the SCI method are very comparable. The results suggest that remagnetization occurred at an inclination of 54.6-62.4° (corresponding to a paleolatitude of 35.1°N < 38.1°N < 43.7°N). If we compare this value to the APW path of Eurasia (Torsvik et al., 2008a), this coincides very well with values predicted for post-Paleocene times (Fig. 2.7), which supports remagnetization, likely during folding. 8) datasets that have an inclination that is too low to be explained by flattening (maximum flattening factor allowed: $f=0.3$, see Fig. 2.7b) compared to the APW path. The flattening factor f relates the ratio of the observed inclination I_{obs} to the inclination of the applied field I_f (King, 1955), according to

$$\tan I_{obs} = f \tan I_f \quad (1)$$

In our paleomagnetic results, I_f is the geomagnetic field at the time of NRM acquisition. Typical values of f are 0.4-0.6 in sediments, but can be as low as 0.3 in red beds (Tauxe and Kent, 1984). Therefore, we use a lower boundary cut-off of $f \geq 0.3$ than can be expected from the APW path (Torsvik et al., 2008a). We also rejected site TD13 and the site in Crimean sediments from Rusakov et al. (1971), because the inclination of the reported data is, even when taking the error into account, higher than the present-day GAD field inclination at the sampling locality.

Two sites with the same age that were sampled in close proximity within the same sedimentary sequence were rejected, because their mean ChRM directions are very different (site KL and KJ, see Supplementary data).

5. Results

5.1 Results – this study

After applying the above reliability criteria, there are nine remaining datasets from the 41 datasets for the paleolatitude reconstruction of Crimea and the Pontides in Jurassic-Cretaceous times. The nine remaining datasets are from three age ranges: Callovian-Berriasian (~164.7-140.2 Ma, six sites), Aptian-Albian (~125.0-99.6 Ma, one site) and Coniacian-Santonian (~89.3-83.5 Ma, two sites) (Fig. 2.6b). The oldest two intervals consist of datasets from both Crimea and the Pontides; the middle age interval contains only Crimean data, and the youngest interval consists only of datasets from the Pontides.

Two of our datasets that were taken from upper Jurassic rocks have similar ages: sites UJ and KO. Because of their proximity and the difference in bedding tilt, we performed a fold test. The equal-area plots of directions from both limbs before and after tilt correction (Fig. 2.2j-1) show that in geographic coordinates the two sites have significantly different directions, while after tectonic tilt correction the directions

Figure 2.4 Equal area projections of the ChRM directions of all sites (except those where $N = 0$; Table 1). Open (closed) symbols denote projection on upper (lower) hemisphere. Large black (blue) symbols with black circle indicate respectively the mean directions and their cone of confidence (α_{95}) after (before) tilt correction. Red (small) circles indicate the individual directions rejected by the Vandamme cut-off angle (Vandamme, 1994). Black lines indicate the great circles that were used to calculate the best fitting ChRM directions (McFadden and McElhinny, 1988). Red star indicates the present-day geocentric axial dipole direction at the sampled location. See *Appendix 8*

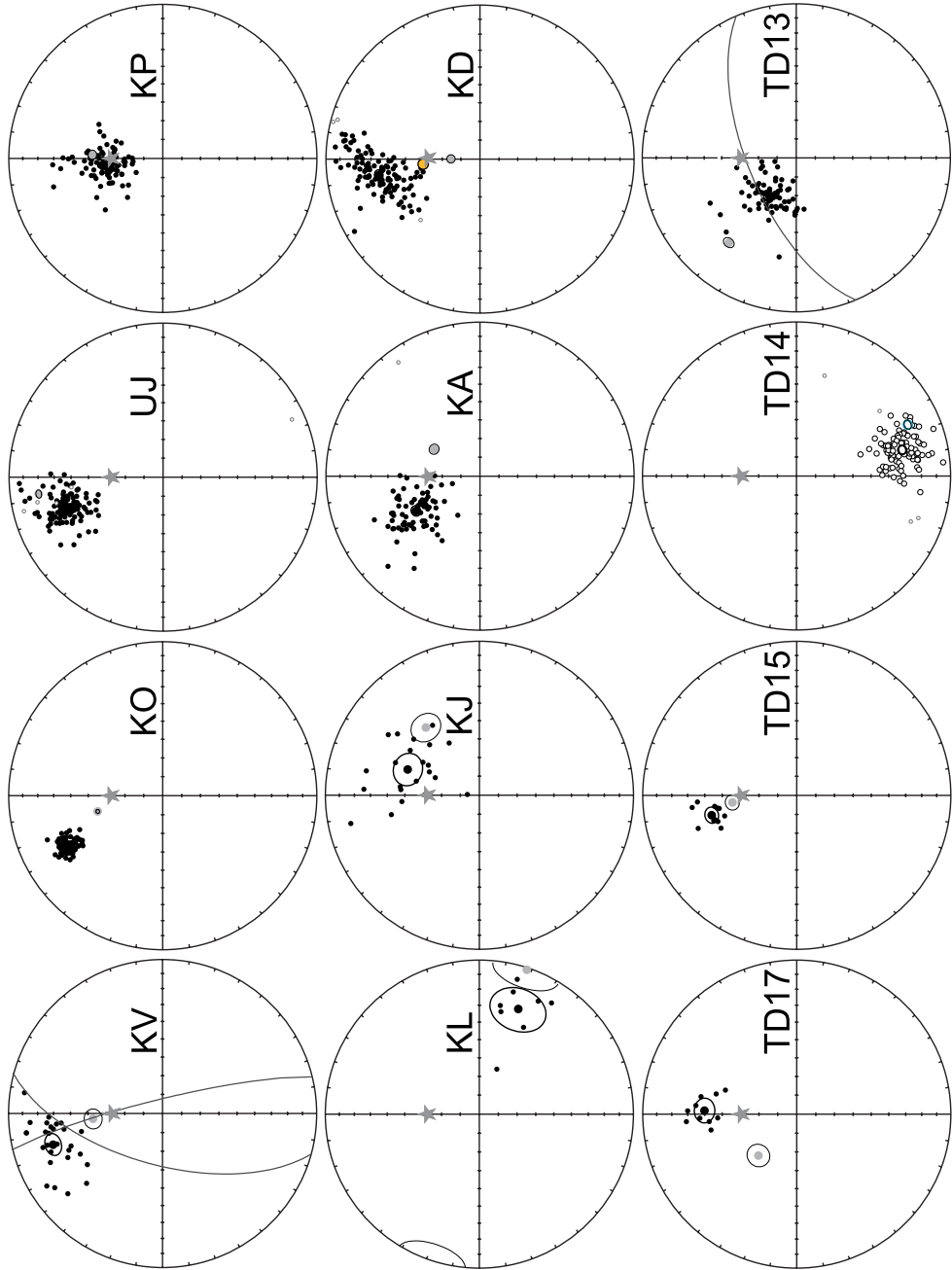
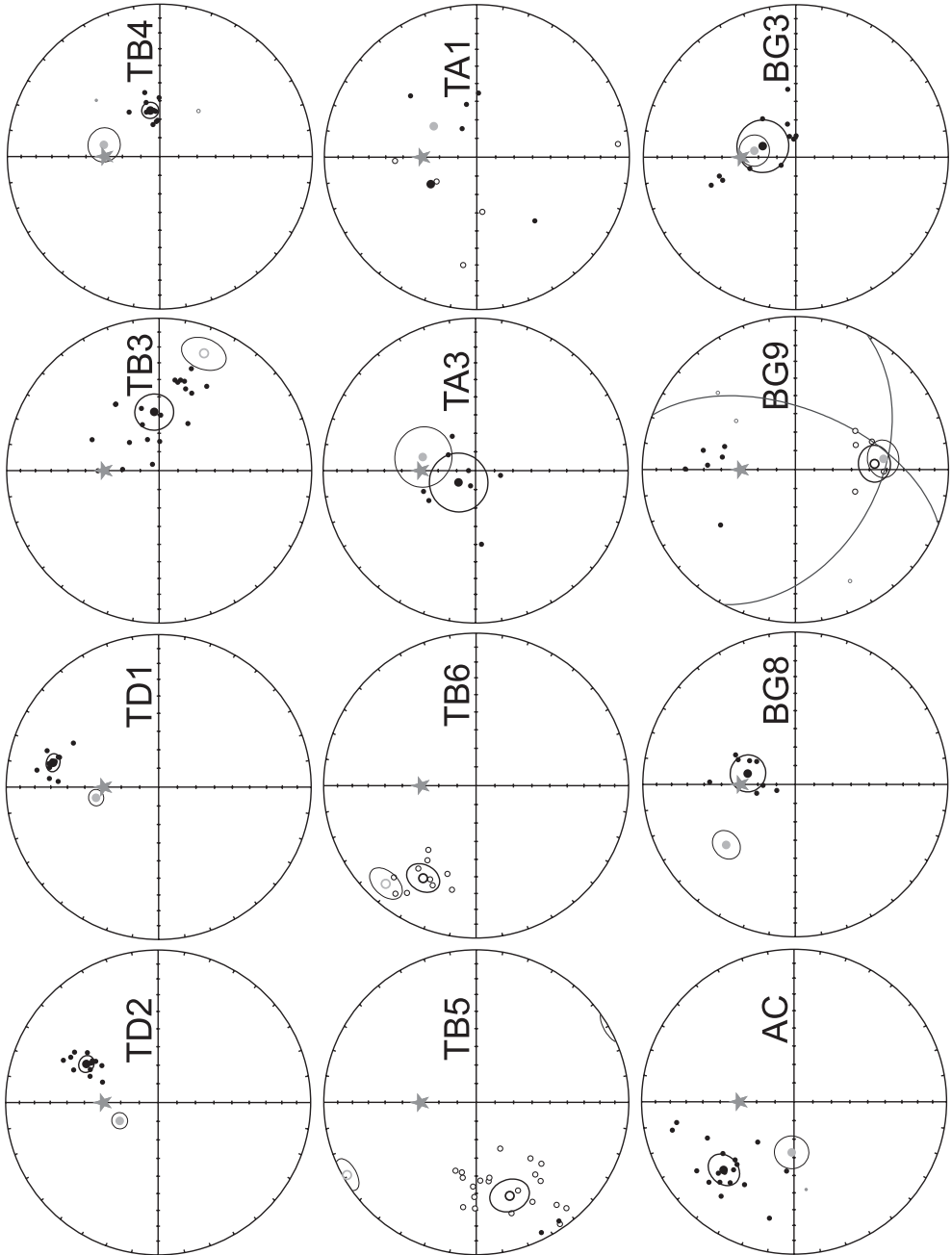
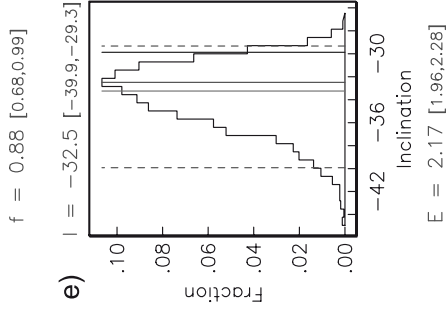
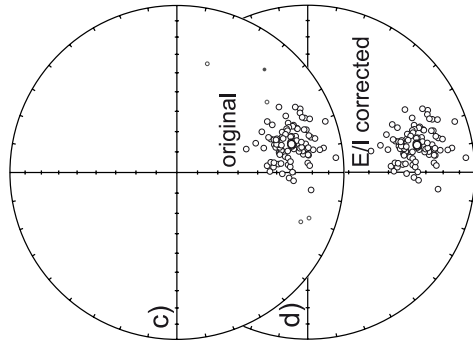
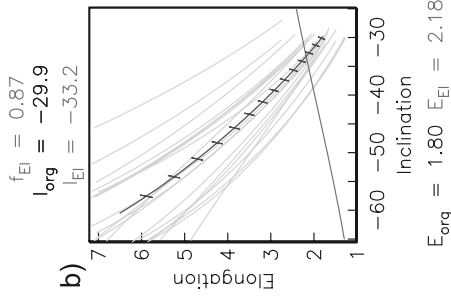
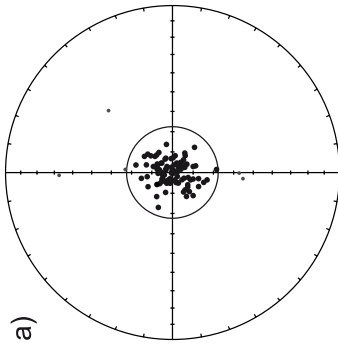


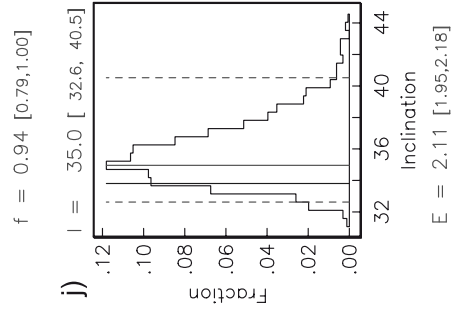
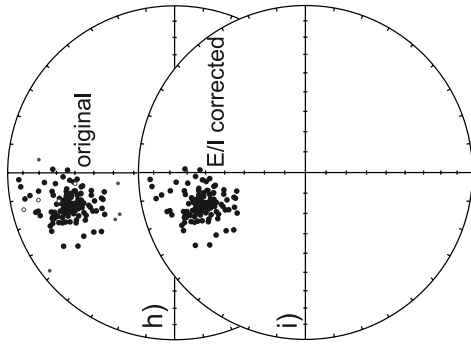
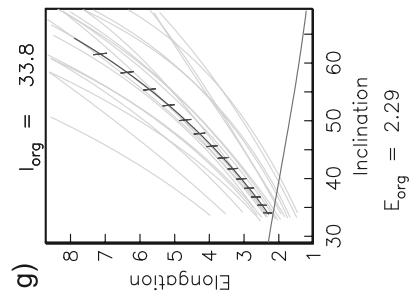
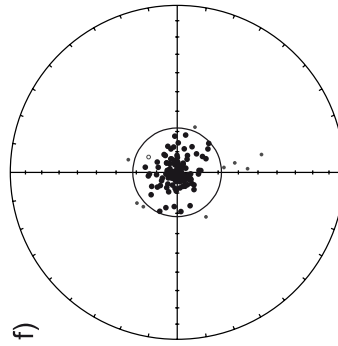
Figure 2.4
(continued)
See Appendix 8



TD 14



UJ



of both sites form a single cluster. The nonparametric fold test of Tauxe and Watson (1994) (Fig. 2.2j-1) is considered to be positive because closest grouping is reached close to full unfolding (95% bootstrap errors: 88%–96%). The small deviation from 100% significance may be caused by orientation or bedding plane errors. This fold test checks for maximum clustering, but this need not always be the ideal case (McFadden, 1998), while also a well-recorded secular variation distribution would have a slight elongation at this latitude, which is not necessarily compatible with maximum clustering. Furthermore, the two groups of pre-tilting directions that can be seen within the data of site KO (Fig. 2.2j), and that form one cluster after tectonic tilt correction (Fig. 2.4), give an extra indication that the ChRM direction is a pre-folding direction. Hence, we conclude that the magnetization of site UJ and KO was acquired before folding, even though the tilt corrected means just fail to have a common true mean direction (ctmd). To determine whether two distributions have a ctmd, we used the reversal test developed by McFadden and McElhinny (1990) and their classifications (A, B, C, indeterminate). The classifications are based on the critical angle γ_c and the angle γ between the means. Because we use their test with simulation, the test is equivalent to using the V_w statistical parameter of Watson (1983).

In the oldest interval (~ 164.7 - 140.2 Ma), we have six datasets (two from the Pontides and four from Crimea); four of these were corrected for inclination error with the E/I method (Tauxe and Kent, 2004). The E/I method was carried out on the datasets before and after applying a variable cut-off to the datasets (Vandamme, 1994) (see section 4.1). The difference between both approaches is negligible (Fig. 2.6), on average the calculated paleolatitude correction after applying the E/I method is not significant and only ~ 2 - 3° higher than before applying the method (Fig. 2.5). All datasets in the oldest age interval have a trend in paleolatitude that is consistent with the APW path (decreasing from $\sim 21^\circ\text{N}$ at ~ 165 Ma to $\sim 16^\circ\text{N}$ at ~ 140 Ma) (Fig.

Figure 2.5 a)-h) Equal-area projections of the individual VGP directions before E/I correction (a and f) and equal-area projections of the individual ChRM directions before (c and h) and after (d and i) E/I correction (symbols as in Figure 2.4) (Tauxe and Kent, 2004) with corresponding elongation vs. inclination (b and g) and fraction (of 5000 bootstraps) vs. inclination plots (e and j) for TD14 (a-d) and UJ (e-h). In the elongation vs. inclination plots the E/I for the TK03.GAD model (green line) and for the datasets (red barbed line) for different degrees of flattening are plotted. The red barbs indicate the direction of elongation (horizontal is E–W and vertical is N–S). Also shown are examples (yellow lines) from 20 (out of 5000) bootstrapped data sets. The crossing points (if the dataset intersects the model) represent the inclination/elongation pair most consistent with the TK03.GAD model, given as inc_{EI} (in green) above the panel; inc_{org} = original inclination, E_{org} = original elongation of the dataset, E_{EI} and inc_{EI} are the elongation and inclination according to the E/I model, respectively. In the fraction/inclination plot, a histogram of intersecting points from 5000 bootstrapped data sets is shown. The most frequent inclination (solid red vertical line; dashed red vertical lines denote the 95% bootstrap error) is given as value (and error range) on top of the panel; the inclinations of the original distribution (blue vertical line) or the intersection with the model (green vertical line) are indicated; E = the elongation (and error range) resulting from the bootstrapped data sets. See Appendix 9

2.6), except for one dataset (KA). Site KA yields a paleolatitude that is $\sim 31^\circ\text{N}$, which is higher than the other datasets. Among Aptian-Albian (~ 125.0 - 99.6 Ma) rocks, one site from Crimea (KP) passed the reliability criteria. Site KP yields a paleolatitude that is within error (ΔI_x and age error) with the paleolatitude predicted by the APW paths (Besse and Courtillot, 2002; Torsvik et al., 2008a), before and after correction with the E/I method. Unfortunately, the site has a relatively large age error (± 12.7 Ma). The two datasets from the Pontides from the youngest age group (~ 89.3 - 83.5 Ma) yield paleolatitudes that are very comparable (TA2) to slightly lower (TA5) than the paleolatitudes that are predicted by the APW paths (Besse and Courtillot, 2002; Torsvik et al., 2008a), both before and after correction with the E/I method.

5.2 Results – literature data

All data reported for the area of interest from the global paleomagnetic database (GPMDB) are listed in Table 2.2 and Fig. 2.7. The studies in the GPMDB are from Van

Figure 2.6 Grey shaded areas in all three panels indicate the periods of true polar wander and the sense of motion it would cause in the circum-Black Sea area, calculated by Steinberger and Torsvik (2008). CCW: counterclockwise; CW: clockwise; TMVSG08: Torsvik et al. (2008); ST08: Steinberger and Torsvik (2008); BC02: Besse and Courtillot (2002); MEKB05: Muttoni et al. (2005); SBSC07: Satolli et al. (2007); SBC08: Satolli et al. (2008). All shown data are calculated in Black Sea coordinates (42.5°N , 31°E). a) Age versus latitude plot with the African APW path and its $\Delta\lambda$ error envelope calculated from the ΔI_x of Torsvik et al. (2008a) (pink shaded area, 250-0 Ma), the APW path of Besse and Courtillot (2002) (purple curve, from 200-0Ma), the TPW corrected APW path of Steinberger and Torsvik (2008) (green curve, 250-0 Ma). Blue circles with $\Delta\lambda$ error bars calculated from the ΔI_x : data from the study by Muttoni et al. (2005). Green circles with their $\Delta\lambda$ error bars calculated from the ΔI_x or dp/dm error bars: literature data used in the reconstruction by Muttoni et al. (2005). Red circles with $\Delta\lambda$ error bars calculated from the ΔI_x error bars: data from the study by Satolli et al. (2007; 2008). Yellow diamonds with $\Delta\lambda$ error bars calculated from the ΔI_x and age error bars: data from Aiello et al. (2008). More information about the data: see section 6. b) Age versus latitude plot with the Eurasian APW path and its $\Delta\lambda$ error envelope calculated from the ΔI_x error envelope of Torsvik et al. (2008a) (blue shaded area, 250-0 Ma), the APW path of Besse and Courtillot (2002) (purple curve, from 200-0Ma), the TPW corrected APW path of Steinberger and Torsvik (2008) (green curve, 250-0 Ma). Thin purple lines (250-0 Ma) indicate the position of the pole path calculated for flattening factors (f) between 1.0 and 0.3, with steps of 0.1. Small yellow circles with $\Delta\lambda$ error bars calculated from the ΔI_x and age error bars: rejected data from this study; large blue circles with $\Delta\lambda$ error bars calculated from the ΔI_x and age error bars: accepted data from this study. Green squares with $\Delta\lambda$ error bars calculated from the ΔI_x and age error bars indicates the paleolatitude of site KD after 40% unfolding, stippled line shows the path along fixed paleolatitude until it intersects the APW path, indicating the possible moment of remagnetization. c) Age versus latitude plot with the Eurasian APW path and its $\Delta\lambda$ error envelope calculated from the ΔI_x error envelope of Torsvik et al. (2008a) (blue shaded area, 250-0 Ma), the APW path of Besse and Courtillot (2002) (purple curve, from 200-0Ma), the TPW corrected APW path of Steinberger and Torsvik (2008) (green curve, 250-0 Ma). Blue large circles as in Fig. 2.7b; pink large circles: data after correction with the E/I method (Tauxe and Kent, 2004) on which a variable cut-off has been applied (Vandamme, 1994) before correction with the E/I method with their 95% bootstrap error range; grey large circles: data after correction with the E/I method (Tauxe and Kent, 2004) on which a variable cut-off has been applied (Vandamme, 1994) after correction with the E/I method. *See Appendix 10*

Data recalculated to 42.5°N/31°E

#	Authors	Age	Δ Age	N (total #) N (statistics)	Dec	ΔD _i	Inc	Δk _i	λ	k	U _{g5}	Δλ+	Δλ-	K	A95	Rej.
Crimea																
1	Anferova (1971)	98.5	1.5	13	328.4	2.9	58.5	2.0	392	600.0	2.0	2.3	2.2	362.1	2.2	1.6
2	Anferova (1971)	134.0	6.0	21	357.2	10.1	45.1	11.3	26.6	15.0	9.0	10.3	8.1	13.4	9.0	1.5,6
3	Anferova (1971)	168.5	3.5	18	348.2	9.1	45.9	9.9	27.3	22.0	8.0	9.1	7.4	19.2	8.1	1.5,6
4	Pechersky et al. (1993)	106.0	6.0	15	349.3	9.2	43.9	10.6	25.7	24.3	7.3	9.3	7.5	22.3	8.3	5.6
5	Pechersky et al. (1993)	168.5	7.5	48	4	101.6	24.9	30.9	38.1	16.7	13.0	35.9	20.3	15.9	23.8	5
6	Pechersky et al. (1993)	168.5	7.5	22	97.4	10.9	43.9	12.5	25.7	12.0	9.0	11.3	8.7	11.0	9.8	5.6
7	Pechersky et al. (1993)	168.5	7.5	43	138.6	8.6	45.2	9.5	26.7	24.0	5.0	8.5	7.0	21.3	7.7	6
8	Pechersky and Safonov (1993)	161.0	15.0	67	30.1	3.4	52.5	3.0	33.1	999.9	4.7	30.8	2.8	716.5	2.9	7
9	Pechersky and Safonov (1993)	130.5	30.5	2	351.6	61.1	49.0	56.5	29.9	34.8	4.7	-90.8	33.7	27.8	49.4	6
10	Pechersky and Safonov (1993)	149.5	1.5	21	4	308.1	15.7	44.8	17.6	26.4	49.0	4.7	17.3	44.0	14.0	6
11	Pechersky and Safonov (1993)	149.5	1.5	45	353.3	16.9	49.6	187.0	30.4	6.8	8.0	6.7	5.7	5.3	165.4	5
12	Pechersky and Safonov (1993)	155.5	2.5	19	326.0	16.7	36.0	23.3	20.0	12.1	14.3	20.1	13.5	13.4	15.7	5.6,7
13	Pechersky and Safonov (1993)	158.0	5.0	42	37.1	12.2	61.0	7.7	42.1	84.8	5.7	10.0	8.2	45.6	9.0	5.6,7
14	Pechersky and Safonov (1993)	168.5	7.5	34	1	121.9	>90	43.1	92.8	25.1	15.4	6.2	50.9	14.5	71.4	6
15	Pechersky and Safonov (1993)	168.5	3.5	28	31.8	7.6	40.6	9.6	23.2	18.1	6.6	7.7	6.5	16.1	7.0	5
16	Pechersky and Safonov (1993)	148.5	2.5	8	329.5	16.7	36.0	23.3	20.0	12.1	14.3	20.1	13.5	13.4	15.7	5.6,7
17	Pechersky and Safonov (1993)	149.5	1.5	7	357.1	12.2	61.0	7.7	42.1	84.8	5.7	10.0	8.2	45.6	9.0	5.6,7
18	Pechersky and Safonov (1993)	145.5	5.5	10	343.2	14.5	49.3	14.3	30.2	20.0	5.3	15.0	10.9	15.8	12.5	5.6,7
19	Pechersky and Safonov (1993)	153.5	7.5	17	5.3	6.4	54.4	5.3	34.9	70.1	5.6	5.6	4.9	47.3	5.2	7
20	Anferova (1971)	115.5	9.5	216	1	11.0	11.0	48.6	11.1	29.6	80.0	9.0	11.0	64.6	9.6	1
21	Pechersky and Safonov (1993)	149.5	1.5	66	3	347.7	17.1	32.7	25.5	17.8	49.2	11.5	21.1	58.2	16.3	5
22	Rusakov (1971)	118.5	6.5	37	357.2	5.7	68.9	2.4	52.3	116.0	2.0	3.6	3.4	46.8	3.5	see text
Pontides																
23	Van der Voo (1968)	77.4	11.9	6	343.6	8.4	44.7	9.4	26.3	90.0	7.0	8.3	6.8	81.0	7.5	5.6
24*	Saribudak (1989)	86.4	2.9	57	349.5	13.2	41.9	16.0	24.2	27.0	11.8	14.4	10.5	26.1	12.0	5
25	Van der Voo (1968)	173.0	27.0	8	320.9	6.3	10.1	12.2	5.1	51.0	8.0	6.5	6.2	79.3	6.3	6
26	Van der Voo (1968)	48.1	7.7	16	317.0	7.2	41.4	8.9	23.8	33.0	16.0	7.2	6.1	32.3	6.6	6
27	Saribudak (1989)	114.8	15.2	5	2.6	4.4	-2.0	8.8	1.0	190.0	5.6	2.4	6.4	303.7	4.4	4,6,8
28**	Onbay Bayburdi (1979)	82.5	17.5	7	343.8	16.7	54.4	13.7	34.9	30.6	9.6	16.3	11.7	20.6	13.6	1,2,2,5,6
29	Van der Voo (1968)	160.4	19.2	6	330.7	13.5	44.4	15.3	26.1	35.0	11.0	14.4	10.5	31.8	12.1	5,6
30	Evans et al. (1982)	161.0	15.0	134	95.1	12.2	53.4	10.5	33.9	3.5	7.7	11.7	9.0	2.4	10.1	3.5
31	Channell et al. (1996) group 1	86.4	2.9	59	5	336.3	6.8	43.0	8.0	25.0	166.4	5.9	6.7	156.6	6.1	ind. in # 36
32	Channell et al. (1996) group 2	86.4	2.9	47	3	325.0	20.1	46.9	21.2	28.1	58.7	16.2	23.1	49.7	17.7	ind. in # 36
33	Channell et al. (1996) group 3	86.4	2.9	116	9	328.1	7.5	43.4	8.8	25.3	62.2	6.6	7.5	57.9	6.8	ind. in # 36
34	Channell et al. (1996) group 4	86.4	2.9	71	6	355.0	13.2	41.3	16.2	23.7	32.4	11.9	14.5	10.6	12.1	ind. in # 36
35	Channell et al. (1996) group 5	86.4	2.9	63	5	7.8	19.9	40.6	24.9	23.2	18.5	18.3	24.5	18.5	18.3	ind. in # 36
36***	Channell et al. (1996) group 1-5	86.4	2.9	356	5	3	30.9	41.1	3.8	23.6	765.4	2.4	2.9	755.3	2.8	2.7
37	Channell et al. (1996) group 6	86.4	2.9	69	5	91.2	35.1	32.8	51.8	17.9	5.3	36.7	61.4	6.3	33.2	4
38	Channell et al. (1996) group 7/8	187.6	12.0	101	9	351.4	23.7	65.8	11.7	48.0	26.3	10.2	18.1	11.9	15.6	ind. in # 39
39***	Channell et al. (1996) group 7/8	187.6	12.0	101	9	7.5	60.5	4.8	41.5	155.9	4.1	6.0	5.3	85.3	5.6	5.6
40	Channell et al. (1996) group 8/9	86.4	2.9	58	6	354.7	14.0	46.9	14.8	28.1	36.2	11.3	14.7	30.7	12.3	ind. in # 42
41	Channell et al. (1996) group 10	86.4	2.9	119	10	349.7	10.1	46.3	10.9	27.6	35.0	8.3	10.2	30.2	8.9	ind. in # 42
42***	Channell et al. (1996) group 8/9-10	86.4	2.9	177	16	6.7	43.7	7.8	25.5	46.9	5.8	6.6	5.6	37.8	6.1	6.1
43	Channell et al. (1996) group 11/12	160.4	19.2	49	3	21.7	>90	65.5	60.6	47.7	7.6	48.3	-82.1	3.5	79.9	4

* For the average of Saribudak (1989) (study 24), only seven of the eight published sites were used, as was entered in the GPMDB, namely G001-06, C01, BA01, ER01, DE01, S101, S102 (so without KA01)

** The average of Onbay & Bayburdi (1979) (study 28) was based on sites G1-G5 and O1-O2.

*** The combined inclination-only datasets were calculated by Channell et al. (1996) to a reference point at 41°N, 36°E

Table 2.2
Data from published studies. #=#number assigned to the study; N (total #)=total number of specimens incorporated in the study; N (statistics)=number of combined sites or individual specimens that were used for calculation of the averages and statistics; Δλ+ and Δλ- are the positive and negative latitude errors. Other parameters as for Table 2.1.

der Voo et al. (1968), Anferova et al. (1971), Rusakov (1971), Orbay and Bayburdi (1979), Evans et al. (Evans et al., 1982), Pechersky and Safonov (1993), and Pechersky et al. (1993). A full author list could not be traced for Pechersky et al. (1993). We added the data of Channell et al. (1996). Many of the published data were rejected after applying the reliability criteria. For the Pontides, only three out of 13 results were accepted (indicated in bold in Table 2.2), all three from the combined results of Channell et al. (1996). None of the 22 Crimean datasets passed the reliability criteria.

A major problem with the Crimean data in the database is that they can often not be traced back to the original publication. In some cases, the k (precision parameter), α_{95} values and number of samples of datasets that were combined in the GPMDB do not coincide with our calculations. The number of samples used for the calculations also differed sometimes between the paper and the database. In one case, a single dataset was entered three times into the database, under different authors, and combined with several other sub-datasets.

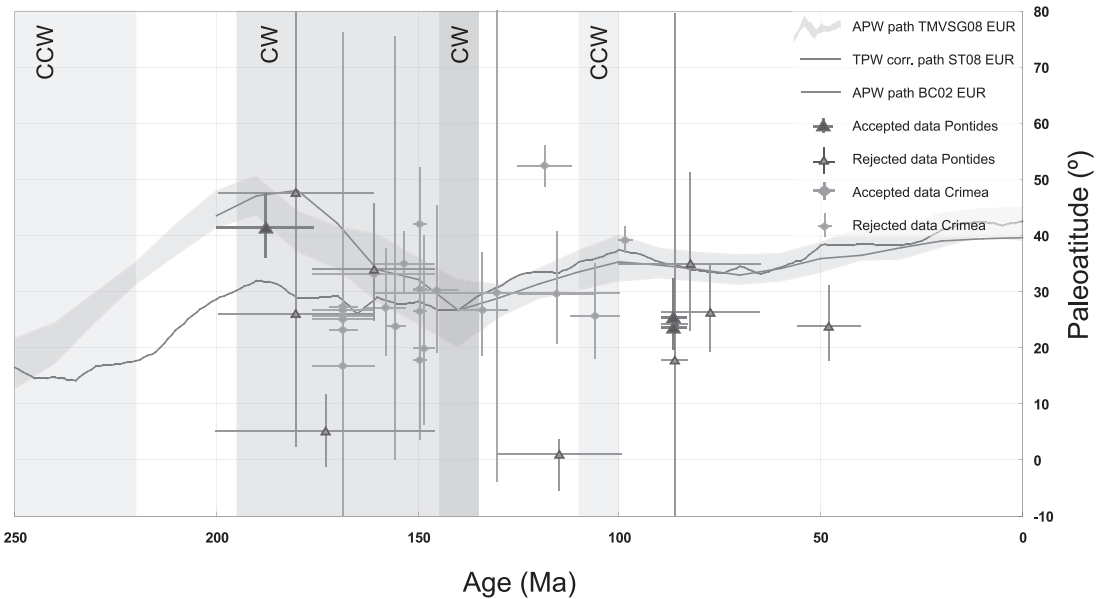


Figure 2.7 Age versus latitude plot with the Eurasian APW path and its $\Delta\lambda$ error envelope calculated from the ΔI_x error envelope of Torsvik et al. (2008a) (blue shaded area, 250-0 Ma), the APW path of Besse and Courtillot (2002) (purple curve, from 200-0 Ma), the TPW corrected APW path of Steinberger and Torsvik (2008) (green curve, 250-0 Ma). Thin purple lines (250-0 Ma) indicate the position of the pole path calculated for flattening factors (f) between 1.0 and 0.3, with steps of 0.1. Small green diamonds (small blue triangles) with $\Delta\lambda$ error bars calculated from the ΔI_x and age error bars: rejected data from the GPMDB data from Crimea (Pontides); large green diamonds (large blue triangles) with $\Delta\lambda$ error bars calculated from the ΔI_x and age error bars: accepted data from the GPMDB data from Crimea (Pontides). In the data for the Pontides, also data from Channell et al. (1996) were included. Abbreviations in legend as in Fig. 2.6. See Appendix 11

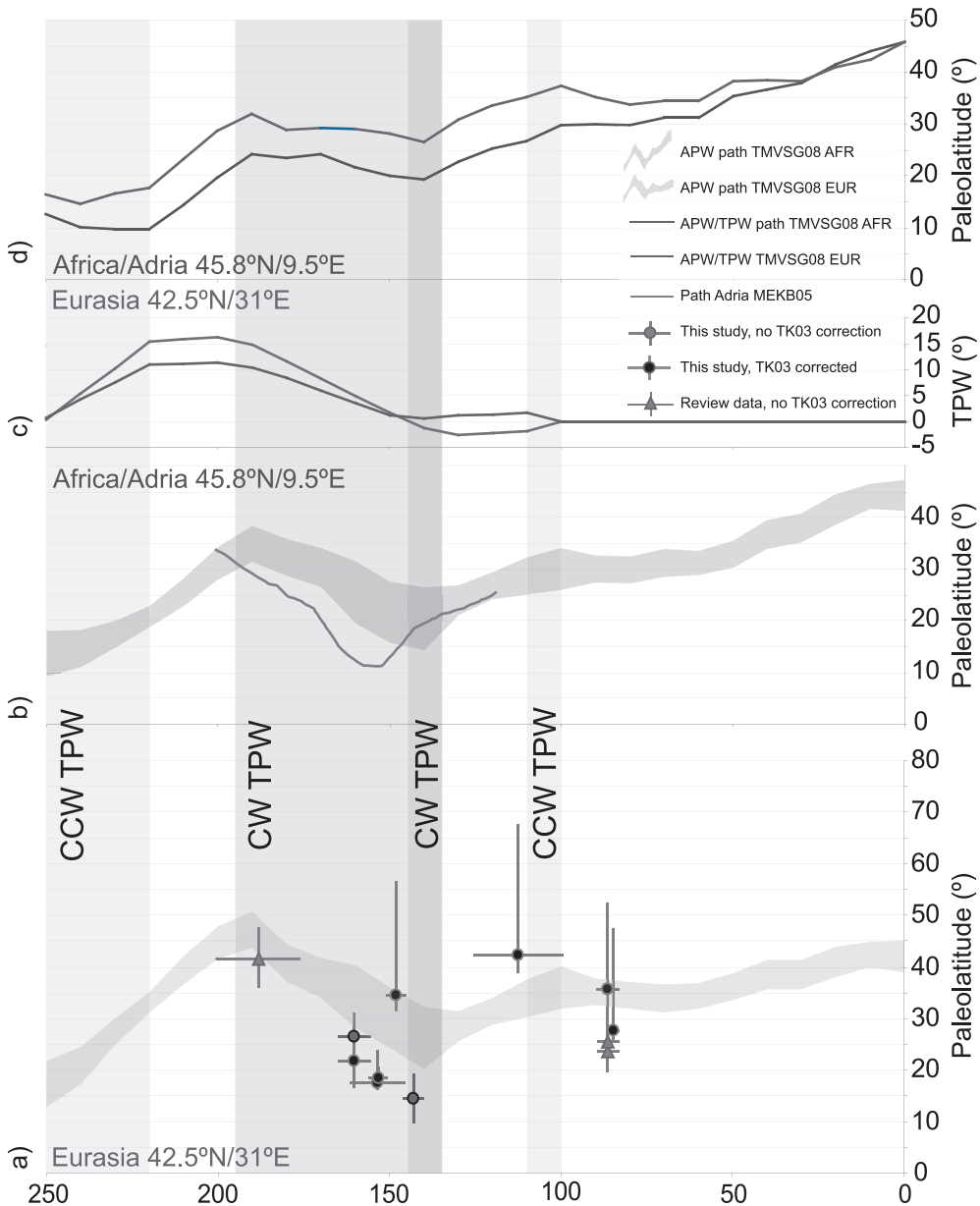
6. Discussion

Data from five out of six sites from Callovian-Berriasian (~164.7-140.2 Ma) rocks show very consistent behavior and suggest that the Pontides (sites TD14, TD2) and Crimea (sites KO, UJ, KV) were not situated at significantly different latitudes in late Jurassic times (Figs. 2.6 and 2.8), which would imply close vicinity of the Pontides and Crimea in this period. Therefore, even if there was an oceanic basin separating the Pontides and Crimea in this time span, it was of limited dimension (no more than several hundreds of km). Our data (except site KA) yield paleolatitudes that are significantly lower (~1600 km) than the paleolatitude expected from the APW paths of Besse and Courtillot (2002) and Torsvik et al. (2008a). The consistent low paleolatitudes from Callovian to Berriasian (~164.7-140.2 Ma) rocks from Pontides and Crimea, show a southward moving trend (Figs. 2.6 and 2.8), which is parallel to the trends in the Eurasian APW paths (Besse and Courtillot, 2002; Torsvik et al., 2008a) in the same interval.

Data from Aptian-Albian (~125.0-99.6 Ma) rocks from Crimea (site KP) yield a paleolatitude that is slightly higher than the paleolatitudes predicted by the APW paths, but identical within error (Figs. 2.6 and 2.8), both before and after correction with the E/I method (Figs. 2.6 and 2.8, Table 2.1). Coniacian-Santonian (~89.3-83.5 Ma) data from the Pontides from site TA5 reveal a paleolatitude that, after correction with the E/I method, plot on the APW path, whereas the paleolatitude from site TA2 is slightly lower, but within error, to the late Cretaceous APW paths (Besse and Courtillot, 2002; Torsvik et al., 2008a). The datasets from upper Cretaceous formations published by Channell et al. (1996) however, yield slightly lower latitudes than predicted by the APW paths. This could be the result of inclination shallowing, because the data were not corrected for this. The accepted site of Liassic age from Channell et al. (1996) plots within error of the APW path.

Our low latitudes in middle Jurassic to early Cretaceous times, compared to the Eurasian APW paths, are in line with the low latitudes of Adria as part of the African plate, presented in the study of Muttoni et al. (2005). From a magnetostratigraphic study on sections in the Northern Apennines (Italy) by Satolli et al. (2007; 2008), a pole path for Adria was calculated for the ~100-150 Ma interval (Fig. 2.6a). Their paleolatitudes in the ~125-145 Ma interval are in line with the data presented by Muttoni et al. (2005). However, in the critical interval prior to 145 Ma that displays the southward movement of Adria, their calculated paleolatitude is higher than predicted by the scenario of Muttoni et al. (2005), and comparable to the APW paths. Therefore, they disagree with Muttoni et al.'s (2005) scenario of a more southerly position of Africa in the middle to late Jurassic times, compared to the APW paths. The two datapoints from a study by Aiello et al. (2008) on Greek radiolarian cherts that have a small age error (<5 Myr, Fig. 2.6) yield also a paleolatitude that is much lower than expected from the African APW path. In the critical interval, the sampled localities are also a

Figure 2.8 a) Age versus latitude plot with the Eurasian APW path and its $\Delta\lambda$ error envelope calculated from the ΔI_x error envelope of Torsvik et al. (2008a) (blue shaded area, 250-0 Ma), the APW path of Besse and Courtillot (2002) (purple curve, from 200 -0Ma), blue large circles as in Fig. 2.6b; grey large circles as in Fig. 2. 6c, blue triangles as in Fig. 2.7. b) Age versus latitude plot with the African APW path and its $\Delta\lambda$ error envelope calculated from the ΔI_x of Torsvik et al. (2008a) (pink shaded area, 250-0 Ma). Grey curve: curve calculated by Muttoni et al. (2005). c) Curve indicating the amount of TPW through time for the African (in red) and Eurasian (in blue) continents. d) TPW corrected APW paths for Africa (in red) and Eurasia (in blue) from Steinberger and Torsvik (2008). All paths and datapoints are recalculated to the locations indicated in the figure. Abbreviations in legend as in Fig. 2.6. See Appendix 12



part of the African plate (Fig. 2.1b). Data from Aiello et al. (2008) from Greek radiolarian cherts, do support the scenario of Muttoni et al. (2005), but do not pass our reliability criteria due to too large age errors and too small datasets (Fig. 2.6a).

Muttoni et al. (2005) conclude that the southward movement and clockwise motion of Africa is underestimated by the APW path of Besse and Courtillot (2002) because of smoothing of the data. This discrepancy remains if their results are compared to the pole path of Torsvik et al. (2008a), because both paths are nearly identical from the start of the critical time interval (~ 160 Ma) onwards (Figs. 2.6, 2.7 and 2.8). Smoothing seems a likely mechanism, because of the relatively low amount of data entries in the global APW path of Torsvik et al. (2008a): the average number of data entries per 10 Myr sliding window in the pole path is 27 (320-0 Ma), whereas this is only 13 in the critical time span (160-140 Ma). The pole path calculated by Satolli et al. (2008) does not support Muttoni's scenario, but in their study they do recognize an abrupt change in plate movement direction around ~ 141 Ma. Therefore, Satolli et al. (2007) propose the possibility of TPW in this time span.

From our six datasets from rocks that were deposited at the southern Eurasian margin, five do show a much lower paleolatitude than expected from the Eurasian APW paths, out of which four yield a paleolatitude that is within error lower than the APW path (TD14, KO, UJ and KV). This suggests that Muttoni et al.'s (2005) scenario wherein the cusp in the African APW paths is underestimated, seems not only valid for Africa, but also for Eurasia. The fact that datasets from other pre- and post-TPW Jurassic and Cretaceous periods from the Pontides and Crimea (Fig. 2.8) plot within error on the APW path except for two sites that were not corrected for inclination error, confirms that we have a good control on paleolatitude. Because Africa and Eurasia were separated and partly surrounded by subduction zones, which serve as an anchor into the mantle, it is unlikely that both plates moved ~ 1600 km back and forth with respect to the mantle (Fig. 2.1b). Therefore, we conclude that the latitudinal shift is most likely the result of TPW. We concur with Muttoni et al. (2005) that the cusp in the APW paths is smoothed, and because these smoothed paths were used to calculate the TPW events by Steinberger and Torsvik (2008), the Jurassic TPW event was probably larger than determined by Steinberger and Torsvik (2008).

7. Conclusions

Here, we tested whether a recently published strong southward Jurassic to early Cretaceous cusp in the African APW path at the position of Adria can also be found on the Eurasian plate in the present-day circum-Black Sea area. We have presented large paleomagnetic datasets (41) from Jurassic and Cretaceous sediments from Crimea (Ukraine) and the Pontides (Turkey) that were part of the Eurasian plate. To correct for inclination error in sediments, we used the statistical E/I method of Tauxe and Kent on datasets with a sufficient number of samples. Our data were combined with 43 published datasets. After applying strict reliability criteria on all 84 datasets, only

12 datasets were accepted. Five out of six late Jurassic to early Cretaceous datasets plot significantly (~ 1600 km) lower than the paleolatitudes calculated by the Eurasian APW paths confirming that the southward cusp of Africa is also observed in Eurasia. Moreover, the datasets from Crimea and the Pontides display very similar paleolatitudes in this time span, and therefore imply their proximity in the late Jurassic to early Cretaceous. Furthermore, the southward trend of the paleolatitudes between ~ 165 -140 Ma emphasizes the trend observed in the APW paths.

The weaker signature of this southward cusp in the APW paths, can result from data smoothing. This is very likely for a period with a low amount of high quality datasets and a sharp change in motion.

There are two mechanisms to explain this southward translation of the Eurasian and African plates in the eastern Mediterranean realm: 1) movement of the African and Eurasian plates with respect to the surrounding plates, 2) movement of the entire crust and mantle with respect to the Earth's core: true polar wander (TPW), recently quantified by Steinberger and Torsvik (2008) for the critical time span. Because it is unlikely that Africa and Eurasia moved with such high speed with respect to the surrounding plates in a time span where both continents were surrounded by subduction zones, wherein the subducting slabs function as their anchors in the mantle, we regard the possibility of TPW the most likely mechanism to explain the low latitudes.

8. Acknowledgements

We would like to acknowledge the following people for their help in the field: Wout Krijgsman, Martijn Deenen, Aline Saintot, Stephen Vincent, Vladimir Bakhmutov, Sergei Bolotov, Oleg Rusakov, Evgeniy Polyachenko, Galina Slivinskaya, Sergei Yudin, Elena Yudina, Viktor Yudin, Aral Okay, Bora Rojay, Pinar Ertepinar Kaymakçı and Ane Wiersma. V.V. Arkadiev is thanked for age determination of Crimean ammonite samples. We would like to thank Bernhard Steinberger for providing the Eurasian and African TPW-corrected paths. MJMM acknowledges the Netherlands Research Centre for Integrated Solid Earth Sciences (ISES) and the Netherlands Organization for Scientific Research (NWO) for financial support. DJJvH acknowledges financial support from Statoil (SPlates project).

Supplementary data

A summary of all results can be found in Table 2.1 and Figures 2.2-2.7. HT=high temperature; HCF=high coercive force; LT=low temperature; LCF=low coercive force.

KV

The samples of site KV were collected from (Tithonian-)Berriasian beige limestones, on top of the Ai Petri limestone plateau, within approximately 20 meters of stratigraphy. A number of 44 samples was demagnetized, of which five thermally and 39 using combined thermal and AF demagnetization. Initial intensities range from ~ 50 -1000 $\mu\text{A}/\text{m}$. No systematic LT or LCF direction is visible in the samples. The resulting HT/HCF ChRM direction that was isolated between $\sim 140^\circ\text{C}$ - 370°C .

KO

From the dark grey Kimmeridgian limestones of site KO that were sampled within approximately 10 meters of stratigraphy near the Uchan Su waterfalls in the Ai Petri plateau, 107 specimens were demagnetized. Twelve samples were demagnetized thermally and 95 samples using combined thermal and AF demagnetization. Initial intensities range from $\sim 2,000$ - $10,000$ $\mu\text{A}/\text{m}$. Until $\sim 150^\circ\text{C}$ or 150°C plus ~ 10 mT, a LT/LCF component is present in the samples. The direction of the LT/LCF is $D=358.5^\circ$ and $I=57.8^\circ$, which is similar to the present-day GAD field on Crimea. The resulting HT/HCF ChRM direction was isolated between $\sim 150^\circ\text{C}$ - 480°C or 150°C plus ~ 10 mT- 70 mT. Correction for inclination error is not significant.

UJ

The samples of site UJ were taken from early Kimmeridgian limestones within the Ai Petri plateau within approximately 4 meters of stratigraphy. The age is based on biostratigraphic dating on *Thalassinoides* burrows and corals. From the 101 samples that were drilled, 129 specimens were demagnetized, of which 99 samples thermally and 30 samples using combined thermal and AF demagnetization. Initial intensities range from ~ 1500 - 8000 $\mu\text{A}/\text{m}$. A direction that is similar to the present-day GAD field on Crimea is present in the samples until $\sim 210^\circ\text{C}$ or 150°C plus ~ 20 mT. The direction of this LT/LCF component ($N=101$) is $D=353.7^\circ$ and $I=60.7^\circ$. The resulting ChRM direction was isolated between $\sim 210^\circ\text{C}$ - 360°C or 150°C plus ~ 20 mT- 60 mT. Correction for inclination error was not significant.

KP

The samples of site KP were drilled in Aptian-Albian clays (Druschits et al., 1981; Baraboshkin, 2003) that were deposited on top of a fossiliferous hardground in the Kirpichnoe quarry (Novomykolaivka village). All samples were taken within approximately 6 meters of stratigraphy. The color of the clays is different per site and ranges from beige, grey and blue to orange/reddish. At this site, 128 samples were collected, of which 113 specimens were demagnetized using combined thermal and AF demagnetization procedures, and one sample using thermal demagnetization. Intensities after heating until 150°C range from ~ 200 - 76000 $\mu\text{A}/\text{m}$, depending on the color of the clays. No consistent LCF component is present in the samples. The HCF ChRM component was isolated between $\sim 150^\circ\text{C}$ plus 10 mT and ~ 70 mT (and between 100°C and 360°C for the thermally demagnetized sample). Correction for inclination error was not significant.

KL & KJ

Siltstones (KL) and sandstones (KJ) of Bajocian age (national park, near kordon Ammonalnie). The sandstones and siltstones are intercalated with lava flows. The low number of lava flows did not allow paleomagnetic analyses on the lava flows. Samples of site KJ and KL were taken within respectively ~ 5 and ~ 2 meters of stratigraphy. At site KL, 17 samples were collected, whereas at site KJ 33 samples were collected. Starting intensities range between ~ 3600 - 14000 $\mu\text{A}/\text{m}$ (KL) and ~ 400 - 1200 $\mu\text{A}/\text{m}$ (KJ).

Eight samples from site KL were demagnetized thermally between 20°C and 570°C . The ChRM component was isolated between $\sim 150^\circ\text{C}$ and 480°C . From site KJ, 25 samples were demagnetized thermally between 20°C and 570°C and eight samples combined thermal and AF demagnetization (150°C plus 90 mT). The ChRM was isolated between 150°C and 480°C or between 150°C and 40 mT.

Both sites were drilled within each others proximity (~ 500 meters apart) and within

sediments of the same age. Therefore, the ChRM direction should be comparable. However, the large difference between the isolated ChRM directions indicates that the rocks have been remagnetized.

KA

Grey limestones of Tithonian age (according to the fieldguide of Nikishin et al. (2008), the age is upper Tithonian, we used the more conservative Tithonian age) were sampled (N=118) at site KA (Chatyr Dag plateau) within ~30 meters of stratigraphy. Samples were mainly demagnetized using combined thermal (until 150°C) and AF demagnetization, and two samples were thermally demagnetized. Typical intensities after heating until ~150°C range from ~25-300 $\mu\text{A}/\text{m}$. Until ~150°C plus 15 mT a LT/LCF component is present in the sample that is similar to the present-day GAD field on Crimea. A HCF/HT ChRM component was isolated between ~150°C plus 15 mT and between ~100-450°C. Correction for inclination error was not significant.

KH

At site KH 97 samples were collected from Callovian clays and calcarenites at cape Meganom. In total, 36 sites were drilled spread throughout an area of ~1-2 km², and 36 samples were demagnetized thermally until a maximum of 600°C. Initial intensities range from ~200-2000 $\mu\text{A}/\text{m}$. The paleomagnetic direction in most samples highly differs, and therefore no ChRM direction could be calculated.

KD

Valanginian-Hauterivian carbonate rich siltstones were collected at site KD. A total of 87 samples were collected within 6 subsets. Intensities after heating until 150°C range from ~200-1300 $\mu\text{A}/\text{m}$. 118 samples were demagnetized using combined thermal (until 150°C) and AF demagnetization. One sample was demagnetized thermally (ChRM isolated between 240°C and 420°C). There is no clear LT/LCF component present in the samples. The mean ChRM direction (isolated between 15 mT and 50-100 mT) of the combined subsets (after tectonic correction) is N=113, D=350.9°, I=33.8°. The ChRM directions that were calculated per subset yield different directions and do not pass the fold test (Tauxe and Watson, 1994). The maximum clustering of the data can be found at 40% unfolding, at a direction of D=354.9° and I=54.6° (N=113, k=57.5, α_{95} =1.8, ΔD_x =3.0, ΔI_x =2.0). Results obtained by using the SCI method developed by Shipunov (1997) and modified by Waldhör and Appel (2006) for the 6 subsets gives very comparable results. Minimizing A (the sum of the amount of angles) results in D=357.3 and I=62.4 (N=6, α_{95} =4.0°, km=207.5). On average the syn-folding remagnetization direction is D=354.9° ± 3.9°, I=57.5 ± 2.9°.

KF

The calcarenites and clays from site KF were dated upper Tithonian on the basis of ammonites (*Paraulacosphintes cf. transitorius*) by V.V. Arkadiev (pers. comm.). 97 cores were drilled, of which 15 specimens were demagnetised thermally. Starting intensity of the samples ranges from ~200-1800 $\mu\text{A}/\text{m}$. Samples show erratic and inconsistent behavior, therefore no ChRM direction could be determined.

TD17

Maastrichtian to Paleocene red pelagic limestones of the Ballıkaya Formation (Yikilmaz et al., 2002). The stratigraphic thickness of the sampled interval is ~3 meters. Starting intensities

range from ~ 4000 - $8000 \mu\text{A}/\text{m}$. From the 15 drilled cores, 4 samples were AF demagnetized and 10 samples were thermally demagnetized. AF demagnetization did not result in a substantial decrease in NRM intensity, so the ChRM component isolated between ~ 200 - 610°C is carried by hematite. There is no clear LT component present in the samples.

TD15

The site consists of Pliensbachian calc-arenites and siltstones (Okay et al., 1991). Combined thermal (until 150°C) and AF demagnetization (5 specimens) and thermal demagnetization (12 specimens) give completely different results. Thermomagnetic runs carried out on the samples could not reveal what the cause of this discrepancy is. Initial intensities range typically from $\sim 1,500$ - $5,500 \mu\text{A}/\text{m}$. For calculation of the ChRM direction we only took thermally demagnetized samples into account. This HT component was isolated between $\sim 150^\circ$ and $\sim 510^\circ\text{C}$. Uncorrected for bedding tilt this direction is very close to the present-day GAD field in the western Pontides, and therefore possibly a remagnetization direction.

TD14

The samples of site TD14 were taken from grey limestones of the Taşçıbayırı Formation that is part of the Bilecik Group (Altiner et al., 1991). Their age is Callovian-Oxfordian in age. Site TD14 consists of 108 demagnetized specimens, of which 25 specimens were demagnetized thermally, and 83 using combined thermal and AF demagnetization. Initial intensities range from $\sim 1,000$ - $80,000 \mu\text{A}/\text{m}$. An LT/LCF component is present in the samples until $\sim 300^\circ\text{C}$ or $\sim 150^\circ\text{C}$ plus 30mT, which is very close to the present-day geo-axial dipole (GAD) field in the western Pontides. The direction of this LT/LCF component ($N=24$) is $D=3.9^\circ$ and $I=57.5^\circ$. The resulting HT/HCF component was isolated between ~ 310 - 520°C or 150°C plus 35 mT/ 300°C and 90mT. Correction for inclination error was not significant.

TD13

Samples were taken from Aptian-Albian limestones (base of the section is Aptian, the top of the section is (mid-)Albian, biostratigraphic dating by D. Altiner). The sampled stratigraphic thickness is approximately 100 meters. 70 cores were sampled, from which 83 specimens were demagnetized, 22 by thermal demagnetization, and 61 by combined thermal (until 150°C) and AF demagnetization. Initial intensities range from ~ 250 - $10,000 \mu\text{A}/\text{m}$. A LT/LCF component is present in the samples until $\sim 250^\circ\text{C}$ or 150°C plus ~ 30 mT. This LT/LCF component is close to the present-day GAD field in the western Pontides. The direction of this LT/LCF component ($N=21$) is $D=6.6^\circ$ and $I=51.5^\circ$. The resulting HT/HCF component, that was isolated between $\sim 250^\circ\text{C}$ - 600°C or between $\sim 150^\circ\text{C}$ plus 30 mT and ~ 60 mT, that represents the ChRM ($N=75$) is $D=305.5^\circ$, $I=64.8^\circ$. This is higher than the present-day field inclination in the Pontides, making the results suspect.

TD2

The samples of the beige limestones of site TD2 were taken from the Callovian-Oxfordian Taşçıbayırı Formation, that is part of the Bilecik Group (Altiner et al., 1991). Site TD2 consists of 36 samples, of which 12 samples were demagnetized thermally and 34 using combined thermal (until 150°C) and thermal demagnetization. Initial intensities range from ~ 1000 - $14,000 \mu\text{A}/\text{m}$. A LT/LCF component is present in the samples until $\sim 250^\circ\text{C}$ or 150°C plus ~ 20 mT. This field is very distinctive from the present-day GAD field in the western Pontides. The HT/HCF component that was isolated between $\sim 250^\circ\text{C}$ - 500°C or 150°C plus ~ 15 mT and 60 mT, yields a direction ($N=29$) of $D=24.5^\circ$, $I=44.9^\circ$.

TD1

Pliensbachian sandstones of the Bayırköy Formation (Okay et al., 1991) were sampled at site TD1. A number of 12 samples was demagnetized, of which six thermally and six using combined thermal (until 150°C) plus AF demagnetization. Initial intensities range from ~1000-1500 $\mu\text{A}/\text{m}$. The ChRM component was identified between ~100°C-300°C or ~150°C plus 10 mT and 100 mT. The discrepancy between both methods in the low temperature and AF range probably results from a small viscous component that was picked up by the samples in the time lag between both demagnetization procedures. To remove this component, an AF field of 10 mT was required. The ChRM component yields a direction ($N=11$) of $D=13.0^\circ$, $I=29.7^\circ$.

TB3

The 105 cores of site TB3 were sampled in the Callovian limestones from the Bilecik Group (Abadiye village)(Koçyiğit et al., 1991). Approximately 20 meter of stratigraphy was sampled. Initial intensities range from ~15-2000 $\mu\text{A}/\text{m}$. In total, 29 samples were demagnetised (13 using combined thermal (until 150°C) and AF demagnetization and 16 using thermal demagnetization). A LT/LCF component that resembles the present-day GAD field at the sampling location seems present in the samples until ~180°C. The HT/HCF component was isolated between ~210-420°C or between ~210°C and 100 mT.

TB4

Upper Jurassic to lower Cretaceous limestones (Bilecik Group) were sampled in ~20 meters of stratigraphy at site TB4 (15 cores). Samples were taken from ~20 meters of stratigraphy. Initial intensities range between ~150-550 $\mu\text{A}/\text{m}$. Thermal demagnetization of 15 samples, resulted in the isolation of a ChRM component between ~200-570°C, which is possibly a present-day GAD overprint.

TB5

73 red limestone samples from the Liassic Bayırköy Formation (Trafo member)(Altuner et al., 1991) were taken at site TB5. Thermal demagnetization of 27 specimens until 570°C resulted in the isolation of a LT component that is similar to the present-day GAD direction until ~150°C. The ChRM was probably not recovered from the samples, possibly because of problems with the oven at temperatures >300°C. The interpreted direction comes from the temperature range between 150-300°C.

TB6

Red siltstone samples (26 cores) from the Liassic Bayırköy Formation (Trafo member)(Altuner et al., 1991) were taken at site TB6 within ~5 meters of stratigraphy, out of which 10 samples were demagnetized thermally until 570°C. Initial NRM intensities range from ~8000-10,000 $\mu\text{A}/\text{m}$. This resulted in the isolation of a LT component that resembles the present-day GAD field until ~150°C. The ChRM direction was isolated between ~200-570°C.

TB1

Limestones from the upper Jurassic to lower Cretaceous Bilecik Group were sampled (15 cores) in the lowermost part of the Bilecik Group, just above the Bayırköy Formation, implying that their age is Callovian. Initial intensities ranges from ~100-4000 $\mu\text{A}/\text{m}$. Combined thermal (until 150°C) and AF demagnetization (8 samples) and thermal demagnetization (5 samples) was applied on the samples. Erratic behavior however, did not result in the isolation of a ChRM

direction.

TA1

Limestones from the upper Jurassic to lower Cretaceous İnaltı Formation. Starting intensities range from ~ 25 - $125 \mu\text{A}/\text{m}$. Stratigraphic thickness sampled: ~ 30 meters. 24 cores were taken, out of which 11 samples were demagnetised thermally and 4 using combined thermal (until 150°C) and AF demagnetisation. The paleomagnetic direction (isolated between $\sim 20^\circ$ - 240°C and ~ 15 - 80 mT) in most samples highly differs, and is therefore not useable.

AC

Uppermost Tithonian to lower Berriasian limestones (dating by D. Altiner) were sampled (43 cores) at site AC. The age is probably lower Berriasian, based on the presence of *Calpionella* alpine, *Crassicollaria parvula*, *Spirillina* sp., *Globochaete* alpine, *Calpionella* alpine, *Spirillina* sp. and *Globochaete* alpine in the samples. Samples were taken within ~ 15 meters of stratigraphy. NRM intensities after heating until 150°C range from ~ 300 - $15,000 \mu\text{A}/\text{m}$. Combined thermal (until 150°C) and AF demagnetization of 20 cores and thermal demagnetization of 2 cores, resulted in the isolation of a LT that was present until $\sim 150^\circ\text{C}$ in most samples. The ChRM direction was isolated between $\sim 150^\circ\text{C}$ plus 20 mT and 80 mT or between ~ 200 - 450°C .

AD

Kimmeridgian-Hauterivian (probably Valanginian) limestones, dated on the basis of *Cadosina* sp. and *Spirillina* sp. (dating by D. Altiner), were sampled at site AD (60 cores). The age is probably Valanginian, based on the facies of the limestones (radiolarian wackestone), that is typical for this age in the region. Samples were taken within ~ 20 meters stratigraphy. Intensities after heating until 150°C range from ~ 15 - $100 \mu\text{A}/\text{m}$. Combined thermal (until 150°C) and AF demagnetization on 30 samples did not result in the isolation of a characteristic component, due to erratic and differing sample behavior.

BG8

Callovian (partly dolomitic) limestones (Rojay and Altiner, 1998) from the Vermiş village section were sampled from ~ 15 meters of stratigraphy (56 cores). Intensities after heating until 150°C range between 150 - $350 \mu\text{A}/\text{m}$. Combined thermal (until 150°C) and AF demagnetization of 10 samples resulted in the isolation of a ChRM direction between $\sim 150^\circ\text{C}$ plus 30 mT and 90 mT .

BG9

Callovian-Valanginian macro-fossil rich grainstones were sampled (62 cores) at site BG9 (Rojay, 1995)(B. Rojay, pers. comm.). The samples were taken from ~ 10 meters stratigraphy. Intensities after heating until 150°C are ranging from 50 - $250 \mu\text{A}/\text{m}$. Combined thermal (until 150°C) and AF demagnetization of resulted in the isolation of the ChRM between $\sim 150^\circ\text{C}$ plus 25 mT and 55 mT .

BG3

A Liassic ammonitico rosso level (red siltstones, equivalent to the Bayırköy Formation) was sampled at site BG3 within ~ 20 meters of stratigraphy. 82 samples were taken, of which 16 samples were demagnetized using combined thermal and AF demagnetization. Initial intensities range from ~ 300 - $17,000 \mu\text{A}/\text{m}$. A very steep ChRM component was isolated between $\sim 150^\circ\text{C}$ plus 15 mT and 90 mT , although thermal treatment of those samples is favored.



View on the Karadag mountains

CHAPTER 3

Jurassic arc volcanism on Crimea (Ukraine): implications for the paleo-subduction zone configuration of the Black Sea region

The early Cretaceous and younger opening of the Black Sea has obliterated much of the older subduction record that resulted from Tethyan subduction below southeastern Europe. The earlier Mesozoic evolution was dominated by opening and closure of the Tethys oceans between Gondwana and Laurasia and consumption of the Tethys was, at least in part, accommodated along the southern Eurasian margin. Crimea (Ukraine), a peninsula in the northern Black Sea, represents the northernmost region of southeastern Europe that exposes a record of a pre-Cretaceous Tethyan active margin. To shed new light on the paleosubduction zone configuration of the southeastern European margin in the Jurassic, we report $^{40}\text{Ar}/^{39}\text{Ar}$ isotope dating on 10 samples and whole rock geochemistry on 31 samples from Jurassic magmatic rocks from the Crimean peninsula. The samples can be subdivided into two age groups: middle Jurassic (~172-158 Ma) and uppermost Jurassic to lowermost Cretaceous (~151-142 Ma), that both have a subduction-related geochemical signature. The ages of the younger group contrast with previously assigned biostratigraphic ages of the units under and overlying the volcanic complex. This suggests that the latter were possibly juxtaposed by faulting. We argue that the Crimean volcanics represent a fragment of a long-lived volcanic arc overlying the southeastern European continental margin. These data therefore provides evidence for Jurassic northwards subduction below the Eurasian margin, preceding the opening of the Black Sea as a back-arc basin. We argue that the corresponding Jurassic trench was already positioned south of the Turkish Pontides and the Caucasus belt, implying a very shallow slab angle in the Jurassic.

Maud J.M. Meijers, Berend Vrouwe, Douwe J.J. van Hinsbergen, Klaudia F. Kuiper, Jan Wijbrans, Gareth R. Davies, Randell A. Stephenson, Nuretdin Kaymakci, Liviu Matenco and Aline Saintot

1. Introduction

Much remains to be understood about the Mesozoic configuration of subduction zones in the present-day Black Sea region. Fundamentally different views on the number, as well as the location and polarity of subduction zones in this region in Jurassic times prevail in the literature (Şengör and Yilmaz, 1981; Robertson and Dixon, 1984; Kazmin et al., 1987; Kent and May, 1987; Dercourt et al., 2000; Stampfli and Borel, 2002; Barrier and Vrielynck, 2008; Moix et al., 2008). Geodynamic reconstructions display a complex subduction zone configuration in the present-day eastern Mediterranean region (Figs. 3.1 and 3.2), resulting from two simultaneously interacting large-scale plate tectonic processes: 1) the early stages of Pangea break-up by opening of the central Atlantic ocean, imposing a widely dispersed sinistral strike-slip movement of Laurasia to the north relative to Gondwana to the south (Favre and Stampfli, 1992; Stampfli and Borel, 2004), and 2) south-to-north motion of blocks rifting away from Africa, accommodated by subduction of the (Paleo- and Neo-) Tethys oceans beneath the southern Eurasian margin (Fig. 3.2) (Şengör and Yilmaz, 1981). The Jurassic paleo-position of the subduction zones and continental blocks along the southern Eurasian margin in the present-day Black Sea region, however, is poorly constrained, because opening of the Black Sea since the early Cretaceous has obscured much of the geological record. A key area in the present-day Black Sea region is the Crimean peninsula. Here, heavily deformed Triassic-lower Jurassic turbiditic sediments are covered by an upper Jurassic carbonate platform (Mileyev et al., 1997; Voznesensky et al., 1998). Magmatic intrusions that are observed within the Triassic-lower Jurassic sequence are of unknown geochemical composition. Whether these volcanics along the southern European margin relate to rifting in a back-arc setting or locate the volcanic arc of a Jurassic subduction zone is a matter of debate (Nikishin et al., 2001; Saintot et al., 2006b; Saintot et al., 2007). Here, we provide critical constraints on the genesis of Jurassic magmatism on Crimea. To this end, we carried out $^{40}\text{Ar}/^{39}\text{Ar}$ isotope dating and major and trace element X-ray fluorescence (XRF) analysis on supposedly Jurassic Crimean volcanics. The results will be used to infer the plate tectonic setting for Crimea during volcanism, and we place this interpretation in context with respect to the Greater Caucasus and Turkish Pontides.

2. Geological setting

2.1 Main geological units in the circum-Black Sea region

The circum-Black Sea region contains a number of continental terranes and oceanic units, which are briefly reviewed here.

In northern Turkey, three continental units are combined into the **Pontides** belt. This belt comprises the Strandja Massif and the İstanbul Zone in the west, the bulk is represented by the Sakarya Zone (Fig. 3.1) (Okay et al., 1996). The Pontides are bounded in the north by the Black Sea and in the south by the İzmir-Ankara-Erzincan ophiolitic suture zone. The İstanbul Zone is structurally the highest zone,

and the Sakarya Zone is structurally the lowest zone (Okay et al., 2001a). The age of the Pontides basement is Paleozoic (Bozkurt et al., 2008; Okay et al., 2008). For the purpose of this study, we will only describe the Istanbul and Sakarya Zones.

The **Istanbul Zone** comprises non-metamorphic Paleozoic, Mesozoic and Cenozoic sedimentary sequences overlying pan-African/Cadomian crystalline basement (Chen et al., 2002; Ustaömer et al., 2005). The Paleozoic affinity of the Istanbul zone is debated (Chen et al., 2002), but there is general consensus based on its stratigraphy and lack of metamorphism – that in Mesozoic times it can be considered as a fragment of Moesia that rifted southward during the opening of the western Black Sea basin in the late Cretaceous (Üstaömer and Robertson, 1993; Okay et al., 1994b).

The **Sakarya Zone** has a strongly deformed late Paleozoic basement (Topuz and Altherr, 2004; Topuz et al., 2004; Topuz et al., 2007; Bozkurt et al., 2008; Okay et al., 2008) and is overlain by the locally metamorphosed Karakaya Complex of Triassic to earliest Jurassic age, and a younger discordant Mesozoic to Cenozoic (volcano-) sedimentary cover (Chen et al., 2002; Ustaömer et al., 2005). Blueschists and eclogites

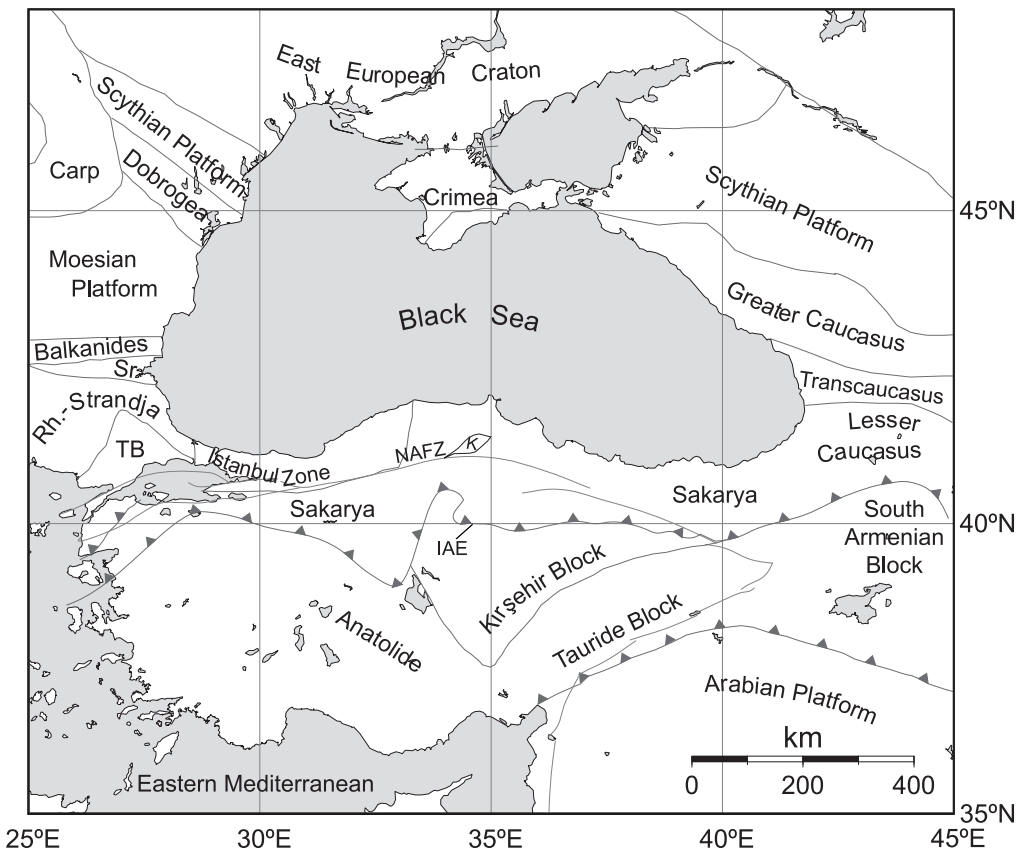
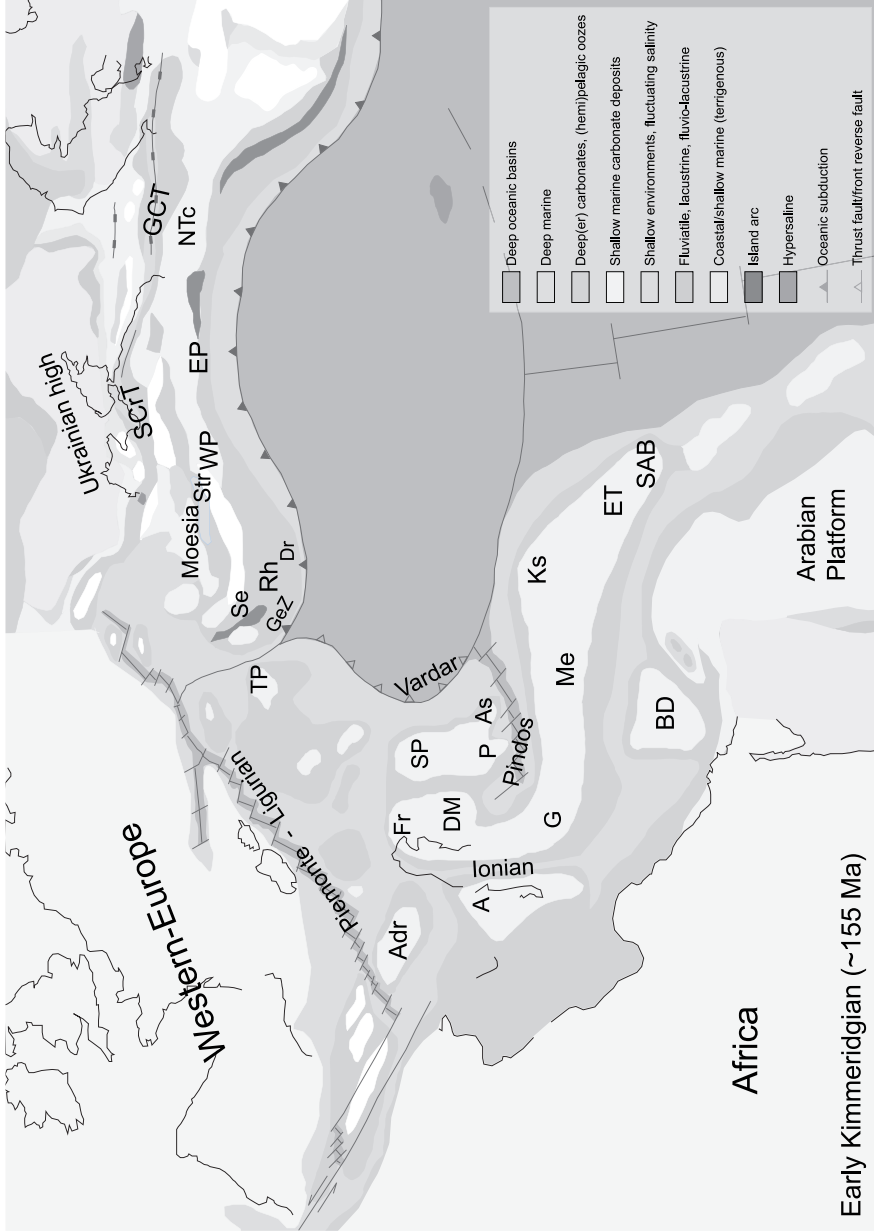


Figure 3.1 Map showing the most important tectonic blocks and sutures in a present-day geographical map. Carp= Carpathians, IAE= İzmir-Ankara-Erzincan suture, K= Kargı Massif, NAFZ= North Anatolian Fault Zone, Rh.= Rhodope, Sr= Srednogorie, TB= Thrace basin.



have been recovered from the Karakaya complex, marking its affinity with a latest Triassic subduction zone (Bozkurt et al., 1997; Okay et al., 2002). Triassic deposits present in the Karakaya Complex are either interpreted as an inverted (back-arc) rift basin or as a subduction accretion complex (Genç and Yılmaz, 1995; Okay and Göncüoğlu, 2004; Pickett and Robertson, 2004).

A window within the Sakarya Zone in the central Pontides (Fig. 3.1) exposes the **Kargı Massif** (Fig. 3.1). This massif consists of northwest dipping tectonic slices, that are separated by post-Jurassic thrust faults. These contain HP-LT metamorphic sequences consisting of metabasites, metaophiolites, and micaschists. Formerly, the Kargı Massif was interpreted as a Paleo-Tethyan pre-Jurassic subduction-accretion complex (Tüysüz, 1990; Ustaömer and Robertson, 1997), but on basis of dating of HP-LT metamorphism at ~105 Ma (early Cretaceous), Okay et al. (2006) reinterpreted the Kargı Complex as a lower Cretaceous subduction-accretion complex resulting from northward subduction below the Pontides.

The Sakarya and İstanbul zones share a post-Triassic volcano-sedimentary cover. The eastern part of the Sakarya Zone (i.e. the eastern Pontides) however, has a different lower to middle Jurassic stratigraphy, consisting of volcanics and volcano-sedimentary units (Yılmaz et al., 2003; Yılmaz and Kandemir, 2006), interpreted as related to a volcanic arc (Şen, 2007). These cannot be traced into the western and central Pontides, where only lower Jurassic continental to shallow marine clastic rocks, intercalated with ammonitico-rosso levels are exposed (Altınır et al., 1991). In the central and western Pontides, there is no recorded Jurassic magmatism, and therefore no evidence for subduction. Middle Jurassic (Callovian) to lower Cretaceous platform carbonates (İnaltı Formation) cover the entire Pontides (Görür, 1997; Tüysüz, 1999; 2010).

The İstanbul zone was once separated from the Sakarya Zone by the so-called **Intra-Pontide ocean** (Şengör and Yılmaz, 1981; Okay et al., 1994b; Robertson and Ustaömer, 2004). The timing of opening and closure of the Intra-Pontide ocean, however, remains controversial. Interpretations are based on the presence of metamorphosed sediments that are assumed to have been deposited in a Triassic rift, and on the presence of ophiolitic units. Opening of the ocean was proposed to range from Triassic to early Jurassic times, and closure may have started in Aptian-Albian times, coeval with the incipient rifting of the western Black Sea basin (Şengör and Yılmaz, 1981; Okay et al., 1994b; Robertson and Ustaömer, 2004; Hippolyte et al., 2010). Based on ophiolite emplacement, the full closure of the Intra-Pontide suture is proposed to have occurred in late Cretaceous (Turonian) times (Robertson and Ustaömer, 2004). However, the ophiolitic units have also been interpreted as being part of the ophiolites that were formed in a single Mesozoic northern Neo-Tethys ocean. Emplacement of those 'so-called' Intra-Pontide ophiolites results from left-lateral strike slip according to Elmas and Yiğitbaş (2001). They argue that the similar post-middle Jurassic sedimentary cover of the Sakarya and İstanbul Zones evidences the juxtaposition of the two zones

before the late Jurassic.

The eastern and western **Black Sea** basins are generally regarded as back-arc basins that opened resulting from Neo-Tethys subduction below the Pontides. Timing of the opening of the eastern Black Sea basin is not well constrained as a result of poor stratigraphic exposure, and estimates vary from early Cretaceous (Nikishin et al., 2003; Kriachtchevskaia et al., 2010) to early Cenozoic (Robinson et al., 1995a; Robinson et al., 1996) and Eocene (Vincent et al., 2005). The western Black Sea basin opened in early Cretaceous times (Barremian-Albian) (Robinson et al., 1996; Görür, 1997; Tüysüz, 1999), and the interpretation of the Black Sea as a back-arc basin (Okay et al., 1994b) would suggest northward subduction below the Pontides in this time span.

The **Anatolide-Tauride block** constitutes the whole of Turkey south of the İzmir-Ankara-Erzincan (IAE) suture zone (Fig. 3.1). It consists of Pan-African basement that rifted away from the Gondwana margin in early Mesozoic times (Özgül, 1976; Şengör and Yilmaz, 1981; Satır and Friedrichsen, 1986; Şengör et al., 1988; Kröner and Şengör, 1990; Hetzel and Reischmann, 1996; Loos and Reischmann, 1999; Gessner et al., 2004). The cover mainly consists of Cambrian to Tertiary sediments, mostly carbonates (Özgül, 1976; Monod, 1977; Şengör and Yilmaz, 1981; Altın et al., 1999; Özer et al., 2004; Mackintosh and Robertson, 2009). Collision of the Anatolide-Tauride block with the Pontides started in latest Cretaceous to early Paleocene and continued until the Eocene.

The **South Armenian block** is also of Gondwana origin (Knipper and Khain, 1980; Kazmin et al., 1987) and is regarded as the eastern continuation of the Anatolide-Tauride block (Fig. 3.1). In the Jurassic to early Cretaceous, intra-oceanic subduction within the Tethys ocean north of the South Armenian block formed a volcanic arc (Rolland et al., 2009). After consumption of the entire oceanic crust south of the arc by the Cenomanian (~98 Ma), obduction of the arc started. Final shortening between Eurasia and the South Armenian Block ended when the oceanic crust north of the arc was entirely consumed by subduction under Eurasia in the Santonian (~83 Ma) (Rolland et al., 2009). Final collision of the South Armenian Block with the Eurasian margin took place in Paleocene to early Eocene times (Sosson et al., 2010).

The Pontides and the Anatolide-Tauride-South Armenian block are separated by the east-west trending **İzmir-Ankara-Erzincan (IAE) suture zone**. Closure of the ocean once separating the Anatolide-Tauride block from the Pontides, started around 90 Ma evidenced by widespread metamorphic sole ages below ophiolites attributed to the IAE (Yalınz et al., 2000; Çelik et al., 2006; Moix et al., 2008). Since that time Africa-Europe convergence was accommodated south of the Pontides (Şengör and Yilmaz, 1981; Görür et al., 1984; Dilek and Altunkaynak, 2009; Kaymakci et al., 2009). This 90 Ma and younger subduction below the Pontides is in good agreement with the location of the volcanic arc on the Pontides, as proven by deposition of volcanics and volcanoclastics of the Yemişliçay Formation (~89-83 Ma) and younger volcano-

sedimentary formations (Okay et al., 2001b; Hippolyte et al., 2010).

To the northeast of the eastern Pontides, the prominent **Greater Caucasus** fold-and-thrust belt is located (Fig. 3.1). The Greater Caucasus, of which Crimea is the western prolongation, has basement formed by the Scythian Platform, i.e. the thinned margin of the East European Platform (Nikishin et al., 1996; Saintot et al., 2006b). The volcano-sedimentary cover of the Greater Caucasus is of Permian and younger age. Importantly, the Sinemurian/Pliensbachian to Aalenian are rift-related series, that include MORB-resembling tholeiitic basalts of Aalenian age (~173 Ma, that may be comparable to the rift-related sequences in the eastern Pontides (Lordkipanidze et al., 1989; Okay and Şahintürk, 1997). Banks and Robinson (1997) envisaged that this area was occupied by en-echelon sets of rhomb-shaped rift basins, situated at the southern Eurasian margin. The Bajocian is characterized by calc-alkaline lavas, comparable to those in the Transcaucasus area (Fig. 3.1) (Adamia et al., 1981). The Greater Caucasus middle Jurassic volcanics have a subduction-related signature. However, it has been proposed that the volcanics resulted from back-arc spreading in the vicinity of a subduction zone south of the Transcaucasus terrane in the Lesser Caucasus, or that the volcanic arc encompassed the Greater Caucasus in Bajocian times, due to a shallowing of the subducting slab, causing arc-volcanism ~200 km from the trench (Saintot et al., 2006a; McCann et al., 2010).

2.2 Plate tectonic history

There is some consensus as to the subduction zone configuration in the circum-Black Sea region prior to and following the Jurassic. In the late Triassic, the Anatolide-Tauride-South Armenian block (Fig. 3.1) - a continental terrane of African origin - rifted from the African margin, leading to the formation of intervening oceanic basins (Fig. 3.2) (Şengör and Yilmaz, 1981). This movement had roughly a south to north sense. Apparent polar wander paths display little net S-N convergence between Africa and Eurasia until 120 Ma (Besse and Courtillot, 2002; Torsvik et al., 2008a), and the rifting of terranes away from the northern African margin must therefore have been accommodated by consumption of the Neo-Tethyan oceanic lithosphere by subduction along the southern Eurasian margin. The Triassic Karakaya complex, either interpreted as an inverted (back-arc) rift basin or as a former subduction zone (Genç and Yilmaz, 1995; Okay and Göncüoğlu, 2004; Pickett and Robertson, 2004), probably represents this subduction zone. This is further supported by the presence of Triassic blueschists (Bozkurt et al., 1997; Okay et al., 2002).

In Cretaceous times, there is evidence for northward subduction of Neo-Tethyan oceanic crust south of the Pontides, from ophiolitic fragments with metamorphic soles of 90 Ma and younger ages that are present within, as well as south of the east-west trending İzmir-Ankara-Erzincan suture zone (Yalınız et al., 2000; Çelik et al., 2006; Moix et al., 2008). A widespread record of a mid-Cretaceous and younger volcanic arc record is located in the Pontides (Okay et al., 2001b; Rice et al., 2006;

Hippolyte et al., 2010). An indication for pre-90 Ma Cretaceous subduction below the Pontides comes from cooling ages of subduction-accretion material in the Kargı window (Fig. 3.1) in the central Pontides, suggesting northward subduction below the Pontides from at least as early as ~105 Ma ago (Okay et al., 2006).

Very different views, however, exist on the subduction zone configuration of the modern Black Sea region in the Jurassic. For example, Dercourt et al. (1993; 2000) and more recently Barrier and Vrielynck (2008) place the Pontides at the southern continental margin of Eurasia in Jurassic times until the Cretaceous initiation of opening of the Black Sea. Alternative reconstructions by Stampfli and Borel (2002), Robertson et al. (2004) and Moix et al. (2008) separate the Pontides in Triassic to middle Jurassic times from the continental Eurasian margin by the small oceanic Küre basin. Supposedly, this ocean closed during southward subduction in late Triassic-middle Jurassic times (Stampfli and Kozur, 2006).

2.3 Geology of Crimea

Boreholes indicate that Crimea is underlain by Paleozoic and/or older Eurasian basement (Muratov, 1969; Letavin, 1980; Kruglov and Tsytko, 1988; Mazarovich and Mileev, 1989; Milanovsky, 1991; Gerasimov, 1994). It is likely part of the Scythian platform, which is the thinned margin of the East European Platform (EEP) (Gorbachev and Bogdanova, 1993; Stephenson et al., 2004; Saintot et al., 2006b). The basement is covered by a Mesozoic-Cenozoic clastic and carbonate sedimentary series, locally intruded by minor (sub-)volcanic series. South-vergent thrusting deformed Triassic to middle Jurassic turbidite sequences prior to upper Jurassic carbonate platform deposition (Koronovsky and Mileev, 1974; Khain, 1984). The deep-water turbidite sequences are intruded by magmatic bodies that were previously dated as Bajocian, based on cross-cutting relationships and faunal evidence (Spiridonov et al., 1990b, 1990a; Latyshev and Panov, 2008; Sysolin and Pravikova, 2008).

The Bajocian magmatism comprises volcanic complexes (with hypabyssal intrusive and extrusive bodies) and isolated igneous rocks in the Bodrak and Pervo-maisk-Ayu-Dag areas in western and central Crimean mountains, as well as the Karadag volcanic complex in eastern Crimean mountains (Fig. 3.3a). The Karadag complex consists of a volcano-sedimentary succession that was dated as Bajocian-Callovian on the basis of Bajocian fauna that intercalate with the lower volcanic sequence, and Bathonian to lower Callovian fauna that are present within the overlying sedimentary sequence (Voznesensky et al., 1998). Page et al. (1998), Latyshev and Panov (2008) and Sysolin and Pravikova (2008) suggest a tholeiitic island-arc setting for the production of these volcanics, based on geochemical analysis. Ages however, have not been confirmed by isotopic dating. The upper Jurassic to lower Cretaceous (Berriasian) sequences consist of platform carbonates (Krajewski and Olszewska, 2006), and to the east comprise conglomerates and turbidite sequences. The conglomerate and turbidite sequences are of Kimmeridgian age. Zonenshain et al. (1990) proposed that the peb-

bles of the conglomerates were derived from the Pontides. More recently, it was argued that the conglomerates were probably sourced from within the basin itself (Hein, 2005). The upper Jurassic to lowermost Cretaceous (lower Berriasian) is folded and thrust (Mileyev et al., 1995; Nikishin et al., 1998), and unconformably overlain by an upper unit of lower Cretaceous (upper Berriasian) to Eocene rift-related sequences (Zonenshain and Le Pichon, 1986), probably related to the opening of the Black Sea.

3. Analyses & Results

3.1 Sampling

We collected volcanic samples in the Bodrak/Simferopol area and from the Karadag

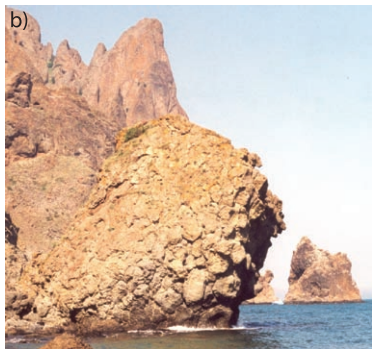
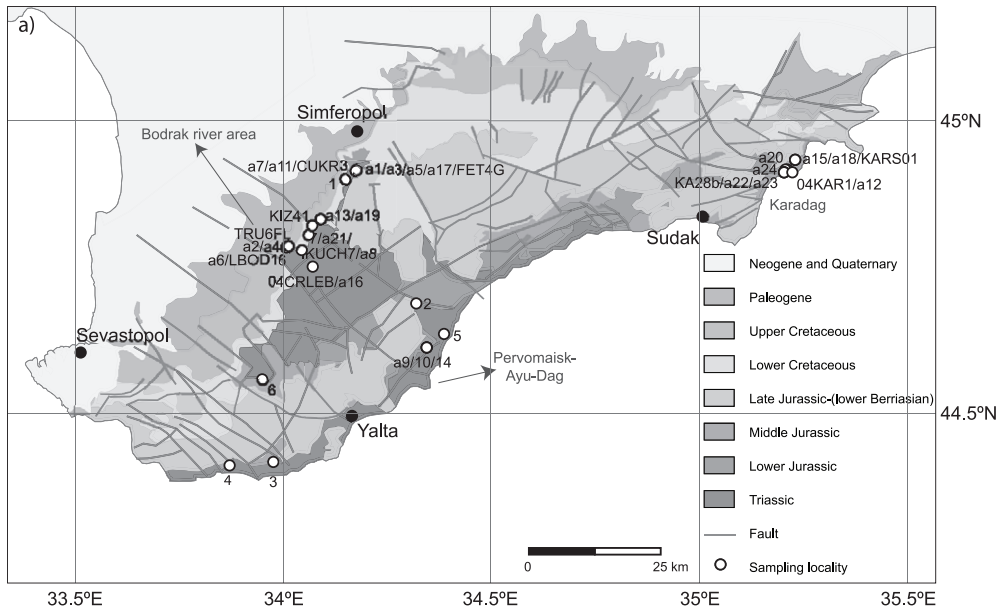


Figure 3.3 a) Geological map of Crimea, based on Derenyuk et al. (1984) and Panek et al. (2009), with our sampling locations indicated. b) Tilted pillows from Karadag (top to the left; sample 04KAR1). c) Verticalized columnar lava flow from Karadag (top to the left). See Appendix 14

volcanic edifice for isotopic dating and geochemical analysis (Fig. 3.3a). The samples were collected from intrusive rocks (plutonic bodies, hypabyssal sills and feeder dykes) and extrusive rocks (typically pillow lavas, rhyolitic nuées ardentes and columnar lava flows; Fig. 3.3b and c). Thirty-one samples were collected for XRF major and trace element analysis, and ten samples were selected for $^{40}\text{Ar}/^{39}\text{Ar}$ dating (Table 3.1).

3.2 $^{40}\text{Ar}/^{39}\text{Ar}$ dating

The ten freshest samples from the Crimean peninsula were selected for $^{40}\text{Ar}/^{39}\text{Ar}$ dating after microscope inspection (Figs. 3.4 and 3.5, Tables 1 and 2). Groundmass, plagioclase and biotite were separated using standard mineral separation techniques. All samples were first crushed and sieved. Plagioclase and biotite crystals (either 125-250 μm or 200-250 μm fractions, see Table 3.2) were separated using heavy liquid separation and a Frantz magnetometer, followed by mineral picking under the microscope. For groundmass (samples KA28b and FET4G) the 250-500 μm fraction was selected for analysis. For the groundmass of sample KA28b we performed heavy liquid separations using two separate density ranges: $2.70 > \rho > 2.66 \text{ g/cm}^3$ and $\rho < 2.66 \text{ g/cm}^3$. For sample FET4G we used the density fraction of $2.90 > \rho > 2.70 \text{ g/cm}^3$. All separated fractions were leached with 1 N HNO_3 for one hour in an ultrasonic bath to clean samples before final re-picking by hand.

From all samples ~18-30 mg of material was wrapped in aluminum foil and loaded in a 15 mm ID quartz vial. Only for samples KARS01 and KA28b (both groundmass samples) 6 mg and 3 mg of material was loaded respectively, due to low

KARS01	nuée ardente (rhyolite)	vitroclastic; white/green color; >25% pumiceous; fresh plagioclase, low amount however
04CRLEB	andesite	large fraction fresh hornblende; fresh biotite (large fraction, but less common than amphibole); porphyritic texture with interstitial calcite; pseudomorph glass?; pseudomorph augite; fresh plagioclase (common)
KA28b	trachyte	fresh plagioclase phenocrysts; porphyritic and microlithic texture; some plagioclase contains calcite
04KAR1	pillow lava (basaltic) andesite	porphyritic & finely microlithic texture with vesicles in the glass; augite (slightly pleochroic); very fresh plagioclase; vesicles probably filled with clay
IKUCH7	(trachy-) andesite	chlorite probably pseudomorph in glass; plagioclase is interfingered with a matrix of chlorite (pseudomorph); alkali-feldspar grains present (one twin); probably phenocrysts of plagioclase; perhaps interstitial quartz; no ferromagnesium silicate
LBOD16	basalt	very fresh plagioclase; a lot of calcite in matrix, in patches; porphyritic and microlithic texture; some augite present; maybe some olivine present
FET4G	andesitic lava with columnar joints	porphyritic and microlithic texture; calcite is replacing the plagioclase; feldspar not very fresh, but twins are visible; phenocrysts of plagioclase; plagioclase microliths; microcrystalline quartz present in vesicles
CUKR3	alkali-syenite-monzonite	some fresh amphibole present; K-feldspar is more or less fresh; plagioclase; iron oxides; interstitial quartz; completely crystalline; probably an intrusion, because minerals had time to grow over each other; no glass.
KIZ41	andesitic lava	phenocrysts of brown amphibole (hornblende) with black rims formed by iron oxides; biotite; few phenocrysts of zoned plagioclase; porphyritic and microlithic texture; matrix (~90%) is essentially made of feldspar microcrystals, iron oxides and calcite.
TRU6FL	andesitic lava	almost completely crystalline rock, consists of 80% feldspar (orthose and plagioclase, sometimes zoned); remaining 20% twinned augites and iron oxides; porphyritic and microlithic texture

Table 3.1 Mineralogy of the samples selected for $^{40}\text{Ar}/^{39}\text{Ar}$ dating, determined from microscope inspection.

amounts of material available. Between each set of 5 samples and at top and bottom positions, the in-house Drachenfels sanidine standard (25.26 ± 0.03 Ma, modified from Wijbrans et al. (1995)) was used as neutron fluence monitor. The loaded quartz vial was irradiated for 18 hours in the Cd-lined RODEO P3 position of the High Flux Reactor in Petten, the Netherlands. $^{40}\text{Ar}/^{39}\text{Ar}$ incremental heating experiments were carried out at the VU University of Amsterdam, the Netherlands. Standards were fused using a Synrad 48-5 50W CO_2 laser. Samples were spread out evenly in a sample tray with 6 mm diameter holes and incrementally heated with a Raylase scan head as a beam delivery and diffuser system. In total, we performed 13 incremental heating experiments, on either plagioclase (8), groundmass (4) or biotite (1). For two samples both plagioclase and groundmass was separated (KA28b and FET4G) to validate the obtained ages.

After purification the gas was analysed with a Mass Analyzer Products LTD 215-50 noble gas mass spectrometer. Beam intensities were measured in a peak-jumping mode in 0.5 mass intervals over the mass range 40-35.5 on a Balzers 217 secondary electron multiplier. After every four steps system blanks were measured. Mass discrimination was monitored by frequent analysis of aliquots of air. By interpolating between the individually measured standard using a second-order polynomial fitting the irradiation parameter J was determined for each unknown sample.

Ages were calculated using the in-house developed ArArCalc software (Koppers, 2002). All $^{40}\text{Ar}/^{39}\text{Ar}$ ages were calculated using Steiger and Jäger (1977) decay constants at the 2σ level and include the analytical error and error in irradiation parameter (J). Correction factors for neutron interference reactions are $2.7 \pm 0.03 \times 10^{-4}$ for $(^{36}\text{Ar}/^{37}\text{Ar})_{\text{Ca}}$, $6.99 \pm 0.13 \times 10^{-4}$ for $(^{39}\text{Ar}/^{37}\text{Ar})_{\text{Ca}}$ and $1.83 \pm 0.2 \times 10^{-2}$ for $(^{40}\text{Ar}/^{39}\text{Ar})_{\text{K}}$.

The results of the $^{40}\text{Ar}/^{39}\text{Ar}$ analyses are summarized in Table 3.2 and Figure 3.4 and 3.5. Full analytical data are given in the Supplementary Data. All steps yielding less than 2% $^{39}\text{Ar}_{\text{k}}$ were excluded in incremental heating spectra, but are included in the full analytical data tables (Tables 1 and 2). To define a reliable plateau age; i) at least three successive incremental heating steps should be included for calculation of a plateau age. ii) The steps that are used to calculate the plateau ages should represent more than 50% of the total $^{39}\text{Ar}_{\text{k}}$ released (e.g. Fleck et al. 1977). The mean squared weighted deviation (MSWD) over the plateau steps is a measure for plateau homogeneity, and should ideally range between 1.0 and 2.0, this was, however not always the case (Table 3.2). We also checked for a relatively constant K/Ca ratio in the successive included incremental heating steps. The $^{40}\text{Ar}/^{36}\text{Ar}$ ratio was monitored to assess excess argon in the system (i.e. within 2σ error of 295.5). If no plateau age could be calculated or the sample suffered from excess argon, an isochron age was determined. This was the case for samples CUKR3 and IKUCH7. For sample KARS01 we decided to use the plateau age, despite the high MSWD value (2.49), because of the poor determination of the inverse isochron intercept (Table 3.2). The isotopic ages from the

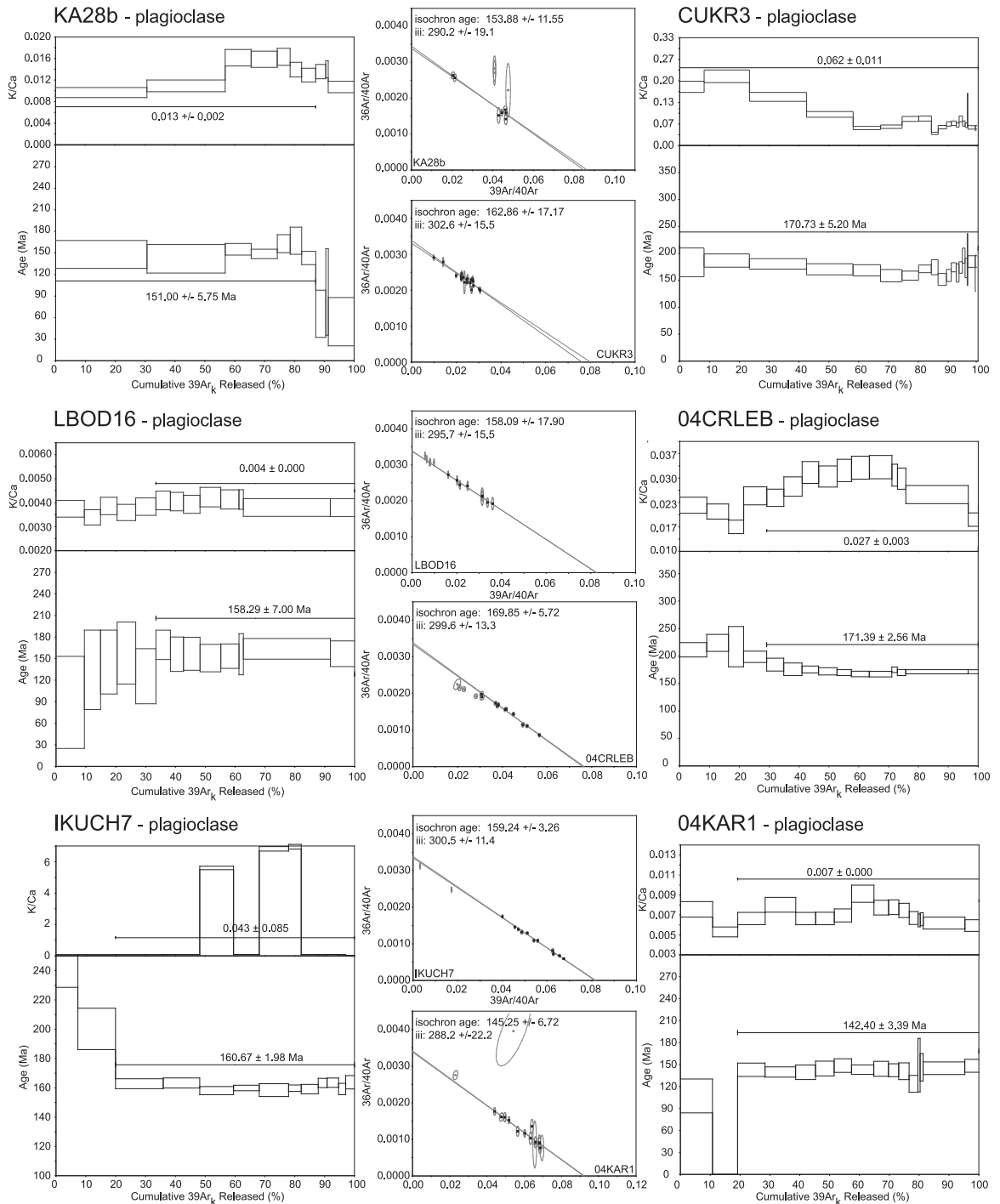


Figure 3.4 Figure showing the incremental heating $^{40}\text{Ar}/^{39}\text{Ar}$ spectra of 11 samples. The width of the bars/steps represents the 2σ analytical error. Weighted mean plateau ages are displayed. For all samples, also the K/Ca and inverse isochron diagrams with their ages and inverse isochron intercept (iii) are shown.

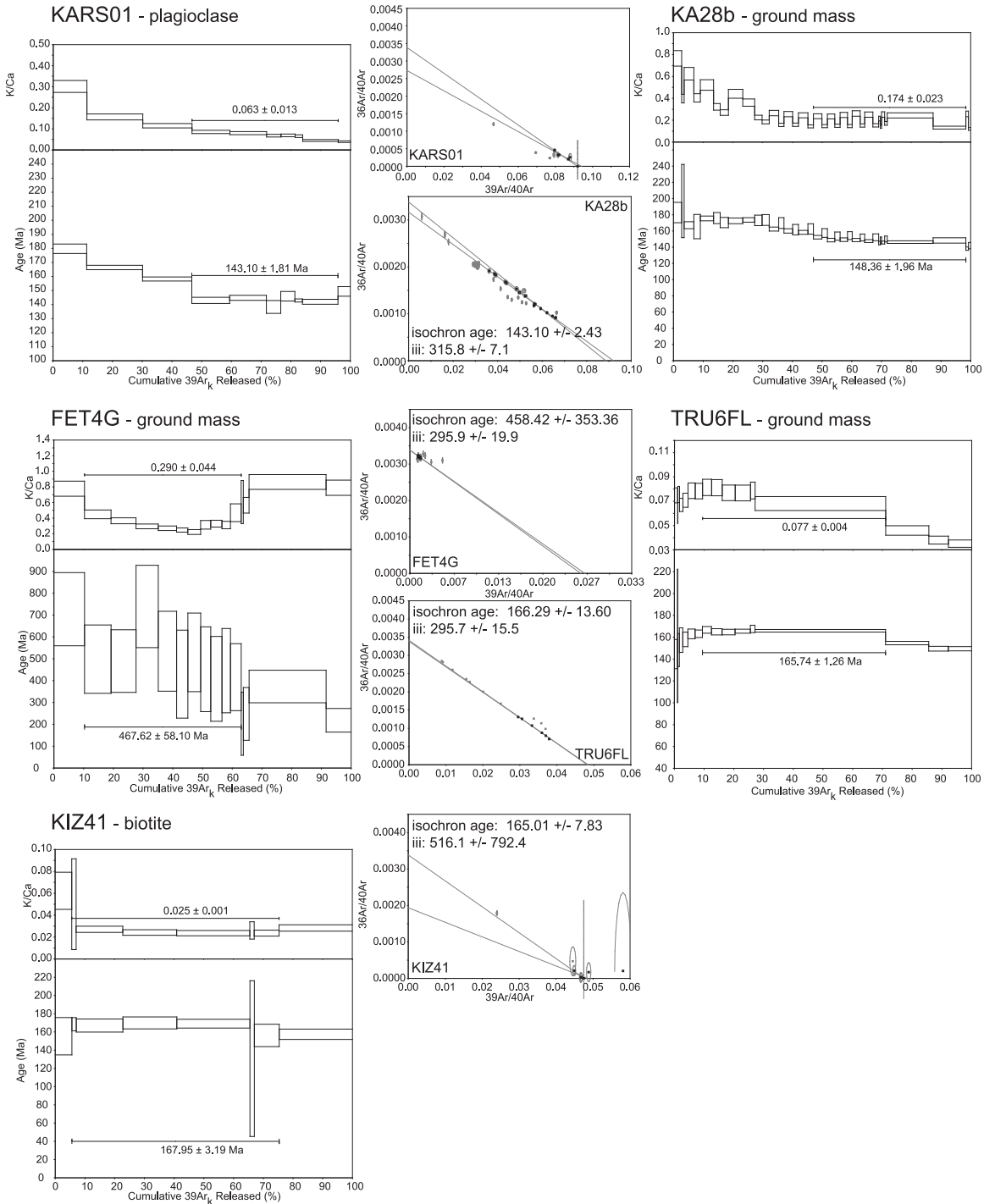


Figure 3.4 (continued)

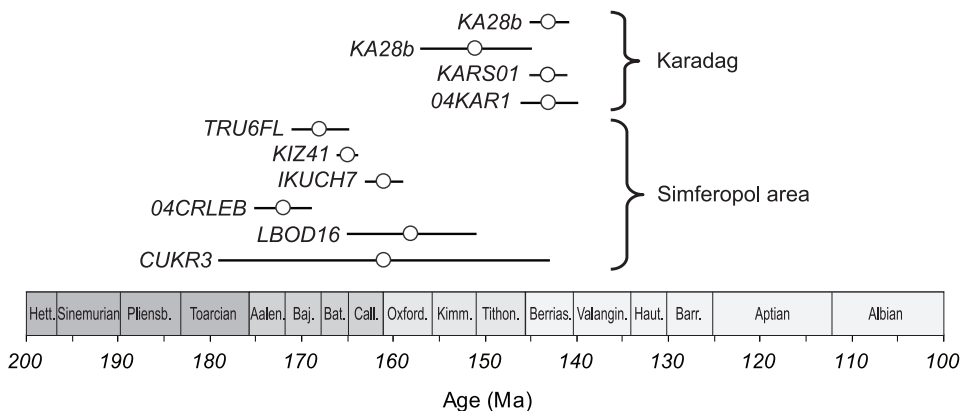


Figure 3.5 Figure showing the $^{40}\text{Ar}/^{39}\text{Ar}$ ages. There are clearly two age groups that are also geographically spread over two areas: the Karadag volcanic edifice and the Bodrak/Simferopol area. Hett.= Hettangian; Pliensb.= Pliensbachian; Aalen.= Aalenian; Baj.= Bajocian; Bat.= Bathonian; Call.= Callovian; Oxford.= Oxordian; Kimm.= Kimmeridgian; Tithon.= Tithonian; Berrias.= Berriasian; Valangin.= Valanginian; Haut.= Hauterivian; Barr.= Barremian.

groundmass of both KA28b samples with different densities yielded comparable plateau ages (151 ± 3 Ma and 149 ± 2 Ma) that are likely to be high estimates of the true emplacement age because of a high initial $^{40}\text{Ar}/^{36}\text{Ar}$ ratio of 315.8 ± 6.9 that indicates the presence of excess ^{40}Ar . The data were combined in a single isochron age of 143 ± 2 Ma that we feel dates the emplacement event more reliably. From the remaining eleven processed samples, eight plateau ages and a single isochron age were calculated. The two fractions of groundmass of sample FET4G did not yield geologically meaningful results.

3.3 Geochemistry

Major and trace elements were determined from 31 samples by XRF measurements on fused glass beads and pressed powder pellets at the VU University Amsterdam. International standards are used for calibration and in-house samples run as internal monitors. Results are displayed in Table 3.3. Loss on ignition (LOI) were determined at 1000°C to provide an indication of the degree of low temperature alteration. The LOI vary from 1.1 to 20.1%. The major element compositions of samples with LOI's higher than 6% (samples 3, 4, a6 and a16) are not considered further.

From the TAS classification diagram (Irvine and Baragar, 1971; Le Maître et al., 1989) (Fig. 3.6) a subalkaline to tholeiitic trend can be observed in the samples, that range in composition from basaltic andesites to dacites (older age group) and dacites to rhyolites (the two yellow triangles; younger age group, Karadag). The most mafic rock (a1) contains 8.6 wt% MgO and is a trachybasalt. Moderately compatible trace element contents (REE, Sr, Zr etc.) have abundances comparable to E-MORB; i.e. in the range of 5-10 times that of primitive mantle (Sun and McDonough, 1989). In contrast, the large ion lithophile element (LILE, e.g. Rb, Ba and K) record signifi-

Irradiation	sample ID	Lab ID	Mineral	Fraction (mm)	J (±0.4%)	Plateau age (Ma)	MSWD	N	$^{39}\text{Ar}_K$ (%) in plateau	^{40}Ar (%)	K/Ca	Total fusion age (Ma)	Inverse isochron age (Ma)	Inverse isochron intercept
VU65-B2	FET4G	07MX363	plagioclase	200-250	0.0075000	No plateau	-	-	-	-	-	4134.9 ± 9.7	-	-
VU65-B3	KA28b	07MX364	plagioclase	200-250	0.0075540	151.0 ± 5.8	2.00	7 (5)	81.34	45.07	0.013 ± 0.002	201.3 ± 57.6	153.8 ± 11.6	290.2 ± 19.1
VU65-B4	CUKR3	07MX365	plagioclase	125-250	0.0075580	470.7 ± 5.2	3.53	19 (1)	99.96	31.73	0.062 ± 0.011	174.3 ± 4.4	162.9 ± 17.2	302.6 ± 15.5
VU65-B5	LBD016	07MX366	plagioclase	200-250	0.0075630	158.3 ± 7.0	0.39	13 (5)	66.53	32.50	0.004/0.000	148.5 ± 9.6	158.1 ± 17.9	295.7 ± 15.5
VU65-B6	04CRLEB	07MX368	plagioclase	200-250	0.0075670	171.3 ± 2.6	1.53	15 (4)	70.85	55.33	0.027 ± 0.003	184.1 ± 3.5	169.9 ± 5.7	299.6 ± 13.3
VU65-B8	IKUCH7	07MX369	plagioclase	125-250	0.0075760	469.4 ± 2.9	2.42	21 (3)	81.41	68.28	0.039 ± 0.045	176.8 ± 6.4	159.2 ± 3.3	300.5 ± 11.4
VU65-B9	04KAR1	07MX370	plagioclase	200-250	0.0075800	143.2 ± 2.9	0.45	16 (4)	70.56	64.38	0.007 ± 0.000	112.3 ± 3.3	145.3 ± 6.7	288.2 ± 22.2
VU65-B10	KARS01	07MX371	plagioclase	125-250	0.0075840	143.1 ± 1.8	2.49	10 (4)	49.18	92.25	0.063 ± 0.013	154.4 ± 1.7	139.9 ± 5.5	365.6 ± 110.6
VU65-B11	KA28b	07MX373	ground mass	250-500	0.0075880	152.0 ± 2.5	2.00	20 (13)	24.43	49.68	0.150 ± 0.007	162.8 ± 3.1	140.4 ± 7.9	319.4 ± 15.8
VU65-B12	KA28b	07MX374	ground mass	250-500	0.0075930	148.5 ± 1.8	0.59	19 (15)	16.91	66.37	0.248 ± 0.012	161.0 ± 2.3	142.8 ± 10.0	319.1 ± 40.7
Comb.	KA28b	Comb.	ground mass	250-500	-	448.4 ± 2.0	4.55	39 (23)	50.15	59.72	0.174 ± 0.023	161.3 ± 2.1	143.1 ± 2.4	315.8 ± 7.1
VU65-B14	FET4G	07MX375	ground mass	250-500	0.0076010	467.6 ± 58.4	0.29	15 (6)	45.24	5.32	0.290 ± 0.044	473.7 ± 42.2	458.4 ± 353.4	295.9 ± 19.9
VU52-B8	KIZ41	05MY313	biotite	250-500	0.0046470	168.0 ± 3.2	1.03	10 (4)	66.22	96.82	0.025 ± 0.001	162.5 ± 3.7	165.0 ± 7.8	516.1 ± 792.4
VU52-B4	TRU6FL	05MY027	ground mass	250-500	0.0046620	165.7 ± 1.3	0.54	17 (11)	61.59	70.34	0.077 ± 0.004	161.1 ± 1.2	166.3 ± 3.0	292.9 ± 13.6

Table 3.2 Summary of $^{40}\text{Ar}/^{39}\text{Ar}$ results. MSWD: mean square weighted deviates, N: number of steps included (excluded) in the plateau age, $^{39}\text{Ar}_K$ (%): percentage of $^{39}\text{Ar}_K$ released by plateau steps, $^{40}\text{Ar}_T$: radiogenic amount of ^{40}Ar . Errors are given at 95% confidence level. Ages were calculated using the in-house developed ArAr-Calc software (Koppers, 2002). All $^{40}\text{Ar}/^{39}\text{Ar}$ ages were calculated using Steiger and Jäger (1977) decay constants at the 2 level and include the analytical error and error in irradiation parameter (J). Correction factors for neutron interference reactions are $2.7 \pm 0.03 \times 10^{-4}$ for $(^{36}\text{Ar}/^{37}\text{Ar})\text{Ca}$, $6.99 \pm 0.13 \times 10^{-4}$ for $(^{39}\text{Ar}/^{37}\text{Ar})\text{Ca}$ and $1.83 \pm 0.2 \times 10^{-2}$ for $(^{40}\text{Ar}/^{39}\text{Ar})\text{K}$. Strikethrough plateau ages indicate error plateaus.

Sample	1	2	3	4	5	6	7	a1	a2	a3	a4	a5	a6	a7	a8	a9	a10
Original sample code	n/a	n/a	n/a	n/a	n/a	n/a	n/a	FET4H	TRU6FL	FET4	TRU6DY	FET4G	LBOD16	CUKR3	IKUCH7	NCHA21	MCHA21
Rock type	andesite	basaltic andesite	basalt	basalt	rhyolite	basaltic andesite	andesite	andesitic basalt	andesitic basalt	grano-diorite	basalt	andesite	basalt	alkali-syenite-monzonite	(trachy-) andesite	rhyolite	rhyolite
Major elements																	
SiO ₂ (%)	59.09	52.48	33.34	46.97	71.88	52.95	57.02	50.79	53.55	59.43	51.00	56.78	48.90	56.54	57.01	70.45	68.12
TiO ₂ (%)	1.25	0.76	0.65	0.71	0.14	0.74	0.71	1.13	0.70	1.40	0.79	1.58	0.63	1.21	0.68	0.30	0.29
Al ₂ O ₃ (%)	14.78	18.08	13.76	15.71	14.19	16.15	17.71	16.33	18.90	13.91	21.32	14.38	15.48	15.31	18.60	15.56	14.97
Fe ₂ O ₃ (%)	9.99	9.53	9.02	9.03	3.39	10.25	8.33	10.93	9.61	10.54	8.63	12.02	8.81	10.93	8.44	5.15	4.97
MnO (%)	0.14	0.16	0.24	0.20	0.12	0.16	0.12	0.19	0.17	0.15	0.12	0.14	0.34	0.14	0.19	0.14	0.14
MgO (%)	4.23	5.72	2.18	5.10	0.17	10.23	3.33	8.60	4.69	3.78	3.20	2.81	4.56	5.36	2.61	0.45	0.41
CaO (%)	4.87	8.22	38.07	17.23	1.95	5.00	7.33	6.61	8.22	3.70	8.01	5.45	17.95	3.75	7.07	3.31	3.64
Na ₂ O (%)	5.48	3.98	0.75	2.87	5.22	4.58	3.48	4.61	3.17	5.67	4.81	6.11	1.56	5.47	3.74	4.77	4.40
K ₂ O (%)	0.35	0.54	0.01	0.28	1.22	0.12	0.62	0.16	0.57	0.10	1.22	0.18	0.36	0.45	1.00	1.30	1.20
P ₂ O ₅ (%)	0.10	0.09	0.15	0.10	0.05	0.11	0.10	0.16	0.07	0.13	0.09	0.16	0.07	0.11	0.26	0.10	0.10
BaO (%)	0.01	0.02	0.00	0.09	0.02	0.02	0.02	0.06	0.01	0.00	0.02	0.00	0.02	0.01	0.04	0.02	0.02
MgO+CaO (%)	9.10	13.94	40.25	22.33	2.12	15.23	10.66	15.21	12.91	7.08	11.21	8.26	22.51	9.11	9.68	3.76	4.05
sum (%)	100.28	99.59	98.18	98.29	98.35	100.32	98.75	99.97	99.67	98.41	99.19	99.60	98.67	99.28	99.63	101.53	98.25
LOI (%)	3.42	4.06	20.07	13.16	2.36	4.90	2.11	4.49	1.40	4.70	3.96	5.49	10.14	2.68	2.35	3.50	4.16
Trace elements																	
V	324	262	282	260	6	258	198	329	303	323	288	348	283	315	80	15	16
Cr	12	41	27	429	7	353	6	168	13	9	8	3	648	23	6	4	4
Co	34	36	24	36	43	43	20	41	25	42	23	32	48	32	13	5	4
Ba	41	135	21	800	190	173	141	504	115	149	2	156	38	311	188	205	205
Sc	28	31	47	39	7	29	22	32	29	31	27	32	41	29	15	15	16
Ga	15	16	27	15	16	15	18	15	17	13	18	14	15	13	15	17	17
Zn	67	75	63	78	76	102	78	71	81	79	67	83	75	75	72	89	78
Cu	12	20	48	57	1	63	11	116	35	42	51	16	91	37	3	2	1
Ni	10	18	20	119	4	107	5	46	7	13	9	5	195	16	4	5	6
Mo	ppm	1	1	1	1	1	1	2	2	3	2	2	2	3	2	3	3
Nb	1.6	1.0	1.0	1.0	2.6	1.2	1.2	2.5	1.1	1.5	1.6	1.6	1.2	1.6	3.3	3.3	3.3
Y	28	17	15	12	35	16	24	18	20	34	18	40	15	28	21	37	36
Zr	85	47	43	40	152	46	64	52	44	92	45	104	35	82	88	137	136
Sr	121	240	74	445	109	276	188	451	255	45	488	85	210	137	357	196	125
Rb	4.1	14.8	6.3	35.7	3.2	11.7	19.5	9.3	2.8	24.7	6.5	7.5	5.8	35.9	36.8	33.9	33.9
Th	ppm	1.2	2.4	1.6	4.5	2.0	1.3	1.1	1.1	1.1	1.1	1.1	1.1	1.1	2.2	3.9	4.2
Pb	ppm	1.1	7.7	2.5	1.8	1.3	3.3	2.2	5.2	2.2	4.4	4.4	4.4	1.1	3.6	6.6	5.9
La	ppm	3.9	9.7	6.4	15.9	6.0	6.2	9.3	2.7	3.4	5.8	3.8	4.7	1.1	11.3	13.9	13.7
Ce	ppm	12.4	14.2	21.1	6.7	44.0	11.3	18.7	17.4	10.8	14.6	12.9	11.6	4.4	11.0	32.1	38.9
Pr	ppm	2.8	3.0	3.4	2.1	5.5	2.8	3.3	3.4	2.5	3.3	3.1	3.2	1.8	2.6	5.4	5.1
Nd	ppm	10.2	9.8	13.8	5.0	21.0	9.3	12.1	11.1	9.7	12.1	10.3	9.2	6.8	8.2	17.9	17.5
Sm	ppm	2.8	2.7	2.5	1.6	4.1	2.5	2.7	2.9	2.3	2.7	3.3	2.2	2.7	3.7	3.7	3.1

Table 3.3 Geochemical data (major and trace elements) from whole rock analyses of 31 samples.

Sample	a11	a12	a13	a14	a15	a16	a17	a18	a19	a20	a21	a22	a23	a24
Original sample code	04CRPET	04KAR1	PAR2	OCHA21	KARSD	04CRLEB	FET4B	KARS2	04CRPAR	04KAR2	KIZ41	KA28b	KA28b	04KAR3
Rock type	andesite	(basaltic) andesite	trachyte	rhyolite	rhyolite (nuée ardente)	andesite	andesitic basalt	rhyolite (nuée ardente)	andesite	rhyolite	andesite	trachyte	trachyte	rhyolite
Major elements														
SiO ₂	57.16	58.05	64.98	68.90	76.12	46.32	54.87	75.13	65.98	69.06	58.95	70.20	66.37	69.17
TiO ₂	1.01	0.88	0.36	0.30	0.09	1.24	1.09	0.09	0.36	0.85	0.81	0.69	0.65	0.68
Al ₂ O ₃	16.51	17.75	16.91	15.84	11.62	16.98	16.02	12.23	17.21	13.27	17.76	14.46	16.29	15.19
Fe ₂ O ₃	9.70	7.30	4.35	10.93	5.20	10.93	10.45	0.82	4.38	5.63	7.54	3.54	4.35	3.05
MnO	0.14	0.15	0.15	0.14	0.04	0.19	0.19	0.07	0.14	0.26	0.08	0.11	0.17	0.12
MgO	4.97	2.92	1.57	0.47	0.36	9.85	7.64	0.37	1.48	0.86	2.74	0.37	0.78	0.38
CaO	4.44	9.06	4.13	3.13	4.44	12.76	2.89	1.27	4.34	1.40	5.60	4.04	5.66	2.01
Na ₂ O	4.90	2.74	5.01	3.89	3.61	1.64	6.47	4.58	7.23	3.65	3.79	3.63	3.63	7.54
K ₂ O	0.65	0.31	1.09	1.13	1.92	0.49	0.12	3.91	1.65	2.20	1.52	1.51	1.75	1.30
P ₂ O ₅	0.11	0.23	0.12	0.11	0.02	0.29	0.10	0.01	0.12	0.32	0.15	0.23	0.22	0.25
BaO	0.01	0.01	0.03	0.03	0.04	0.03	0.01	0.05	0.05	0.00	0.02	0.08	0.05	0.03
MgO+CaO	9.41	11.98	5.70	3.60	1.88	22.61	10.53	1.64	5.82	2.26	8.34	4.41	6.44	2.39
sum	99.61	99.40	98.69	99.11	96.17	100.73	99.84	96.81	100.28	99.08	98.81	99.01	99.91	99.72
LOI (%)	4.20	2.11	2.82	4.29	5.79	7.13	2.82	4.76	2.98	1.25	1.35	0.56	1.12	1.19
Trace elements														
V	298	296	59	17	4	353	292	3	56	150	123	71	105	44
Cr	29	6	1	4	4	583	43	2	2	9	37	3	9	2
Co	26	19	9	5	1	51	40	2	8	10	13	7	6	6
Ba	113	114	277	200	370	287	49	367	429	16	179	699	434	219
Sc	27	27	10	15	2	38	34	2	10	21	23	16	18	14
Ga	19	17	15	19	9	17	16	9	15	9	18	14	16	8
Zn	82	78	68	82	34	81	68	44	64	111	86	68	63	88
Cu	31	68	3	1	1	58	33	33	2	6	11	5	8	2
Ni	15	8	4	5	5	196	25	5	5	5	16	5	5	5
Nb	3	2	3	3	3	2	3	3	3	3	3	3	3	3
Mo	2.2	1.7	1.6	3.2	2.1	3.4	1.1	2.1	1.7	3.7	3.0	3.5	3.1	3.4
Y	27	26	19	35	19	21	29	14	18	32	25	29	29	39
Zr	79	72	84	135	74	62	74	74	84	116	89	101	113	116
Sr	63	275	184	184	231	357	155	147	176	18	214	206	239	33
Rb	2.8	4.0	22.8	27.6	40.4	18.7	1.6	60.8	23.1	2.1	24.2	25.1	33.9	15.4
Th	2.9	2.5	1.5	4.2	7.1	1.3	0.7	7.1	2.0	5.3	2.0	3.3	4.3	4.2
Pb	7.8	14.6	9.5	12.9	17.7	12.4	2.4	15.0	11.7	17.2	9.2	6.6	7.8	8.8
La	16.5	35.4	24.9	37.9	34.2	24.4	9.3	27.2	23.8	49.7	22.2	35.8	43.7	38.0
Ce	3.5	4.8	3.5	5.4	4.2	3.7	2.5	3.3	4.0	6.1	4.1	4.9	5.9	5.4
Pr	10.3	17.2	13.0	20.3	13.5	14.9	10.0	10.6	13.5	26.1	12.6	14.8	20.8	19.4
Nd	2.9	3.4	2.1	3.5	2.0	4.0	2.7	1.3	2.4	4.5	2.8	2.8	3.8	3.7

Table 3.3 (continued)

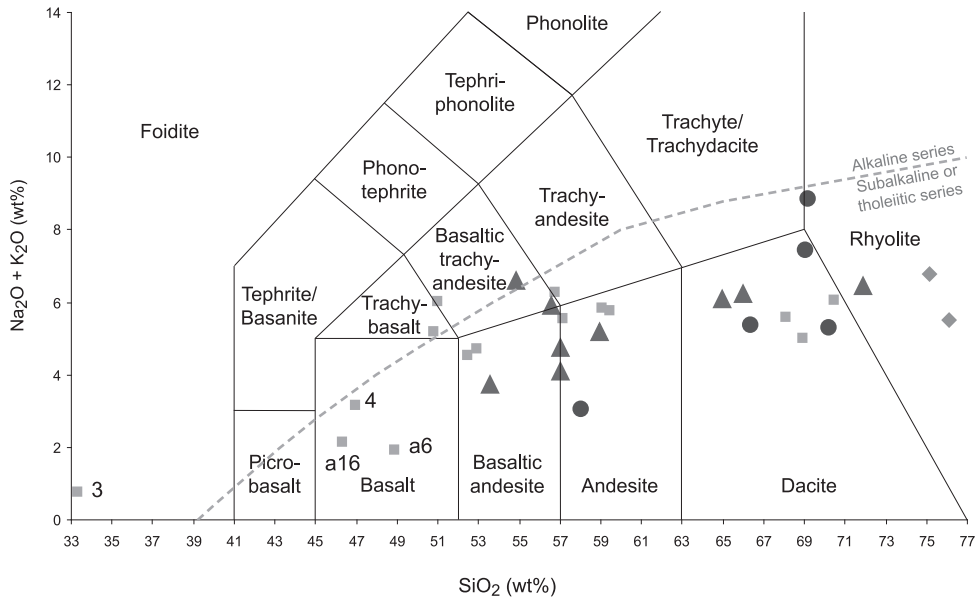
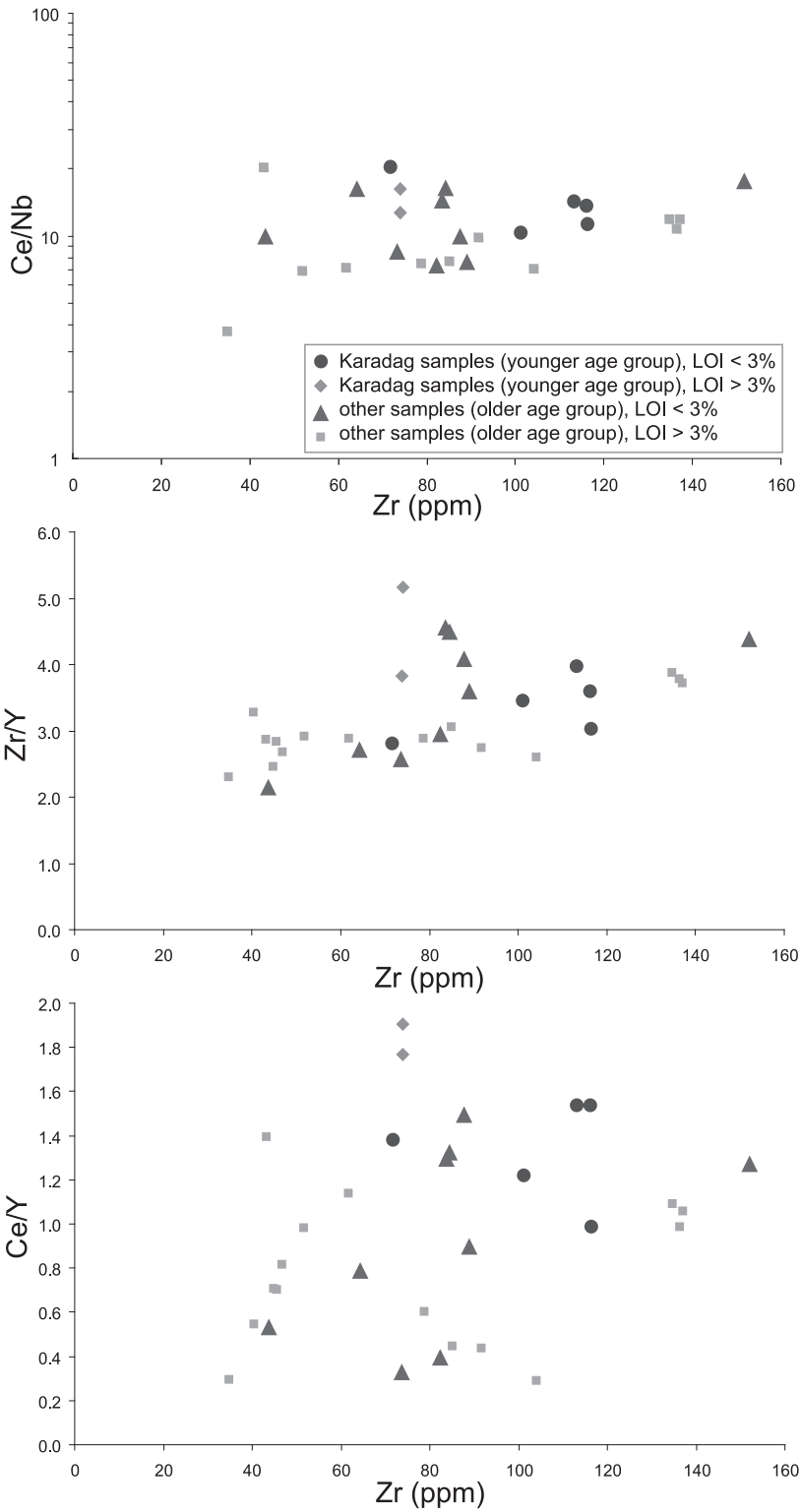


Figure 3.6 Plot of magmatic rocks (subdivided in four series, as indicated in the figure) in TAS classification diagram that displays $(\text{Na}_2\text{O} + \text{K}_2\text{O})$ versus SiO_2 (Le Maitre et al., 1989). Area above (below) the dotted line indicates the alkaline (subalkaline or tholeiitic) field after Irvine and Baragar (1971). Legend as for Figure 3.7

cant variations but with most concentrations significantly higher than the E-MORB and the most mafic samples with >30 times primitive mantle. This general enrichment in LILE contrasts with that of the high field strength elements (HFSE, e.g. Nb), which is close to primitive mantle values in the more mafic samples and always below E-MORB concentrations. The low Nb concentration compared to the LILE and LREE is a characteristic of subduction-related volcanism. In a Ce/Nb versus Zr diagram (Fig. 3.7a), the elevated Ce/Nb ratios of the entire suite compared to values between 1.8 and 3 for MORB and E-MORB. However, there is no clear trace element difference between the older and younger age groups of volcanics.

The similarity in the trace element geochemistry between the two volcanic suites is emphasized in Figure 3.7b. The entire sample suites show a general coherent differentiation trend in a Zr/Y versus Zr diagram (Fig. 3.7b). The Ce/Y ratio in Figure 3.7c is used as a proxy for REE fractionation. The relatively large range in Ce/Y indicates that either the entire suite has undergone variable fractionation involving some minor phases or that there have been different degrees of partial melting in the source. We rule out the possibility of greater fractional crystallization being the dominant

Figure 3.7 a) Ce/Nb ratio versus Zr diagram of all data. The high Ce/Nb ratio is an indication for subduction related volcanism. b) Zr/Y ratio versus Zr diagram of all data. The high Zr/Y ratio is an indication for subduction related volcanism. c) Ce/Y ratio versus Zr diagram of all data. Note that the samples of the younger age group have on average a higher Ce/Y ratio, indicating so a greater LREE/HREE fractionation.



process because of coherence of diagrams showing Zr/Y, Zr/Nb or Ce/Nb versus Zr. Therefore, it is more likely that the LREE/HREE fractionation is caused by partial melting processes in the mantle, possibly resulting from variations in heat or water in the source or variable amounts of decompression.

4. Discussion

4.1 Nature and age of Crimean volcanism

Our $^{40}\text{Ar}/^{39}\text{Ar}$ ages define two age groups: an older age group (middle-late Jurassic ages, ~172-158 Ma) and a younger age group (late Jurassic-early Cretaceous, ~151-142) (Fig. 3.5). The older group comes from the Bodrak/Simferopol area, whereas the younger group comes from the Karadag volcanic edifice on the southeastern shore of the island.

Magmatic rocks from both age groups belong to similar magmatic complexes. The magmatics of the older group (Simferopol area) are present as plutonic bodies, sills and feeder dykes within the pre-upper Jurassic sedimentary units and as lava flows. Magmatic rocks from the younger group (Karadag) are present within an isolated volcanic complex, and have not been seen to interfinger with the Triassic-Jurassic stratigraphy. From the major and trace element analysis, however, we cannot make a clear distinction between the younger and older age groups (Figs. 3.6 and 3.7). Therefore, we conclude that volcanics of both age groups result from the same geological processes. The geochemistry is in line with a setting above a subduction zone, and the similarity of the geochemistry between the two age groups leads us to suggest that Crimea provides a record for a long-lived (~30 Myr), relatively stable volcanic arc. This places Crimea in this time period in an overriding plate of a subduction zone that lies to the south of Crimea, because there is no evidence for a suture north of the peninsula.

The middle Jurassic ages for the Crimean volcanics in the Bodrak area are in agreement with proposed ages from earlier studies (Spiridonov et al., 1990a, 1990b). The latest Jurassic to earliest Cretaceous ages (151-142 Ma) from the Karadag volcanics, however, conflict with ages obtained from biostratigraphic dating. Further, no remnants of volcanics or ashes have been found intercalating with time-equivalent, uppermost Jurassic platform carbonates.

Muratov (1960) and Voznesensky et al. (1998) reported that the lower part of the volcanic sequence yields Bajocian (~176.6-167.7 Ma) fauna, and that the Karadag volcanic complex is overlain by Bathonian to lower Callovian clays (167.7-161.2 Ma) (Ogg, 2004). Alternatively, if the stratigraphy were properly dated, the contact between the overlying Jurassic rocks and the Karadag volcanic complex must be a thrust. This is possible given the tectonized nature of the Karadag complex: the sequence is heavily folded and faulted (Fig. 3.3b and c) (Voznesensky et al., 1998). The upper Jurassic platform carbonates are much less deformed than the Karadag volcanic complex. Possibly, the deformation of the Karadag complex is related to its location of

Karadag at the Black Sea coast. Eocene and younger compression and inversion of the Black Sea margins could have affected the coastal outcrops.

The fact that no remnants of latest Jurassic to earliest Cretaceous volcanism can be traced in the upper Jurassic platform carbonates may have three possible explanations: This could imply that either a) the upper Jurassic carbonates or b) the Karadag volcanic complex have an allochthonous origin or that c) the volcanics erupted in intra-Berriasian times, the Berriasian on Crimea being marked by an unconformity.

The first of these possibilities, an allochthonous origin of the carbonate platform – emplaced during the Berriasian – has been proposed by Milejev et al. (1996). This however, seems very unlikely, because it would imply that exactly the time-interval that is covered by the carbonate platform is missing in the entire Crimean stratigraphy, except for the Kimmeridgian conglomerates (see Geology of Crimea section). Furthermore, Milejev et al. (1996) propose a displacement of the carbonate platform of only 15-20 km, which would still not explain the absence of volcanics in the carbonate platform. If the carbonate platform would have been transported further than the distance proposed by Milejev et al. (1996), the most likely origin of an allochthonous carbonate platform would be from the Turkish Pontides. In the Turkish Pontides however, the carbonate platform covers also the Callovian interval (Altiner et al., 1991; Rojay and Altiner, 1998), in contrast to Crimea. It would therefore be unlikely that the entire carbonate platform, except for the Callovian part, would have been transported from the Pontides.

The second possibility is an allochthonous origin of the Karadag aged volcanic complex, but this only transfers the problem of the presence of uppermost Jurassic to lowermost Cretaceous volcanics to other areas, because in the Greater Caucasus and the Pontides there are also no remnants of volcanism present in carbonates of this age.

The third option, the eruption of the volcanics in the middle Berriasian, instead of the latest Jurassic-earliest Cretaceous, is in agreement with our obtained ages (Fig. 3.5). This time interval is marked by uplift and erosion on Crimea, followed by conglomerate deposition in the late Berriasian. Volcanic activity would then occur during emersion and erosion of the carbonate platform. The third option is the most likely mechanism to reconcile the ages of the volcanics with the regional biostratigraphic constraints. After the cessation of volcanism in the Berriasian, Crimea was covered with rift-related sediments. The rift sediments are likely associated with the opening of the Black Sea basins, as a result of back-arc spreading. Crimea was thus in an overriding plate position in the Jurassic (as earlier proposed by Zonenshain and Le Pichon (1986)), and remained so after the arrest of arc volcanism, during the early Cretaceous and younger development of the Black Sea.

4.2 Implications for the Jurassic circum-Black Sea paleosubduction zone configuration

The $^{40}\text{Ar}/^{39}\text{Ar}$ isotopic dating of Crimean volcanics reveals an age range of ~172-

142 Ma and our geochemical analyses suggest that volcanism is subduction-related. Therefore, we conclude that long-lived (~30 Myrs) Jurassic to earliest Cretaceous subduction took place below Crimea (Fig. 3.8a). These results indicate that the distance between Crimea and the subduction zone was more or less constant, as there is no major change from tholeiitic basalts to more evolved andesitic-rhyolites.

The presence of a volcanic arc places Crimea on the overriding plate of a subduction zone. Given the fact that Crimea overlies Scythian basement of the East European Platform (Stephenson et al., 2004; Saintot et al., 2007), subduction must have been directed northward (Fig. 3.8a). This contradicts reconstructions of Stampfli and Borel (2002) who prefer a southward Jurassic subduction zone between Crimea and the Pontides, with a polarity of subduction below the Pontides. For the southward subduction of the Küre ocean below the Pontides, as envisaged by Moix et al. (2008), we can now conclude that it must have been closed by 170 Ma, for since that time we can demonstrate northward subduction.

Northward subduction below Crimea from middle Jurassic to early Cretaceous times thus implies the presence of a northward directed subduction zone south of Crimea. There are two possible options for the location of an approximately east-west trending trench: 1) between Crimea, and the İstanbul and Sakarya zones and 2) south of the Pontides. Because the eastern Pontides also have a volcanic arc record in the middle Jurassic (Şen, 2007), the trench should be positioned south of the eastern Pontides, as well as south of the Greater Caucasus and Lesser Caucasus, because of the subduction-related middle Jurassic volcanics in those areas.

One possible configuration is the presence of a subduction zone between the Sakarya terrane and Crimea (Fig. 3.1), which would be supported by the lack of evidence for metamorphism and strong deformation of the western Pontides. However, because the eastern Pontides were positioned in an overriding plate position, this configuration would require a transform fault between the western and eastern Pontides, which seems to be precluded by the apparent continuity of the basement terranes from the western to the eastern Pontides.

It thus seems most likely that the Pontides as a whole were positioned in an overriding plate position in the Jurassic. An important implication of this inference, however, is that the volcanic arc in the western and central Pontide segment is located ~500 km to the north of the subduction zone, when correcting for ~100-150 km of extension related to the opening of the Black Sea (Cloetingh et al., 2003; Starostenko et al., 2004; Shillington et al., 2008). Comparable estimates would be reached for the Transcaucasus and Caucasus segment. Although this distance is large, given general trench-arc distances on the order of 100-200 km, it is not exceptional. Arc-trench distances of 400 km (e.g. South American Andes) or even 600 km (Aleutian trench) (Gutscher et al., 2000) are generally attributed to flat-slab subduction (Brocher et al., 1994; Gutscher et al., 2000; van Hunen et al., 2002).

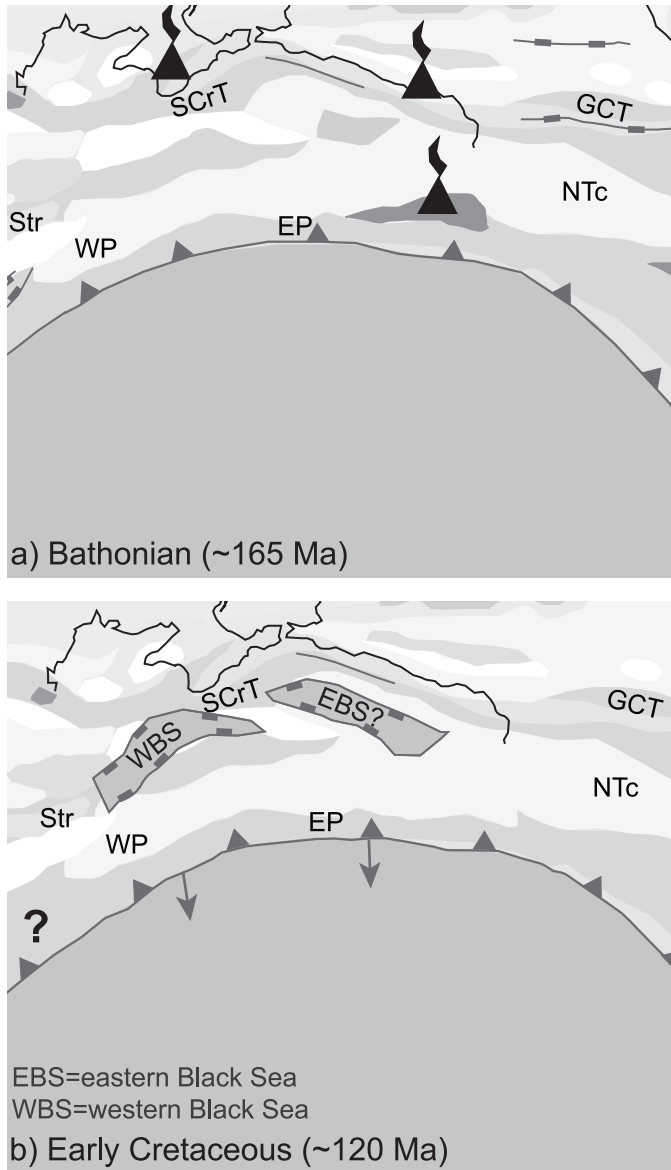


Figure 3.8 Proposed paleo-subduction zone configuration for the circum-Black Sea region in a) the middle Jurassic (~165 Ma) and b) the early Cretaceous (~120 Ma). Abbreviations as for Figure 3.2. See Appendix 15

A fairly continuous trench south of the Pontides to at least as far east as the Caucasus region thus seems the most likely configuration in the middle Jurassic to early Cretaceous (Fig. 3.8a). In early Cretaceous times, this subduction zone likely started to retreat, with the Black Sea basin opening as back-arc basin (Fig. 3.8b).

5. Conclusions

This study shows that the sampled Crimean volcanics - previously assumed to be middle Jurassic in age - have $^{40}\text{Ar}/^{39}\text{Ar}$ ages between 172 Ma and 142 Ma (~middle Jurassic to earliest Cretaceous, i.e. ~Bajocian to Berriasian) (Fig. 3.8a). Our new geo-

chemical data suggest that these volcanics were formed in a subduction setting on the overriding plate, indicating a period of long-lived northward subduction (~ 30 Myr) below the Eurasian margin. The trench-arc distance through time appears more or less constant, as there is no significant change from tholeiitic basalts to more evolved andesitic-rhyolites. After the period characterized by arc-volcanism, the area is subject to (back-arc) rifting, with the opening the Black Sea basins (Fig. 3.8b). We propose that the subduction trench was located south of the Turkish Sakarya Zone and the Caucasus, as suggested by middle Jurassic arc-volcanics in those regions, placing them in the overriding plate. This would require flat-slab subduction, because the distance from Crimea to the trench, prior to Black Sea opening, is estimated at ~ 500 km.

The area north, south and east of the present-day Black Sea (represented by the Sakarya Zone, Crimea and the Caucasus terranes) shows a history of middle Jurassic to earliest Cretaceous arc-volcanism, followed by a period of rifting

6. Acknowledgements

The geochemistry data are part of the MSc thesis of BV, the research was carried out at VU University Amsterdam. We would like to thank Françoise Chalot-Prat for her help with inspection of the thin sections. Roel van Elzas is thanked for his help in the mineral-separation lab. The authors would like to thank a number of people for their help in the field and for discussion: Vladimir Bakhmutov, Sergei Bolotov, Tommy McCann, Françoise Chalot-Prat, Martijn Deenen, Wout Krijgsman, Yann Rolland, Oleg Rusakov and Stephen Vincent. DJJvH acknowledges StatoilHydro for financial support (SPlates Model project). MJMM acknowledges the Netherlands Research Centre for Integrated Solid Earth Sciences (ISES) and the Netherlands Organization for Scientific Research (NWO) for financial support. The sampling campaigns in 2002 and 2004 were partly funded by the Middle East Basins Evolution (MEBE) program.

Supplementary data

Table with all individual incremental heating steps for all samples used for $^{40}\text{Ar}/^{39}\text{Ar}$ dating. Missing steps were not interpreted, because the amount of released argon was too high, leading to peak suppression. $^{40}\text{Ar}_r$: radiogenic amount of ^{40}Ar released in incremental heating step; $^{39}\text{Ar}_k$ (%): percentage of $^{39}\text{Ar}_k$ released in incremental heating step; 1s: 1σ ; 2s: 2σ . Third column indicates the steps that are used for age calculation.

Supplementary data

Incremental Heating	Watt	$^{40}\text{Ar}/^{39}\text{Ar}$	1σ	$^{37}\text{Ar}/^{39}\text{Ar}$	1s	$^{36}\text{Ar}/^{39}\text{Ar}$	1σ	Age (Ma)	$\pm 2\sigma$	$^{40}\text{Ar}(r)$ (%)	$^{39}\text{Ar}(k)$ (%)	K/Ca $\pm 2\sigma$
VU65												
FET4G (plagioclase) (J = 0.0075000 ± 0.0000225)												
07MX363A	0.50 W	9.08264	0.35622	-6.01089	0.91456	-0.14715	0.01263	0.00 ± 0.00	0.00 ± 0.00	0.00	0.00	0.000 ± 0.000
07MX363B	1.00 W	-59.64192	10.45852	-4.73224	0.90565	-0.11349	0.02077	0.00 ± 0.00	0.00 ± 0.00	44.40	0.00	0.000 ± 0.000
07MX363E	1.90 W	-69.69275	9.28513	-0.24599	0.03290	-0.18994	0.02674	0.00 ± 0.00	0.00 ± 0.00	19.49	0.00	0.000 ± 0.000
07MX363F	2.20 W	-50.25462	3.67285	-0.24361	0.01706	-0.24226	0.01763	0.00 ± 0.00	0.00 ± 0.00	0.00	0.00	0.000 ± 0.000
07MX363G	2.50 W	-75.01205	3.93039	-0.37390	0.01927	-0.38068	0.02090	0.00 ± 0.00	0.00 ± 0.00	0.00	0.00	0.000 ± 0.000
07MX363H	2.80 W	-100.13552	5.50035	-0.47199	0.02507	-0.42840	0.02402	0.00 ± 0.00	0.00 ± 0.00	0.00	0.00	0.000 ± 0.000
07MX363M	4.50 W	-2822.54257	656.62164	-50.78928	11.82279	-11.75207	2.74203	0.00 ± 0.00	0.00 ± 0.00	0.00	0.00	0.000 ± 0.000
07MX363N	4.90 W	-549.63206	48.65185	-10.95603	0.97400	-2.65483	0.24597	0.00 ± 0.00	0.00 ± 0.00	0.00	0.00	0.000 ± 0.000
07MX363O	5.30 W	-223.14242	12.95399	-3.52168	0.20579	-1.19838	0.08331	0.00 ± 0.00	0.00 ± 0.00	0.00	0.00	0.000 ± 0.000
07MX363P	5.80 W	-448.80294	36.44174	-5.05899	0.41229	-2.02316	0.17450	0.00 ± 0.00	0.00 ± 0.00	0.00	0.00	0.000 ± 0.000
07MX363Q	6.60 W	-289.46194	14.29323	-2.84163	0.14217	-1.42177	0.08662	0.00 ± 0.00	0.00 ± 0.00	0.00	0.00	0.000 ± 0.000
07MX363S	9.00 W	-1193.06316	144.99494	-7.63230	0.93056	-4.92189	0.60942	0.00 ± 0.00	0.00 ± 0.00	0.00	0.00	0.000 ± 0.000
07MX363U	3.50 W	-417.15589	33.43650	-0.36017	0.01883	-1.13813	0.06569	0.00 ± 0.00	0.00 ± 0.00	19.39	0.00	0.000 ± 0.000
KA28b (plagioclase) (J = 0.0075000 ± 0.0000225)												
07MX364A	0.50 W	9060.19932	1194.12078	80.81506	11.97605	30.28673	4.00870	1191.89 ± 1652.07	1.29	0.29	0.005 ± 0.002	
07MX364B	1.00 W	2538.37445	861.85963	102.40491	35.07349	8.34625	2.83518	906.45 ± 788.04	3.16	6.38	0.004 ± 0.003	
07MX364G	2.50 W	45.42710	0.74775	43.11671	2.06251	0.12826	0.00277	147.86 ± 19.39	24.14	28.57	0.010 ± 0.001	
07MX364H	2.80 W	47.71630	1.01972	38.32878	1.90399	0.13615	0.00322	141.87 ± 19.86	22.09	24.46	0.011 ± 0.001	
07MX364M	4.50 W	22.09895	0.13301	26.15782	1.23839	0.04236	0.00100	155.10 ± 8.08	52.79	8.13	0.016 ± 0.002	
07MX364N	4.90 W	21.05825	0.13266	26.61765	1.26163	0.04069	0.00075	148.61 ± 6.58	52.97	8.16	0.016 ± 0.002	
07MX364O	5.30 W	21.15396	0.16556	25.89902	1.25321	0.03702	0.00162	162.86 ± 12.52	58.05	4.03	0.016 ± 0.002	
07MX364P	5.80 W	22.82480	0.19746	30.21127	1.46747	0.04286	0.00247	166.99 ± 18.87	55.06	3.60	0.014 ± 0.001	
07MX364Q	6.60 W	21.18432	0.21632	32.54211	1.60172	0.04437	0.00112	142.93 ± 9.25	50.35	4.40	0.013 ± 0.001	
07MX364R	7.60 W	23.95576	0.14726	31.01997	1.51875	0.07327	0.00413	65.36 ± 32.87	19.94	3.14	0.014 ± 0.001	
07MX364S	9.00 W	20.58141	0.23984	30.11271	1.70367	0.05387	0.00773	95.75 ± 60.28	34.32	0.79	0.014 ± 0.002	
07MX364U	3.50 W	23.81901	0.19433	39.05795	1.92178	0.07784	0.00416	54.26 ± 33.58	16.51	8.06	0.011 ± 0.001	

CUKR3 (plagioclase) (J = 0.0075580 ± 0.0000378)													
07MX365A	0.50 W	4	1667.14852	134.46059	8.22280	3.06419	5.59043	0.45774	205.00 ± 575.45	0.95	0.04	0.052 ± 0.039	
07MX365B	1.00 W	4	100.53199	0.45409	2.36528	0.11258	0.29305	0.00370	183.25 ± 26.63	14.05	8.18	0.181 ± 0.017	
07MX365C	1.30 W	4	50.07093	0.27147	2.00591	0.09154	0.12127	0.00168	186.55 ± 12.28	28.75	15.19	0.214 ± 0.020	
07MX365D	1.60 W	4	40.28764	0.26806	2.85286	0.13088	0.09010	0.00132	180.41 ± 9.66	34.47	19.13	0.150 ± 0.014	
07MX365E	1.90 W	4	43.05264	0.22252	4.45187	0.20298	0.10270	0.00138	170.32 ± 10.34	30.33	15.59	0.096 ± 0.009	
07MX365F	2.20 W	4	40.17337	0.25650	7.88740	0.36377	0.09451	0.00139	168.39 ± 10.41	32.04	9.20	0.054 ± 0.005	
07MX365G	2.50 W	4	44.46881	0.16032	7.36177	0.33867	0.11155	0.00155	158.53 ± 11.42	27.19	7.19	0.058 ± 0.005	
07MX365H	2.80 W	4	37.16573	0.13860	5.20516	0.24301	0.08619	0.00115	158.56 ± 8.37	32.59	5.56	0.082 ± 0.008	
07MX365I	3.10 W	4	32.85045	0.15720	5.13196	0.24248	0.08615	0.00097	171.16 ± 7.13	39.94	4.28	0.083 ± 0.008	
07MX365J	3.40 W	4	44.80319	0.20620	11.35770	0.53723	0.10967	0.00190	174.11 ± 13.92	29.68	2.24	0.038 ± 0.004	
07MX365K	3.70 W	4	36.49235	0.14891	7.53308	0.35762	0.08651	0.00151	151.47 ± 11.05	31.59	2.81	0.057 ± 0.005	
07MX365L	4.10 W	4	36.14515	0.13645	6.40556	0.32369	0.08300	0.00154	158.89 ± 11.28	33.55	1.59	0.067 ± 0.007	
07MX365M	4.50 W	4	35.99165	0.13425	6.21608	0.31144	0.07831	0.00117	174.09 ± 8.46	37.08	1.67	0.069 ± 0.007	
07MX365N	4.90 W	4	39.76774	0.20224	6.78030	0.35546	0.09413	0.00232	163.50 ± 16.87	31.41	0.95	0.063 ± 0.007	
07MX365O	5.30 W	4	32.51388	0.14487	5.19991	0.28762	0.06634	0.00147	173.68 ± 10.68	40.97	1.13	0.082 ± 0.009	
07MX365Q	6.60 W	4	37.12304	0.17748	6.28981	0.37001	0.07627	0.00194	195.62 ± 13.99	40.64	0.90	0.068 ± 0.008	
07MX365R	7.60 W	4	38.01595	0.17300	6.80926	0.36967	0.08569	0.00247	172.79 ± 18.03	34.82	0.72	0.063 ± 0.007	
07MX365S	9.00 W	4	42.20455	0.32386	3.79494	0.82332	0.09467	0.00668	188.45 ± 48.49	34.43	0.20	0.113 ± 0.049	
07MX365T	2.50 W	4	44.75760	0.17373	7.62911	0.37278	0.10549	0.00151	184.78 ± 10.73	31.71	3.09	0.056 ± 0.005	
07MX365U	3.50 W	4	70.36362	0.56259	8.03543	0.56777	0.19817	0.00479	163.05 ± 33.71	17.69	0.35	0.053 ± 0.008	
LBOD16 (plagioclase) (J = 0.0075630 ± 0.0000378)													
07MX366A	0.50 W		-59576.12476	54196.60635	-647.08761	589.78057	-198.45107	180.54936	0.00 ± 0.00	1.65	0.00	0.000 ± 0.000	
07MX366B	1.00 W		38117.74189	17668.33797	2085.64220	971.24824	127.81990	59.26657	0.00 ± 0.00	1.35	0.00	0.000 ± 0.000	
07MX366C	1.30 W		1920.95931	86.11813	269.43786	17.09861	6.56248	0.30455	53.70 ± 765.12	0.17	1.64	0.001 ± 0.000	
07MX366D	1.60 W		1024.01573	30.06767	197.84419	10.62988	3.51582	0.11251	13.81 ± 423.69	0.09	4.25	0.002 ± 0.000	
07MX366E	1.90 W		353.87228	2.58266	131.64137	6.02708	1.22551	0.01795	33.26 ± 138.02	0.63	6.89	0.003 ± 0.000	
07MX366F	2.20 W		281.24244	1.85162	123.67796	5.68052	0.96343	0.01368	93.36 ± 102.64	2.28	7.73	0.003 ± 0.000	
07MX366G	2.50 W		202.94199	1.59287	120.18356	5.56271	0.69781	0.01010	91.87 ± 72.59	3.12	6.07	0.003 ± 0.000	
07MX366H	2.80 W		193.05984	1.39771	117.55789	5.44968	0.68047	0.01039	20.07 ± 81.11	0.70	5.74	0.003 ± 0.000	
07MX366I	3.10 W		160.17840	0.83772	106.32013	4.92267	0.54980	0.00802	89.06 ± 64.09	3.87	6.42	0.004 ± 0.000	
07MX366J	3.40 W		140.46673	1.03368	116.67559	5.45408	0.47506	0.00732	134.42 ± 55.25	6.69	3.67	0.003 ± 0.000	
07MX366K	3.70 W		114.08679	0.70591	103.32641	4.84260	0.37917	0.00580	145.23 ± 44.42	9.01	3.75	0.004 ± 0.000	

07MX366L	4.10 W	117.26754	0.77519	110.54515	5.19854	0.38897	0.00573	157.70 ± 43.19	9.50	4.22	0.004 ± 0.000
07MX366M	4.50 W	94.28522	0.48664	104.01440	4.90487	0.31726	0.00479	125.48 ± 38.33	9.37	4.59	0.004 ± 0.000
07MX366N	4.90 W	43.57238	0.24083	97.90603	4.64044	0.13291	0.00237	169.16 ± 20.40	27.79	3.27	0.004 ± 0.000
07MX366O	5.30 W	46.22139	0.20207	98.97421	4.69187	0.14548	0.00280	156.14 ± 23.94	24.07	2.96	0.004 ± 0.000
07MX366P	5.80 W	57.33392	0.25660	101.60690	4.85994	0.18372	0.00268	156.76 ± 22.97	19.45	3.76	0.004 ± 0.000
07MX366Q	6.60 W	37.58902	0.15255	94.88317	4.54630	0.11640	0.00210	150.78 ± 19.09	28.63	4.70	0.004 ± 0.000
07MX366R	7.60 W	29.67591	0.13710	96.95341	4.67246	0.08958	0.00176	153.40 ± 17.00	36.86	4.11	0.004 ± 0.000
07MX366S	9.00 W	29.70034	0.25789	97.04654	4.78421	0.08900	0.00344	156.13 ± 28.62	37.51	1.00	0.004 ± 0.000
07MX366T	2.50 W	27.45394	0.13957	104.94102	5.09326	0.08187	0.00120	163.63 ± 14.41	42.37	19.72	0.004 ± 0.000
07MX366U	3.50 W	25.69720	0.11943	104.98678	5.13412	0.07765	0.00178	156.82 ± 17.87	43.30	5.49	0.004 ± 0.000
04CRLEB (plagioclase) (J = 0.0075670 ± 0.0000378)											
07MX368G	2.50 W	43.25432	0.70798	18.79290	0.91202	0.09657	0.00215	211.42 ± 13.07	37.49	9.07	0.023 ± 0.002
07MX368H	2.80 W	47.43333	0.85532	20.32220	1.00305	0.10773	0.00267	223.96 ± 15.48	36.30	7.29	0.021 ± 0.002
07MX368I	3.10 W	49.59872	1.91159	25.33878	1.38813	0.11849	0.00413	217.16 ± 36.61	33.48	5.05	0.017 ± 0.002
07MX368J	3.40 W	35.18118	0.42043	16.90165	0.80812	0.07215	0.00136	198.64 ± 10.25	43.23	7.74	0.025 ± 0.002
07MX368K	3.70 W	31.99022	0.47270	17.25990	0.82778	0.06535	0.00136	184.45 ± 11.71	43.93	5.72	0.025 ± 0.002
07MX368L	4.10 W	32.20120	0.42493	15.37061	0.73308	0.06777	0.00127	176.03 ± 11.38	41.61	6.12	0.028 ± 0.003
07MX368M	4.50 W	26.21667	0.19819	13.50932	0.63865	0.04708	0.00070	175.59 ± 6.31	51.04	5.55	0.032 ± 0.003
07MX368N	4.90 W	26.80958	0.20351	13.99392	0.66295	0.05014	0.00076	172.22 ± 6.61	48.89	6.17	0.030 ± 0.003
07MX368O	5.30 W	24.00019	0.14082	13.27971	0.62982	0.04103	0.00063	169.94 ± 5.30	53.89	4.82	0.032 ± 0.003
07MX368P	5.80 W	23.70358	0.11948	12.97785	0.62006	0.04063	0.00064	167.39 ± 5.09	53.71	5.99	0.033 ± 0.003
07MX368Q	6.60 W	22.05559	0.14747	12.91668	0.62289	0.03509	0.00060	167.19 ± 5.14	57.66	7.57	0.033 ± 0.003
07MX368R	7.60 W	20.14988	0.11580	13.82812	0.66990	0.02677	0.00060	175.12 ± 5.03	66.21	1.85	0.031 ± 0.003
07MX368S	9.00 W	25.88324	0.11871	14.26695	0.69177	0.04770	0.00072	169.97 ± 5.55	49.94	2.81	0.030 ± 0.003
07MX368T	2.50 W	19.36004	0.10207	16.66837	0.80793	0.02595	0.00036	171.42 ± 3.76	67.25	20.91	0.025 ± 0.002
07MX368U	3.50 W	17.40000	0.07791	22.67915	1.10933	0.02111	0.00034	171.51 ± 3.62	74.55	3.35	0.019 ± 0.002
IKUCH7 (plagioclase) (J = 0.0075760 ± 0.0000379)											
07MX369A	0.50 W	816.78437	6.10770	5.99933	0.28927	2.64960	0.03802	418.35 ± 208.84	4.20	0.43	0.071 ± 0.007
07MX369B	1.00 W	317.02758	1.11786	6.19366	0.27821	0.99129	0.01233	309.48 ± 80.91	7.76	6.68	0.069 ± 0.006
07MX369C	1.30 W	57.80362	0.28307	5.90549	0.26607	0.14499	0.00194	200.19 ± 14.14	26.69	11.49	0.073 ± 0.007
07MX369D	1.60 W	21.13124	0.07857	5.78776	0.26160	0.03105	0.00044	162.80 ± 3.39	58.75	14.54	0.074 ± 0.007
07MX369E	1.90 W	21.87565	0.07836	5.59809	0.25453	0.03338	0.00043	163.30 ± 3.43	56.94	11.15	0.077 ± 0.007
07MX369F	2.20 W	19.56023	0.07432	0.07676	0.00076	0.02530	0.00034	158.08 ± 2.79	61.79	10.32	5.602 ± 0.111

07MX369G	2.50 W	4	14.78314	0.05855	5.27598	0.24230	0.01020	0.00018	159.90 ± 1.89	82.45	7.84	0.081 ± 0.007
07MX369H	2.80 W	4	24.99590	0.07618	0.06305	0.00066	0.04360	0.00059	158.45 ± 4.38	48.47	8.95	6.820 ± 0.143
07MX369I	3.10 W	4	15.26231	0.05758	0.06184	0.00067	0.01030	0.00025	159.76 ± 2.20	80.08	3.86	6.953 ± 0.151
07MX369J	3.40 W	4	17.85889	0.07137	5.45620	0.25370	0.02088	0.00040	159.10 ± 3.23	67.88	5.18	0.079 ± 0.007
07MX369K	3.70 W	4	15.86571	0.06381	5.43485	0.25402	0.01299	0.00038	163.33 ± 3.15	78.53	2.71	0.079 ± 0.007
07MX369L	4.10 W	4	18.42677	0.06111	5.14440	0.24181	0.02152	0.00041	163.52 ± 3.20	67.71	3.51	0.083 ± 0.008
07MX369M	4.50 W	4	15.94448	0.06665	5.77704	0.27492	0.01448	0.00049	159.17 ± 3.89	76.05	2.17	0.074 ± 0.007
07MX369N	4.90 W	4	15.57017	0.06174	6.42760	0.31120	0.01502	0.00062	153.16 ± 4.79	74.78	1.52	0.067 ± 0.006
07MX369O	5.30 W	4	15.83425	0.05986	7.10430	0.34457	0.01553	0.00062	155.35 ± 4.76	74.59	1.09	0.060 ± 0.006
07MX369P	5.80 W	4	18.47303	0.08462	6.49766	0.31378	0.02256	0.00051	161.74 ± 4.08	66.71	1.53	0.066 ± 0.006
07MX369Q	6.60 W	4	18.14429	0.07821	7.40326	0.35685	0.02101	0.00044	164.35 ± 3.62	69.03	1.79	0.058 ± 0.006
07MX369R	7.60 W	4	17.50069	0.08943	9.62878	0.47729	0.02188	0.00108	155.48 ± 8.20	67.43	0.55	0.044 ± 0.004
07MX369S	9.00 W	4	15.52418	0.08223	10.30155	0.53096	0.01431	0.00104	159.53 ± 7.93	78.04	0.56	0.041 ± 0.004
07MX369T	2.50 W	4	20.25475	0.11129	20.98114	1.01956	0.03237	0.00047	163.79 ± 4.56	61.03	2.67	0.020 ± 0.002
07MX369U	3.50 W	4	20.26752	0.08074	19.84851	0.97686	0.03367	0.00054	157.80 ± 4.59	58.71	1.47	0.021 ± 0.002

04KAR1 (plagioclase) (J = 0.007580 ± 0.0000379)

07MX370C	1.30 W		254.27861	17.02662	37.55667	3.12606	1.04718	0.08091	0.00 ± 0.00	0.00	4.55	0.011 ± 0.002
07MX370D	1.60 W		76.71812	2.58987	48.91956	2.66074	0.37779	0.02665	0.00 ± 0.00	0.00	7.60	0.008 ± 0.001
07MX370E	1.90 W		41.72352	1.13653	54.71001	2.78941	0.12968	0.00357	107.18 ± 23.12	18.61	9.45	0.008 ± 0.001
07MX370G	2.50 W		17.47510	1.49789	76.73996	3.57198	0.08982	0.00587	0.00 ± 0.00	0.00	7.39	0.005 ± 0.000
07MX370H	2.80 W	4	21.71093	0.11094	61.93309	2.85504	0.05499	0.00089	142.87 ± 9.11	47.91	8.07	0.007 ± 0.001
07MX370I	3.10 W	4	18.61324	0.07300	51.68555	2.38758	0.04226	0.00063	139.81 ± 7.01	55.05	9.00	0.008 ± 0.001
07MX370J	3.40 W	4	19.30220	0.11243	61.98053	2.87849	0.04772	0.00099	139.45 ± 9.88	52.55	5.85	0.007 ± 0.001
07MX370K	3.70 W	4	20.06113	0.21464	61.89788	2.89721	0.04895	0.00087	144.59 ± 10.09	52.50	5.49	0.007 ± 0.001
07MX370L	4.10 W	4	16.98059	0.10157	59.30051	2.78114	0.03672	0.00091	148.62 ± 9.28	63.95	5.10	0.007 ± 0.001
07MX370M	4.50 W	4	16.06631	0.06818	45.62372	2.14519	0.03102	0.00058	143.03 ± 6.43	65.59	6.58	0.009 ± 0.001
07MX370N	4.90 W	4	15.18758	0.08948	53.54222	2.53579	0.03008	0.00110	144.24 ± 10.21	69.59	4.31	0.008 ± 0.001
07MX370O	5.30 W	4	14.13538	0.05974	53.25902	2.52473	0.02695	0.00090	142.24 ± 8.83	73.71	3.01	0.008 ± 0.001
07MX370P	5.80 W	4	14.11154	0.05771	55.45911	2.64709	0.02786	0.00128	140.90 ± 11.42	73.00	3.06	0.007 ± 0.001
07MX370Q	6.60 W	4	14.93955	0.07518	61.49762	2.95238	0.03685	0.00121	123.65 ± 11.46	59.95	2.61	0.007 ± 0.001
07MX370R	7.60 W		14.56344	0.10459	63.66854	3.12702	0.02972	0.00461	149.10 ± 36.53	74.57	0.65	0.006 ± 0.001
07MX370S	9.00 W		13.76223	0.08885	62.57492	3.09376	0.02741	0.00224	146.24 ± 18.70	77.40	0.88	0.007 ± 0.001
07MX370T	2.50 W	4	14.45595	0.06268	66.29234	3.21452	0.03118	0.00067	144.99 ± 8.63	72.83	12.28	0.006 ± 0.001

07MX370U	3.50 W	4	13.91276	0.05409	68.91918	3.37423	0.02927	0.00065	148.32 ± 8.82	77.34	4.13	0.006 ± 0.001
KAR501 (plagioclase) (J = 0.0075840 ± 0.0000379)												
07MX371A	0.50 W		134.56295	2.51551	1.72475	0.78447	0.38158	0.01437	278.02 ± 87.62	16.31	0.13	0.249 ± 0.227
07MX371B	1.00 W		21.40369	0.07366	1.42529	0.06701	0.02611	0.00043	179.73 ± 3.36	64.47	9.94	0.301 ± 0.028
07MX371C	1.30 W		14.37929	0.04460	2.73888	0.12372	0.00637	0.00016	166.39 ± 1.55	88.43	16.48	0.157 ± 0.014
07MX371D	1.60 W		12.95447	0.04017	3.73304	0.16902	0.00405	0.00014	158.20 ± 1.44	93.04	14.53	0.115 ± 0.010
07MX371E	1.90 W	4	12.52561	0.04375	5.01810	0.22882	0.00706	0.00026	142.97 ± 2.20	86.51	11.18	0.085 ± 0.008
07MX371F	2.20 W	4	12.15449	0.03892	5.37139	0.24635	0.00543	0.00020	144.79 ± 1.79	90.31	10.84	0.080 ± 0.007
07MX371G	2.50 W	4	11.32432	0.04489	6.32301	0.29582	0.00631	0.00067	131.96 ± 5.22	87.97	4.23	0.068 ± 0.006
07MX371H	2.80 W	4	12.23601	0.04300	6.19442	0.28701	0.00818	0.00055	136.41 ± 4.26	84.27	4.19	0.069 ± 0.006
07MX371I	3.10 W	4	10.82246	0.04313	6.54149	0.31621	0.00081	0.00085	142.92 ± 1.10	99.98	2.24	0.065 ± 0.006
07MX371J	3.40 W		10.91570	0.04340	6.26788	0.30859	0.00681	0.00105	124.77 ± 8.01	86.12	2.18	0.068 ± 0.007
07MX371K	3.70 W		11.00937	0.04428	6.65702	0.32343	0.00765	0.00075	123.23 ± 5.79	84.28	1.77	0.064 ± 0.006
07MX371L	4.10 W		10.63465	0.04500	6.53554	0.32142	0.00004	0.00091	140.53 ± 1.15	99.98	1.84	0.065 ± 0.006
07MX371M	4.50 W		10.65618	0.06190	7.46576	0.37150	0.00070	0.00108	140.89 ± 1.58	99.98	1.16	0.057 ± 0.006
07MX371N	4.90 W		11.87146	0.06062	8.60349	0.42709	0.00909	0.00114	131.00 ± 8.76	83.15	1.16	0.050 ± 0.005
07MX371O	5.30 W		10.49839	0.05438	9.00737	0.50270	0.00377	0.00150	133.97 ± 11.46	96.21	0.90	0.047 ± 0.005
07MX371P	5.80 W		10.68519	0.04572	8.95226	0.47382	0.00565	0.00075	129.19 ± 5.86	91.04	1.09	0.048 ± 0.005
07MX371Q	6.60 W		10.68993	0.05843	8.18640	0.41367	0.00737	0.00127	121.89 ± 9.77	85.72	1.15	0.052 ± 0.005
07MX371R	7.60 W		11.71104	0.11130	8.19219	0.57579	0.00623	0.00434	139.26 ± 32.80	89.84	0.29	0.052 ± 0.007
07MX371S	9.00 W		11.54631	0.05135	8.71744	0.51784	0.00403	0.00169	146.05 ± 12.79	95.71	0.58	0.049 ± 0.006
07MX371T	2.50 W	4	11.41742	0.03648	9.52510	0.46420	0.00491	0.00016	141.98 ± 1.77	93.93	10.47	0.045 ± 0.004
07MX371U	3.50 W		12.51859	0.04311	10.88295	0.53687	0.00707	0.00041	149.37 ± 3.42	90.23	3.64	0.039 ± 0.004
KA28b (ground mass) (J = 0.0075880 ± 0.0000379)												
07MX373B	1.00 W		1853.10875	13.84198	2.09687	0.17279	6.11077	0.08667	556.41 ± 438.68	2.57	0.24	0.205 ± 0.034
07MX373C	1.30 W		510.92439	1.72479	0.85915	0.04707	1.64027	0.02039	328.34 ± 132.57	5.15	1.14	0.500 ± 0.055
07MX373D	1.60 W		167.54986	0.54016	1.08077	0.05260	0.51588	0.00642	196.98 ± 45.09	9.07	2.04	0.398 ± 0.039
07MX373E	1.90 W		61.45342	0.19139	1.06317	0.04909	0.16545	0.00206	165.42 ± 14.81	20.58	5.34	0.404 ± 0.037
07MX373F	2.20 W		34.39160	0.10617	1.33389	0.06117	0.07110	0.00089	175.94 ± 6.39	39.22	5.43	0.322 ± 0.030
07MX373G	2.50 W		31.99422	0.09839	1.59152	0.07344	0.06456	0.00081	170.42 ± 5.88	40.76	6.82	0.270 ± 0.025
07MX373H	2.80 W		32.40284	0.09853	1.91331	0.08822	0.06532	0.00083	173.09 ± 6.04	40.90	6.13	0.224 ± 0.021
07MX373I	3.10 W		33.37392	0.10103	2.33098	0.10789	0.06859	0.00086	173.58 ± 6.21	39.82	5.88	0.184 ± 0.017
07MX373J	3.40 W		33.34039	0.10286	2.72889	0.12701	0.06962	0.00086	169.83 ± 6.25	38.94	4.37	0.157 ± 0.015

07MX373K	3.70 W	31.78275	0.09946	2.70381	0.12608	0.06655	0.00083	161.66 ± 6.05	38.80	4.76	0.159 ± 0.015
07MX373L	4.10 W	31.73102	0.09652	2.99022	0.14042	0.06621	0.00082	162.57 ± 5.98	39.08	4.53	0.144 ± 0.013
07MX373M	4.50 W	27.60254	0.08521	2.94183	0.13883	0.05360	0.00067	157.50 ± 4.92	43.47	4.52	0.146 ± 0.014
07MX373N	4.90 W	25.83957	0.07837	2.87712	0.13608	0.04863	0.00062	153.70 ± 4.61	45.27	4.38	0.149 ± 0.014
07MX373O	5.30 W	25.53026	0.07828	2.93721	0.13935	0.04744	0.00059	154.29 ± 4.37	46.00	3.86	0.146 ± 0.014
07MX373P	5.80 W	22.96393	0.07132	2.83243	0.13566	0.03934	0.00050	152.01 ± 3.76	50.35	3.74	0.152 ± 0.015
07MX373Q	6.60 W	22.72070	0.06942	2.80223	0.13470	0.03845	0.00049	152.24 ± 3.69	50.97	4.78	0.153 ± 0.015
07MX373R	7.60 W	20.58894	0.06744	3.06508	0.15102	0.03236	0.00049	148.33 ± 3.72	54.73	1.03	0.140 ± 0.014
07MX373S	9.00 W	20.04578	0.06229	2.51063	0.12229	0.02987	0.00040	150.16 ± 3.03	56.96	2.12	0.171 ± 0.017
07MX373T	2.50 W	19.02808	0.05814	3.24394	0.15729	0.02713	0.00034	148.34 ± 2.60	59.22	27.01	0.132 ± 0.013
07MX373U	3.50 W	19.26320	0.06042	3.56596	0.17644	0.02973	0.00044	141.93 ± 3.37	55.86	1.88	0.120 ± 0.012
KA28b (ground mass) (J = 0.0075930 ± 0.0000380)											
07MX374B	1.00 W	490.73954	1.73536	0.55584	0.04011	1.56345	0.01958	356.71 ± 125.14	5.87	0.93	0.773 ± 0.112
07MX374C	1.30 W	120.48000	0.39265	0.54198	0.02662	0.35257	0.00440	211.03 ± 30.64	13.56	1.99	0.793 ± 0.078
07MX374D	1.60 W	55.80710	0.17375	0.56164	0.02596	0.14150	0.00176	182.79 ± 12.56	25.15	4.46	0.765 ± 0.071
07MX374E	1.90 W	26.18652	0.08362	0.68773	0.03166	0.04555	0.00058	167.15 ± 4.30	48.80	5.32	0.625 ± 0.058
07MX374F	2.20 W	22.45560	0.06856	0.82318	0.03780	0.03070	0.00039	175.49 ± 2.97	59.88	7.25	0.522 ± 0.048
07MX374G	2.50 W	24.18330	0.07403	0.97314	0.04484	0.03740	0.00047	172.54 ± 3.52	54.62	7.83	0.442 ± 0.041
07MX374H	2.80 W	21.58644	0.06667	1.19019	0.05477	0.02837	0.00036	173.67 ± 2.75	61.60	6.50	0.361 ± 0.033
07MX374J	3.40 W	19.62394	0.06163	1.61891	0.07517	0.02491	0.00032	162.38 ± 2.49	63.13	5.16	0.265 ± 0.025
07MX374K	3.70 W	20.28906	0.06204	1.68057	0.07853	0.02780	0.00035	160.10 ± 2.69	60.17	4.73	0.256 ± 0.024
07MX374L	4.10 W	18.92192	0.05761	1.75446	0.08210	0.02366	0.00031	158.35 ± 2.40	63.77	5.21	0.245 ± 0.023
07MX374M	4.50 W	17.74462	0.05397	1.81640	0.08530	0.02131	0.00028	152.35 ± 2.21	65.32	4.64	0.236 ± 0.022
07MX374N	4.90 W	17.55392	0.05353	1.83176	0.08651	0.02163	0.00028	148.79 ± 2.22	64.42	4.04	0.234 ± 0.022
07MX374O	5.30 W	17.69332	0.05459	1.73322	0.08221	0.02193	0.00028	149.31 ± 2.23	64.15	4.04	0.248 ± 0.024
07MX374P	5.80 W	16.84416	0.05160	1.64330	0.07852	0.01915	0.00025	148.84 ± 1.99	67.17	4.36	0.261 ± 0.025
07MX374Q	6.60 W	16.07186	0.04898	1.71038	0.08183	0.01690	0.00021	147.58 ± 1.78	69.77	4.47	0.251 ± 0.024
07MX374R	7.60 W	15.03354	0.05206	1.98708	0.09851	0.01434	0.00025	144.33 ± 2.08	72.86	0.91	0.216 ± 0.021
07MX374S	9.00 W	15.16667	0.04716	1.70437	0.08362	0.01432	0.00022	145.78 ± 1.85	72.99	1.71	0.252 ± 0.025
07MX374T	2.50 W	15.44996	0.04663	1.76080	0.08511	0.01515	0.00019	146.30 ± 1.63	71.92	25.06	0.244 ± 0.024
07MX374U	3.50 W	15.02815	0.04785	1.66923	0.08331	0.01586	0.00025	138.21 ± 2.04	69.69	1.40	0.257 ± 0.026
FET4G (ground mass) (J = 0.0076010 ± 0.0000380)											
07MX375C	1.30 W	13944.56876	340.74801	0.94118	0.30470	41.80811	1.13574	4640.66 ± 323.94	11.40	1.71	0.457 ± 0.296

07MX375E	1.90 W	1829.29692	7.90016	0.69505	0.05370	5.73722	0.07318	1267.58 ± 277.31	7.33	7.11	0.618 ± 0.096
07MX375F	2.20 W	825.69304	2.92445	0.55295	0.03435	2.57360	0.03218	726.74 ± 167.43	7.90	9.40	0.777 ± 0.097
07MX375G	2.50 W	665.97509	2.23689	0.95768	0.05977	2.11251	0.02632	498.08 ± 156.36	6.28	8.14	0.449 ± 0.056
07MX375H	2.80 W	612.09968	1.96892	1.17297	0.06101	1.93311	0.02396	489.32 ± 143.22	6.69	7.66	0.366 ± 0.038
07MX375I	3.10 W	930.74259	3.11228	1.45849	0.07543	2.92485	0.03628	739.27 ± 188.29	7.15	6.82	0.295 ± 0.030
07MX375J	3.40 W	792.83286	2.96001	1.58743	0.08484	2.53013	0.03169	534.36 ± 182.72	5.71	5.63	0.271 ± 0.029
07MX375K	3.70 W	810.90960	2.89659	1.73575	0.09366	2.62509	0.03280	429.61 ± 201.24	4.36	3.45	0.247 ± 0.027
07MX375L	4.10 W	776.05111	2.60303	1.93088	0.13489	2.47518	0.03083	529.19 ± 179.72	5.77	3.93	0.222 ± 0.031
07MX375M	4.50 W	800.13734	2.93237	1.36478	0.11959	2.58146	0.03213	452.01 ± 193.98	4.68	3.09	0.315 ± 0.055
07MX375N	4.90 W	778.45041	2.86124	1.30383	0.08659	2.52179	0.03138	408.09 ± 194.08	4.29	3.46	0.329 ± 0.044
07MX375O	5.30 W	790.80520	3.45770	1.37858	0.10472	2.55192	0.03240	445.55 ± 192.80	4.66	2.60	0.312 ± 0.047
07MX375Q	6.00 W	621.68987	2.21208	0.91550	0.11108	1.98875	0.02481	415.87 ± 153.23	5.48	3.30	0.469 ± 0.114
07MX375R	7.60 W	502.50487	2.12864	0.70950	0.16152	1.64777	0.02107	202.80 ± 144.16	3.11	0.65	0.606 ± 0.276
07MX375S	9.00 W	433.98006	1.46578	0.76049	0.06761	1.40332	0.01774	247.78 ± 120.88	4.46	1.77	0.565 ± 0.100
07MX375T	2.50 W	310.08889	0.97640	0.49786	0.02735	0.94724	0.01167	373.12 ± 74.48	9.74	23.63	0.863 ± 0.095
07MX375U	3.50 W	204.08787	0.67123	0.54439	0.03356	0.63350	0.00779	218.46 ± 54.06	8.29	7.67	0.790 ± 0.097

VU 52

KIZ41 (biotite) (J = 0.0046470 ± 0.0000139)

05MY313B	0.04 W	35.64991	0.75964	4.64331	1.90817	0.08227	0.01938	95.81 ± 91.13	32.82	1.72	0.092 ± 0.076
05MY313C	0.05 W	22.36096	0.20001	6.87311	0.93692	0.01233	0.00443	155.29 ± 20.45	86.10	5.47	0.062 ± 0.017
05MY313D	0.06 W	20.98581	0.95500	1.44316	7.28252	0.00058	0.03753	167.57 ± 170.49	99.71	0.49	0.298 ± 3.004
05MY313E	0.06 W	4	0.46697	8.54291	3.53852	0.00201	0.01908	168.45 ± 7.25	100.00	1.44	0.050 ± 0.041
05MY313F	0.09 W	4	0.09395	15.70742	0.82009	0.00884	0.00153	167.04 ± 7.18	93.71	15.35	0.027 ± 0.003
05MY313G	0.11 W	4	0.08590	17.60443	0.92881	0.00520	0.00138	169.89 ± 6.55	99.22	17.72	0.024 ± 0.003
05MY313H	0.13 W	4	0.08275	18.02204	0.92344	0.00543	0.00099	169.05 ± 4.83	99.06	24.08	0.024 ± 0.002
05MY313I	0.17 W	4	0.32766	16.33266	2.48042	0.00779	0.01829	130.73 ± 85.42	93.96	1.44	0.026 ± 0.008
05MY313J	0.25 W	4	0.11843	18.01350	1.03734	0.00820	0.00262	156.16 ± 12.27	94.97	8.18	0.024 ± 0.003
05MY313K	fsn	41.25782	0.10915	15.03944	0.77096	0.07786	0.00122	157.43 ± 5.67	47.08	24.10	0.028 ± 0.003

TRU6FL (ground mass) (J = 0.0046620 ± 0.0000140)

05MY027A	0.03 W	187.02836	4.14293	3.64307	0.72146	0.56904	0.02526	154.71 ± 100.55	10.24	0.06	0.118 ± 0.047
05MY027B	0.04 W	112.22882	0.38920	5.72192	0.23635	0.32099	0.00309	144.53 ± 13.38	15.88	1.04	0.075 ± 0.006
05MY027C	0.04 W	60.71936	0.87386	6.48612	0.70171	0.13964	0.01347	161.19 ± 60.98	32.87	0.09	0.066 ± 0.014
05MY027D	0.05 W	108.66407	0.37970	5.66878	0.25049	0.30731	0.00345	148.20 ± 15.10	16.84	0.57	0.076 ± 0.007

05MY027E	0.06 W	84.57166	0.23137	6.39298	0.25877	0.22202	0.00252	157.33 ± 11.23	23.01	1.13	0.067 ± 0.005
05MY027F	0.07 W	64.17476	0.18281	6.04593	0.24730	0.15261	0.00150	157.97 ± 6.66	30.46	1.73	0.071 ± 0.006
05MY027G	0.08 W	49.59893	0.12940	5.44689	0.22221	0.10088	0.00098	163.03 ± 4.42	40.75	2.41	0.079 ± 0.006
05MY027H	0.08 W	40.10783	0.09315	5.46677	0.22368	0.06872	0.00075	163.15 ± 3.42	50.43	2.47	0.078 ± 0.006
05MY027I	0.09 W	33.74830	0.08259	5.26444	0.21669	0.04558	0.00066	166.69 ± 3.06	61.31	3.04	0.081 ± 0.007
05MY027J	0.10 W	32.59442	0.08070	5.27971	0.21656	0.04245	0.00061	164.92 ± 2.85	62.77	3.56	0.081 ± 0.007
05MY027K	0.11 W	29.94021	0.07676	5.56920	0.23245	0.03367	0.00053	164.68 ± 2.53	68.22	4.38	0.077 ± 0.006
05MY027L	0.12 W	27.70210	0.06306	5.57782	0.23542	0.02574	0.00036	165.48 ± 1.82	74.11	5.15	0.077 ± 0.006
05MY027M	0.20 W	26.27543	0.06530	5.43400	0.23854	0.01996	0.00072	167.57 ± 3.38	79.17	1.55	0.079 ± 0.007
05MY027N	0.50 W	26.89867	0.05976	6.28588	0.26499	0.02308	0.00020	165.86 ± 1.19	76.46	43.91	0.068 ± 0.006
05MY027O	0.70 W	26.89444	0.05866	9.30570	0.39486	0.02893	0.00030	154.60 ± 1.57	70.91	14.50	0.046 ± 0.004
05MY027P	1.00 W	27.72126	0.07082	11.22372	0.47970	0.03454	0.00043	149.47 ± 2.15	66.34	6.60	0.038 ± 0.003
05MY027Q	2.00 W	29.36275	0.06288	12.15457	0.52100	0.04039	0.00038	149.46 ± 1.94	62.58	7.83	0.035 ± 0.003



View on the Pontic tombs and castle along the Yeşilirmak river in Amasya

CHAPTER 4

Late Cretaceous to Paleocene oroclinal bending in the central Pontides (Turkey)

The Turkish Pontide fold-and-thrust belt formed since the Paleozoic and is an important element in the Africa-Eurasia convergence and the resulting closure of the Neo-Tethys ocean. It has a peculiar arc-shaped geometry in its central part, along the Black Sea coast, which may have resulted from oroclinal bending. Therefore, we determined the vertical-axis rotation history of this area using paleomagnetism on Cretaceous to Eocene rocks from 47 sites, and by critically analyzing published data. We applied the same reliability criteria to all data.

Our results show that late Cretaceous sites have clockwise and counterclockwise rotations perpendicular to the structural trend in the central Pontides. In the eastern Pontides, they show only local rotations. Paleocene to Eocene rocks in the central and eastern Pontides show no rotation. We conclude that the central Pontide northward arc-shaped geometry results from oroclinal bending in latest Cretaceous to earliest Paleocene times. Timing and scale of geological processes that occurred in the region makes it likely that oroclinal formation resulted from Neo-Tethys closure between the Pontides and the metamorphic promontory of the Anatolide-Tauride Block.

Earlier studies on the southerly located Çankırı Basin reveal that clockwise and counterclockwise rotations occurred in Eocene-Oligocene times. This implies that the entire region underwent continuous deformation from late Cretaceous to Eocene, caused by convergence of the Pontides and the Anatolide-Tauride block, with a southward moving deformation front. Deformation was first localized in the northern part of the central Pontides until the Paleocene, resulting in oroclinal bending, and from at least Eocene times it shifted toward the Çankırı Basin region.

1. Introduction

The Turkish Pontides constitute a fold-and-thrust belt that formed since the Paleozoic as a result of subduction and accretion processes during the closure of the Paleo-Tethys and Neo-Tethys oceans at the southern European margin (Okay et al., 2006; Şengör and Yilmaz, 1981). The Pontides were separated from Eurasia by the opening of the Black Sea basin during Cretaceous-Eocene times (Fig. 4.1a) (Görür, 1988; Hippolyte et al., 2010; Okay et al., 1994; Robinson et al., 1996; Tüysüz, 1999). To the south, the Pontides are separated from the Pan-African Anatolide-Tauride Block by the İzmir-Ankara-Erzincan (IAE) suture zone, which represents the location of closure of the Neo-Tethys (Şengör and Yilmaz, 1981). Collision between the Pontides and the Anatolide-Tauride Block took place in the late Cretaceous to Paleocene, with a final phase in the Eocene (Görür et al., 1984; Kaymakci et al., 2009; Rice et al., 2006; Şengör and Yilmaz, 1981).

The general east-west trend of the Pontide fold-and-thrust belt is disrupted in its central part by a peculiar northward convex geometry along the central Black Sea coast (Fig. 4.1b). This central Pontides geometry could be original, having developed during initial nappe stacking or may represent a younger phase of oroclinal bending (Carey, 1958). Oroclinal bending would require major, regional deformation of the pre-existing east-west striking fold-and-thrust belt. Such a distinct deformation event after a long-lasting process of subduction-accretion along the southern Eurasian margin may help identifying major changes in the geodynamic evolution of the closure of the Neo-Tethys and the roles of continent-continent collision and the opening of the Black Sea.

In this study, we will first test whether the northward convex geometry in the Pontides can be defined as an orocline. To do this, we have collected paleomagnetic samples from 47 sites in the central and eastern Pontides from lower Cretaceous to Eocene rocks to determine the vertical-axis rotation history of the region. In addition, we will constrain timing of eventual rotations, to enable correlation to large-scale geodynamic processes, by determining vertical-axis rotations in rocks taken from a sufficiently large time span (Cretaceous-Eocene). We have also examined paleolatitude data from two of our sites and corrected them for inclination error using the E/I method of Tauxe and Kent (2004) to assess the paleolatitude of the Pontides in the late Cretaceous with respect to the predicted paleolatitude of the southern Eurasian margin from the apparent polar wander (APW) path of Eurasia (Torsvik et al., 2008).

2. Geological Setting

The Pontides in northern Turkey are a late Cretaceous to Paleogene fold-and-thrust belt between the Black Sea in the north and the İzmir-Ankara-Erzincan (IAE) suture zone in the south (Fig. 4.1a) (Okay and Tüysüz, 1999). The IAE suture zone separates the Pontides from the continental Anatolide-Tauride platform, and marks the former position of the subduction zone of a branch of the Neo-Tethys ocean. The Pontides

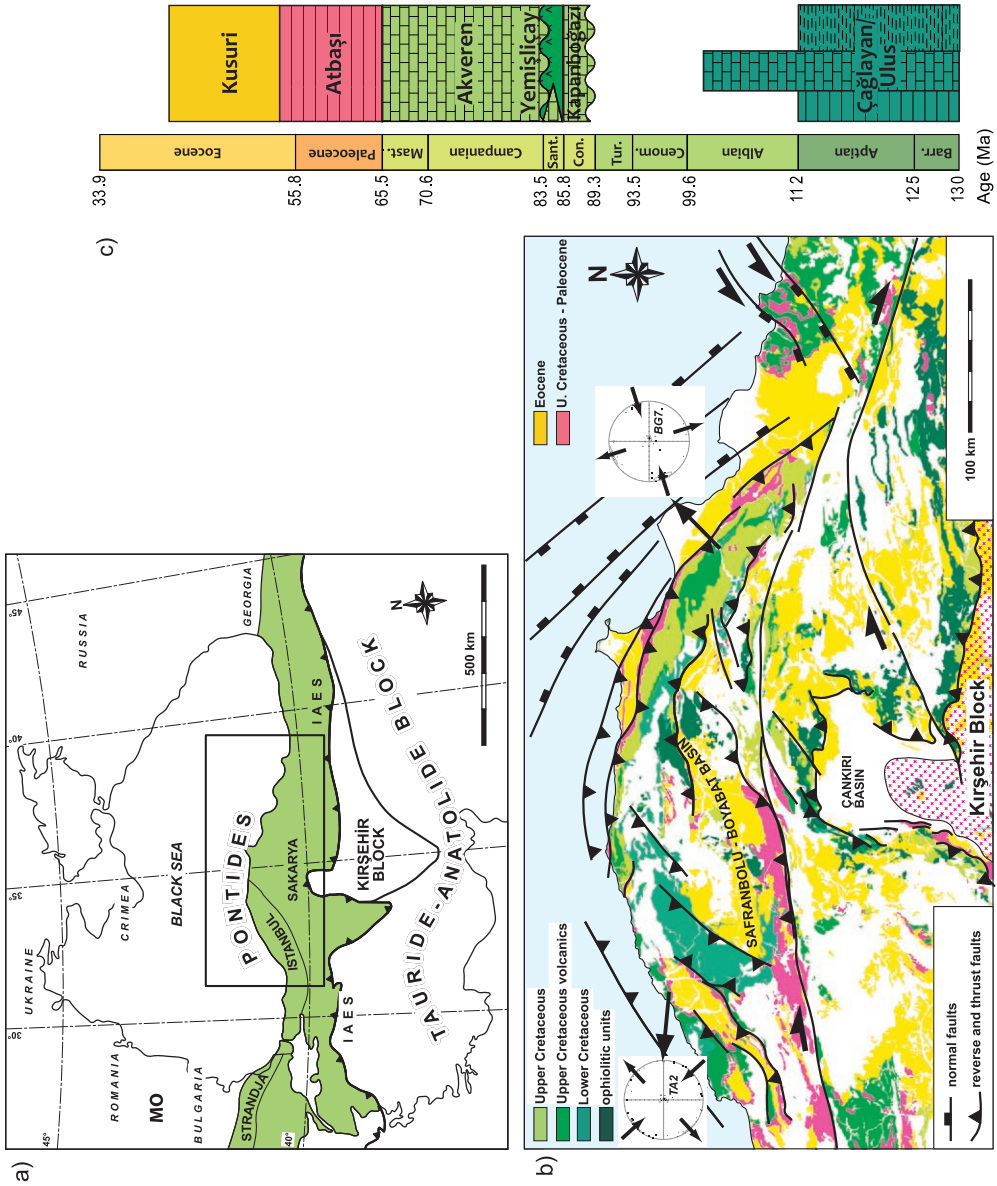


Figure 4.1 a) Map showing the location of the Pontides in relation to the Black Sea, the Izmir-Ankara-Erzincan (IAE) suture, the Kırşehir Block and the Anatolide-Tauride Block. MO indicates the position of the Moesian Platform. b) Zoom of the map in Figure 4.1a, showing the main stratigraphic ages and major structures and basins in the central Pontides. The trend of the faults/basins is roughly NE/SW in the western part of the convex geometry, and NW/SE in the eastern part. In the south the Çankırı Basin and the Kırşehir Block are displayed. The results of the AMS measurements of sites TA2 and BG7 (Fig. 4.8) are also indicated. KM indicates the location of the Kargı Massif. c) Stratigraphic column following Hippolyte et al. (2010) showing the main formations that were sampled in this study. In the Cenomanian-Turonian there is a depositional gap. See Appendix 16

comprise, from west to east, the Strandja Zone, İstanbul Zone and Sakarya Zone (Fig. 4.1a).

The Strandja Zone comprises Variscan continental basement, which was deformed and metamorphosed during Jurassic subduction along the southern margin of the Moesian Platform (Gerdjikov, 2005; Okay et al., 2001). The Strandja Zone is covered by metamorphosed Triassic to middle Jurassic sequences, tectonically overlain by allochthonous Triassic sequences.

The Sakarya Zone is structurally the lowest of these zones and underthrusts the Strandja and İstanbul Zones (Okay et al., 2001). Unlike the İstanbul Zone, it includes a strongly deformed Variscan basement and the locally metamorphosed pre-Jurassic Karakaya Complex, which is described either as a mid-late Triassic subduction-accretion complex, or as an inverted rift basin (e.g. Genç and Yılmaz (1995), Pickett and Robertson (2004), Okay and Göncüoğlu (2004)).

The İstanbul Zone is structurally the highest zone and is separated from the Strandja Zone by a right-lateral strike-slip fault (Okay et al., 2001). It comprises non-metamorphic Ordovician to Carboniferous sedimentary sequences that were deformed during the Permo-Carboniferous, and are overlain by Triassic sediments (Okay et al., 1994). Based on its stratigraphy it is assumed that it is a detached block of the Moesian Platform that displaced southward during the opening of the western Black Sea basin (Okay et al., 1994) (Fig. 4.1a).

The Sakarya and İstanbul Zones share a post-Triassic volcano-sedimentary cover, composed of lower Jurassic continental to shallow marine clastic rocks, with several ammonitico-rosso levels (Altınler et al., 1991). In the eastern part of the Sakarya Zone (in general called the eastern Pontides), the lower and middle Jurassic units comprise volcanic and volcanoclastic sequences (Yılmaz and Kandemir, 2006; Yılmaz et al., 2003), which are largely missing in the central and western Pontides. Platform carbonates of the İnaltı Formation of mid-Jurassic (Callovian) to early Cretaceous age cover the entire Pontides, except for the Strandja Zone. The entire cover of the Pontides consists of Cenomanian-Maastrichtian volcano-sedimentary sequences collectively named as Yemişliçay Formation in Turkey and Srednogorie Zone in the Balkans (Okay et al., 1994; Sinclair et al., 1997; Zimmerman et al., 2008). The Paleozoic basement of the Pontides suggests a Eurasian origin (Bozkurt et al., 2008; Okay et al., 2008), as opposed to the Pan-African origin of the Anatolide-Tauride belt (Hetzl and Reischmann, 1996; Kröner and Şengör, 1990; Satır and Friedrichsen, 1986; Şengör et al., 1988).

The Pontides have been separated from Europe by the Black Sea since the early Cretaceous (Görür, 1988; Hippolyte et al., 2010; Okay et al., 1994; Tüysüz, 1999). The Black Sea comprises two major (western and eastern) sub-basins. Opening of the western Black Sea basin is generally considered to be early-middle Cretaceous (Barremian-Albian) in age (Görür, 1997; Robinson et al., 1996). Timing of opening

of the eastern Black Sea is still controversial, because of poor exposure of its stratigraphy. Early Cretaceous (Kriachtchevskaia et al., 2010; Nikishin et al., 2003) to early Cenozoic ages (Robinson et al., 1995) and even Eocene ages (Vincent et al., 2005) are proposed, mainly based on incompatible and independent data sets and geophysical, stratigraphical, structural and tectonic modeling studies. It is generally accepted that the Cretaceous to Tertiary units in the Pontides are related to the opening of the Black Sea basins. Therefore, precise dating of these units is crucial in terms of understanding the ages of these basins. In this study we followed the stratigraphic classification scheme of Hippolyte et al. (2010), which is the most up-to-date and precise classification, based on 165 nannoplankton ages (Fig. 4.1c) belonging to every lithostratigraphical unit in the Pontides. The most important difference with respect to former studies (i.e. Görür (1997) and Tüysüz (1999)) is related to the stratigraphic positions and ages of the Kapanboğazı/Yemişliçay and Akveren formations. The Kapanboğazı/Yemişliçay formations are stratigraphically transitional and now ascribed to the Coniacian to Santonian. The Akveren Formation is now considered to be of Campanian to Maastrichtian age.

The syn-rift deposits of Görür (1997) of the western Black Sea basin in the Pontides comprise the Hauterivian-Albian Çağlayan/Ulus Group (Hippolyte et al., 2010). The Cenomanian-Turonian interval is marked by a hiatus: deposition resumed during the Coniacian and gave way to the deposition of red pelagic limestones (Kapanboğazı Formation) that gradually pass upwards into volcanics and volcanoclastic turbidites (Yemişliçay Formation) of Coniacian-Santonian age (Hippolyte et al., 2010). In Campanian-Maastrichtian times the Akveren/Alaplı limestone formations and siliciclastic turbidites of the Gürsöku Formation were deposited. They are followed by deposition of limestones and marls of the Atbaşı Formation in the Paleocene. The turbiditic Kusuri Formation was deposited during the Eocene along the present-day Black Sea coast, (Özcan et al., 2007; Robinson et al., 1995), as well as volcano-sedimentary units of Eocene age that were deposited along a narrow band along the IAE suture zone (Keskin et al., 2008). Nummulitic limestones were deposited further away from the Black Sea coast in shallow water basins, developing over compressional structures (Kaymakci et al., 2009; Özcan et al., 2007; Robinson et al., 1995).

The continental Anatolide-Tauride Block is located south of the IAE suture zone. The promontory of the Anatolide-Tauride Block in the central part of the bend in the Pontides and IAE suture zone that forms the present study area is the metamorphosed Kırşehir Block (Görür et al., 1984). At the contact between the Pontides and the Anatolide-Tauride Block, the Çankırı Basin developed as a late Cretaceous forearc and Paleogene foreland basin, straddling the IAE suture zone at the northernmost tip of the Kırşehir Block (Fig. 4.1b). Metamorphism of the Kırşehir Block followed northward intra-oceanic subduction and southward ophiolite emplacement over the Kırşehir Block during the Cenomanian to Turonian (Kaymakci et al., 2009; Whitney

et al., 2001; Yalınız et al., 2000). This was followed by late Cretaceous to Paleocene northward oceanic subduction below the Pontides, as evidenced by the development of an upper Cretaceous volcanic arc on the Pontides (Kaymakci et al., 2009; Okay et al., 2001; Okay et al., 2006; Rice et al., 2006; Tüysüz and Tekin, 2007) and the development of a forearc basin in the Çankırı region (Kaymakci et al., 2009). Exhumation of the Kırşehir Block started at the end of the Cretaceous (Boztuğ and Jonckheere, 2007; Görür et al., 1984) and continued during the Paleogene (Boztuğ et al., 2009; Boztuğ et al., 2009; Gautier et al., 2002; Isik, 2009). This implies that the Kırşehir Block may have formed a rigid indenter in the Paleogene, between the Anatolide-Tauride Block and the Pontides, which led to the development of a foreland basin in the Çankırı region (Kaymakci, 2000; Kaymakci et al., 2009).

The Pontides were underthrust during Cenomanian-Turonian times (~100-89 Ma) by the Kargı Massif, which was interpreted by Okay et al. (2006) as a micro-continental sliver of Neo-Tethyan origin, north of the Anatolide-Tauride Block.

3. Paleomagnetic sampling, analysis and results

3.1 Paleomagnetic sampling

In total, 1301 cores from 47 sites were sampled in the central and eastern Pontides, in lower Cretaceous to Eocene deposits, with a minimum of 7 up to as much as 149 cores per site; a single core often provided multiple specimens for paleomagnetic analysis (see Table 4.1). Samples were collected using a gasoline powered motor drill or an electric drill with generator, depending on the rock type. Sample orientations were measured with a magnetic compass, and sample orientations as well as bedding tilt were corrected for present-day declination, ranging from 4 to 5° W. Ages were assigned to formations according to Hippolyte et al. (2010) and those for the trachyandesites of site BD4 according to Eyüboğlu (2009).

3.2 Paleomagnetic analysis

Out of 1301 cores, 1064 specimens were demagnetized. The samples were demagnetized using alternating field (AF) and thermal (TH) progressive stepwise demagnetization methods. Approximately half of the samples that were AF demagnetized were

Table 4.1 Sampled paleomagnetic sites. Age of the sites according to (2010), formation name, rock type, latitude and longitude of the site. Number of sampled cores (Nc), polarity of the ChRM directions (pol, tilt corrected), use of great circle analysis (if used, indicated with Gc) (McFadden and McElhinny, 1988). Number of samples after application of a variable cut-off on the VGPs of the ChRM direction (N) (Vandamme, 1994), over the number of samples that were measured (Na). Declination (D), inclination (I) and declination (ΔD_x) and inclination (ΔI_x) errors determined from the A95 of the poles, with corresponding estimate of the precision parameter (k) and cone of confidence (α_{95}) determined from the ChRM directions for in situ and tilt corrected data. Latitude (λ) and longitude (ϕ) with corresponding estimate of the precision parameter (K) and cone of confidence determined from the mean virtual geomagnetic pole (VGP). Rej.: reason of rejection of site (reason of exclusion of the site (if excluded), according to criteria mentioned in section 3.3).

Site	Age	Formation	Rocktype	Latitude	Longitude	Nc	Pol	Gc	CHRM directions - in situ	CHRM directions - tilt corrected	CHRM D	N/A	D	ΔDx	I	Δix	k	α95	CHRM D	N/A	D	ΔDx	I	Δix	palat	k	α95	VGP's λ	φ	K	A95	Rej.		
A1	Barremian-Apitan	Çeğlayan	shales	41.7	32.4	14	n		14/14	21.3	12.3	19.2	22.2	9.9	13.3	14/14	18.9	12.2	28.1	19.6	15.0	10.4	12.9	58.7	175.4	12.4	11.8							
A2	Barremian-Apitan	Çeğlayan	shales	41.7	32.4	14	n		15/15	66.5	34.5	61.0	21.2	5.8	17.4	15/15	228.5	99.9	86.9	51.1	83.8	5.8	17.4	37.5	26.7	2.6	29.9	4.6						
A3	Barremian-Apitan	Çeğlayan	shales	41.7	32.4	14	n		7/14	45.1	11.5	31.9	17.3	27.9	11.6	7/14	33.1	18.7	53.6	15.9	34.1	27.9	11.6	63.0	127.7	16.3	15.4							
A4	Coniacian-Santonian	Kapanböğazi	red pelagic limestones	41.7	32.4	10	r	Gc	7/7	210.5	9.9	-44.2	11.3	28.5	11.5	7/7	213.3	9.7	-41.5	11.9	23.9	28.5	11.5	57.1	144.7	47.2	8.9							
EE	Coniacian-Santonian	Yemişliçay	clays/volcanoclastics	41.3	31.5	15	r	Gc	14/14	331.5	8.2	40.3	10.3	24.2	8.3	14/14	320.2	9.0	48.2	9.1	29.2	24.1	8.3	55.7	162.2	26.7	7.8							
EE	Coniacian-Santonian	Kapanböğazi	red pelagic limestones	41.3	31.5	15	r	Gc	12/13	169.2	6.4	-44.6	7.3	56.7	5.8	12/13	170.0	5.9	-39.7	7.5	22.5	56.7	5.8	69.4	-121.3	65.1	5.4							
EK	Coniacian-Santonian	Kapanböğazi	red pelagic limestones	41.3	31.6	19	n	Gc	14/14	328.6	3.2	36.6	4.4	141.0	3.4	14/14	322.6	3.9	47.9	4.0	29.0	138.1	3.4	57.3	-68.5	136.9	3.4							
EZ	Barremian-Albian	Çeğlayan	shales	41.4	31.7	17	n		10/14	38	11.7	61.0	7.4	54.3	6.6	10/14	275.1	16.7	57.7	12.1	38.4	16.9	10.7	27.6	-39.7	39.1	11.1	13.1	4.5					
K1	Campanian-Maastrichtian	Akveren	limestones	41.6	34.4	12	n		13/14	346.6	18.5	70.9	6.9	41.6	6.5	13/14	354.0	7.4	-43.4	6.7	25.3	41.4	6.5	22.9	-130.1	39.1	6.7	4						
K2	Eocene	Kusuri	shales	41.5	34.7	12	n		14/14	354.9	6.3	41.0	7.8	41.2	6.3	14/14	1.7	8.7	53.6	7.4	34.1	41.2	6.3	82.5	-156.2	31.6	7.2							
K3	Barremian-Albian	Çeğlayan	shales	41.6	34.8	12	r	Gc	13/14	168	17.3	44.0	19.7	7.1	16.7	12/14	186.2	14.9	-43.6	17.2	25.5	12.2	12.9	73.1	-164.8	11.4	13.4							
K4	Coniacian-Santonian	Yemişliçay	flysch	41.7	34.9	13	n		8/14	356.4	22.7	56.3	17.3	13.0	16.0	8/14	143.5	29.3	56.5	22.0	37.1	13.0	16.0	-4.5	63.3	6.8	23.0	4.5						
K5	Campanian-Maastrichtian	Akveren	spartic limestones	41.8	35.0	14	r	Gc	4/7	227.2	11.1	-39.7	14.2	65.7	11.4	4/7	207.8	8.5	-30.9	13.0	16.7	73.3	10.8											
K6	Eocene	Kusuri	marls	41.9	35.1	14	n		10/14	18.3	12.0	47.0	12.7	17.9	11.7	10/14	368.1	99.9	86.8	9.9	83.6	18.0	11.7	48.3	34.8	7.0	19.7	4.6						
K7	Campanian-Maastrichtian	Gürsöklü/Akveren	marls	41.7	35.2	12	r	Gc	7/14	206.6	10.9	-3.1	21.7	30.8	11.0	7/14	207.0	16.8	-33.9	24.4	18.6	41.4	14.5											
K5_K7	Campanian-Maastrichtian	Gürsöklü/Akveren	limestones/marls	41.3	32.0	19	r	Gc	11/21	212.9	11.1	-16.6	20.7	11.4	14.1	11/21	208.3	7.7	-30.2	12.0	16.2	41.5	7.2	54.7	163.1	39.2	7.4							
K8	Paleocene	Abtaşı	marly/sandy limestones	41.7	35.3	13	n		10/14	8.9	37.0	71.0	13.2	13.6	13.6	10/14	355.3	11.6	32.0	17.5	17.4	13.6	13.6	65.3	-133.9	19.9	11.1							
K9	Coniacian-Santonian	Kapanböğazi	red pelagic limestones	41.0	36.1	13	n		9/14	31.3	2.9	6.0	5.7	326.0	4.6	11/14	36.8	11.8	42.9	13.9	24.9	12.1	13.7	55.5	142.4	19.3	10.7							
K10	Coniacian-Santonian	Kapanböğazi	red pelagic limestones	41.1	36.0	7	n		13/13	7.7	2.2	37.4	3.0	324.6	2.3	13/13	55.9	2.7	43.0	3.2	25.0	324.4	2.3	41.4	127.2	284.4	2.5							
D1	Eocene	Kusuri	sands and silts	41.4	32.0	15			0/7																									
D2	Eocene	Kusuri	rudist/sandstones	41.3	32.0	12	r		12/14	182.5	4.8	2.4	9.6	37.6	7.2	12/14	182.0	6.5	-35.6	9.1	19.7	37.6	7.2	68.3	-153.1	51.2	6.1							
D3	Eocene	Kusuri	mudstones/marls	41.3	32.0	13	n		13/14	24.4	70.3	8.6	24.9	8.5	8.5	13/14	353.7	6.8	28.7	10.6	16.3	24.9	8.5	63.4	-134.3	41.3	6.5							
D4	Campanian-Maastrichtian	Akveren	limestones	41.2	32.2	15	n		8/14	318.1	28.6	52.8	24.7	10.6	17.8	8/14	304.8	14.8	-3.2	29.6	-1.6	10.6	17.8	48.6	-127.2	14.9	14.8	4						
D5	Paleocene	Abtaşı	red and green marls	41.2	32.2	12	n+H	Gc	5/7	206.5	22.7	-44.8	25.4	10.8	24.4	5/7	166.5	19.5	-21.8	34.3	11.3	10.8	24.4	57.9	-122.5	16.9	19.1							
F1	Eocene	Kusuri	marls	40.8	37.2	15	r	Gc	13/34	129.9	4.3	-40.5	5.4	83.4	4.4	13/34	177.4	5.5	-53.1	4.7	33.6	108.3	4.0	82.6	-125.8	83.9	4.6							
F2	Eocene	Kusuri	limestones	40.9	37.3	13	r		15/19	176.2	10.2	-37.2	13.9	13.7	10.7	15/19	171.3	10.0	-35.3	14.2	19.5	14.0	10.6	67.3	-121.0	17.3	9.5							
F3	Paleocene	Abtaşı	clayey limestones	40.9	37.3	15	n	Gc	24/27	3.4	3.5	38.8	4.6	80.3	3.3	23/27	3.6	6.2	62.8	3.6	44.2	94.3	3.1	85.8	74.8	48.0	4.4	6						
F4	Paleocene	Abtaşı	silt/sand/mudrocks	41.1	37.2	13	n	Gc	8/13	186.5	9.5	-61.8	5.8	110.6	5.3	8/13	205.3	10.6	-64.1	5.8	45.9	110.4	5.5	71.1	-104.2	58.0	7.3	6						
F5	Paleocene	Abtaşı	clayey limestones	41.1	36.3	8	n		10/11	251.2	99.9	-71.4	54.6	1.6	62.7	10/11	314.8	99.9	-41.7	89.3	24.0	1.6	62.7	12.6	102.1	1.5	66.8	4						
KE1	Maastrichtian	Akveren	oolitic limestones	41.1	31.9	65			0/19																									
KE2	Eocene	?	sandy mudstones	41.2	31.5	41	r	Gc	28/47	175.7	5.8	-12.3	11.1	19.1	6.4	27/47	181.5	6.4	-30.8	9.8	18.6	22.2	6.0	65.4	-152.0	21.8	6.1							
KE3	Paleocene	Abtaşı	marls and limestones	41.7	32.4	34	n		38/54	395.2	3.9	41.3	4.8	37.8	3.8	38/54	9.1	5.5	52.3	4.9	32.9	34.6	4.0	78.6	170.1	26.5	4.6							
KE4	middle Eocene	Kusuri	clays	41.6	32.3	51	n		9/12	349.4	15.2	-0.2	30.4	9.1	18.1	9/12	350.7	16.4	18.1	30.0	9.3	9.1	18.1	56.7	-130.8	11.1	16.2							
KE5	middle Eocene	Kusuri	shaly marls	41.6	32.4	51	n		25/47	6.6	12.8	35.6	17.9	5.5	13.6	25/47	38.8	18.9	53.6	16.0	34.1	5.3	14.0	58.8	123.3	4.5	15.5							
KE6	middle Eocene	Kusuri	nummulitic limestones	41.2	32.7	31	r		33/44	185.5	11.7	-35.1	16.6	5.4	11.9	33/44	185.5	11.7	-35.1	16.6	19.4	5.4	11.9	67.7	-161.1	6.1	11.0							
KE7	early Eocene	Hacıhallı	mudstones/shale	41.2	32.6	48	n		57/61	352.8	2.6	40.6	3.3	58.3	2.5	57/61	353.0	3.1	48.7	3.1	29.7	57.1	2.5	77.1	-119.0	48.9	2.7							
KE8	early Eocene	Hacıhallı	arkosic sands	41.4	33.8	48	n		0/19																									
KE9	Paleocene	Abtaşı	marly limestones	41.9	34.6	21	n	Gc	18/32	12.5	5.5	-20.4	9.8	33.0	6.1	18/32	7.0	8.4	52.3	7.4	32.9	33.0	6.1	79.4	-179.3	25.3	7.0							
KE10	Eocene	Kusuri	silty/sandy clays	41.9	35.1	27	n		14/22	29.5	6.1	-18.6	11.1	28.4	7.6	13/22	31.1	5.4	15.9	10.1	8.1	40.6	6.6	46.5	167.1	61.2	5.3							
KE11	early Eocene	Kusuri	yellow sands	41.4	35.1	10	n		8/8	353.6	12.4	52.8	10.8	40.6	8.8	8/8	354.2	7.3	-9.2	14.3	4.6	40.7	8.8	43.7	-136.9	58.8	7.3	4.5						
KE12	middle Eocene	Kocayay	nummulitic limestones	41.5	34.7	19	n		6/6	350.2	11.2	63.8	6.2	154.9	5.4	6/6	191.8	4.0	15.3	7.5	7.8	154.6	4.0	-39.5	19.5	285.9								

heated until 150°C before AF demagnetization to remove possible stress in magnetite grains caused by surface oxidation at low temperatures (Van Velzen and Zijdeveld, 1995), see also Gong et al. (2008). The largest part of the samples was demagnetized by AF demagnetization, and TH demagnetization was applied to test reproducibility of the AF results.

Orthogonal vector diagrams (Zijderveld, 1967) were used to display demagnetization of the NRM (Fig. 4.2). Sample ChRM directions were determined using principal component analysis (Kirschvink, 1980) on approximately five to seven successive AF or temperature steps in the majority of the samples. Samples that yielded NRM directions that were intermediate between two overlapping coercivity or temperature components, were analyzed using the great-circle approach (McFadden and McElhinny, 1988). With this method, the direction that lies closest on the great circle to the average direction from well-determined NRM directions can be determined (e.g. TA5.10B, Fig. 4.2). Usage of the great-circle approach is indicated in Table 4.1 and Figure 4.3.

The majority of the samples has a characteristic remanent magnetization (ChRM) carried by magnetite, as is evidenced by typical maximum unblocking temperatures below 600°C or maximum unblocking fields of 60-100 mT. Occasionally, lower temperatures are sufficient to determine the ChRM, typically in the range 360-480°C which suggests that the remanence is mainly carried by greigite (Roberts, 1995; Rowan et al., 2009; Vasiliev et al., 2008). In a number of cases there is also clear evidence for (additional) hematite as a carrier of the NRM (see below).

Examples of comparable results of AF and thermal demagnetization can be found in Fig. 4.2 (EK19.A/EK.19B, K8.6/K8.11 and TA2.40A/TA2.137A). In the pink/red pelagic limestones of the Kapanboğazi Formation (sites TA2 and EK), the magnetic carrier is magnetite, because the samples reach the origin between ~570°C-600°C, enabling AF demagnetization (see Fig. 4.2). Examples of rocks wherein the main magnetic carrier is hematite are sites BG5 and BG7 (Fig. 4.2, BG5.72B and BG7.37A). Thermal demagnetisation on these samples was carried out until 630°C to reach the origin. Therefore, AF demagnetization until 90 mT after heating until 150°C resulted in a relatively small decrease of the NRM (Fig. 4.2, BG5.29A). Since both sites BG5 and BG7 and sites TA2 and EK were taken from the red pelagic limestones of the Kapanboğazi Formation, we conclude that the magnetic carrier within this formation ranges from magnetite to hematite dominated rocks.

From the ChRM directions, site means as well as virtual geomagnetic poles (VGP) and their means were calculated. A variable cut-off (Vandamme, 1994) was applied on the VGPs per site and we calculated the error in declination (ΔD_x) and the error in inclination (ΔI_x) separately, following Butler (1992). We favor this approach because it more realistically describes the directional distributions, that become increasingly ellipsoidal (elongated) with lower latitudes (Creer et al., 1959). To determine whether two distributions share a common true mean direction (CTMD),

we use the test developed by McFadden and McElhinny (1990) and their classification (A,B,C, indeterminate) based on the critical angle γ_c and the angle γ between the means. We use their test with simulation, which effectively is equivalent to using the Watson (1983) V_w parameter. Sites K5 and K7 were combined, as they shared a CTMD (Table 4.1).

Data from two sites were corrected for inclination shallowing in sediments, using the elongation/inclination (E/I) method of Tauxe and Kent (2004). Since a large number of individual directions is required to apply the model (preferably $N > 100$), we only applied this method to our sites TA2 and TA5.

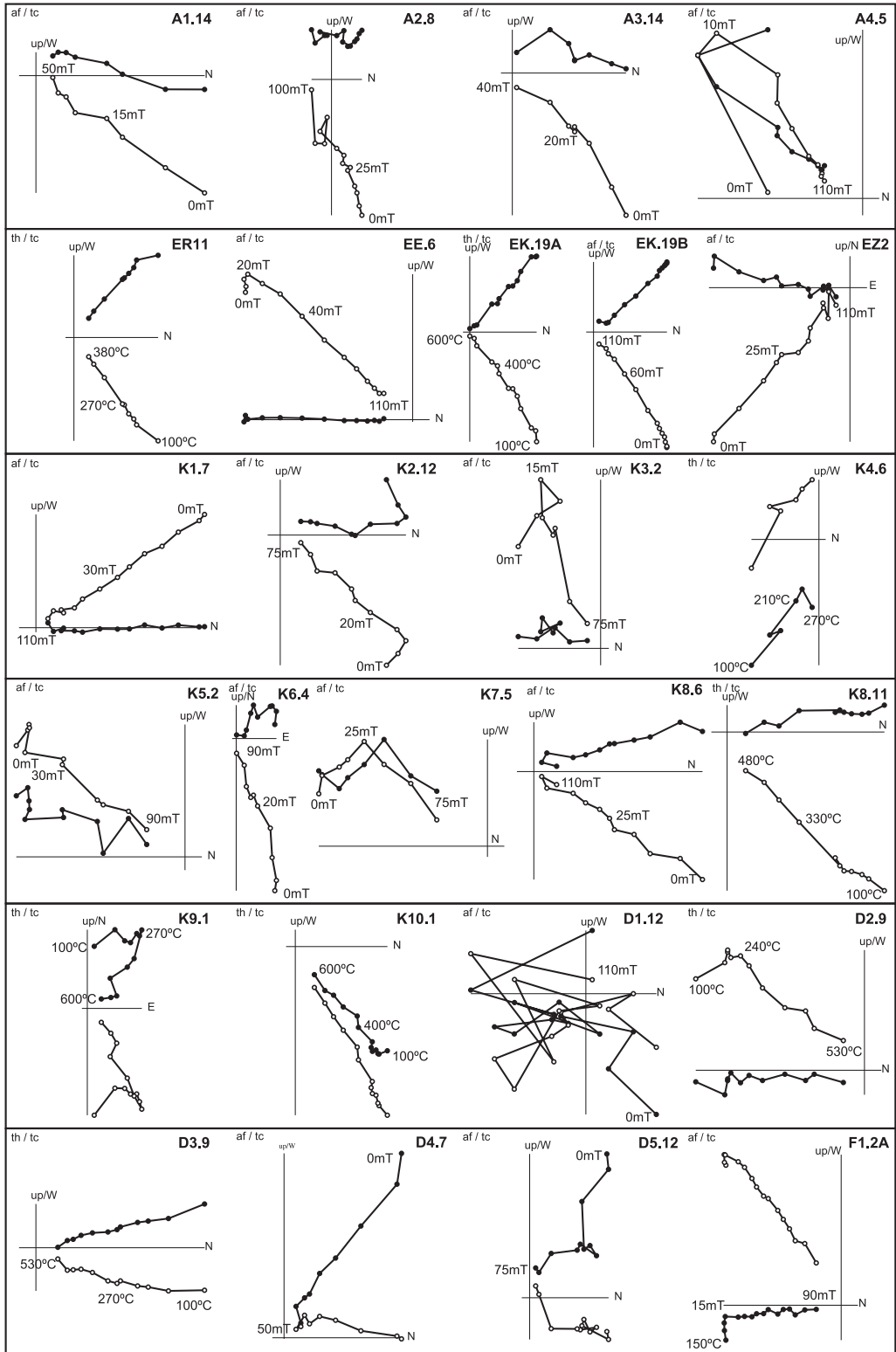
On samples from sites TA2 and BG7, measurements to determine the anisotropy of magnetic susceptibility (AMS) were performed to determine the magnetic fabric of the sediments and to assess whether they have a mainly sedimentary or tectonic fabric. This may be indicative for the amount of strain the rocks underwent after deposition (Hrouda, 1982), since the maximum axis of the AMS tensor (k_{max}) will start aligning with the direction of maximum extension (i.e. perpendicular to the direction of maximum compression). Jelinek statistics (Jelinek, 1981, 1984) were used for these calculations.

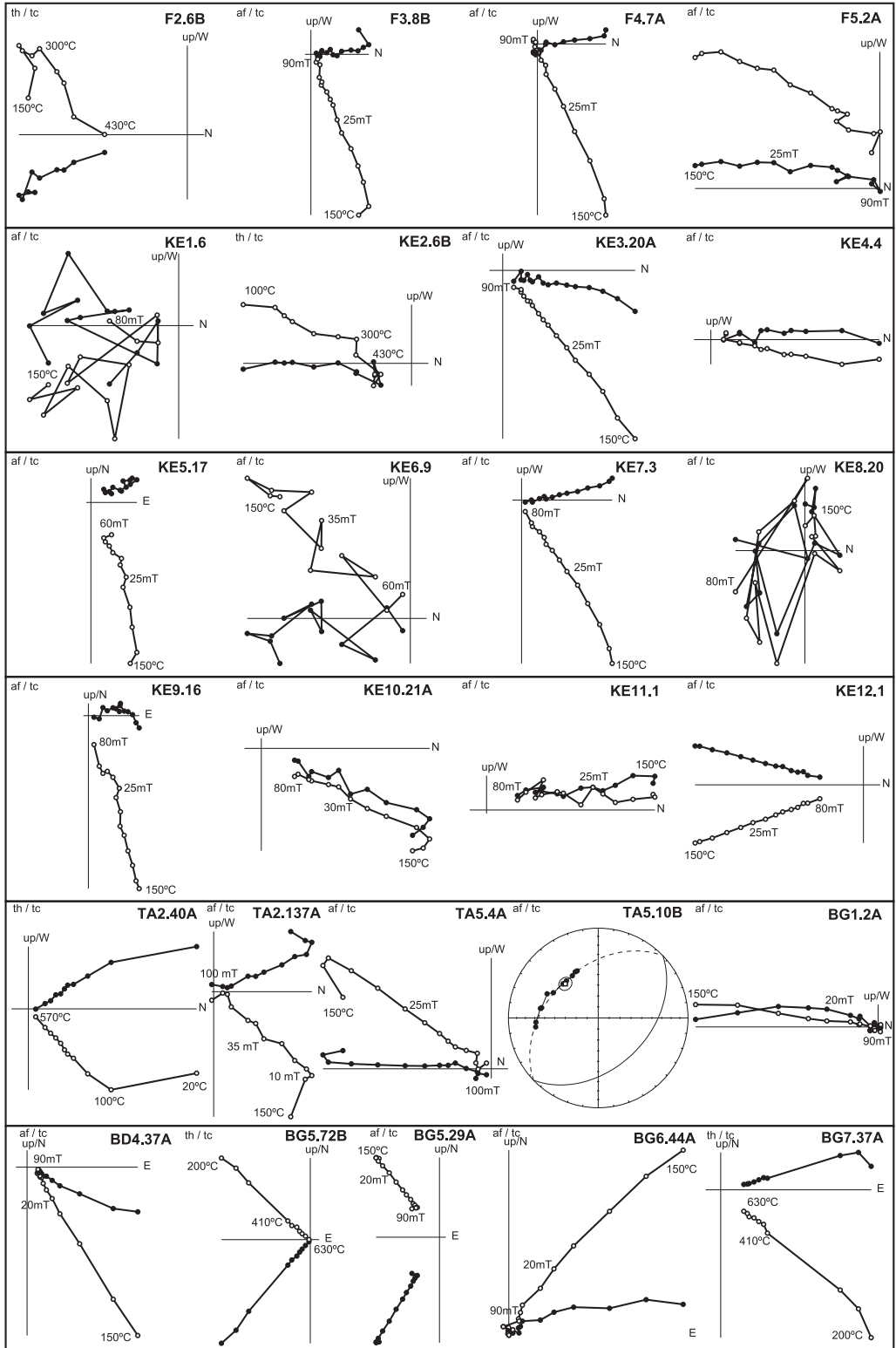
3.3 Reliability criteria

The new data we present in this study, as well as previously published data, collected from Cretaceous, Paleocene and Eocene rocks, are obviously subject to many sources of error. Therefore we have chosen the following reliability criteria, applied to both our own and published data sets.

Data(sets) with the following characteristics were excluded from further analyses: 1) Datasets sampled close to/in a major fault zone, 2) samples from datasets that were demagnetized using bulk demagnetization, 3) datasets that do not have a minimum amount ($N \geq 5$) of samples (sediments) or sites (magmatic rocks), 4) datasets with suspect directions (i.e. N/down or S/up directions) that may result from a (partial) overprint (e.g. K1, see Fig. 4.2, specimen K1.7) or large measuring errors caused by very low NRM intensities (Fig. 4.2, specimens D1.12, KE1.6 and KE 8.20), 5) datasets that carry a direction which in geographic coordinates are not distinguishable from the present-day geocentric axial dipole field direction, 6) datasets with an inclination that is lower than can reasonably be expected from flattening. The flattening factor (f) relates the ratio of the observed inclination to the inclination of the (applied) field (King, 1955). In natural sediments the flattening factor may range between zero (fully flattened) and unity (no flattening). However, typical values of f are 0.4-0.6 in sediments, but can be as low as 0.3 in red beds (Tauxe and Kent, 1984).

Figure 2 (next two pages) Orthogonal vector diagrams (Zijderveld, 1967), showing characteristic demagnetization diagrams for all sampled sites. Closed (open) circles indicate the projection on the horizontal (vertical) plane.





For all data, we use a lower boundary cut-off of $f \geq 0.3$. Finally, we rejected two sites (F3, F4) with an inclination more than 10° higher than suggested by the APW path (Torsvik et al., 2008).

An overview of previous paleomagnetic studies on 29 sites/localities in Cretaceous, Paleocene and Eocene rocks in the Pontides, north of the North Ana-

No.	Description	Site lat	Site lon	Age	Age error	Dec	Inc	N/Ns	k	α_{95}	Study	Paleo-latitude	Remarks	Reason of exclusion
Western Limb														
1	Eocene volcanics	40.8	30.9	44.9	11.0	212.0	55.8	2m	22.9	16.3	Sanbudak et al. 1990	36.3		1
2	Paleocene sediments	40.3	30.7	60.7	4.9	187.3	-30.1	33/3s	15.9	32.0	Evans & Hall 1990	16.2	sites 10-13	1
3	Yemişliçay Formation basalt	41.9	33.0	86.4	2.9	188.3	-27.0	6/1v	69.0	8.1	Sanbudak 1989	14.3	CI01	3
4	Yemişliçay Formation andesite	41.6	32.4	86.4	2.9	182.8	-53.4	6/1v	67.1	8.2	Sanbudak 1989	34.0	BA01	3
5	Yemişliçay Formation andesite	41.3	31.4	86.4	2.9	163.3	-56.7	5/1v	20.0	17.5	Sanbudak 1989	37.3	ER01	3
6	Yemişliçay Formation andesite	41.2	31.9	86.4	2.9	339.3	37.0	5/1m	63.3	9.7	Sanbudak 1989	20.6	DE01	3
7	Yemişliçay Formation volcanoclastics	41.3	31.7	86.4	2.9	336.8	41.3	59/5ms	166.4	5.9	Channell et al. 1996	23.7	group 1	
8	Yemişliçay/Kapanboğazi Formation	41.7	32.4	86.4	2.9	325.7	45.4	47/3ms	58.7	16.2	Channell et al. 1996	26.9	group 2	
9	Yemişliçay/Kapanboğazi Formation	41.9	33.2	86.4	2.9	329.1	41.6	116/9ms	62.2	6.6	Channell et al. 1996	23.9	group 3	
Central zone														
10	Yemişliçay Formation andesitic tuff	41.6	34.4	86.4	2.9	1.9	29.4	23/1m	243.0	4.3	Sanbudak 1989	15.7	G001-06	
11	Yemişliçay/Kapanboğazi Formation	41.9	33.7	86.4	2.9	356.0	40.3	71/6ms	32.4	11.9	Channell et al. 1996	23.0	group 4	
Eastern Limb														
12	Eocene volcanics	41.6	35.9	44.9	11.0	182.0	-28.0	5/1m	194.0	5.5	Sanbudak 1989	14.9	BF01	3
13	Eocene volcanics	41.6	35.9	44.9	11.0	172.7	-32.3	5/1m	243.6	4.9	Sanbudak 1989	17.5	BF02	3
14	Eocene volcanics	41.2	36.4	44.9	11.0	141.1	-39.4	2/1m	N/A	N/A	Sanbudak 1989	22.3	SA01	3
15	Eocene volcanics	40.6	37.1	44.9	11.0	152.4	-42.5	54/10m	19.2	11.3	Tatar et al. 1995	24.6	north of NAFZ	1
16	Eocene volcanics	40.4	37.0	44.9	11.0	144.1	-47.5	63/8m	54.0	7.6	Tatar et al. 1995	26.8	south of NAFZ	1
17	Yemişliçay Formation basalt	42.0	35.0	86.4	2.9	154.9	-39.0	6/1m	157.2	5.3	Sanbudak 1989	22.0	SI01	3
18	Yemişliçay Formation basalt	42.0	34.9	86.4	2.9	161.3	-33.0	6/1m	44.0	10.2	Sanbudak 1989	18.0	SI02	3
19	Yemişliçay/Kapanboğazi Formation	41.8	34.8	86.4	2.9	9.1	40.2	63/5ms	18.5	18.3	Channell et al. 1996	22.9	group 5	
20	Vezirohan/Kapanboğazi Formation	40.6	35.8	86.4	2.9	93.8	38.3	69/5ms	5.3	36.7	Channell et al. 1996	21.5	group 6	1
21	Middle-Upper Eocene volcanics *	40.7	37.0	48.1	7.7	140.0	-36.0	9/2m	11.0	16.0	Van der Voo 1968	20.0	sites S-T	3
22	Çağlayan Formation andesites	41.0	36.0	114.8	15.2	186.3	3.2	5/1m	190.0	5.6	Sanbudak 1989	1.6	KA01	3,6
Eastern Pontides														
23	Eocene limestones and volcanics	40.4	39.6	44.9	11.0	345.0	35.0	82/9ms	68.0	6.2	Kissel et al. 2003	19.3	Gümüshane	
24	Eocene tuffs and dykes	40.5	37.7	44.9	11.0	50.3	34.4	52/2m	31.4	17.7	Orbay & Bayburti 1979	18.9	O3-O4	2
25	Upper Cretaceous limest. & volc. **	40.8	39.9	77.4	11.9	346.0	40.0	23/6ms	90.0	7.0	Van der Voo 1968	22.8	sites F-L	
26	Upper Cretaceous tuffs and dykes	40.5	37.7	77.4	11.9	346.8	49.9	24/17m	30.6	9.6	Orbay & Bayburti 1979	30.7	G1-G5, O1-O2	2
27	Kapanboğazi Formation	40.8	39.6	86.4	2.9	357.2	44.2	73/6s	36.2	11.3	Channell et al. 1996	25.9	group 8/9	
28	Kapanboğazi Formation	41.2	41.9	86.4	2.9	353.1	43.2	129/10s	35.0	8.3	Channell et al. 1996	25.2	group 10	
29	Lower-Middle Jurassic sed. and volc. ***	40.5	39.3	180.4	19.2	153.5	-36.5	31/6ms	35.0	11.0	Van der Voo 1968	20.3	sites M-R	

Sites marked with asterisks were assigned a different age than the age in the mentioned publication

Old ages: *Cretaceous, **Upper Cretaceous-Eocene, ***Cretaceous

Number 29 (Van der Voo, 1968), marked *** has a newly assigned age that is too old for this study

tolian Fault Zone (NAFZ) is listed in Table 4.2. Most studies were carried out on Cretaceous rocks (18 studies), and data from nine Eocene localities were published (9), especially from the eastern Pontides (Fig. 4.4). Only one study on Paleocene rocks was published. One site from a study by Van der Voo (1968) was previously assigned a Cretaceous age, but the most recent Turkish geological map (1:500.000 scale) (Şenel et al., 2001) assigns a lower-middle Cretaceous age to those rocks. Two other sites from the study by Van der Voo (1968) were also given a new age according to the geological map (Table 4.1). Overall, the study carried out by Channell et al. (1996) and data from several sites analyzed by Sarıbudak (1989) and Kissel et al. (2003) were included for further analysis. In Table 4.2 we indicated which sites were excluded from further discussion as well as the reason for exclusion.

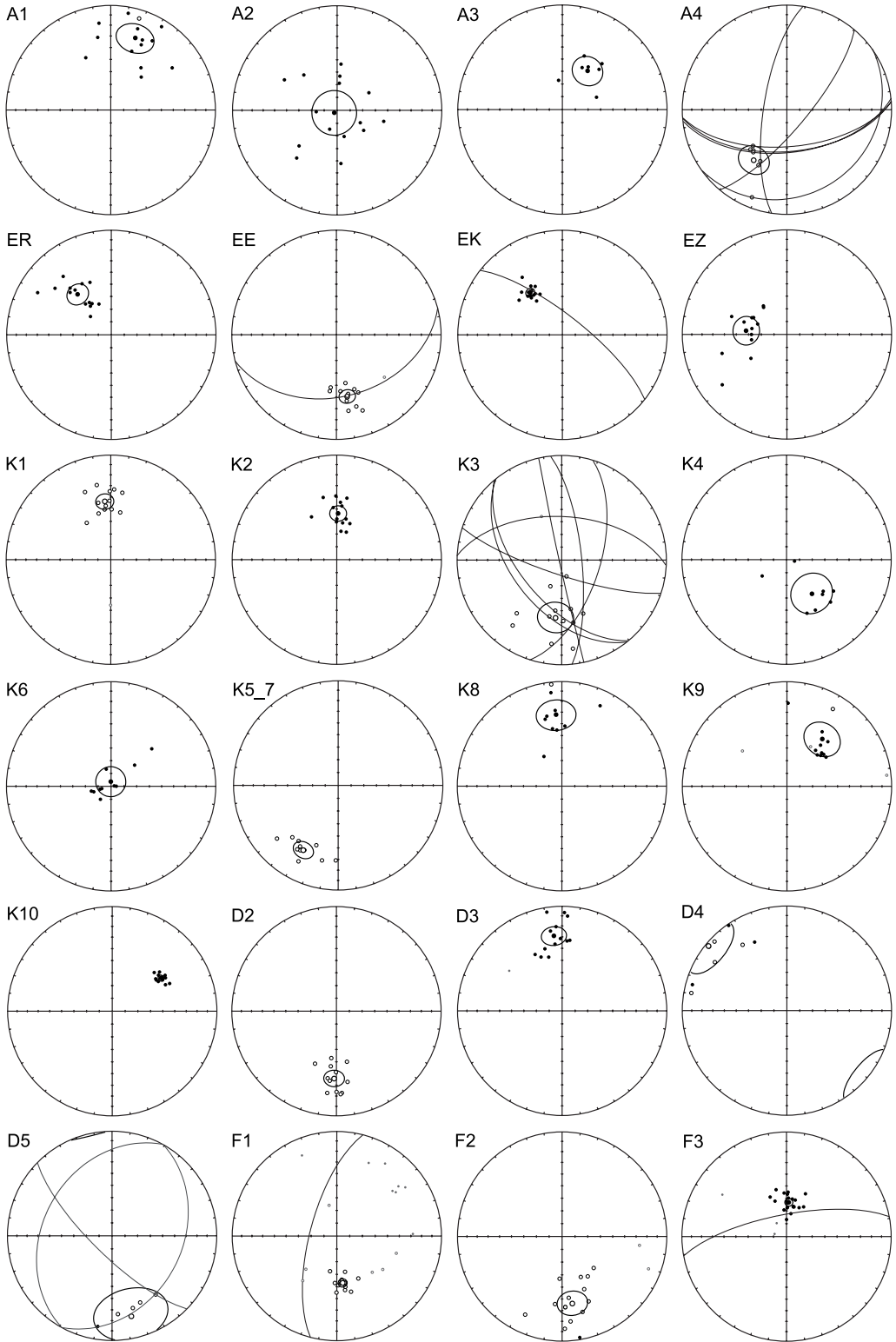
4. Paleomagnetic results

Examples of orthogonal vector diagrams (Zijderveld, 1967) and equal area projections of the ChRM directions of all sites are given in Figs. 4.2 and 4.3. After critical analysis of all measured sites, we have excluded 15 out of the sampled 47 sites (~32%) from further analysis (Fig. 4.5a-d).

On the basis of this study, combined with literature data, we define four distinct areas in the Pontides – the western limb, the central zone, the eastern limb, and the eastern Pontide area – that have distinct rotation patterns (Fig. 4.5e). From the rotation patterns in upper Cretaceous rocks, we can conclude that these were rotated counterclockwise (until $\sim 40^\circ$) in the western limb and clockwise (until $\sim 40^\circ$) in the eastern limb, whereas no or only local rotations were found in the central zone and eastern Pontides (Fig. 4.5e,f). Rocks from the four accepted Paleocene sites contain no significant rotation in all four segments. Furthermore, none of the eight accepted Eocene sites show a significant rotation. This means that we can demonstrate little or no vertical axis rotations in the Paleocene and the Eocene in the northern parts of the Pontides.

To allow comparison of the paleolatitudinal position from the Pontides with the APW path, we corrected two of our sample sets (sites TA2 and TA5) for inclination error with the E/I method (Tauxe and Kent, 2004) (Fig. 4.6). Correction is allowed because of the high quality of the datasets and the large number of analyzed

Table 4.2 Paleomagnetic data from previous studies. No.= site number assigned to the sites. Numbers correspond to the numbers in Figs 4.4 and 4.5. Site number bold: accepted site. Description of the sampled site (age and formation sampled). Site latitude (site lat), site longitude (site lon), age (assigned according to (Luterbacher et al., 2004; Ogg, 2004; Ogg et al., 2004)), declination (dec), inclination (inc), number of samples (N) from number of sites (Ns) from magmatic rocks (m), sedimentary rocks (s) or a combination of both (ms). Estimate of the precision parameter (k) and cone of confidence (α_{95}) determined from ChRM directions. Cited study and calculated paleolatitude from ChRM directions. Remarks refer to site name in the cited study. Reason of exclusion of the site (if excluded), according to criteria mentioned in section 3.3.



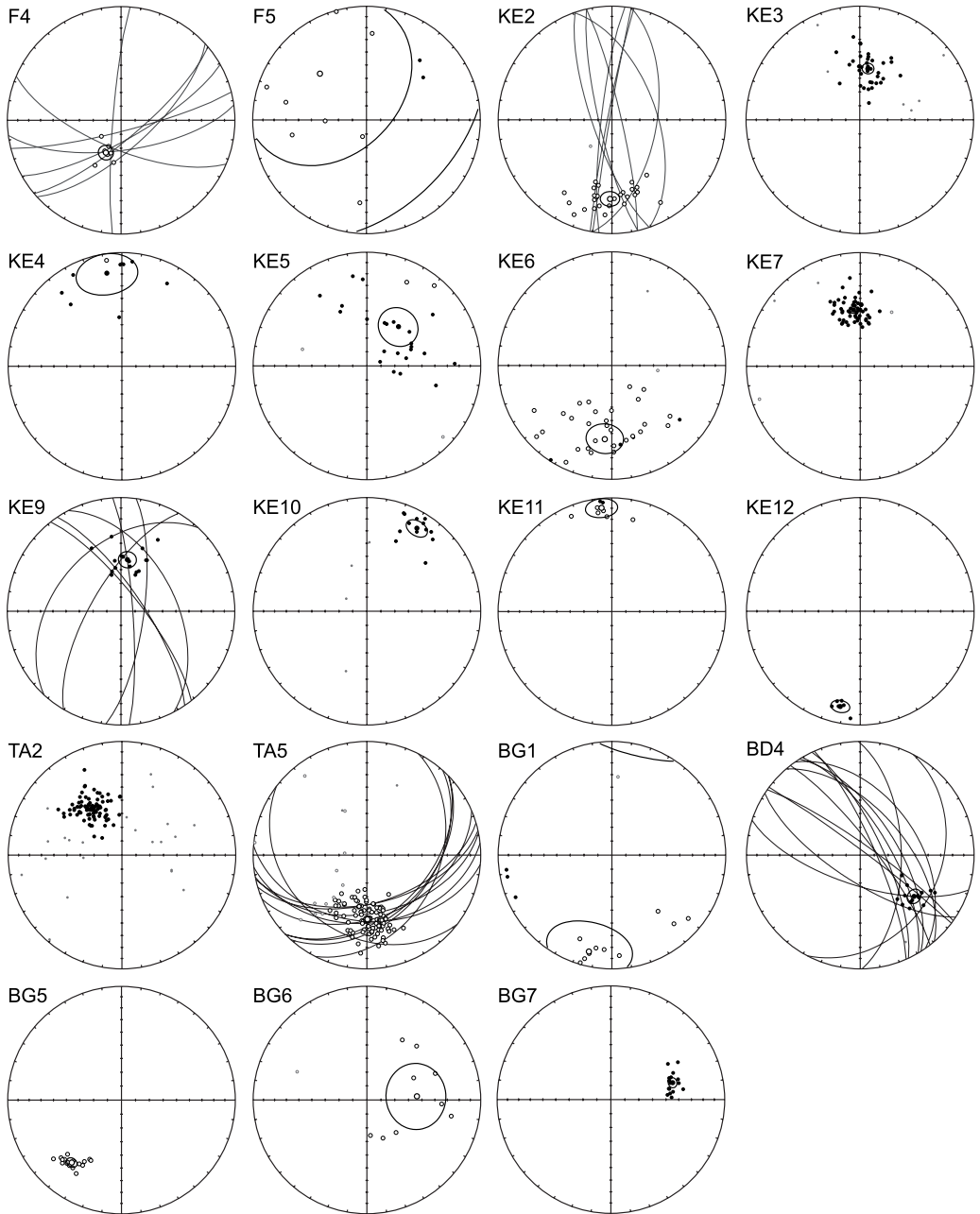
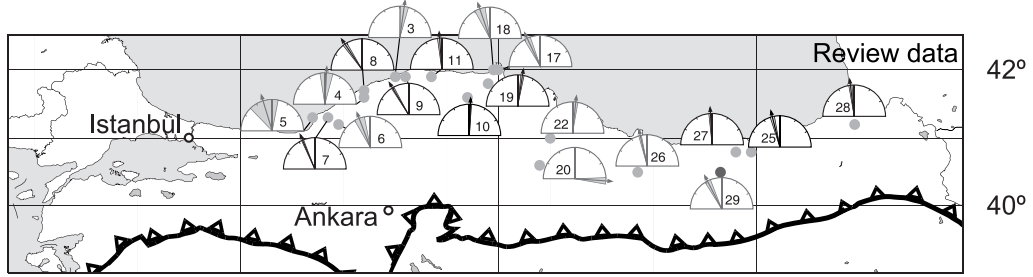


Figure 4.3 Equal area projections of the ChRM directions of all sites (Table 4.1). Open (closed) symbols denote projection on upper (lower) hemisphere. Large symbols indicate respectively the mean directions and their cone of confidence (α_{95}). Smaller symbols indicate the individual directions rejected by the Vandamme cut-off angle (Vandamme, 1994). Black lines indicate the great circles that were used to calculate the best fitting ChRM directions (McFadden and McElhinny, 1988).

a) late Cretaceous (green ●) and Jurassic (blue ●) sites



b) Paleocene (red ●) & Eocene (yellow ●)

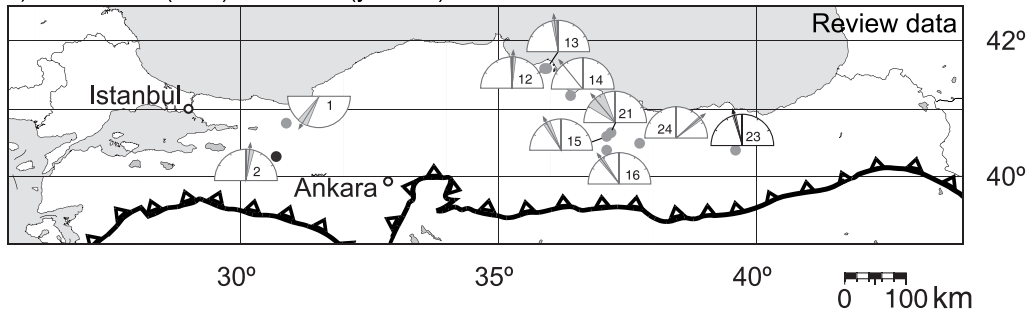


Figure 4.4 Paleomagnetic data from previous paleomagnetic studies. a) Rotation vectors measured from Jurassic (sites in blue) and Cretaceous (sites in green) rocks of all previous paleomagnetic studies. b) Rotation vectors measured from Paleocene (sites in red) and Eocene (sites in yellow) rocks of all previous paleomagnetic studies. ΔD_x envelopes of the rotation vectors shown in grey. Diagrams shown in red indicate rejected sites. Numbers correspond to the numbers in Table 4.2. See Appendix 17

samples. Site TA2 was sampled in red pelagic limestones of Coniacian-Santonian age, while the turbiditic volcanoclastics of site TA5 have a Santonian age according to Hippolyte et al. (2010). Because of the normal paleomagnetic signal in site TA2 and the reversed paleomagnetic signal of TA5, the latter must be younger and late Santonian in age, since the magnetization has to be post-Cretaceous Normal Superchron. The original paleolatitude for site TA2 is 29.7°N , and for TA5 it is 25.7°N . Correction for both sites is small. For TA2 the TK03 corrected paleolatitude is $40.2^\circ > 31.3^\circ > 29.2^\circ\text{N}$, for site TA5 this is $35.0^\circ > 26.6^\circ > 25.5^\circ\text{N}$, which is insignificant (within the 95% bootstrap errors) in both cases (Fig. 4.6). Within error, these TK03.GAD corrected inclinations are not significantly different than the inclination expected from the APW path.

In Figure 4.7, the paleolatitudes with their error (calculated from ΔI_x) are displayed. The left panel shows the data from the literature review, the right panel the data from our study. We also show the expected paleolatitudes when a flattening factor ($f = 0.3 - 0.9$) is applied to sediments (King, 1955). The data distribution clearly shows the effect of inclination shallowing in sediments: the majority of the data yield lower values than the expected values from the APW path.

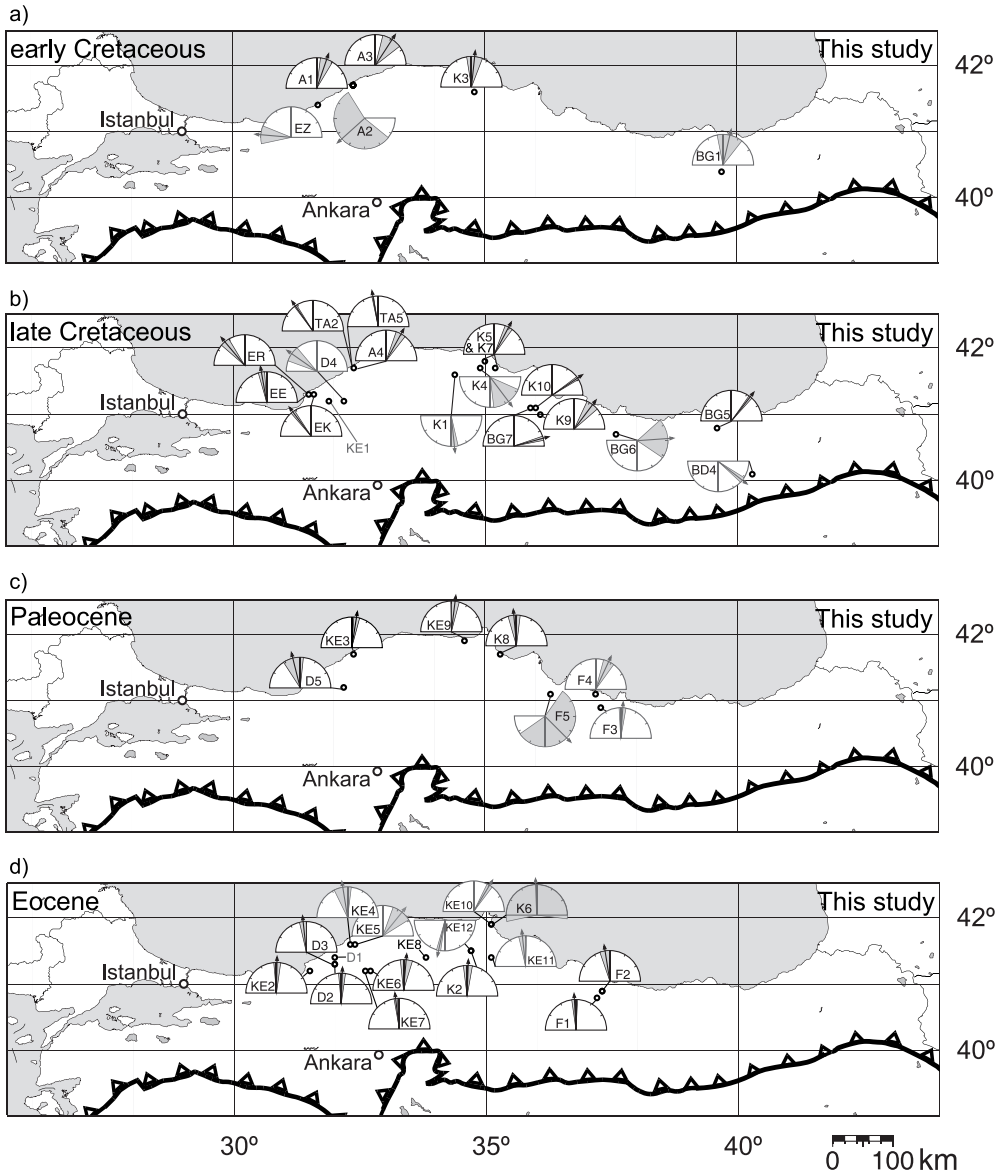


Figure 4.5 a-d) Paleomagnetic data from our study. ΔD_x errors of the rotation vectors are shown in grey. Numbers correspond to those in Table 4.2. Diagrams shown in red indicate rejected sites. Rotations measured from a) early Cretaceous rocks, b) late Cretaceous rocks, c) Paleocene rocks and d) Eocene rocks. See Appendix 18

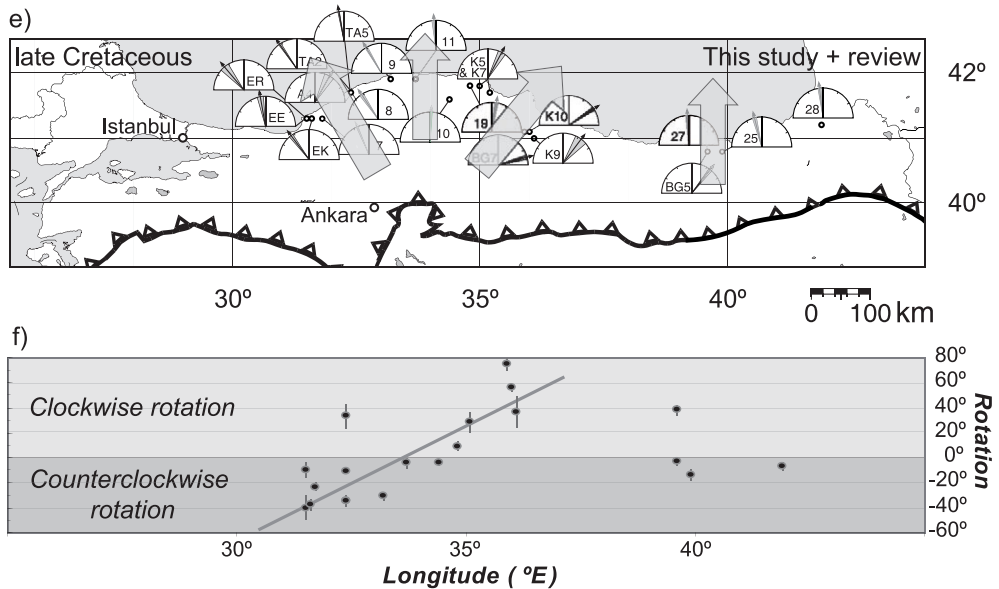
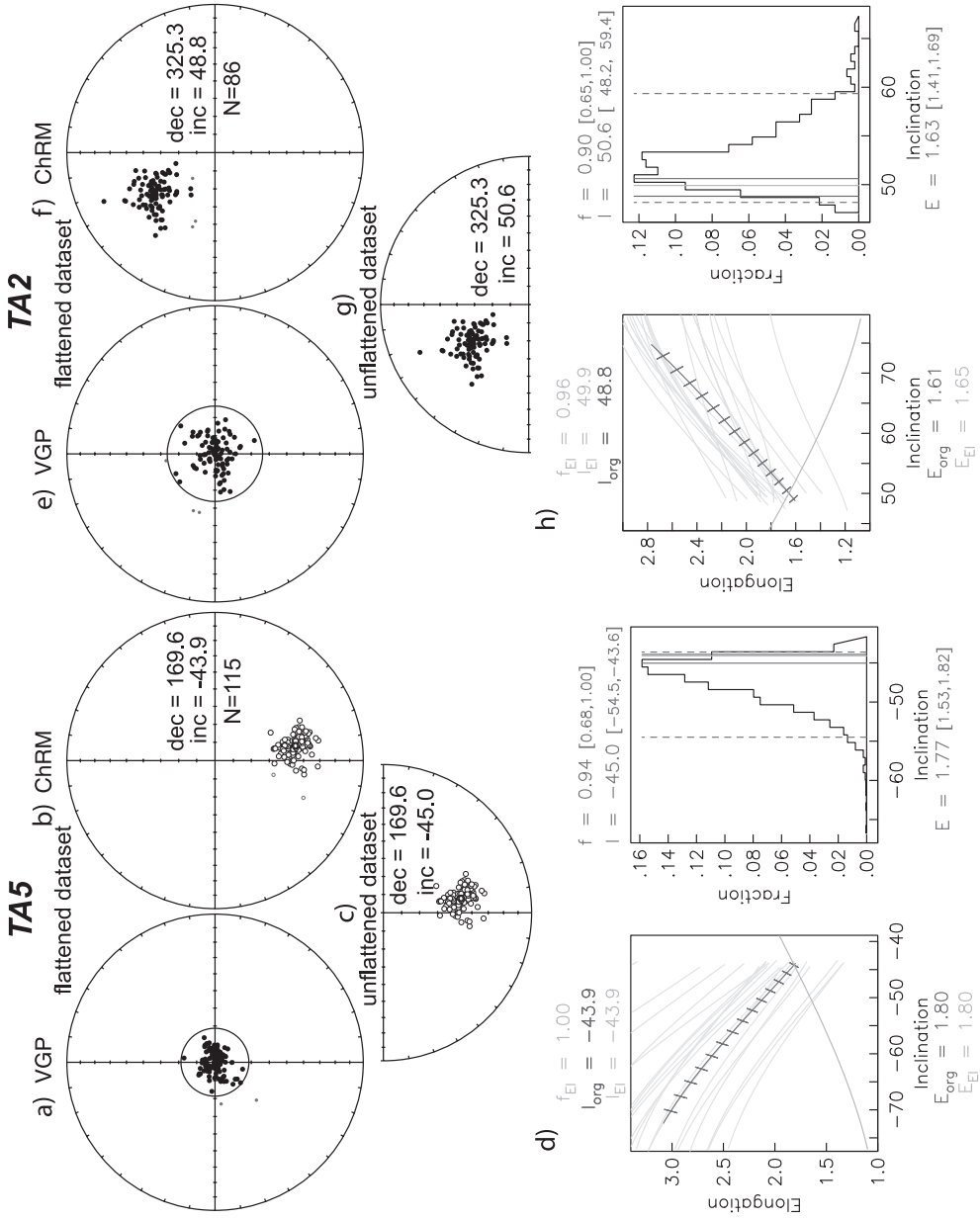


Figure 4.5 (continued) e) Map showing a compilation of all data from our study and from literature data from late Cretaceous rocks that pass our quality criteria. ΔD_x errors of the rotation vectors are shown in grey. Numbers correspond to those in Table 4.2. f) Longitude versus rotation (declination) plot with all accepted datasets included. A clear trend from CCW rotation to zero rotation to CW rotation can be observed in the central Pontides. See Appendix 19

Figure 4.6 a)-h) Equal-area projections of the individual VGP directions before E/I correction (a and e) and equal-area projections of the individual ChRM directions before (b and f) and after (c and g) E/I correction (symbols as in Figure 4.5) (Tauxe and Kent, 2004) with corresponding elongation vs. inclination (d and h, left panels) and fraction (of 5000 bootstraps) vs. inclination plots (d and h, right panels) for TA5 (a-d) and TA2 (e-h). In the elongation vs. inclination plots the E/I for the TK03.GAD model (green line) and for the datasets (red barbed line) for different degrees of flattening are plotted. The red barbs indicate the direction of elongation (horizontal is E–W and vertical is N–S). Also shown are examples (yellow lines) from 20 (out of 5000) bootstrapped data sets. The crossing points (if the dataset intersects the model) represent the inclination/elongation pair most consistent with the TK03.GAD model, given as inc_{EI} (in green) above the panel; inc_{org} = original inclination, E_{org} = original elongation of the dataset, E_{EI} and inc_{EI} are the elongation and inclination, respectively. In the fraction/inclination plot, a histogram of intersecting points from 5000 bootstrapped data sets is shown. The most frequent inclination (solid red vertical line; dashed red vertical lines denote the 95% bootstrap error) is given as value (and error range) on top of the panel; the inclinations of the original distribution (blue vertical line) or the intersection with the model (green vertical line) are indicated; E = the elongation resulting from the bootstrapped data sets. See Appendix 20



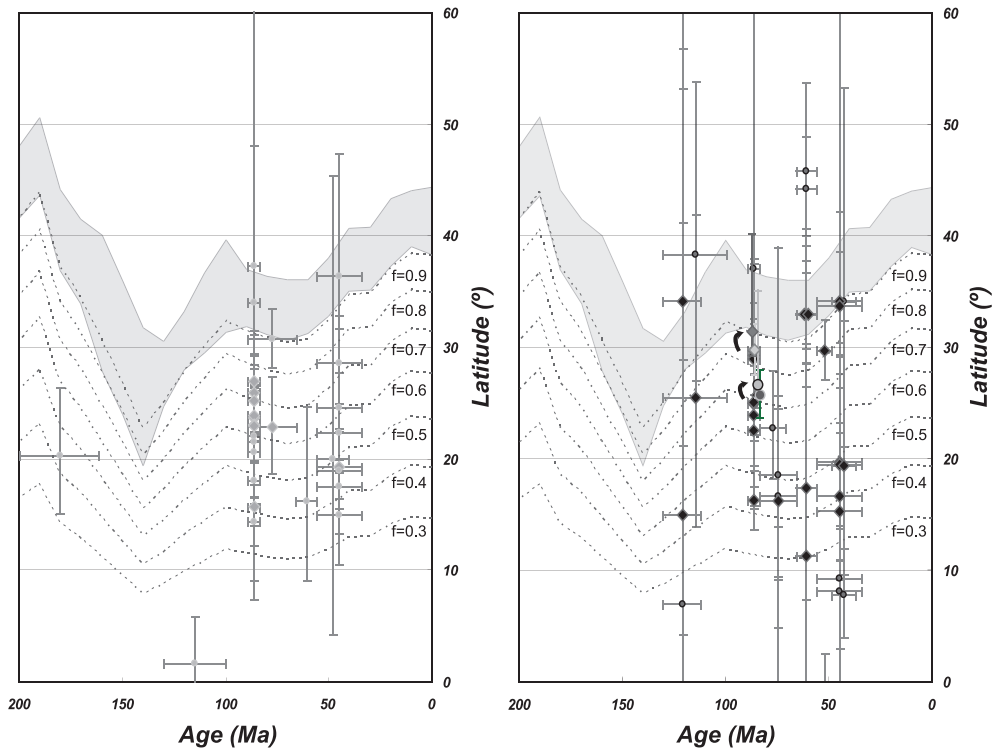


Figure 4.7

Paleolatitude versus age diagrams showing the expected paleolatitude for Eurasia with its $\Delta\lambda$ error envelope (in grey) calculated from the ΔI_x according to Torsvik et al. (2008). Blue dotted lines show latitude versus age curve when a flattening of 0.9-0.3 was applied to the values calculated by the APW path (King, 1955). Left panel: large green diamonds (accepted) and small green circles (rejected) indicate paleolatitude with the $\Delta\lambda$ calculated from the ΔI_x that was obtained from A95 using the Creer transformation (Creer, 1962) on α_{95} , usually given in literature (Table 4.2). Right panel: large red diamonds (accepted) and small red circles (rejected) indicate paleolatitude with the $\Delta\lambda$ calculated from the ΔI_x (using A95) from this study. Blue diamonds (green circles) showing the paleolatitude of site TA2 (TA5) before and after correction with the E/I method of Tauxe & Kent (2004) with their error bars ($\Delta\lambda$ calculated from the ΔI_x for uncorrected datasets, 95% bootstrap error range for the TK03.GAD corrected datasets).

See Appendix 21

On samples of sites TA2 and BG7, AMS measurements were performed (Fig. 4.8). The alignment of the maximum axis is parallel to the structural trend in the area (Fig 1b), and perpendicular to the declination measured in the samples (Fig. 4.4). When back-rotating the anisotropy axes according to the paleomagnetic declination, the maximum axis (lineation) aligns in an east-west direction, implying EW extension or NS compression.

5. Discussion

On the basis of this paleomagnetic study we show that the convex northward shape of the Pontides is reflected in declinations of upper Cretaceous rocks (~90-83 Ma, in one

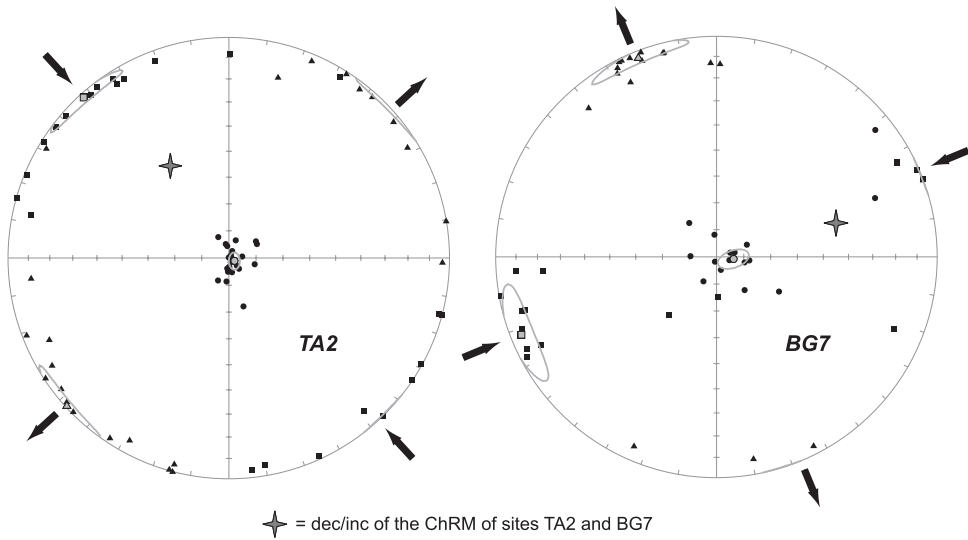


Figure 4.8 Equal-area projections of the AMS (anisotropy of the magnetic susceptibility) for sites TA2 (left panel) and BG7 (right panel). Yellow, large symbols indicate the mean of the tensor mean axes (k_{\min} , k_{int} , k_{\max}) and their error ellipses (Jelinek, 1981). Arrows represent inferred extension/compression directions. Red star indicates the ChRM direction of the rocks from sites TA2 and BG7. *See Appendix 22*

case in rocks of ~83-65 Ma (K5-7). The sampled Paleocene and Eocene rocks do not show significant variations across the region. Hence, we conclude that the Pontides is an orocline that formed between latest Cretaceous (~83 Ma) and Paleocene (65 Ma). We suggest that the AMS directions are inherited from an early north-south compressional event and were rotated during orocline formation, because the magnetic lineations are nearly parallel when their present orientation is corrected for the paleomagnetically determined vertical-axis rotations at both sites. This is in contrast to the conclusions of Scheepers and Langereis (1994) who argued that the end phase of tectonic rotations (in the southern Apennines, Italy) probably corresponds to a blocking of the system. They concluded that the alignment of the magnetic lineation must have taken place (just) after tectonic rotations. On the contrary, in the Gran Sasso range (northern Apennines, Italy) Sagnotti et al. (1998) found magnetic lineations assuming a nearly parallel trend when their orientation is corrected for the vertical axis rotations. Moreover, their pattern of the magnetic lineation trends does not appear affected by recent extensional tectonics or by the development of late out-of-sequence thrusts. Their observations strengthen our interpretation that the magnetic lineation in the sedimentary sequences of the central Pontides was induced at an early stage of tectonic deformation, during an early pre-rotational compressional phase. It seems that neither orocline formation or post-Cretaceous compression re-aligned the AMS directions (Fig. 4.8).

It is important to note that the magnitude of Coniacian to Campanian

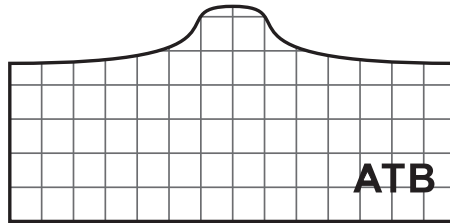
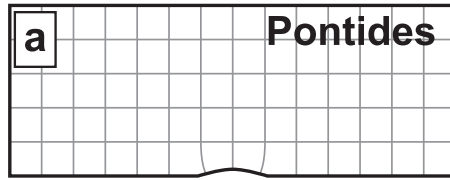
rotations is longitude-dependent (Fig. 4.5f) and there is no rotation detected in the Paleocene units. This implies that the orocline formation in the Pontides took place approximately during the Maastrichtian to earliest Paleocene (70-65 Ma). However, Kaymakcı et al. (2003) and İşseven and Tüysüz (2006) have reported that there are clockwise and counterclockwise rotations during the Eocene-Oligocene interval in respectively the eastern and western side of the Çankırı Basin located to the south of the center of the orocline. In addition, there is general consensus that the convergence and related compressional deformation between the Anatolide-Tauride Block and the Pontides was continuous during the late Cretaceous to Eocene (Kaymakcı et al., 2003; Kaymakcı et al., 2009; Okay et al., 1994; Okay and Tüysüz, 1999; Robinson, 1997; Robinson et al., 1996; Şengör and Yılmaz, 1981; Tüysüz, 1999; Tüysüz and Tekin, 2007).

The rocks from Eocene sites in the northern part of the Pontides contain no rotation while there are strong clockwise and counterclockwise rotations in the southern part of the Pontides, within the Çankırı Basin (Kaymakcı et al., 2003), and clockwise rotations east of the Çankırı Basin and IAE suture zone (İşseven and Tüysüz, 2006). This implies southwards migration of the deformation front and shortening within the heart of the orocline between Maastrichtian to Oligocene. Deformation caused by ongoing convergence between Africa and Eurasia was more or less evenly distributed in the region while the shortening was taken up in the south along the Izmir-Ankara-Erzincan suture zone.

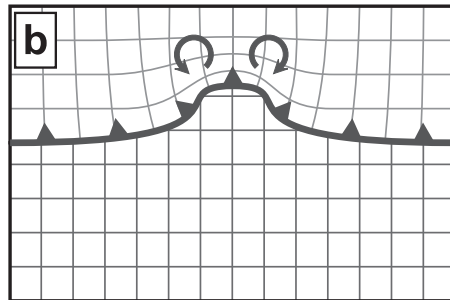
The time constraints on orocline formation now allow us to assess which geodynamic processes may have caused it. There are several possible candidates that may explain oroclinal bending in the Pontides. These include 1) opening of the Black Sea basins, 2) collision of a continental sliver or seamount/oceanic plateau that was located south of the Eurasian margin within the Neo-Tethys ocean and north of the Anatolide-Tauride Block, or 3) collision with the Anatolide-Tauride Block. Orocline formation in the Pontides occurred in latest Cretaceous-early Paleocene times and, therefore, timing of the above mentioned three options plays an important role.

There are two main scenarios for the opening of the western Black Sea basin. According to Görür (1988) the opening of the western Black Sea basin is early Cretaceous (Albian to Cenomanian). According to Tüysüz (1999), however, the main opening of the western Black Sea basin took place later, during the Turonian to Maastrichtian. This discrepancy in timing is mainly caused by imprecise dating and the fact that a major unconformity between the lower and upper Cretaceous sequences was underestimated and regarded as a local event. The updated stratigraphy provided by Hippolyte et al. (2010) (Fig. 1c) suggests that opening of the western Black Sea basin might have taken place in two different phases. The first phase took place from the Hauterivian to Albian while the main opening took place from the Coniacian to Santonian. These phases were separated by mid-Cretaceous (Albian to Turonian) up-

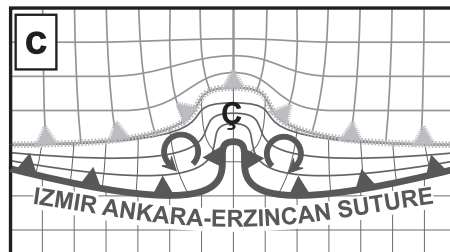
Campanian-Maastrichtian



End of Cretaceous

Indentation: rotation of the
Pontides

Eocene-Oligocene



**Thin skinned thrusting:
Thrusting propagates
southwards. No Paleogene
rotation in the Pontides and main
rotations in the Çankırı Basin**

Figure 4.9 Conceptual model explaining the rotational history of the central Pontide orocline and the Çankırı Basin. a) Campanian-Maastrichtian: Anatolide-Tauride Block (ATB) approaches the Pontides, b) latest Cretaceous: collision of ATB with the Pontides causes orocline formation in the central Pontides, c) Eocene-Oligocene: thin-skinned thrusting propagates southwards, rotation in the central Pontides stops and concentrates in the Çankırı Basin. *See Appendix 23*

lift and erosion that lasted approximately 10 Myrs. Opening of the eastern Black Sea basin probably took place in a sense oblique to the margin of the (eastern) Pontides (Robinson et al., 1996), and opening ages vary from early Cenozoic to Eocene ages (Robinson et al., 1995; Shillington et al., 2008; Vincent et al., 2005). We conclude that the timing of opening of the Black Sea basins does not coincide with oroclinal bending, because rotation of the limbs certainly occurred after the pre-Santonian opening of the western Black Sea basin.

The second possible candidate for orocline formation is the accretion of the Kargı microcontinent. Accretion of Kargı took place in Cenomanian-Turonian times (Okay et al., 2006), which pre-dates oroclinal bending. The scale of the Kargı complex in comparison to the scale of the orocline (Fig. 4.1b) raises questions on the feasibility of this mechanism, and although collision might be responsible for the mid-Cretaceous unconformity in the central Pontides, the scale and the early timing of collision do not make this event a likely candidate to explain the orocline.

The collision of the Pontides and the Anatolide-Tauride Block is the third possible mechanism. The metamorphosed promontory of the Anatolide-Tauride Block, the Kırşehir Block, is located just south of the hinge point of the Pontides orocline (Fig. 4.1b). Part of the collisional history can be reconstructed from the Çankırı Basin that straddles the IAE suture zone. The evolution of the Çankırı Basin can be clearly subdivided into two phases: a late Cretaceous to middle Paleocene forearc evolution, and a late Paleocene-early Miocene foreland evolution phase (Kaymakci et al., 2009). The first phase marks a northward jump of subduction to the southern margin of the Pontides in the Santonian, leading to the deposition of arc volcanics and volcanoclastics of the Yemişliçay Formation (Kaymakci et al., 2009; Okay et al., 2001). This period coincides with extension in the Kırşehir Block (Boztuğ et al., 2009; Gautier et al., 2008; Isik, 2009), that continued until the Maastrichtian and possibly early Paleocene. Although this may (partly) overlap with the formation of the orocline, a direct relationship between extension in the Kırşehir Block and oroclinal bending seems unlikely, since the Çankırı forearc basin suggests free subduction of the northern Neo-Tethys below the Pontides. By the late Paleocene the northern Neo-Tethys separating the Pontides and the Anatolide-Tauride Block was entirely consumed and collision between the Anatolide-Tauride Block and the Pontides occurred (Okay et al., 2001). This was recorded by flysch deposition, unconformable on top of the CACC (Kaymakci et al., 2009). The age of collision of the Kırşehir Block and Anatolide-Tauride Block with the Pontides seems not in conflict with the proposed age of orocline formation, and therefore is the most plausible mechanism to explain the northward convex geometry of the Pontides.

A study on the rotational history of the Çankırı Basin was performed by Kaymakci et al. (2003). The formation of the striking omega shape of the Çankırı Basin was examined by performing paleomagnetic, AMS and paleostress measurements. Those data suggest that the omega shape of the Çankırı Basin was caused by ongoing

indentation of the Kırşehir Block and Anatolide-Tauride Block until the Oligocene, not affecting the central Pontides orocline (Fig. 4.9). Several paleomagnetic datasets from Eocene rocks in the study by (İşseven and Tüysüz, 2006) are in agreement with this scenario. The absence of studies on pre-Eocene rocks does not enable constraining initiation of rotation in the Çankırı Basin. Therefore, we cannot speculate on the possibility of simultaneous rotation in the Çankırı Basin and the Pontides orocline in the latest Cretaceous to earliest Paleocene times. However, the absence of rotation in the northern parts of the Pontides during the Paleocene to Oligocene in contrast with the presence of strong rotations in its southern parts may imply that the shortening and deformation front migrated southwards since the Paleocene (Fig. 4.9). This scenario also implies that the Eocene-Oligocene rotations in the southern parts of the Pontides are related to thin-skinned thrusting within the suture zone.

To assess the position of the Pontides in the late Cretaceous with respect to the Eurasian polepath, we corrected two of our sites for an inclination error, from which we have sufficient individual directions, using the E/I method of Tauxe & Kent (2004). Figure 4.6 a-h shows that inclination correction for Coniacian-Santonian site TA2 and Santonian site TA5 is limited to a few degrees. After correction for inclination error, the original inclination is within the 95% bootstrap error margin, meaning that the correction is not significant. Figure 4.6i shows that both sites plot 3 to 7 degrees in latitude lower than the expected paleolatitude from the Eurasian polepath ($\sim 34^\circ\text{N}$). We note however, that the A95 error envelope of the polepath ($2\text{-}3^\circ$) overlaps with the error margins of the TK03 corrected values. Indeed, small differences of only a few degrees are close to the practical resolution limit (5°) of paleomagnetic studies.

It is obvious that nearly all reported paleolatitudes are much lower than expected from the APW path, which can largely be explained by flattening. We calculated expected flattened latitudes from f -factors as low as 0.3 (Fig. 4.7), that can explain the observed, low paleolatitudes. Paleolatitudes were earlier assessed in a study by Channell et al. (1996), suggesting a gap in the APW path between Eurasia and Pontides of approximately 10° in paleolatitude (Fig. 4.7), when compared to the polepath of Torsvik et al. (2008). However, those data were all taken from sediments and not corrected for inclination error. Correction for inclination error on those data would probably result in a smaller gap between the Eurasian APW path and the location of the Pontides.

6. Conclusions

Analysis of a large number (47 sites, more than 1000 cores) of paleomagnetic data, supplemented with published data, from rocks ranging in age from early Cretaceous to Eocene reveals that the northward convex shape of the central Pontides fold-and-thrust belt can be defined as an orocline that formed in latest Cretaceous to earliest Paleocene times. Orocline formation requires a deformation event such that the pre-

existing structures are bent.

Collision and indentation of the Anatolide-Tauride Block and its metamorphic promontory, the CACC, with the Pontides in late Paleocene times seems to be the most likely mechanism for oroclinal formation, considering the timing of oroclinal bending and the timing of collision between the Kırşehir Block and the Anatolide-Tauride Block with the Pontides. Paleomagnetic data from Eocene to Miocene rocks from the more southward located Çankırı Basin (İşseven and Tüysüz, 2006; Kaymakci et al., 2003), show strong rotations from Eocene to at Oligocene times in this area, suggesting that the shortening and deformation front migrated southward.

Furthermore, the majority of the paleolatitude data from the sampled sites and literature data show a (much) lower paleolatitude than predicted by the Eurasian APW path. Inclination error correction with the E/I-method of two of our sites that allow correction ($N = \sim 100$), predicts paleolatitudes that are within error identical to the Eurasian APW path. This, once more, shows that paleolatitude data from sediments should be interpreted with care.

7. Acknowledgements

The authors would like to thank Bora Rojay and Yener Eyüboğlu for their help in the field to find suitable outcrops for sampling. Pınar Ertepinar, Ane Wiersma and Mustafa Kaya are also thanked for their help in the field. This work was financially supported by the Netherlands Research Centre for Integrated Solid Earth Sciences (ISES) and the Netherlands Organization for Scientific Research (NWO).



View on the Tauride chain from Beyşehir Gölü

CHAPTER 5

Pervasive Paleogene remagnetization of the central Taurides fold-and-thrust belt (southern Turkey) and implications for rotations in the Isparta Angle

The Turkish Anatolide-Tauride block rifted away from the northern margin of Gondwana in the Triassic, which gave way to the opening the southern Neo-Tethys. By the late Paleocene to Eocene, it collided with the southern Eurasian margin, leading to the closure of the northern Neo-Tethys ocean. To determine the position of the Anatolide-Tauride block with respect to the African and Eurasian margin we carried out a paleomagnetic study in the central Taurides belt, which constitutes the eastern limb of the Isparta Angle. The sampled sections comprise Carboniferous to Paleocene rocks (mainly limestones). Our data suggest that all sampled rocks are remagnetized during the late Paleocene to Eocene phase of folding and thrusting event, related to the collision of the Anatolide-Tauride block with the Eurasia. To further test the possibility of remagnetization, we use a novel end-member modeling approach on 176 acquired isothermal remanent magnetization (IRM) curves. We argue that the preferred three end-member model confirms the proposed remagnetization of the rocks.

Comparing our data to the post-Eocene declination pattern in the central Tauride belt, we conclude that our clockwise rotations are in agreement with data from other studies. We then combine our results with previously published data from the Isparta Angle that includes our study area. We cast doubt on the spatial and temporal extent of an earlier reported early to middle Miocene remagnetization event. We further argue that tilt corrected directions of the Triassic data from the southwestern Antalya nappes (western Taurides) that were earlier reported to be remagnetized, are in good agreement with other studies from the area that show a primary origin of their characteristic remanent remagnetization. This implies that we document a clockwise rotation for the southwestern Antalya Nappes since the Triassic that is remarkably similar to the post-Eocene ($\sim 40^\circ$) rotation of the central Taurides. For published results that are clearly remagnetized, we argue that remagnetization has occurred in the Paleocene to Eocene.

1. Introduction

Rifting and subduction of the Tethys oceans led to the northward drift of continental blocks, away from the Gondwanan margin, and their accretion to the Eurasian margin in Mesozoic times (Şengör and Yilmaz, 1981). Paleomagnetism is a widely used technique to reconstruct paleolatitudes of accreted terranes and their vertical-block rotations. Turkey exposes such a terrane – the Anatolide-Tauride block (ATB) – a continental fragment that rifted away from Gondwana in the early Mesozoic (Fig. 5.1) (Gessner et al., 2004; Hetzel and Reischmann, 1996; Kröner and Şengör, 1990; Şengör and Yilmaz, 1981). It collided with the southern margin of Eurasia in late Paleocene to Eocene times (Kaymakci et al., 2009; Okay et al., 2001). The analysis of timing and rates of opening and closing of the Tethys ocean that accommodated the northward drift of the ATB from Gondwana to Eurasia is essential to reconstruct its plate tectonic history. The available published reconstruction scenarios rely mainly on geological interpretations of the relict, intensely deformed rocks and pre-Alpine basement that are now exposed within the collision zone. Dissimilarity of most of the proposed models related to the position of the ATB with respect to the African margin from Permian to Jurassic times (Mackintosh and Robertson, 2009; Moix et al., 2008; Robertson et al., 2004; Şengör, 1984; Şengör and Yilmaz, 1981; Stampfli and Borel, 2002) indicate that there is large degree of freedom in the interpretations, which is mainly due to a lack of reliable data to constrain paleo-positions of the tectonic blocks.

In this contribution, we aimed at constraining the paleolatitudinal position of the ATB, and its position with respect to the African and Eurasian margins. We conducted a paleomagnetic study for the Carboniferous to Eocene stratigraphy of the central Tauride fold-and-thrust belt, to fill the gaps in the existing paleomagnetic data (Gallet et al., 1996; Gallet et al., 2000; Gallet et al., 1992; Gallet et al., 1993, 1994; Piper et al., 2002; Van der Voo and Van der Kleijn, 1970). This study must document, however, that such a paleolatitude reconstruction is not possible due to a regional, pervasive remagnetization event that resets the magnetic record in the central Taurides fold-and-thrust belt. We estimate from our data that this remagnetization event took place in the Paleogene. In addition, we discuss the implications of this finding within the context of previous discussions related to cause and timing of the remagnetization event (Morris and Robertson, 1993; van Hinsbergen et al., 2010a), as well as regional block rotation scenarios of the central Taurides (Kissel et al., 1993; Piper et al., 2002). We will discuss the implications of our findings for these studies and the regional tectonic scenarios that were inferred from them.

2. Geological background

The Anatolide-Tauride block (ATB) in southern Turkey is of peri-Gondwanan origin, indicated by paleontological data and pre-Alpine basement ages (Kröner and Şengör, 1990; Satir and Friedrichsen, 1986; Şengör et al., 1988). The ATB is separated from

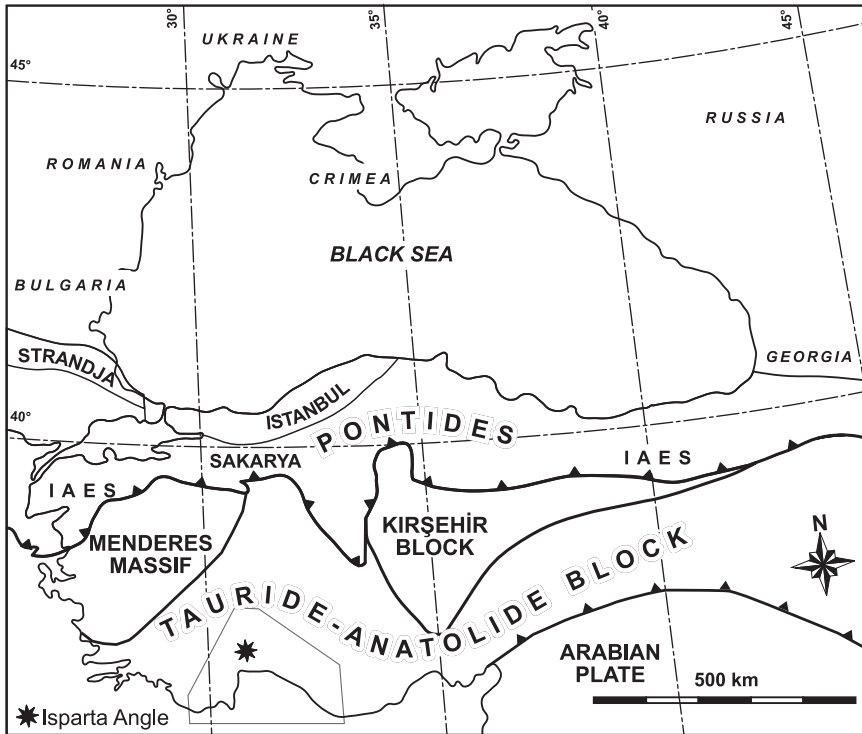


Figure 5.1 a) Map showing the Taurides in the circum-Black Sea region. IAES=İzmir-Ankara-Erzincan suture zone. Grey box indicates the position of Figs. 5.2a-c).

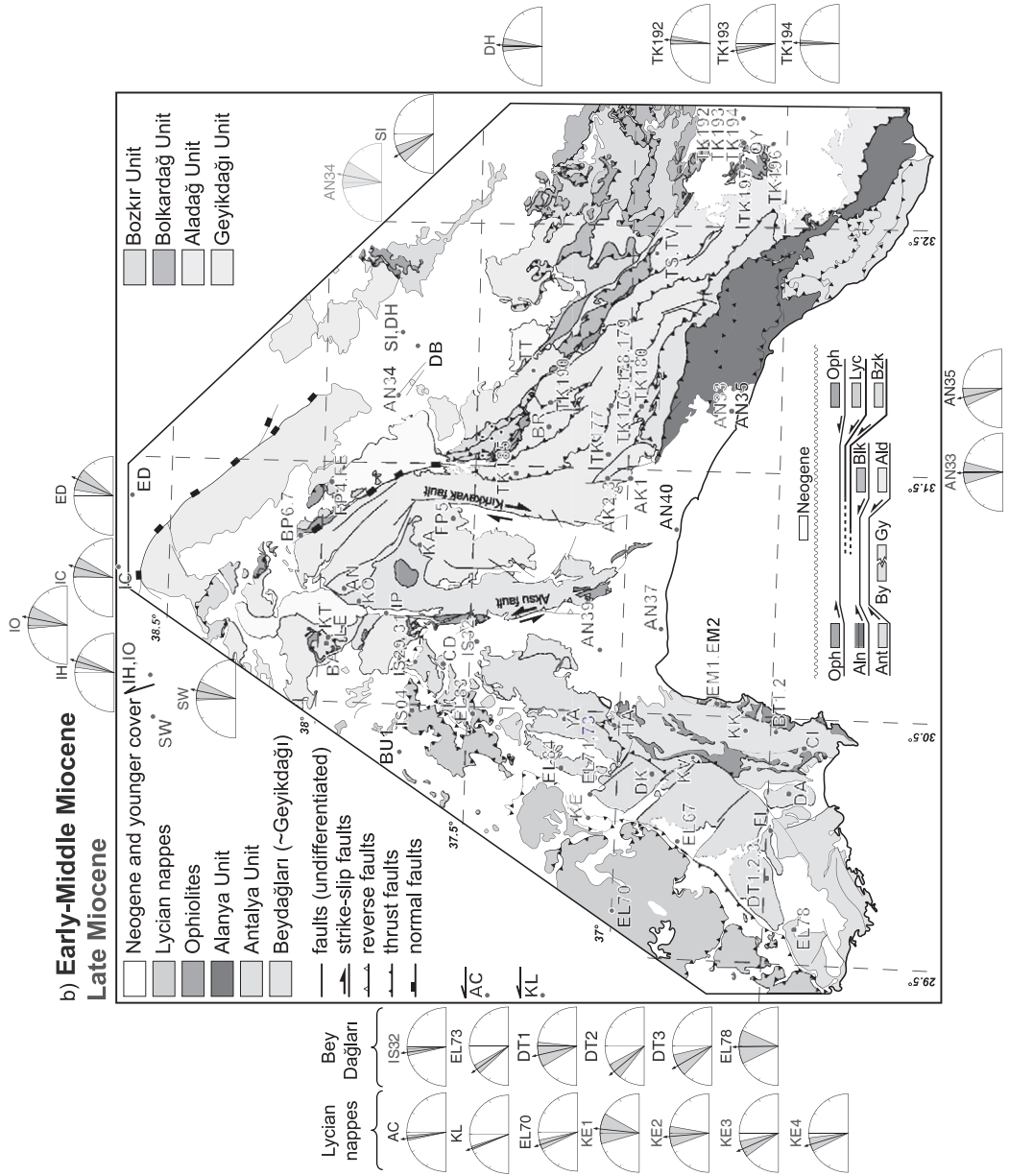
the northward located Pontides, of Eurasian affinity, by the İzmir-Ankara-Erzincan suture zone (Şengör and Yilmaz, 1981). From the African continent it is separated by the still-subducting Levantine lithosphere (along Hellenic-Cyprian trenches), which is likely of oceanic nature (Khair and Tsokas, 1999) (Fig. 5.1). It is generally accepted that after the assemblage of Pangea at the end of the Paleozoic, a large triangular domain - the Paleo-Tethys ocean - occupied the area between the Eurasian and Gondwanan margins (Şengör, 1984). Paleogeographic models related to the size, evolutionary history and subduction polarity of the Paleo-Tethys vary widely (Moix et al., 2008; Robertson et al., 2004; Şengör and Yilmaz, 1981). However, subduction of Paleo-Tethys gave way to rifting off of continental blocks from the northern margin of Gondwana and gave way to opening of the Neo-Tethys ocean during the Mesozoic. Estimates on timing of opening of the southerly located Neo-Tethys ocean between Africa and the ATB vary from late Permian to early Triassic (Moix et al., 2008; Stampfli and Borel, 2002), Triassic (Robertson et al., 2004) to late Triassic (Şengör, 1984; Şengör and Yilmaz, 1981). There is however a general consensus that from late Jurassic to late Cretaceous times the stratigraphic units of the Taurides developed as a passive margin, reflected by platform and shelf carbonates (Gutnic et al., 1979; Monod, 1977; Özgül, 1976).

During the late Cretaceous, the ATB was incorporated into the subduction

system and obducted by ophiolites that originated from northwards subduction of the Neo-Tethys around 90-80 Ma. During the Paleocene to early Eocene it collided with the Pontides after northern Neo-Tethys closure. This resulted in the development of a fold-and-thrust belt that presently forms the Tauride mountain belt (Bağcı and Parlak, 2009; Çelik et al., 2006; Elitok and Drüppel, 2008; Kaymakci et al., 2009; Okay et al., 2001; Robertson et al., 2009; Şengör and Yılmaz, 1981). The ATB is separated from the Pontides by two major crystalline massifs – the Mendere Massif in the west, and the Central Anatolian Crystalline Complex, or Kırşehir Block in central Turkey (Okay et al., 1996, Şengör & Yılmaz 1981). These two complexes are known as the Anatolides and are generally accepted as the metamorphosed northern extension of the ATB which were obducted, metamorphosed and thrust during the late Cretaceous to early Paleogene (Kaymakci et al., 2009; Okay et al., 2001; Robertson et al., 2009). The degree of metamorphism decreases southwards which indicates southward obduction and thrusting. The Taurides (*sensu stricto*) refer to the southern unmetamorphosed part of the ATB.

The ATB comprises sedimentary sequences ranging in age from Cambrian to Tertiary, mostly composed of shallow marine platform type carbonates (Altınler et al., 1999; Dean et al., 1999; Mackintosh and Robertson, 2009; Monod, 1977; Özer et al., 2004; Özgül, 1976; Şengör and Yılmaz, 1981). The Taurides consist of several isopic units (Fig. 5.2) that are overthrust and stacked as nappe sequences, mainly during the late Cretaceous to Oligocene (Andrew and Robertson, 2002; Özer et al., 2004). Paleogeographically, these isopic zones include (from south to north) the Antalya, Alanya, Geyikdağı, Aladağ, Bolkardağı, and Bozkır units. The Geyik Dağ Unit is structurally the lowest and relatively autochthonous unit (Fig. 5.2). Having the similar structural position and stratigraphy, the unmetamorphosed and mildly deformed Beydağları Unit is generally considered as the lateral equivalent of the parautochthonous Geyikdağı Unit (Özgül, 1976). In general, the Geyikdağı Unit is overthrust by the Aladağ, Bolkardağ and Bozkır units from the north (Figs. 5.2 and 5.3). The position and emplacement direction of the Antalya and Alanya units, however, is a matter of debate. The end member models include; 1) all the nappes originated from the north (Ricou et al., 1975), 2) the nappes north of Geyikdağı (Aladağ, Bolkardağ, and Bozkır nappes) originated from the north and the ones in the south (Antalya and Alanya nappes) originated from the south (Dumont et al., 1972; Şengör and Yılmaz, 1981), and 3) all the nappes originated from the north, except for the western part of the Antalya nappes which is thrust over the Beydağları Units (Fig. 5.2) (Ricou et al.,

Figure 5.2 (next three pages) a-c) Maps showing the nappes in the research area. Locations of the sites and declinations with their corresponding ΔD_x (grey shading) from published data are indicated in for four different time intervals. a) Paleozoic-Mesozoic (in dark blue) and Paleogene (in red), b) early-middle Miocene (in dark blue) and late Miocene (in red) and c) Pliocene-Pleistocene. Red site codes indicate the sites that are from the shown age interval. Light blue shading in declination plots indicate the in-situ declinations for sites that are (possibly) remagnetized. See Appendices 24-26



1979).

A long compressive deformation phase that resulted in nappe stacking and ophiolite obduction initiated in the late Cretaceous and continued into the early Eocene (~95-50 Ma) (Okay et al., 2001). This resulted in the deposition of Paleocene to middle Eocene turbidite units on top of the carbonates (Dean and Monod, 1970), that mark the timing of youngest compression-related sedimentation of the ATB, contemporaneous with the collision of the ATB with the Pontides of northern Turkey (Kaymakci et al., 2009; Okay, 1984; Şengör and Yılmaz, 1981; Tüysüz, 1999). Nevertheless, ophiolites and ophiolitic units share the highest structural position, and have metamorphic sole ages of ~95-90 Ma, which mark the minimum age for the onset of (intra-oceanic) subduction north of the ATB (Çelik and Delaloye, 2003; Çelik et al., 2006; Dilek et al., 1999; Dilek and Whitney, 1997; Elitok and Drüppel, 2008; Yalınz et al., 2000).

After Eocene times, the Tauride fold-and-thrustbelt was deformed into a peculiar, triangular bend that is known as the Isparta Angle (Fig. 5.1). To the west, the Taurides fold-and-thrust is overthrust by the Lycian Nappes, over the Bey Dağları platform. The Bey Dağları platform is overthrust by the Antalya Nappes from the east to southeast (Fig. 5.2) (Poisson et al., 2003; Robertson and Woodcock, 1981). During the thrusting of the Lycian Nappes over the Bey Dağları platform in the early Miocene, a lower Miocene foreland basin was established in response to southeastward emplacement of the Lycian Nappes (Collins and Robertson, 1998; Hayward, 1984; Kosun et al., 2009; van Hinsbergen, submitted; van Hinsbergen et al., 2010b). This was followed by a middle to latest Miocene counterclockwise vertical axis rotation episode (Kissel and Poisson, 1987; Morris and Robertson, 1993) that affected the entire western limb of the Isparta Angle, including the Lycian Nappes and Bey Dağları region, and which was bounded in the east by transpression partitioned along the Aksu thrust and Kırkkavak strike-slip fault (Fig. 5.2) (Kissel and Poisson, 1987; Morris and Robertson, 1993; van Hinsbergen et al., submitted; van Hinsbergen et al., 2010b). This is reflected by strong folding and thrusting of the lower to uppermost Miocene stratigraphy in the Aksu and Köprüçay Basins which are bordered by these faults (Çiner et al., 2008; Flecker et al., 1995; Glover and Robertson, 1998; Poisson et al., 2003).

The eastern limb of the Isparta Angle (central Taurides), where we conducted our study, has a significantly different late Cenozoic history. The late Cretaceous to Eocene compression episode formed the fold-and-thrust belt of the central Taurides, which is structurally (but not temporarily) equivalent to the Lycian Nappes to the west. The central Taurides fold-and-thrust belt is unconformably overlain by Miocene marine and terrestrial deposits in the Beyşehir, Manavgat, Ermenek and Mut basins, which are only very mildly deformed by normal and strike-slip faults (Bassant et al., 2005; Çiner et al., 2008; Deynoux et al., 2005; Eris et al., 2005). A paleomagnetic study by Kissel et al. (1993) showed evidence for strong clockwise rotation over an

angle of approximately 40° measured in Eocene rocks of the fold-and-thrust belt, whereas available data from the Miocene show no significant rotations here. Hence, they argued that the eastern limb of the Isparta Angle underwent a clockwise rotation phase sometime during the late Eocene and Oligocene, as opposed to the much younger middle Miocene rotation with opposite sense that was reconstructed for the western limb.

3. Paleomagnetic sampling, analysis and rock magnetic analysis

3.1 Paleomagnetic sampling

The original focus of this study was to reconstruct the paleolatitude position of the Taurides since the Carboniferous, on the basis of new paleomagnetic data and a reappraisal of previous work. Therefore, we sampled Carboniferous to Paleocene sections and localities in three areas within the Geyik Dağ and Aladağ units in the central Taurides: Fele (north of lake Beyşehir, middle-Jurassic to late Cretaceous rocks), Seydişehir (west of Suğla lake, late Triassic-Paleocene rocks) and Taşkent (south of Hadim, early Carboniferous-early Triassic rocks) (Fig. 5.3). All samples were taken from limestones, except site TT7, which was sampled in siltstones and claystones. Around the village of Taşkent, four sites were sampled (79 cores). Site TV was sampled at the Tournaisian-Visean boundary (Peynircioğlu, 2005). Sites TS1,2,3 were sampled in Changhsingian (upper Permian) limestones (see Supplementary information and Payne al. (2007)). Sites TS4 and TS5 were sampled in Spathian (upper Olenikian, lower Triassic) limestones (see Supplementary information).

The Seydişehir section consists of 22 sites (428 collected cores) and covers a time span from approximately middle Jurassic to Paleocene. A stratigraphic log with assigned biostratigraphic ages of the Seydişehir section (TT1, TT2 and TT20-TT39) is given in Figure 5.4, and covers a time span from middle Jurassic to Paleocene. Several individual sites that are not part of the section (TT0 and TT3-TT7) were sampled around the lower part and above the section (159 collected cores). Those sites yield ages ranging from late Triassic to middle and possibly late Jurassic for the lower part (TT3-TT5) and Campanian-Paleocene for the upper part (TT6-TT7). Those ages were taken from the geological map of Şenel et al. (2001). The lower Jurassic is absent in this region.

Near the village of Fele (Fig. 5.3), we sampled a section (9 sites with 200 cores) covering a time span from middle Jurassic to late Cretaceous, that was previously biostratigraphically dated (Altiner et al., 1999; Yılmaz and Altiner, 2006). Samples were taken from nine regularly spaced sites within the section, that were correlated to the stratigraphic columns in Altiner et al. (1999) and Yılmaz and Altiner (2006). Samples were collected using a motor drill or an electric drill with generator. Sample orientations were measured with a compass, and sample orientations as well as bedding attitudes were corrected for present-day declination ($\sim 4^\circ\text{W}$).

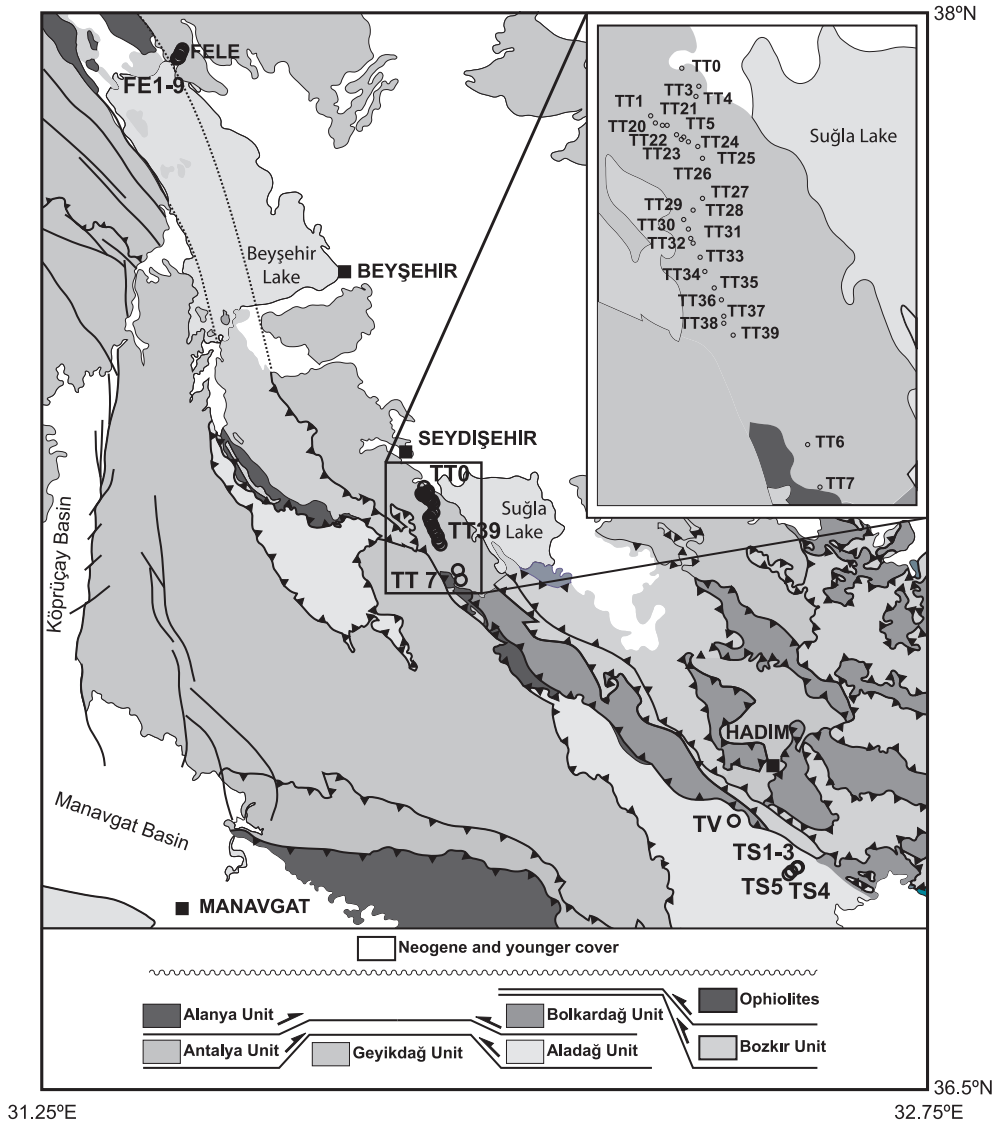


Figure 5.3 Detailed map of the study area, indicating the nappes and the sampling sites. *See Appendix 27*

3.2 Paleomagnetic analysis

Samples were demagnetized using alternating field (AF) and thermal (TH) progressive stepwise demagnetization methods. AF demagnetized samples were pre-heated until 150°C prior to AF demagnetization to remove possible stress in magnetite grains caused by surface oxidation at low temperatures (Van Velzen and Zijdeveld, 1995). Many samples however, gave erratic thermal demagnetization behavior owing to their low NRM intensity, and were therefore only measured thermally until 150°C. The samples were therefore mostly AF demagnetized on the in-house developed robotized

temperature steps. Occasionally, a great-circle approach (McFadden and McElhinny, 1988) was used when samples yielded NRM directions that were intermediate between two components with overlapping coercivity or unblocking temperature spectra (Fig. 5.5g,h,k,l). This method determines the direction that lies closest on the great circle to the average direction from well-determined NRM directions. The majority of the samples, all limestones, have a characteristic remanent magnetization (ChRM) carried by magnetite, as is evidenced by typical maximum unblocking fields of 60-100 mT. Erratic behavior of samples above ~350°C (Fig. 5.5 d and j), also indicates the presence of iron sulfides.

Site mean directions as well as virtual geomagnetic poles (VGP) and their means were calculated from the ChRM directions (Fisher, 1953). Per site, a variable cut-off (Vandamme, 1994) was applied on the VGPs. The sample directions that were rejected on the basis of this cut-off are indicated in Fig. 5.6. We calculated the error

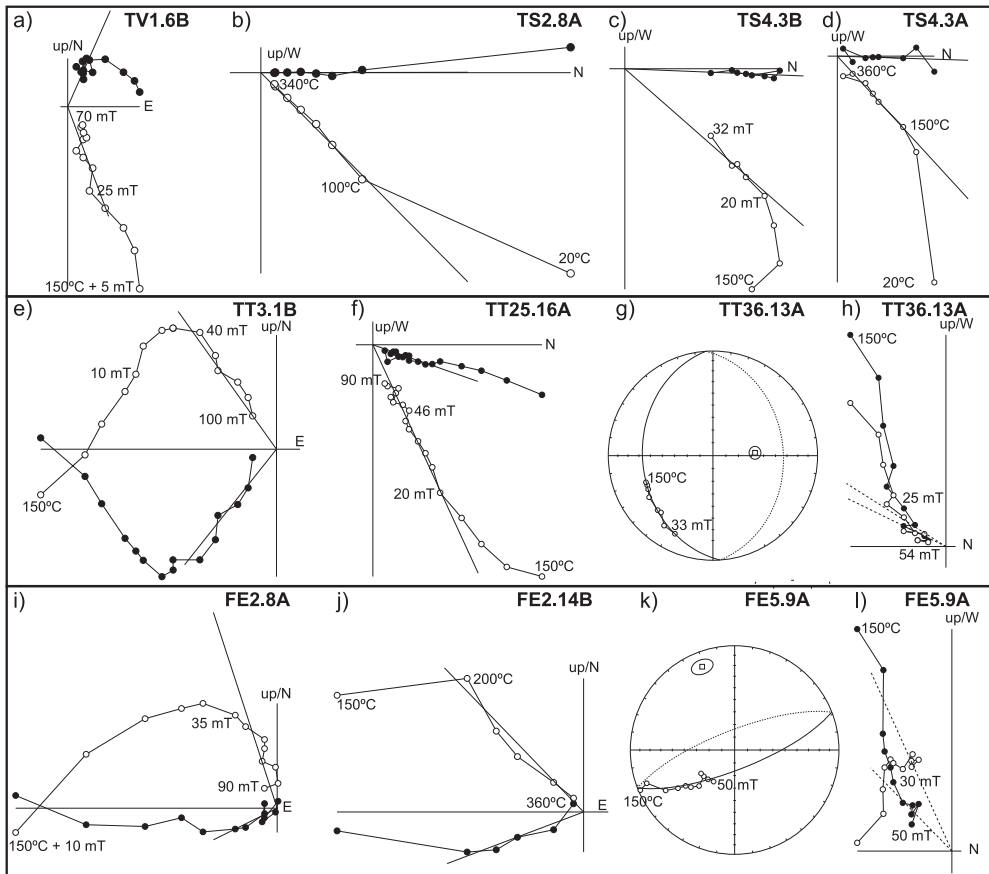


Figure 5.5 Orthogonal vector diagrams (Zijderveld, 1967), showing characteristic demagnetization diagrams for representative sampled sites. Closed (open) circles indicate the projection on the horizontal (vertical) plane. Alternating field and thermal demagnetization steps are indicated. All diagrams are displayed after bedding tilt correction.

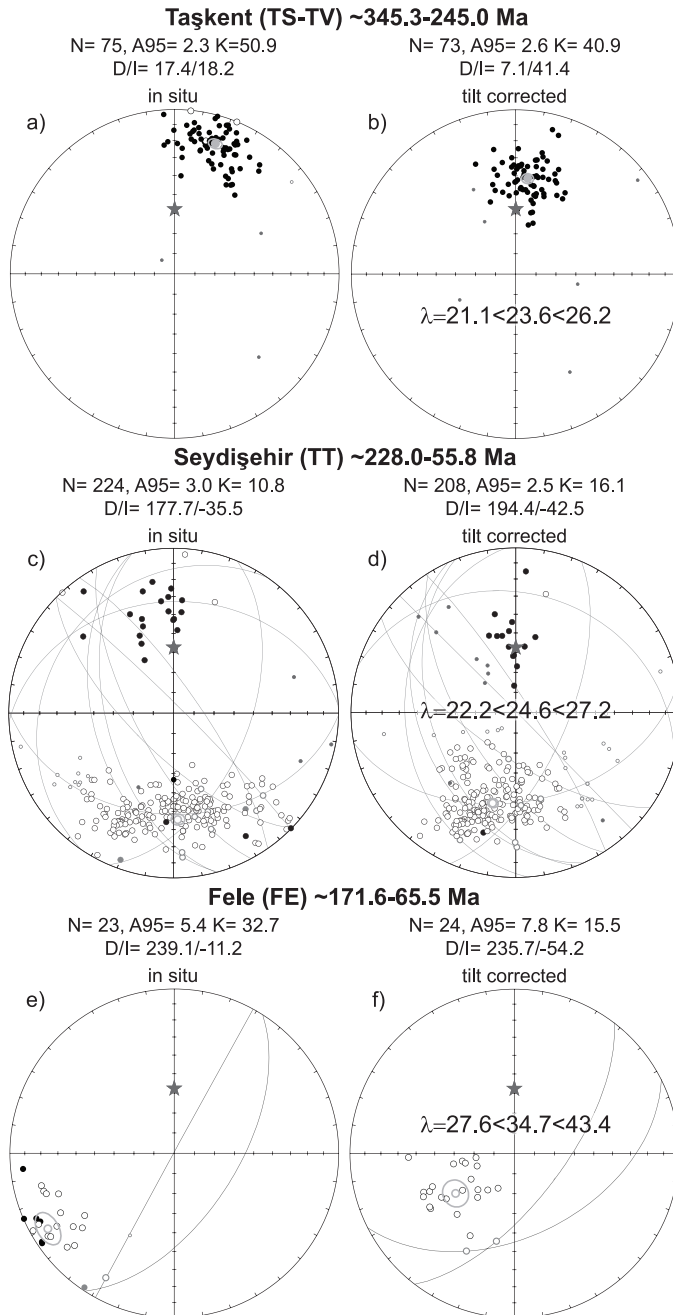


Figure 5.6 Equal area projections of the ChRM directions of all sections (Table 5.1). Open (closed) symbols denote projection on upper (lower) hemisphere. Large black (blue) symbols with black circle indicate respectively the mean directions and their cone of confidence (α_{95}) after (before) tilt correction. Red (small) circles indicate the individual directions rejected after applying a variable cut-off (Vandamme, 1994). Black lines indicate the great circles used to calculate the best fitting ChRM directions (McFadden and McElhinny, 1988). Red star indicates the present-day geocentric axial dipole direction at the sampled location. *See Appendix 28*

in declination (ΔD_x) and the error in inclination (ΔI_x) following Butler (1992). This approach is favored because it more realistically describes the directional distributions that become increasingly elongated with lower latitudes (Creer et al., 1959; Tauxe and Kent, 2004; Tauxe et al., 2008). For all previously published data we calculated the $A95$ from the α_{95} , usually given in literature, using the Creer transformation (Creer, 1962).

3.3 Supporting rock magnetic analyses

Acquisition curves of the isothermal remanent magnetization (IRM)

The paleomagnetic data obtained from this study are most probably subject to remagnetization. Therefore, isothermal remanent magnetization (IRM) curves were acquired, to complement the paleomagnetic analysis and to further characterize the rock magnetic behavior of the samples. We carried out the IRM measurements on 174 specimens from the Seydişehir section, because we intended to run end-member modeling on this section (Gong et al., 2009; Heslop and Dillon, 2007; Heslop et al., 2007; Weltje, 1997), that may indicate remagnetization of the rocks. The Seydişehir section consists of many levels and the rock types (limestones, sandy/shaly limestones, dolomitic limestones, dolomite), compared to Fele and Taşkent localities, and therefore had our preference. Before IRM acquisition, the specimens were pre-heated until 150°C in a magnetically shielded oven and all specimens were first demagnetized at 300 mT in three orthogonal directions, to minimize the influence of magnetic interaction and thermal activation on the shape of the IRM acquisition curves guarantee an IRM curve shape as close as possible to a cumulative log-Gaussian distribution (Heslop et al., 2004). The IRM was acquired in 57 steps until 700 mT, with the in-home developed robotized magnetometer. IRM component analysis to identify the different IRM components was done according to Kruiver et al. (2001). In this approach IRM components are considered cumulative log-Gaussian distributions that are characterized by their saturation isothermal remanent magnetization (SIRM), the peak field at which half of the SIRM is reached ($B_{1/2}$), and the dispersion or width of the corresponding distribution (DP) (Kruiver et al., 2001). In practice many IRM acquisition curves are not entirely cumulative log-Gaussian as a consequence of potentially present magnetic interaction (although in these weakly magnetic sediments it is anticipated to be marginal) and thermal activation characteristic of small magnetic particles (Egli, 2004; Heslop et al., 2004). The IRM acquisition curves could be interpreted with either two or three magnetic components, overlapping in coercivity spectrum. Usually, a low intensity and low coercivity component is observed, a result of slightly skewed-to-the-left data (Heslop et al., 2004). This component is not assigned a physical meaning, because it is a consequence of the method only being able to fit symmetric distributions; its contribution is added to the low-coercivity component.

End-member modeling of the IRM acquisition curves

In a number of cases remagnetization shows up by means of specific magnetic properties. For example, the so-called 'remagnetized' and 'non-remagnetized' trends based on hysteresis parameters are documented for limestones (e.g. Channell and McCabe, 1994). However, many data sets of remagnetized rocks plot in between the two trend-lines which makes the interpretation rather equivocal (e.g. Katz et al., 2000; Zegers et al., 2003). In addition, it is technically not straightforward to measure meaningful hysteresis parameters in weakly magnetic rocks like those in the present investigation. To circumvent these problematic aspects, Gong et al. (2009) proposed to perform end-member modeling on IRM acquisition curves to diagnose remagnetization independent of paleomagnetic directional information. A chemically precipitated suite of magnetic particles as a consequence of burial is expected to have magnetic properties subtly different from a detrital magnetic particle ensemble. IRM acquisition curves determined with a large number of field steps can visualize such small differences. In a study on Cretaceous limestones from the Pyrenees, Gong et al. (2009) discriminated remagnetized and non-remagnetized limestones with a high level of statistical significance (>> 95%). Van Hinsbergen et al. (2010b) used a similar approach to show that Miocene limestones from the Bey Dağları platform (western Turkey) that were overthrust by the Lycian Nappes are not remagnetized, and likely carry a primary NRM.

End-member modeling is a non-parametric inverse technique, meaning that the model is determined from the data. By iterative minimization the data variability is described by a linear combination of a number of invariant points, termed end-members. Both the shape as well as the number of end-members is determined by so-called bi-linear unmixing, which makes the method powerful. Simultaneously, it has potential pitfalls: since (almost) everything is possible, the user must have at least a certain idea about the significance of potential end-members: the solution is mathematically non-unique and the most reasonable geological solution should be targeted (cf. Weltje, 1997). It must be reasonably certain that the entire data variability has been sampled; otherwise the resulting end-members are not representative. We therefore determined IRM acquisition curves for the limestones, dolomitic limestones, sandy limestones, and shaly limestones of the Seydişehir section. The bi-linear unmixing algorithm of Weltje (1997) programmed by D. Heslop in MATLAB was utilized. This algorithm determines the minimum hull around the data space which ensures geologically most interpretable end-members (Weltje, 1997). It starts with a configuration within the data cloud which is iteratively enlarged by moving the end-member compositions minimally, ideally until all data points are included. In practice, it is accepted that some data points remain outside the calculated hull which makes the algorithm less sensitive to outliers, a distinct advantage over other bi-linear unmixing approaches. The algorithm dictates that input curves should be monotonously increasing (Weltje, 1997; Heslop et al., 2007). All IRM curves will be normalized to

their maximum value, thus forming a closed data set. Therefore, the abundances of the various end-members will not be independent, i.e. changes in the abundance of an end-member will affect the abundances of other end-members. The program performs a maximum of 1000 iterations, unless the maximum convexity level of -6 (a descriptor of the distance between the data outside the hull and the calculated minimum hull) is reached earlier. The convexity level at termination is used as a judgment on the quality of the model for the particular data set.

As mentioned earlier on, the signatures of the individual end-members must be understood for an optimal analysis. It is likely that end-members should be interpreted along the lines of magnetic minerals. Therefore, we plotted all IRM acquisition curves and analyzed twenty-one IRM acquisition curves (one from each site) using the cumulative log-Gaussian approach of Kruiver et al. (2001). This is a parametric approach to identify the different coercivity components which serves as a guideline for the interpretation of the end-members. The estimation of the number of meaningful end-members is based on the calculation of the coefficient of determination (r^2 , ranging from 0 to 1) between the input data and the end-member models (Heslop et al. (2007)), that are calculated by the program for 2-9 end-members. A low r^2 ($r^2 < 0.5$) will reflect a non-adequate description of the variance of the input data set. Ideally, the r^2 value is high (> 0.8) and addition of extra end-members will provide only small increase in r^2 . The shape of the end-members should be sufficiently different to avoid over-interpretation of end-members. To ensure monotonously increasing IRM acquisition curves, IRM data were used starting at 8 mT fields. Inspection of the data revealed that the data from lower (pulse) fields were fairly noisy because of very low IRM increments.

4. Paleomagnetic and rock magnetic results

4.1 Paleomagnetic results – demagnetization of the NRM

Taşkent

The samples of sites TV and TS1-3 have initial intensities of ~ 350 - $3000 \mu\text{A}/\text{m}$, those of TS4 and TS5 are lower, ~ 130 - $600 \mu\text{A}/\text{m}$. In the majority of the samples, a low temperature (LT) or low coercive force (LC) component is present until $\sim 200^\circ\text{C}$ or $\sim 150^\circ\text{C}$ plus ~ 25 mT. The ChRM direction was usually isolated between $\sim 200^\circ\text{C}$ and 360°C or between ~ 25 mT and 90 mT in 79 samples (Fig. 5.5). All sites around

Table 5.1 Table showing all data from this study. Lat= latitude of the sites, Long= longitude of the site, Nc= number of collected cores, N= number of cores after interpretation and application of a variable cut-off (Vandamme, 1994), Na= number of analyzed samples, D= declination, I= inclination, ΔD_x = declination error, ΔI_x =inclination error, λ = paleolatitude, k=estimate of the precision parameter determined from the ChRM directions, α_{95} =cone of confidence determined from the ChRM directions, K=precision parameter determined from the mean virtual geomagnetic pole (VGP) direction, A95= cone of confidence determined from the mean VGP direction. $\Delta\lambda^+$ and $\Delta\lambda^-$ are the errors in paleolatitude calculated from the A95. All values are given before and after correction for bedding tilt.

Seydisðíshir	Epoch/Stage	Age (Ma)	Age error (Ma)	Lat	Long	Nc	ChRM directions - in situ							ChRM directions - tilt corrected																	
							N/Na	D	I	ΔD_x	ΔI_x	λ	k	$\alpha 95$	K	$\Delta \lambda^+$	$\Delta \lambda^-$	N/Na	D	I	ΔD_x	ΔI_x	λ	k	$\alpha 95$	K	$\Delta \lambda^+$	$\Delta \lambda^-$			
TT0	late Triassic?	213.8	14.2	37.381	31.885	25	19/27	230.6	-31.7	4.0	6.1	31.3	64.5	4.2	78.2	3.8	4.0	3.7	19/27	221.0	-50.6	5.5	5.2	31.4	66.8	4.1	51.8	4.7	4.9	4.5	
TT1	middle Jurassic?	168.4	7.2	37.372	31.860	20	13/14	157.9	-33.3	4.4	6.5	-11.5	85.8	4.5	99.0	4.2	4.4	4.0	13/14	172.3	-44.1	5.2	5.9	25.8	85.7	4.5	80.2	4.7	5.0	4.3	
TT2	middle Jurassic?	168.4	7.2	37.369	31.865	8	8/8	190.0	-35.1	5.9	8.3	5.0	74.5	6.5	100.7	5.5	5.9	5.2	8/8	200.0	-36.7	6.5	9.0	20.4	74.6	6.5	82.5	6.1	6.7	5.7	
TT3	middle Jurassic?	168.4	7.2	37.373	31.870	31	49/50	204.8	-28.0	2.1	3.3	13.0	74.6	2.4	104.1	2.0	2.0	1.9	49/50	212.0	-36.7	2.2	3.0	20.4	74.8	2.4	97.8	2.1	2.1	2.0	
TT4	middle Jurassic?	168.4	7.2	37.372	31.870	11	16/16	136.2	-18.1	9.4	17.2	-25.6	9.6	12.6	16.7	9.3	10.2	8.8	16/16	172.2	-68.6	34.0	14.2	51.9	8.4	13.5	4.3	20.2	23.9	17.0	
TT5	middle-late Jurassic?	160.55	15.05	37.366	31.873	30	6/14	151.0	-34.6	18.9	27.0	-15.5	13.1	19.2	15.1	17.8	23.7	15.2	6/14	171.2	-44.4	26.4	29.8	26.1	10.7	21.4	9.1	23.5	34.4	18.7	
TT6	Cenomanian-Campanian?	96.6	3.1	37.263	31.920	43																									
TT7	Paleocene	60.85	4.85	37.245	31.923	19	2/4	320.6	40.9	-	-	-22.3	-	-	-	-	-	-	2/4	328.5	42.2	-	-	24.4	-	-	-	-	-	-	
TT20	post-Eocene-pre-Bajocian	173.6	2	37.370	31.867	20	16/18	168.1	-37.9	5.3	7.0	-6.0	49.3	5.3	57.7	4.9	5.2	4.6	15/18	183.8	-48.5	7.1	7.2	29.5	44.6	5.8	38.1	6.2	6.7	5.8	
TT21	Bajocian	169.65	1.95	37.369	31.862	20	18/18	177.5	-44.4	3.3	3.7	-1.3	168.6	2.7	137.4	3.0	3.0	2.8	18/18	198.8	-39.8	2.9	3.7	22.6	168.5	2.7	165.8	2.7	2.8	2.6	
TT22	Bajocian-Callovian	166.6	5.4	37.366	31.871	20	12/17	151.0	-36.0	8.2	11.4	-15.5	31.7	7.8	32.6	7.7	8.6	7.1	12/17	168.8	-39.9	9.5	12.1	22.7	31.6	7.8	25.5	8.8	9.9	7.9	
TT23	Bathonian-Berriasian ?	153.95	13.75	37.364	31.872	20	17/18	171.2	-42.5	4.6	5.5	-4.4	89.0	3.8	73.2	4.2	4.4	4.0	17/18	192.8	-47.3	5.1	5.3	28.5	89.0	3.8	65.0	4.5	4.7	4.3	
TT24	Kimmeridgian-Berriasian	147.95	7.75	37.364	31.875	20	3/8	175.7	-34.2	52.5	74.2	-2.2	6.2	54.4	7.5	48.7	-75.1	41.5	3/8	198.9	-40.7	77.5	86.9	23.3	6.2	54.5	4.8	63.8	56.3	50.8	
TT25	Kimmeridgian-Valanginian	146.05	9.65	37.362	31.879	20	12/18	160.6	-29.3	11.6	18.3	-10.0	10.0	14.4	16.0	11.2	13.0	10.1	12/18	166.3	-37.8	13.5	18.0	21.2	10.0	14.4	12.9	12.5	15.1	11.0	
TT26	Kimmeridgian-Valanginian	146.05	9.65	37.359	31.881	20																									
TT27	Kimmeridgian-Valanginian	146.05	9.65	37.346	31.880	20	2/10	175.1	-36.9	-	-	-2.5	-	-	-	-	-	-	2/10	174.4	-38.7	-	-	21.8	-	-	-	-	-	-	
TT28	Kimmeridgian-Valanginian	146.05	9.65	37.342	31.877	20																									
TT29	Kimmeridgian-Valanginian	146.05	9.65	37.339	31.873	20																									
TT30	Kimmeridgian-Hauterivian	142.85	12.85	37.335	31.875	19																									
TT31	Valanginian-Hauterivian	135.1	5.1	37.332	31.876	22	10/22	358.4	33.6	7.4	10.8	-0.8	21.9	7.0	48.1	7.0	7.7	6.5	10/22	356.2	52.5	11.8	10.4	33.1	22.0	10.5	24.8	9.9	11.2	8.8	
TT32	Valanginian-Hauterivian	135.1	5.1	37.331	31.877	20	8/10	339.1	36.1	12.9	17.9	-10.8	14.9	14.8	21.9	12.1	14.5	10.7	8/10	327.4	58.9	22.0	15.1	39.7	14.9	14.8	11.9	16.8	20.5	14.1	
TT33	Valanginian-Hauterivian	135.1	5.1	37.327	31.879	21																									
TT34	Valanginian-Berriasian ?	132.6	7.6	37.322	31.881	20																									
TT35	Berriasian-Aptian	121	9	37.316	31.882	20	9/18	175.4	-41.2	13.4	16.5	-2.3	20.7	11.6	18.6	12.3	14.7	10.7	9/18	198.4	-54.0	18.4	15.3	34.6	20.7	11.6	12.7	15.0	18.3	12.8	
TT36	Albian	106	6.4	37.312	31.888	19	6/17	186.9	-24.5	18.0	30.5	3.5	9.3	23.2	15.6	17.5	22.7	15.8	6/17	180.2	-45.8	30.1	32.6	27.2	8.0	25.3	7.3	26.5	40.5	20.5	
TT37	Cenomanian-Turonian ?	97.65	8.35	37.307	31.888	19																									
TT38	Coniacian-Maastrichtian	77.4	11.9	37.305	31.889	20																									
TT39	middle Eocene	44.5	4.1	37.301	31.892	20																									
TT all	Carnian-middle Eocene	141.9	86.1	37.362	31.879	567	224/285	177.8	-35.6	3.2	4.5	-1.1	10.6	3.0	10.8	3.0	3.6	3.3	208/285	194.4	-42.5	2.8	3.3	24.6	17.1	2.4	16.1	2.5	2.6	2.4	
Taskent																															
TV	Tournaesian/Visean boundary	345.3	0	36.916	32.400	44	11/17	21.1	15.3	5.5	10.3	10.9	44.9	6.9	71.3	5.4	5.7	5.3	11/17	14.9	44.7	7.4	8.4	26.3	49.9	6.5	47.8	6.9	7.4	6.1	
TS1,2,3	Changhsingian	252.4	1.4	36.845	32.503	30	23/24	24.8	25.5	3.6	6.0	13.0	56.7	4.1	75.8	3.5	3.6	3.4	23/24	12.1	42.9	4.8	5.6	24.9	43.0	4.7	50.1	4.3	4.6	4.0	
TS4	Spathian (upper Olenekian)	248	3	36.839	32.491	49	27/28	11.1	14.9	3.5	6.7	5.6	33.8	4.8	63.7	3.5	3.6	3.5	27/28	359.7	41.5	5.3	6.5	23.9	32.4	5.0	34.0	4.8	5.1	4.6	
TS5	Spathian (upper Olenekian)	248	3	36.835	32.487	25	14/15	15.3	14.5	4.4	8.3	7.8	68.2	4.8	84.8	4.3	4.5	4.3	14/15	3.5	35.7	5.8	8.2	19.8	55.3	5.4	53.6	5.5	5.9	5.2	
TS/TV all	Tournaesian-Olenekian	295.2	50.2	36.900	32.450	148	75/79	17.4	18.2	2.3	4.3	8.9	34.0	-2.8	50.9	-2.3	-2.4	-2.3	73/79	7.1	41.1	2.9	3.5	23.6	38.8	2.7	40.9	2.6	2.6	2.2	
Fe1	Bajocian	169.7	1.95	37.992	31.447	24	4/6	235.3	-6.6	8.5	16.8	35.8	56.3	12.4	117.8	8.5	8.9	8.5	4/6	236.1	-42.3	11.3	13.6	24.5	103.7	9.1	80.5	10.3	11.9	9.2	
FE2	Bajocian-Callovian	166.4	5.2	37.991	31.447	20	6/6	238.8	-7.9	7.5	14.8	39.5	31.1	12.2	80.8	7.5	7.8	7.4	6/6	238.9	-55.9	16.5	12.8	36.4	31.1	12.2	26.7	13.2	15.7	11.3	
FE3	Malm	153.35	7.85	37.988	31.445	20	2/6	224.4	-20.1	-	-	26.1	-	-	-	-	-	-	2/6	221.5	-46.4	-	-	27.7	-	-	-	-	-	-	
FE4	Malm	153.35	7.85	37.986	31.444	20	3/4	235.2	-14.2	36.1	72.1	35.7	10.0	41.3	11.7	37.8	75.4	45.8	3/4	228.3	-57.5	99.9	52.9	38.1	9.8	41.8	5.8	56.6	91.5	35.8	
FE5	Malm	153.35	7.85	37.985	31.443	20	3/6	225.8	-17.5	21.7	39.9	27.2	17.2	30.7	34.2	21.4	29.1	20.6	3/6	213.5	-55.7	29.3	28.6	36.3	17.9	30.1	18.7	29.3	42.4	21.9	
FE6	Berriasian-Albian	122.55	22.95	37.980	37.442	21	2/6	246.4	-26.2	-	-	48.9	-	-	-	-	-	-	2/6	238.2	-67.4	-	-	50.2	-	-	-	-	-	-	
FE7	Cenomanian	96.55	3.05	37.980	31.441	37	4/8	253.1	-9.4	12.6	24.7	68.7	27.3	17.9	54.3	12.6	14.0	12.5	4/8	256.7	-53.5	23.9	20.3	34.0	25.0	18.7	22.8	19.6	25.8	15.9	
FE8	Turonian-Maastrichtian	79.5	14	37.979	31.439	20	0/6												0/6												
FE9	Turonian-Maastrichtian	79.5																													

Taşkent yield very similar paleomagnetic directions (Table 5.1, Figs. 5.6 and 5.7), which is unlikely for the long time interval between early Carboniferous and late Permian/early Triassic. Furthermore, all samples show normal polarities, even though they were deposited in a period of dominantly reversed polarity (Davydov et al. (2004) and Wardlaw et al. (2004)), including the Permo-Carboniferous Reversed Superchron (PCRS). We therefore conclude that the Taşkent sites must have been remagnetized at any time after the early Triassic.

Seydişehir

From the Seydişehir section, 28 sites were sampled (TT0-7 and TT20-TT39), with ages ranging from late Triassic to Paleocene (Fig. 5.4). Ages assigned to the sites, on the basis of biostratigraphy, (see Supplementary information and Table 5.1). The limestone samples yield initial intensities of ~ 100 -2000 $\mu\text{A}/\text{m}$, whereas intensities after pre-heating until 150°C range from ~ 5 -300 $\mu\text{A}/\text{m}$. The silt/claystone samples from site TT7 yield higher intensities pre-heating of ~ 450 -700 $\mu\text{A}/\text{m}$. An LC component up to ~ 30 mT is present in the lowest part of the section (sites TT0-TT3), which resembles the present-day geocentric axial dipole (GAD) direction. The high coercivity (HC) component, interpreted to be the ChRM component, was isolated between ~ 30 mT and 90 mT in 231 samples (Table 5.1, Fig. 5.5). For 10 other samples, we used the remagnetization great-circle approach (Fig. 5.5g and k). Most samples yielded reversed polarities (90%). The majority of the sites yielded a reversed polarity, some sites yielded normal polarities, while in some sites both normal and reversed polarities were detected. The directions are clearly shallower than the GAD direction before tilt correction (Fig. 5.6c). We note that site TT36, which is taken from an Albian interval, yielded reversed polarities, in an interval that is part of the Cretaceous Normal Superchron (CNS). Moreover, all sites yielded very similar paleolatitudes around 30°N (Table 5.1, Fig. 5.6) despite age differences of up to ~ 200 Myrs. Again, we must suspect that all rocks in the Seydişehir section are remagnetized. It is important to note here, that the Paleocene site TT7 (that is significantly younger than the rest of the sites) is based on only two data points. Although the paleomagnetic directions obtained from site TT7 are similar to the data from the entire Seydişehir section, we will not include this site in the discussions. The conclusions on the age of remagnetization based on this site would be speculative.

Fele

From the middle Jurassic to upper Cretaceous of the Fele section, nine sites (FE1-FE9) were sampled. Intensities (after pre-heating) typically range ~ 20 -550 $\mu\text{A}/\text{m}$. Intensities of FE8 and FE9 showed even lower intensities, ranging 20-50 $\mu\text{A}/\text{m}$. For this reason, these two sites revealed no interpretable results. A characteristic component was isolated generally between $\sim 35/40$ mT and 90 mT (Fig. 5.5i-l) in 22 samples. For two other samples, we made use of the great-circle approach (Fig. 5.5k). Rocks from

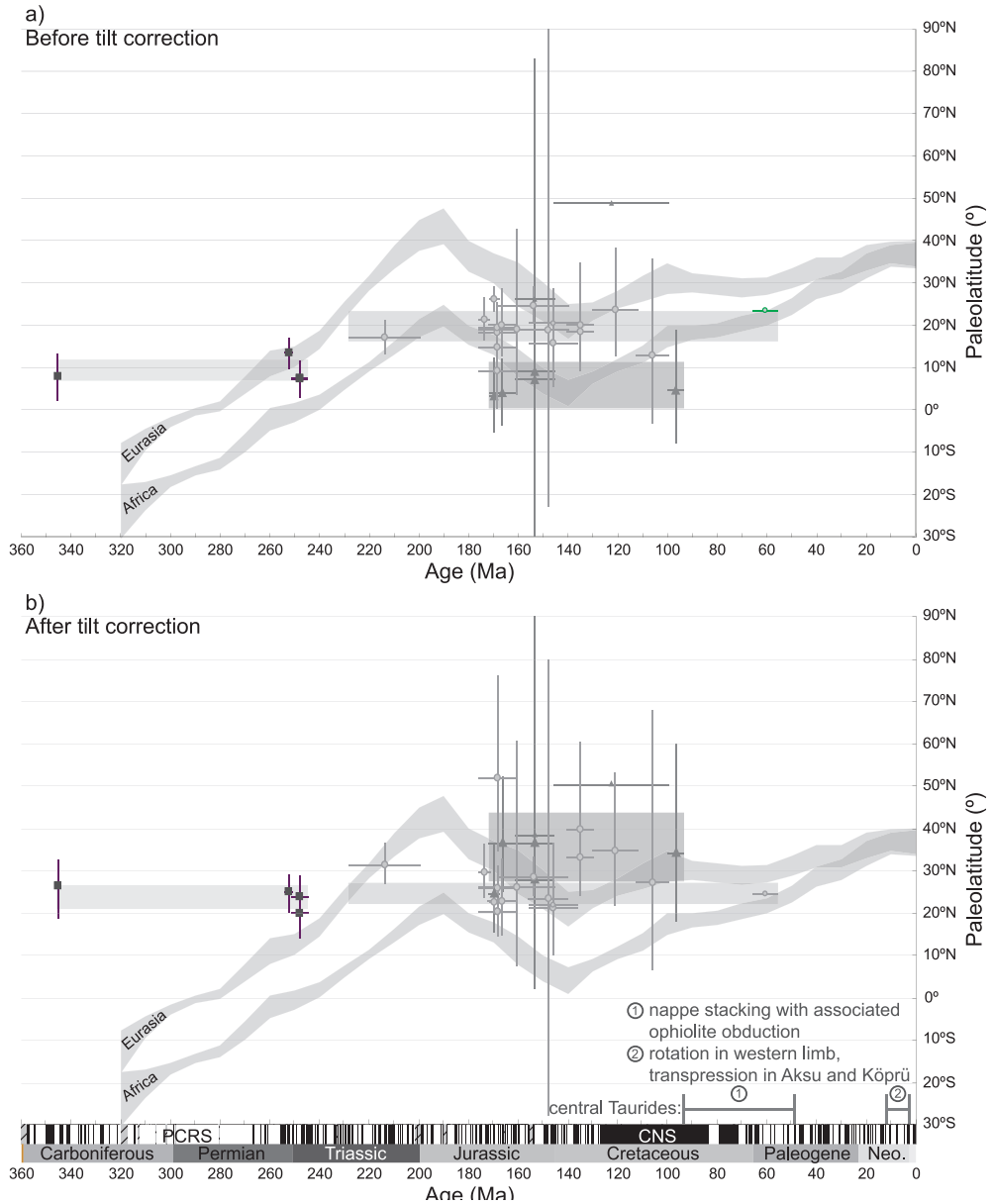


Figure 5.7 Age versus latitude plots of all Tauride data from this study, without tilt correction (a) and with tilt correction (b). Purple squares: data from the Taşkent sites, green circles: data from the Seydişehir section, pink triangles: data from the Fele section. Large shaded squares indicate the average paleolatitude with its error for each area or site. Grey shaded curves: APW path of Torsvik et al. (2008) with its error from 320-0 Ma. Below the curves the magnetic polarity timescale (Ogg et al., 2008) is indicated. PCRCS= Permo-Carboniferous Reversed Superchron, CNS= Cretaceous Normal Superchron, Neo.= Neogene. *See Appendix 29*

all sites, recorded a reversed magnetic polarity (Table 5.1, Fig. 5.6e and f), including site FE7 which has a Cenomanian age. Importantly, the Cenomanian is a stage entirely within the CNS (Ogg et al., 2004). A solely reversed ChRM direction in rocks ranging in age from Bajocian-Maastrichtian, including rocks deposited during the CNS, implies that also this entire section was subject to remagnetization.

4.2 Rock magnetic results

Acquisition curves of the isothermal remanent magnetization (IRM)

First, we will describe the analysis of the IRM acquisition curves using the log-Gaussian approach of Kruiver et al. (2001). Results can be found in Figure 5.8 and Table 5.2. The diagrams show three components: a magnetite component with a $B_{1/2}$ ranging ~50-60 mT and a relatively large DP, and a high coercivity mineral. The high coercivity mineral can be either hematite or goethite, but because the rocks have probably been buried relatively deep, we assume this is a hematite component. The magnetite component is most dominantly present in (partly) dolomitized rocks, and in the upper part of the section in site TT39, where the limestones contain some silt. The hematite component is generally present in non-dolomitic and non-sandy intervals. The third component (without physical meaning) is not always clearly visible, owing to the fairly large DP of the magnetite component. This could be caused by a rather broad grain-size distribution, e.g. resulting from chemical remagnetization where a second generation of small magnetite particles is formed. End-member modeling can visualize potentially small differences amongst the samples, and these can be associated with particular grain-size distributions that must then be explained in terms of the underlying geological processes.

End-member modeling of the IRM acquisition curves

Inspection of the end-member solutions reveals that the two end-member model has a high convexity of (-5.0031, after 1000 iterations) and a lower r^2 value (0.87) (Figs. 5.9a and b). The three end-member model (Fig. 5.9c) has an r^2 of 0.90 (final convexity of -2.501, after 1000 iterations), well above the lower limit of 0.80. Models with a number of end-members >3 have only slightly higher r^2 values and lower final convexity values (Fig. 5.9a). In the four and five end-member models, virtual duplication of end-members occurs which makes those models very unattractive from a mathematical point of view. Moreover those models are difficult to interpret and were discarded. A two end-member model yields a discrimination in a magnetite (with a remagnetized nature, see later on) and hematite end-member (Fig. 5.9b).

The three end-member model is preferred because it appears to show lithological grouping and it represents the break-in-slope of the r^2 vs. number of end-members curve (Fig. 5.9a). The shape of the three end-members (EM 1, 2, 3) is shown in Fig. 5.9c and their partitioning over the samples in Fig. 5.9d. They are interpreted along the lines of magnetic minerals. First, we interpret EM3 (yellow) as caused by hema-

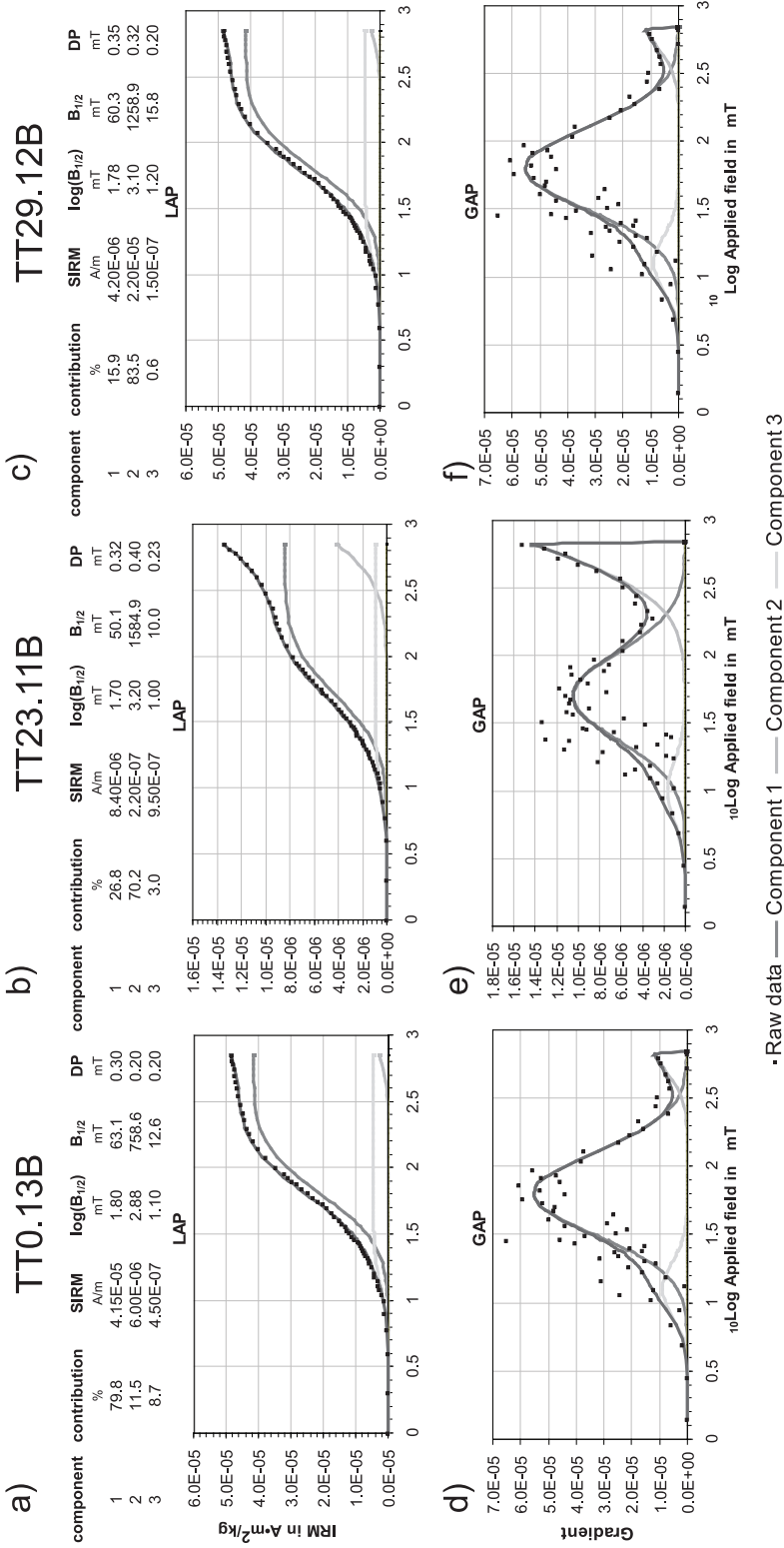


Figure 5.8 a)-c) Examples of IRM component analysis (Kruiver et al., 2001) for three typical samples from the Seydişehir section. A legend for the linear acquisition plots (LAP) and gradient acquisition plots (GAP) is given in the figure. The three distinguished components and their contributions, saturation IRM (SIRM), $\log(B_{1/2})$, $B_{1/2}$ and DP are indicated in the tables. See *Appendix 30*

tite. Samples that contain a large amount of the high coercivity component in the log-Gaussian approach using the log-Gaussian approach of Kruiver et al. (2001), also contain a substantial portion of EM3 (yellow).

EM1 (blue, in Fig. 5.9c) is logically interpreted as representing magnetite. The saturation IRM (SIRM) of this end-member is reached at 500 mT, which is very high for 'classic' magnetite that typically reaches SIRM at 200-300 mT. It is perfectly compatible, however, with the remagnetized magnetite as described by Gong et al. (2009) supporting the remagnetized nature of the present rocks. The majority of the

	%	Am ⁻¹²	mT	mT	mT		%	Am ⁻¹²	mT	mT	mT		
TT22.6B	1	77.6	1.80E-05	1.79	61.66	0.29	TT31.20B	1	8.7	5.60E-06	1.79	61.66	0.36
	2	17.2	4.00E-06	3.00	1000.00	0.30		2	91.3	5.90E-05	3.15	1412.54	0.36
	3	5.2	1.20E-06	1.12	13.18	0.14		3					
TT23.11B	1	26.8	8.40E-06	1.70	50.12	0.32	TT30.19B	1	17.9	2.30E-06	1.83	67.61	0.35
	2	70.2	2.20E-05	3.20	1584.89	0.40		2	81.8	1.05E-05	2.68	478.63	0.27
	3	3.0	9.50E-07	1.00	10.00	0.23		3	0.2	3.00E-08	0.99	9.77	0.05
TT0.13B	1	79.8	4.15E-05	1.80	63.10	0.30	TT25.11B	1	3.3	2.40E-06	1.73	53.70	0.31
	2	11.5	6.00E-06	2.88	758.58	0.20		2	96.6	7.00E-05	3.40	2511.89	0.36
	3	8.7	4.50E-06	1.10	12.59	0.20		3	0.1	1.00E-07	1.20	15.85	0.07
TT39.2B	1	95.0	1.14E-06	1.92	83.18	0.31	TT36.15B	1	51.3	2.00E-06	1.75	56.23	0.30
	2							2	46.2	1.80E-06	2.89	776.25	0.30
	3	5.0	6.00E-08	1.15	14.13	0.28		3	2.6	1.00E-07	1.15	14.13	0.28
TT38.18B	1	8.0	2.80E-06	1.95	89.13	0.67	TT35.16B	1	44.2	6.10E-06	1.67	46.77	0.30
	2	92.0	3.20E-05	2.60	398.11	0.20		2	52.5	7.25E-06	2.91	812.83	0.36
	3							3	3.3	4.50E-07	1.15	14.13	0.28
TT32.16B	1	20.5	2.70E-06	1.79	61.66	0.36	TT34.11B	1	38.5	2.00E-06	1.76	57.54	0.36
	2	79.5	1.05E-05	2.92	831.76	0.27		2	57.7	3.00E-06	2.99	977.24	0.35
	3							3	3.8	2.00E-07	1.00	10.00	0.30
TT21.20B	1	71.0	7.85E-05	1.79	61.66	0.30	TT29.12B	1	15.9	4.20E-06	1.78	60.26	0.35
	2	19.0	2.10E-05	2.95	891.25	0.30		2	83.5	2.20E-05	3.10	1258.93	0.32
	3	10.0	1.10E-05	1.12	13.18	0.20		3	0.6	1.50E-07	1.20	15.85	0.20
TT20.1B	1	77.4	2.23E-05	1.79	61.66	0.29	TT28.17B	1	17.0	1.55E-06	1.85	70.79	0.29
	2	15.6	4.50E-06	2.48	302.00	0.22		2	81.3	7.40E-06	3.21	1621.81	0.40
	3	6.9	2.00E-06	1.15	14.13	0.20		3	1.6	1.50E-07	1.35	22.39	0.20
TT1.9B	1	75.1	2.65E-05	1.82	66.07	0.31	TT27.17B	1	26.6	4.05E-06	1.73	53.70	0.31
	2	17.0	6.00E-06	2.88	758.58	0.30		2	72.4	1.10E-05	3.10	1258.93	0.35
	3	7.9	2.80E-06	1.15	14.13	0.20		3	1.0	1.50E-07	1.35	22.39	0.20
TT37.15B	1	12.0	1.30E-05	1.70	50.12	0.38	TT26.12B	1	21.1	2.70E-06	1.74	54.95	0.30
	2	88.0	9.50E-05	2.95	891.25	0.36		2	78.2	1.00E-05	3.10	1258.93	0.50
	3							3	0.7	9.00E-08	0.90	7.94	0.08
TT33.12B	1	2.6	4.20E-06	1.75	56.23	0.36							
	2	97.4	1.55E-04	3.28	1905.46	0.48							
	3												

Table 5.2 Results of the IRM component analysis (Kruiver et al., 2001). In the columns, the three distinguished components and their contributions are shown: saturation IRM (SIRM), $\log(B_{1/2})$, $B_{1/2}$ and DP.

samples can be seen as mixtures of EM1 and EM3 with only minor contributions of EM2 (purple). The interpretation of EM2 is more complex than that of the other two end-members. It can be a mixture of (relatively soft) magnetite with a tail of hematite. This would be supported by the slightly sandy nature of the limestones with an appreciable EM2 contribution. Alternatively, it could be associated with superparamagnetic magnetite that does not saturate in 700 mT (Gong et al., 2009). The EM2/EM3 ratio is substantially higher in dolomitic limestones and supports this interpretation. In general, dolomitic limestones are associated with high EM1 and low EM3 contributions: only site TT39 has the same characteristics, and consists of shaly limestones.

There is no relation between the EM-distribution and the normal or reversed polarity of the samples. The quality of the demagnetization diagrams does not relate to the end-members either, although dolomitized limestones have higher intensities, and therefore higher quality demagnetization diagrams.

For the interpretation in terms of remagnetization vs. non-remagnetization EM3 is not relevant. EM1 reaches saturation at ~ 500 mT while EM2 is not yet saturated at the highest field of 700 mT. Importantly, a magnetite end-member that reaches SIRM in 200-300 mT fields is not detected in the present data set. This

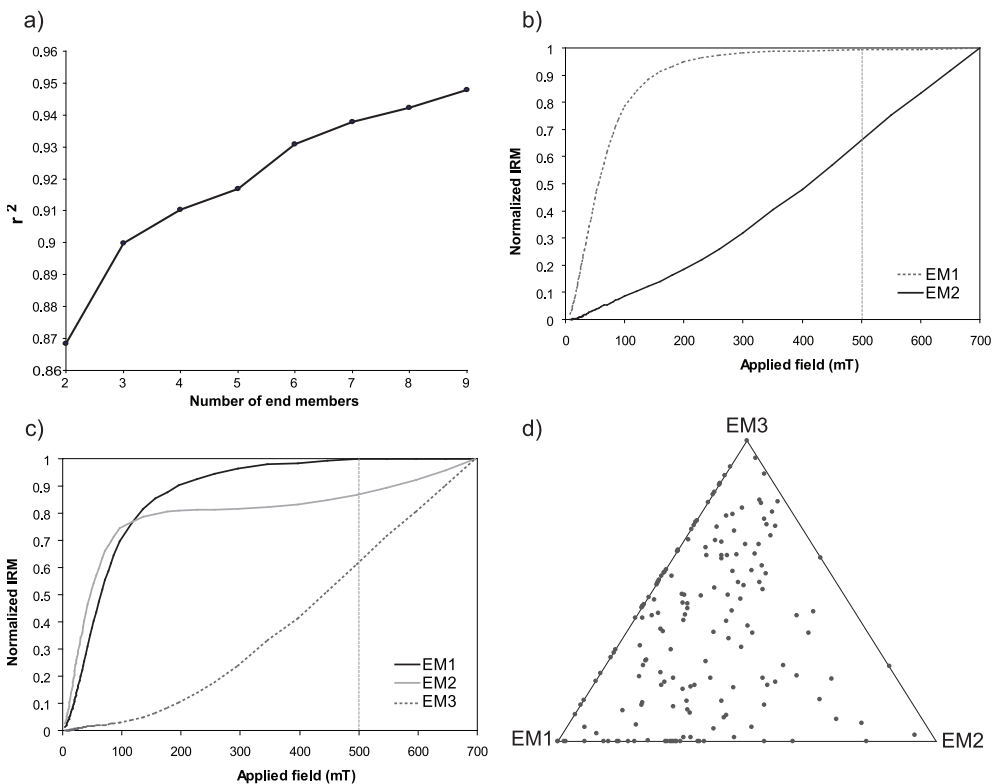


Figure 5.9 a) Diagram showing the r^2 vs. number, b-c) End-member models for the normalized IRM acquisition curves for the two b) and three c) end-member models. d) Ternary plot showing percentages of the three end-members in the end-member model per sample.

implies that it is unlikely that we have non-remagnetized magnetite (that would reach SIRM in 200-300 mT (cf. Gong et al., 2009; van Hinsbergen et al., 2010a). Intriguingly, also in the two end-member model the magnetite EM has a remagnetized nature (it reaches its SIRM at ~ 500 mT). We conclude that the end-member model interpretation strongly supports the paleomagnetic interpretation of remagnetized rocks in this transect.

5. Discussion

The main result of this study is that the three localities in the central Taurides, covering a stratigraphy from Carboniferous to at least upper Cretaceous, underwent remagnetization. We will discuss the implications of this finding in two topics: firstly the regional extent, timing and possible causes of remagnetization. Secondly, we will discuss the implications for the previously inferred vertical axis rotations and paleo-latitudinal position of the Taurides in southern Turkey.

5.1 Timing and cause of remagnetization

We base our conclusions for remagnetization of the Taurides on paleomagnetic (reversed polarities in the CNS and similar inclinations from Carboniferous to Cretaceous rocks) and rock magnetic (IRM end-member modeling) arguments. Morris & Robertson (1993) argued for remagnetization of the Antalya Nappes, based on paleomagnetic arguments (negative fold tests, the lack of reversed polarity samples and area-wide consistency of in-situ mean directions). They argued that this remagnetization event affected also the Bey Dağları region, and that it occurred during Miocene thrusting of the Lycian Nappes over the Bey Dağları platform. In terms of timing, their interpretation for widespread Miocene remagnetization was recently tested and debated by van Hinsbergen et al. (2010a; 2010b) for the Bey Dağları platform. However, the evidence for remagnetization affecting the Antalya Nappes presented by Morris and Robertson (1993) remains firm. On the other hand, Gallet et al. (Gallet et al., 1996; Gallet et al., 2000; Gallet et al., 1992; Gallet et al., 1993, 1994; Gallet et al., 2007) reported Triassic magnetostratigraphies from the Antalya Nappes, suggesting that not the entire nappe stack was remagnetized and does not support the widespread, regional nature of this remagnetization event.

The common setting of our sites in the central Taurides fold-and-thrust belt and their close vicinity render it unlikely that remagnetization is widely spaced in time. Therefore, we will assess the possibility of a common remagnetization process and timing. The reversed polarities in rocks that were deposited during the Cretaceous Normal Superchron demonstrate an age of remagnetization younger than approximately 85 Ma (i.e. the end of the CNS; Ogg et al. (2004)). Results so far reported from Miocene and younger rocks overlying the Taurides yielded normal and reversed polarities with positive reversals tests (Kissel et al., 1993; Kissel and Poisson, 1986; van Hinsbergen et al., 2010a; van Hinsbergen et al., 2010b), which demonstrates that

there is no reason to assume remagnetization of the Miocene. This brackets the timing of remagnetization between 85 and approximately 20 Ma, corresponding to the Burdigalian onset of marine sedimentation on the eastern part of the fold-and-thrust (Bassant et al., 2005).

As discussed previously, the oldest and structurally the highest nappes in the Taurides include the ophiolites (Bozkır, Antalya and Lycian nappes) that occur widespread across southern Turkey. The metamorphic soles of the ophiolites are 95-90 Ma, which is older than the maximum age for remagnetization. After the emplacement of the ophiolites, folding and thrusting of the ATB eventually lead to the development of the fold-and-thrust belt in the early Eocene contemporaneous with the deposition of the youngest foreland basin turbidites. This implies that the remagnetization is possibly related to folding and thrusting during the Paleocene to early Eocene (Özgül, 1983) rather than to ophiolite emplacement during the ~95-90 Ma. Folding and thrusting could also be a candidate for remagnetization in the rocks sampled by Morris and Robertson (1993) in the Antalya Nappes, which underwent nappe stacking in the same time interval (Çelik et al., 2006; Juteau et al., 1977; Robertson and Woodcock, 1981).

Because of very similar tilts in our sampling areas, a fold-test (which would allow assessing whether remagnetization occurred prior to, during, or after tilting) is precluded. Another technique to test syn-tilting remagnetisation is through the use of small circles (Gong et al., 2009; Waldhör and Appel, 2006) Application of this technique, however, is precluded because our sites are most likely rotated with respect to each other after remagnetization (see below). Based on the similar inclinations from all sites after tilt correction, remagnetization probably occurred before tilting or during the early stages of tilting, so in the early stages of folding and thrusting.

If remagnetization occurred after tilting, the in-situ inclinations should coincide with inclinations one can expect for Eurasia since about 85 Ma (i.e. the maximum age for remagnetization, see above), or they should indicate slightly lower inclinations, because the ATB had not sutured with Eurasia at that times. However, the paleolatitudes calculated from inclinations of our sections for the in-situ coordinates are much lower than the Eurasian apparent polar wander path (Torsvik et al., 2008), and even lower than the African APWP at the inferred maximum age of remagnetization and are therefore precluded (Fig. 5.7a). If we apply a full tilt correction, the average calculated paleolatitudes from Taşkent, Seydişehir and Fele (shaded squares, Fig. 5.7b) suggest a paleolatitude that is close to the latitude of Europe during collision, i.e. during the late Cretaceous to early Paleogene. It is therefore most likely that the remagnetization occurred prior to or in the early stages of folding.

Several mechanisms and settings have previously been invoked to explain remagnetization, broadly speaking in two main categories: viscous resetting of existing magnetic minerals at the burial temperature for the burial duration (thermoviscous remagnetization (Kent, 1985). If prevailing burial temperatures are too low to make

this model plausible, neoformation of magnetic minerals by chemical remanent magnetization (CRM) (McCabe and Elmore, 1989) may be an alternative. Fluids are presumed to have delivered the constituents for the newly formed magnetic minerals. Morris and Robertson (1993) suggested that 'orogenic fluids' remagnetized the Antalya Nappes. More recent remagnetization studies, however, are more conservative and do not invoke (large amounts of) external fluid (Blumstein et al., 2004; Katz et al., 2000; Katz et al., 1998; Machel and Cavell, 1999). These latter studies document that diagenetic reactions deliver iron, required to form magnetite, amongst others by reactions involving clay minerals obviating the need for external fluids. When dolomitization of the carbonates is occurring, evolved fluid is reported to have migrated in relation to remagnetization (O'Brien et al., 2007). The role of pressure solution in remagnetization, although equivocal (Elmore et al., 2006; Evans et al., 2003), could be a likely mechanism in the case of the Taurides fold-and-thrust belt, because stylolites are frequently observed.

In other words, it is most likely that the remagnetization was somehow the result of fluids or pressure-build up reactions invoked by folding- and thrusting. Given the continuous sedimentation of the Seydişehir section into the Paleocene-lower Eocene foreland basin deposits, the timing of remagnetization is likely Eocene, and may have influenced all Eocene and older folded and thrust rocks in the central Taurides axis, including those that were used by Kissel et al. (1993) to analyze the Taurides rotation history.

5.2 Implications for regional rotations

Results from previous paleomagnetic studies on Ordovician to Pleistocene rocks in the western and central Taurides are listed in Table 5.3. These studies were conducted for a variety of purposes, including magnetostratigraphy, rotation and paleolatitude studies. In Figure 5.2a-c we indicate the rotation results from all published sites in three time slices (Paleogene, early-middle Miocene and Pliocene-Pleistocene). Because we argue that the rocks of this study were all remagnetized in the late Cretaceous-Eocene, we displayed them in Fig. 5.2a (Paleogene). Our data are combined in three group means (FE, TT and TS-TV), since the sampled areas are relatively small.

In our analysis of our new and published data, we excluded data sets that do not have a minimum number of samples. In sediments, the minimum number of samples is 5; in the case that volcanic rocks were sampled, the minimum required number of flows/sites (with a minimum of demagnetized specimens per lava flow ≥ 5) that constitute one locality is 5, to allow averaging of the secular variation. The accepted sites are indicated in Table 5.3 and their results are displayed in Figs. 5.2a-c and 5.10. From the published data, ten out of 65 data sets were rejected.

We show the rotational data in three time intervals that were chosen on the basis of timing of deformational events. The first time interval covers the Paleozoic-Mesozoic and Paleogene (Fig. 5.2a), and thus includes syn-collisional and younger

rotations. The second interval (early-middle Miocene and late Miocene; Fig. 5.2b) marks a post-collisional deformation phase, which relates to the advance of the Lycian Nappes in the west, and should also include the rotations related to Isparta angle formation. The youngest interval (Plio-Pleistocene; Fig. 5.2c) post-dates the time span of Isparta angle formation (middle Miocene (Langhian) to latest Miocene; van Hinsbergen et al. (2010a).

Morris and Robertson (1993) argue that their Paleozoic-Paleogene data are all remagnetized (except for sites LE and BA). Therefore, these data should be presented in Fig. 5.2a in in-situ coordinates. Recently, however, van Hinsbergen et al. (2010a) showed that remagnetization is most likely not the case for the datasets presented by Morris and Robertson (1993) from Bey Dağları. Therefore, we display these data (CD, DK, FI, DA, YA) after tilt correction. Possibly, also site KO is not remagnetized, considering that the post-tilt direction is very consistent with both BA and LE, and therefore we display this site after correction for bedding attitude. Sites AN, KA and CI are certainly remagnetized and were therefore displayed in in-situ coordinates (blue in Fig. 5.2a), whereas sites HA and KK1-4 are possibly remagnetized, and therefore we displayed them in both in-situ and tilt-corrected coordinates. This is of importance when discussing the Paleozoic-Mesozoic data (Fig. 5.2a), that in general show a disperse pattern, except for the southwestern Antalya nappes. Here, a general clockwise rotation of $\sim 40^\circ$ is visible in the datasets from Morris and Robertson (1993) and Gallet et al. (2000; 1992; 1994), when they are all corrected for bedding tilt (with the exception of the Ordovician site KK1 in Fig. 5.2a). This is rather remarkable, because these clockwise rotations are in agreement with rotations in the central Tauride belt. In particular, all Triassic sites from the southwestern Antalya nappes, both those of Gallet et al. (2000; 1992; 1994) (KV, BT1-2, EM1-2) and those of Morris and Robertson (1993) (HA, KK3), are remarkably consistent, and the calculated paleolatitudes plot within error on the African apparent polar wander path (Fig. 5.10) (Torsvik et al., 2008). Site BA, located in the northern Antalya nappes also yields a paleolatitude that agrees very well with the African apparent polar wander path.

On the contrary, if we do not correct the sites from the southwestern Antalya nappes (KK2-4 and CI) of Morris and Robertson (1993) for bedding tilt, they show exactly opposite rotations to the rotations reported by Gallet et al. (2000; 1992; 1994), but they agree very well with the rotation in Bey Dağları and the Lycian Nappes. It is therefore possible that at least the Triassic sites (except CI) are not remagnet-

Table 5.3 (next two pages) Table showing data from previously published studies. Lat= latitude of the sites, Long= longitude of the site, N= number of samples, D= declination, I= inclination, k=estimate of the precision parameter determined from the ChRM directions, α_{95} =cone of confidence determined from the ChRM directions, λ = paleolatitude, $K_{(VGP)}$ =precision parameter determined from the mean virtual geomagnetic pole (VGP) direction, $A95_{(VGP)}$ = cone of confidence determined from the mean VGP direction, ΔI_x =inclination error, ΔD_x = declination error. $\Delta \lambda^+$ and $\Delta \lambda^-$ are the errors in paleolatitude calculated from the A95.

Tilt corrected

Site	Lat	Long	Age	Age error	N	D	I	k	α_{95}	λ	$K_{(VGP)}$	$A_{95(VGP)}$	ΔI_k	ΔD_x	$\Delta \lambda^*$	$\Delta \lambda^*$	Authors
Pliocene-Pleistocene																	
IS29	37.7	30.7	1.3	0.5	8	5.3	59.0	170.0	3.7	39.8	98.0	5.6	5.0	7.3	6.7	5.8	Kissel & Poisson (1986)
IS31	37.7	30.7	1.3	0.5	9	358.0	58.0	288.0	2.7	38.7	172.0	3.9	3.6	5.0	4.5	4.1	Kissel & Poisson (1986)
BU 1	37.7	30.3	1.3	0.5	9	177.8	-57.7			38.3		10.8	10.0	13.8	12.3	9.6	Van Hinsbergen et al. (2010b)
AN37	36.9	30.9	2.7	0.9	9	186.0	-48.0	270.0	2.8	29.0	221.7	3.5	4.1	4.0	3.1	2.8	Kissel & Poisson (1986)
AN40	36.8	31.3	3.6	1.8	10	358.0	52.0	107.0	4.0	32.6	77.9	5.5	5.9	6.5	5.5	4.8	Kissel & Poisson (1986)
IP*	37.8	30.8	4.4	0.4	20	5.8	52.6	40.1	6.1	33.2	28.6	6.2	6.5	7.4	6.7	5.8	Tatar et al. (2002)
IS04	37.7	30.5	4.5	0.9	9	12.5	46.6	221.0	3.0	27.9	188.8	3.8	4.5	4.2	3.2	3.0	Kissel & Poisson (1986)
AN39	37.1	30.8	4.5	0.9	8	182.0	-52.0	19.0	11.0	32.6	13.8	15.4	16.5	18.4	17.7	12.3	Kissel & Poisson (1986)
DB*	37.6	32.0	5.2	1.7	4	359.0	50.8	33.4	13.4	31.5	25.2	18.7	20.5	22.0	24.4	15.2	Tatar et al. (2002)
late Miocene																	
KE 1	37.2	29.3	6.7	4.9	8	186.2	-23.7			12.4		22.1	38.8	22.7	31.5	20.1	Van Hinsbergen et al. (2010b)
KE 2	37.2	29.4	6.7	4.9	9	354.6	59.6			40.4		11.3	10.0	14.9	12.9	10.0	Van Hinsbergen et al. (2010b)
KE 3	37.2	29.4	6.7	4.9	12	336.2	57.0			37.6		9.3	8.8	11.8	10.4	8.4	Van Hinsbergen et al. (2010b)
KE 4	37.2	29.3	6.7	4.9	20	343.3	54.1			34.6		8.1	8.2	9.9	9.0	7.4	Van Hinsbergen et al. (2010b)
IO*	39.5	30.3	9.3	3.0	13	191.5	-55.7	16.4	10.6	36.2	10.6	13.4	13.0	16.7	15.9	11.5	Gursoy et al. (2003)
DH*	37.7	32.1	9.9	1.0	14	182.5	-46.7	25.6	9.7	27.9	21.8	8.7	10.5	9.9	9.9	7.8	Tatar et al. (2002)
IS32	37.6	30.7	10.5	3.2	8	352.0	43.0	163.0	4.0	25.0	153.4	4.5	5.8	5.0	3.6	3.3	Kissel & Poisson (1986)
AN33	36.7	31.8	10.5	3.2	9	359.0	54.4	24.0	9.5	34.9	16.2	13.2	13.3	16.2	15.6	11.3	Kissel & Poisson (1986)
SW*	38.6	30.4	11.0	3.0	10	192.2	-48.8	20.5	10.9	29.7	16.4	12.3	14.1	14.2	14.6	10.7	Gursoy et al. (2003)
SI*	37.7	32.1	11.6	0.1	5	149.5	-51.8	67.6	11.3	32.4	49.5	11.0	11.8	13.0	12.8	9.7	Tatar et al. (2002)
IC*	38.8	31.0	11.6	0.2	7	196.5	-46.5	27.7	11.7	27.8	23.7	12.6	15.3	14.3	15.2	10.9	Gursoy et al. (2003)
middle Miocene																	
ED*	38.7	31.3	13.0	5.0	11	205.1	-42.1	10.7	14.6	24.3	10.3	14.9	19.8	16.4	18.8	12.7	Gursoy et al. (2003)
TK192	36.7	33.0	14.2	8.9	11	5.0	50.0	97.0	4.6	30.8	75.1	5.3	5.9	6.2	5.0	4.5	Kissel et al. (1993)
TK193	36.7	33.0	14.2	8.9	8	350.0	56.0	268.0	3.4	36.5	171.3	4.2	4.1	5.3	4.6	4.2	Kissel et al. (1993)
TK194	36.7	33.0	14.2	8.9	9	1.0	54.0	369.0	2.8	34.5	252.0	3.2	3.3	3.9	3.3	3.1	Kissel et al. (1993)
AN34	37.8	31.8	14.8	1.2	4	11.3	38.4	23.0	14.0	21.6	24.2	19.1	27.1	20.6	16.5	11.7	Kissel & Poisson (1986)
AN35	36.7	31.8	14.8	1.2	9	347.0	59.0	49.0	7.0	39.8	28.3	9.9	8.8	12.9	12.5	9.7	Kissel & Poisson (1986)
early Miocene																	
EL70	37.0	29.7	17.4	5.6	10	161.0	-30.0	39.0	7.0	16.1	48.5	7.0	11.4	7.3	4.5	4.1	Kissel & Poisson (1987)
EL73	37.1	30.2	17.4	5.6	9	324.0	39.0	57.0	6.0	22.0	59.1	6.8	9.5	7.3	5.1	4.5	Kissel & Poisson (1987)
EL78	36.4	29.7	17.4	5.6	7	359.0	68.0	39.0	18.0	51.1	16.3	15.4	11.0	25.0	26.0	17.9	Kissel & Poisson (1987)
Korkuteil (KL)	37.1	30.1	17.4	5.6	340	339.5	45.5			27.0		2.2	2.7	2.5	4.9	4.3	Van Hinsbergen et al. (2010a)
Dogantas I (DT1)	36.5	29.9	17.4	5.6	35	347.4	41.7			24.0		16.6	22.2	18.2	15.0	10.8	Van Hinsbergen et al. (2010a)
Dogantas II (DT2)	36.5	29.9	17.4	5.6	38	320.2	48.1			29.1		10.3	12.0	11.0	7.9	10.0	Van Hinsbergen et al. (2010a)
Dogantas III (DT3)	36.5	29.9	17.4	5.6	61	330.5	42.9			24.9		14.8	19.3	16.4	13.4	10.0	Van Hinsbergen et al. (2010a)
IH*	39.1	30.6	18.7	1.4	9	197.0	-44.0	45.7	7.7	25.8	41.9	8.0	10.3	8.9	9.0	7.3	Gursoy et al. (2003)
AC*	37.4	29.3	19.5	3.5	7	351.3	48.4			29.4	51.2	3.0	3.4	3.4	3.0	2.8	Van Hinsbergen et al. (2010b)
Paleogene																	
EL67	36.8	30.0	28.5	5.5	7	333.0	40.0	55.0	7.0	22.8	55.7	8.2	11.3	8.9	6.4	5.5	Kissel & Poisson (1987)
YA	37.2	30.5	44.3	21.2	27	312.0	39.0	15.0	7.4	22.0	15.6	7.3	10.2	7.9	5.6	4.9	Morris & Robertson (1993)
CD	37.6	30.7	44.3	21.2	5	352.0	42.0	21.0	16.9	24.2	20.3	17.4	23.1	19.2	16.0	11.3	Morris & Robertson (1993)

Paleogene (continued)																	
EL83	37.5	30.5	44.9	11.0	6	115.0	-16.0	19.0	13.0	8.2	28.3	12.8	24.2	12.9	7.2	6.6	Kissel & Poisson (1987)
EL 84	37.2	30.3	44.9	11.0	8	154.0	-29.0	61.0	6.0	15.5	77.1	6.3	10.5	6.6	4.0	3.7	Kissel & Poisson (1987)
EL71	37.1	30.2	44.9	11.0	8	340.0	32.0	54.0	6.0	17.4	64.7	6.9	10.9	7.3	4.6	4.2	Kissel & Poisson (1987)
TK176	37.1	31.8	44.9	11.0	9	223.0	-15.0	38.0	7.5	7.6	57.1	6.9	13.0	6.9	3.7	3.5	Kissel et al. (1993)
TK177	37.1	31.6	44.9	11.0	7	231.0	-28.0	27.0	11.9	14.9	34.7	10.4	17.4	10.8	6.7	5.9	Kissel et al. (1993)
TK178	37.1	31.8	44.9	11.0	8	212.0	-21.0	18.0	13.6	10.9	28.5	11.2	20.2	11.4	6.6	5.9	Kissel et al. (1993)
TK179	37.1	31.8	44.9	11.0	7	233.0	-17.0	47.0	7.7	8.7	69.4	7.3	13.7	7.4	4.0	3.8	Kissel et al. (1993)
TK180	37.0	31.8	44.9	11.0	10	213.0	-30.0	21.0	9.6	16.1	26.1	9.6	15.7	10.0	6.4	5.6	Kissel et al. (1993)
TK196	36.6	32.9	44.9	11.0	11	13.0	49.0	79.0	5.2	29.9	63.0	5.8	6.6	6.7	5.4	4.8	Kissel et al. (1993)
TK197	36.7	32.8	44.9	11.0	12	38.0	50.0	114.0	4.1	30.8	88.2	4.6	5.2	5.4	4.4	3.9	Kissel et al. (1993)
LE	38.0	30.8	49.7	15.8	6	335.0	29.0	46.0	10.0	15.5	58.1	8.9	14.6	9.2	5.7	5.1	Morris & Robertson (1993)
TK185	37.4	31.5	60.7	4.9	9	233.0	-6.0	45.0	7.8	3.0	71.3	3.1	12.2	6.1	3.1	3.1	Kissel et al. (1993)
TK190	37.3	31.8	60.7	4.9	5	41.0	48.0	14.0	23.0	29.0	11.5	23.6	27.6	27.2	27.3	16.2	Kissel et al. (1993)
DA	36.4	30.2	60.7	4.9	4	344.0	44.0	40.0	14.7	25.8	36.7	15.4	19.6	17.1	14.4	10.5	Morris & Robertson (1993)
FI	36.5	30.1	60.7	4.9	12	354.0	40.0	30.0	7.9	22.8	30.4	8.0	11.0	8.7	6.3	5.4	Morris & Robertson (1993)
DK	36.9	30.3	60.7	4.9	8	349.0	45.0	21.0	12.3	26.6	18.8	13.1	16.4	14.7	12.2	9.3	Morris & Robertson (1993)
Paleozoic-Mesozoic																	
KA	37.7	31.1	77.4	11.9	4	15.0	17.0	47.0	13.6	8.7	69.4	11.1	20.8	11.2	6.3	5.7	Morris & Robertson (1993)
KK	37.9	31.0	82.6	17.1	7	328.0	44.0	47.0	8.9	25.8	43.1	9.3	11.9	10.3	8.1	6.7	Morris & Robertson (1993)
KK4	36.6	30.5	132.6	67.1	40	30.0	40.0	27.0	4.5	22.8	27.4	4.4	6.1	4.8	3.3	3.1	Morris & Robertson (1993)
Akseki 1 (AK1)	37.0	31.5	148.2	2.7	49	303.0	-9.0	11.0	6.0	4.5	17.2	5.1	9.9	5.1	2.6	2.6	Piper et al. (2002)
Felepinar 5 (FP5)	37.6	31.3	158.5	2.8	9	289.0	-24.0	10.0	17.0	12.6	13.6	14.5	25.3	14.8	9.1	7.7	Piper et al. (2002)
Bağınar 6 (BP6)	38.1	31.2	158.5	2.8	9	186.0	-12.0	22.0	11.0	6.1	33.8	9.0	17.4	9.0	4.8	4.6	Piper et al. (2002)
Bağınar 7 (BP7)	38.1	31.2	158.5	2.8	4	162.0	-31.0	39.0	15.0	16.7	47.6	13.5	21.6	14.1	9.4	7.7	Piper et al. (2002)
Akseki 2 (AK2)	37.1	31.5	179.3	3.7	7	276.0	23.0	16.0	15.0	12.0	22.1	13.1	23.2	13.4	8.1	7.0	Piper et al. (2002)
Akseki 3 (AK3)	37.1	31.5	179.3	3.7	6	256.0	8.0	35.0	12.0	4.0	55.0	9.1	18.0	9.1	4.7	4.6	Piper et al. (2002)
Felepinar 4 (FP4)	38.0	31.3	187.6	12.0	7	278.0	-11.0	18.0	15.0	5.6	27.9	11.6	22.6	11.7	6.2	5.9	Piper et al. (2002)
Oyuklu section (OY)	36.7	32.9	204.8	5.2	106	327.9	37.9	21.1	3.1	21.3	22.4	3.0	4.2	3.2	2.1	2.0	Gallet et al. (1997)
Kavur Tepe (KT)	38.0	30.8	210.5	6.5	179	220.2	32.1	40.9	17.4	17.4	49.0	1.5	2.4	1.6	1.0	1.0	Gallet et al. (1993)
Kavaalari Section (KV)	36.3	30.3	212.0	8.0	163	209.5	18.6	17.2	2.7	9.6	25.0	2.3	4.2	2.3	1.2	1.2	Gallet et al. (2000)
HA	37.0	30.4	213.3	37.7	37	37.0	12.0	13.0	6.9	6.1	20.0	5.4	10.5	5.4	2.8	2.8	Morris & Robertson (1993)
BA	38.0	30.7	213.8	14.2	9	320.0	25.0	19.0	12.1	13.1	25.5	10.4	18.0	10.7	6.4	5.7	Morris & Robertson (1993)
CI	36.4	30.4	213.8	14.2	18	309.0	-46.0	10.0	11.8	27.4	8.7	12.4	15.2	14.0	11.8	9.0	Morris & Robertson (1993)
Bolucektasi Tepe 2 (BT2)	36.5	30.5	215.0	5.0	172	59.3	20.1	41.8	1.7	10.4	59.8	1.4	2.6	1.4	0.8	0.8	Gallet et al. (1992)
Erenkolu Mezarlik 2 (EM2)	36.7	30.6	219.5	2.5	24	223.7	-25.2	37.3	4.8	13.2	50.0	4.2	7.3	4.3	2.5	2.4	Gallet et al. (1994)
AN	37.9	31.0	222.3	22.7	13	320.0	68.0	37.0	6.9	51.1	15.4	10.9	7.7	17.5	17.5	13.4	Morris & Robertson (1993)
Bolucektasi Tepe 1 (BT1)	36.5	30.5	225.0	3.0	60	211.0	-11.0	27.1	3.6	5.6	41.9	2.9	5.6	2.9	1.5	1.5	Gallet et al. (1992)
Erenkolu Mezarlik 1 (EM1)	36.7	30.6	225.0	3.0	24	20.7	21.1	45.0	4.5	10.9	63.6	3.7	6.7	3.8	2.1	2.0	Gallet et al. (1994)
KK3	36.6	30.5	225.3	25.7	7	55.0	20.0	8.0	22.0	10.3	11.5	18.6	34.0	18.9	11.5	9.6	Morris & Robertson (1993)
Bademli redbeds (BR)	37.3	31.7	259.0	59.0	19	41.0	13.5	22.0	7.8	6.8	33.5	5.9	11.3	5.9	3.1	3.0	Van der Voo & Van der Kleijn (1970)
KK2	36.6	30.5	275.0	24.0	49	49.0	26.0	15.0	5.3	13.7	19.9	4.7	8.0	4.8	2.8	2.7	Morris & Robertson (1993)
KK1	36.6	30.5	466.0	22.3	27	112.0	29.0	13.0	7.9	15.5	16.4	7.1	11.6	7.3	4.5	4.1	Morris & Robertson (1993)

*N refers to number of combined sites of these studies, the actual amount of demagnetized specimens is lower

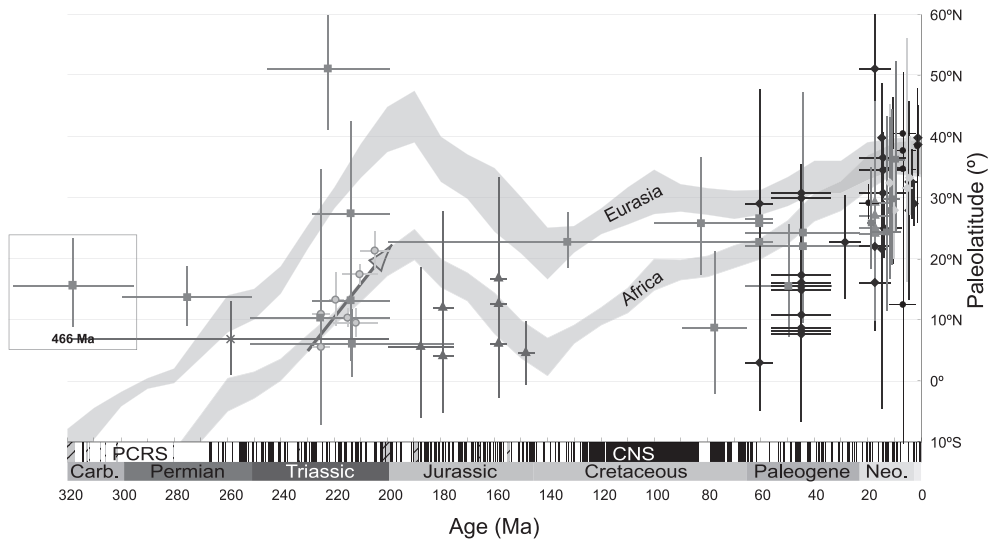


Figure 5.10 Age versus latitude plots of Tauride data from the literature, with tilt correction. Purple squares: Morris and Robertson (1993), red cross: Van der Voo and Van der Kleijn (1970), light green circles: Gallet et al. (2000; 1992; 1993, 1994; 2007), blue triangles: Piper et al. (2002), red diamonds: Kissel et al. (1993; 1987), orange triangles: van Hinsbergen et al. (2010a; 2010b), dark blue circles: van Hinsbergen et al. (submitted), dark green triangles: Gürsoy et al. (2003), light blue diamonds: Tatar et al. (2002). Grey shaded curves: APW path of Torsvik et al. (2008) with its error from 320-0 Ma. Below the curves the magnetic polarity timescale (Ogg et al., 2008) is indicated. PCRCS= Permo-Carboniferous Reversed Superchron, CNS= Cretaceous Normal Superchron, Carb.= Carboniferous. *See Appendix 31*

ized, but a more detailed study on remagnetization is required, for example using the IRM acquisition end-member modeling approach reported here.

The compilation of the post-Mesozoic data sets at first order confirms the generally accepted conclusion of Kissel et al. (1993) that the eastern limb of the Isparta Angle experienced an older clockwise rotation between Eocene and early Miocene time, followed by a counterclockwise rotation in middle-late Miocene time in the western limb (see also van Hinsbergen et al. (2010a)). However, as argued above, it is possible that remagnetization occurred during thrusting of the Taurides. If that is true, also the lower Eocene rocks used by Kissel et al. (1993) to reconstruct rotations of the central Taurides may have been remagnetized. This implies that the reported rotations of Kissel and Poisson (1986, 1987) and Kissel et al. (1993) of the Ordovician to Eocene sites should be regarded as minimum values, as they may have been reset during rotation. This would have no serious implications for the timing of clockwise rotation of the eastern limb of the Isparta Angle, sometime between the early Eocene and early Miocene.

An important implication of an Eocene remagnetization in the early stages of tilting, however, is that the remagnetized declination of our sites could be used to assess the regional rotation pattern of the central Taurides. However, our results do not

concur with a regional 40° clockwise rotation. As can be seen in Figure 5.2a, the rotations in the central Taurides are consistently clockwise. However, the rotation amount varies strongly. The results from the Seydişehir section give only $14 \pm 2.7^\circ$ cw, and for the Taşkent section even less ($7 \pm 2.8^\circ$), significantly less than the 40° of clockwise rotation concluded by Kissel et al. (1993). Our result for the Fele section gives $56 \pm 9.5^\circ$. This latter rotation is not significantly higher than some of the rotations observed by Kissel et al. (1993).

The question thus arises whether there is indeed a regional, central Tauride-wide coherent rotation of 40° . Kissel et al. (1993) report two sites from the Eocene around the Ermenek basin in the south, which give significantly different clockwise rotations of 13 and 38° , despite their close vicinity. Add to these sites our information for a post-remagnetization rotation of 7° , 14° and 56° clockwise from the Taşkent, Seydişehir and Fele sections, and a pattern arises for consistently clockwise rotations, but with strongly varying rotation amounts. These strong, significantly different rotation values suggest that local rotations between sites have played a role. This is not surprising, considering the likely influence of local, thrust-sheet, or strike-slip related rotations, superimposed on a regionally coherent rotation of the central Taurides.

6. Conclusions

The results of our paleomagnetic study on three sections/localities with Carboniferous to Paleocene sediments from the central Taurides show that the sampled rocks are remagnetized. This conclusion is based on paleomagnetic results that display reversed directions in the Cretaceous Normal Superchron as well as remarkably similar post-tilting paleolatitudes in all samples, regardless of their age. Remagnetization directions yield both normal and reversed polarities, proving that the remagnetization was not a short and single event, but likely has occurred throughout a longer time interval. We show additional evidence for remagnetization from a novel end-member modeling approach of IRM acquisition curves from the Seydişehir section. The shape of the end-member that we interpret as the magnetite end-member indicates remagnetization. The remagnetization is likely of chemical origin, caused by internal fluids (because of calcite pressure solution), in line with the presence of stylolites and dolomites in the area.

The close vicinity and common setting of the sampled rocks in the central Tauride fold-and-thrust belt suggests that remagnetization occurred not in a single event but in a time interval that covers both normal and reversed polarities. Reversed remagnetization directions and reliable Burdigalian (~ 20 -16 Ma) data from previous studies bracket the remagnetization event between ~ 85 and 20 Ma. Furthermore, the similar paleolatitudes after tilt correction agree well with the late Cretaceous to Eocene apparent polar wander path, and suggest that remagnetization took place during this time span, just prior to or during the early stages of folding. Continuous sedimentation in the Seydişehir area until the Eocene would likely place the remagnetization in the

Eocene.

Comparison of our results to published data shows that the rotation observed in our remagnetized data agrees well with the general and consistently clockwise trend in the central Taurides. The slightly divergent pattern in rotations, however, show that rotations are not regionally coherent, but are likely and at least in part influenced by local faulting. The post-tilting remagnetization reported by Morris and Robertson (1993) in the southwestern Antalya nappes, is likely not valid for a number of sites of their study. Interestingly, the Triassic tilt-corrected data of Morris and Robertson (1993) agree very well with rotations found by Gallet et al. (2000; 1992; 1994) in Triassic magnetostratigraphic sections. These clockwise rotations coincide with the rotation pattern of the central Taurides, and contrast with the counterclockwise rotations in Bey Dağları and the Lycian Nappes. The paleolatitudes from the Triassic sites also correspond very well to the Triassic apparent polar wander part. An additional study, for instance using the end-member algorithm on IRM acquisition curves, would be required to reevaluate the remagnetized nature of the rocks sampled by Morris and Robertson (1993).

7. Acknowledgements

The authors would like to thank Peter Mackintosh for his help preparing the fieldtrips and Ahmet Peynircioğlu, Pınar Ertepinar and Ayten Koç for their help in the field. Robin Topper is thanked for demagnetization of several sample sets as part of his MSc research. The MATLAB modules and an executable can be found online at: http://www.marum.de/Unmixing_magnetic_remanence_curves_without_a_priori_knowledge.html

Supplementary data Biostratigraphic ages

Seydişehir section

SE-1 Dolomite.

Fossil ?

Age ?

SE-3 Dolomite.

Fossil ?

Age ?

SE-7 Oncoidal packstone.

Selliporella donzellii

Riyadella sp.

Redmondoides lugeoni

'Earlandia' sp.

Timidonella ? sp.
Siphovalvulina sp.
 Bajocian

SE-9 Dolomite
 Fossil ?
 Age ?

SE-11 Bioclastic and peloidal grainstone (with echinoids, pelecypods and sponges etc)
'Conicospirillina' basiliensis
Redmondoides ? sp.
 Miliolidae
Cladocorapsis ? sp.
 Kimmeridgian-Berriasian interval.

SE-13 Bioclastic and intraclastic packstone to peloidal bindstone
 Miliolidae
 Textularidae
 No age-diagnostic fossil.

SE-15 Oncoidal modstone to packstone. Partly dolomitic
 Miliolidae
Cayeuxia ? sp.
 No age-diagnostic fossil.

SE-17 Partly oolitic and peloidal mudstone to packstone
Cayeuxia ? sp.
 No age-diagnostic fossil.

SE-19 Oncoidal and gravelly mudstone to packstone
Belorussiella sp.
'Earlandia' sp.
 Miliolidae
 Ataxophragmiidae
Cayeuxia ? sp.
 Kimmeridgian-Valanginian interval.

SE-21 Oncoidal and partly peloidal mudstone to packstone
Belorussiella sp.
 Miliolidae
Cayeuxia ? sp.
 Probably Kimmeridgian-Valanginian interval

SE-23 Oncoidal and partly peloidal mudstone to packstone
 Ataxophragmiidae
Cayeuxia ? sp.
 No age-diagnostic fossil.

SE-25 Mudstone to wackestone

Salpingoporella annulata

Belorussiella sp.

Miliolidae (*Quinqueloculina*-like)

Most probably Valanginian-Hauterivian interval

SE-27 Mudstone to wackestone

Praechrysalidina infracretacea

Belorussiella sp.

Miliolidae (*Quinqueloculina*-like)

Salpingoporella annulata

Valanginian-Hauterivian interval.

SE-29 Mudstone (partly bindstone) with large gastropods and oncoids

Cayeuxia ? sp.

Miliolidae

Older than Valanginian, repetition.

SE-31 Mudstone to wackestone

Praechrysalidina infracretacea

Haplophragmoides joukowskii

Belorussiella sp.

Miliolidae (*Quinqueloculina*-like)

Salpingoporella annulata

Valanginian-Hauterivian interval

SE-33 Peloidal bindstone

Miliolidae

No age-diagnostic fossil

SE-35 Peloidal and foraminiferal mustone to packstone

Praechrysalidina infracretacea

Nummoloculina sp.

Miliolidae (thin and thick shells)

Barremian to Lower Albian interval (most probably Upper Aptian to Lower Albian)

SE-37 Bindstone

Fossil ?

Age ?

SE-39 Mudstone

Rotorbinella scarsellai

Scandonea ? sp.

Miliolidae

Senonian

SE-41 Mudstone to wackestone with Calcisphaerulidae

Pithonella sp.

Calcisphaerulidae

Rotorbinella ? sp.
Discorbidae
Senonian

SE-43A Planktonic foraminiferal wackestone

Pseudohastigerina micra
Morozovelloides coronotus
Morozovelloides cf. lehneri
Morozovella spp.
Acarinina bullbrooki
Acarinina pseudosubsp. spherica
Acarinina mcgowrani ?
Acarinina spp.
Turborotalia cerroazulensis
Subbotina sp.
Globigerinatheka sp.
Middle Eocene

SE-43B Planktonic foraminiferal wackestone

Morozovelloides coronatus
Morozovelloides spp.
Acarinana spp.
Subbotina sp.
Middle Eocene

Taşkent

TS-1 Algal wackestone

Retroseptellina decrouezae
Paradagmarita ? sp.
Midiella sp.
Nodosinelloides sp.
Geinitzina sp.
Midiella sp.
Changhsingian ?

TS-2 Algal wackestone

Paradagmarita monodi
Retroseptellina decrouezae
Globivalvulina vonderschmitti
Globivalvulina ex gr. cyprica
Dagmarita chanakchiensis
Multidiscus sp.
Hemigordius guvenci
Staffellidae
Mizzia sp.
Gymnocodium bellerophontis
Changhsingian

TS-3 Algal wackestone

Paradagmarita monodi

Louisettita elegantissima

Paraglobivalvulina mira

Septoglobivalvulina sp.

Nodosinelloides sp.

Glomomidiella sp.

Staffella sp.

Gymnocodium sp.

Permocalculus sp.

Changhsingian

TS-4A Peloidal mudstone

Meandrospira pusilla

Nodosaria sp.

Most probably Spathian (Upper Olenekian)

TS-4B Peloidal and foraminiferal grainstone

Hoyenella ex gr. *shengi*

Hoyenella ex gr. *sinensis*

Cornuspira parapriscus

Meandrospira sp.

Pilamina ? sp.

Spathian (Upper Olenekian)

TS-5A Mudstone

Fossil ?

Age ?

TS-5B

Sandy and peloidal mudstone

Hoyenella ex gr. *sinensis*

Meandrospira ? sp.

Spathian (Upper Olenekian)

References

- Abels, H. A., Van Hinsbergen, D. J. J., Boekhout, F., Kitchka, A., Bosch, W., Hamers, M., Van der Meer, D. G., Geluk, M., Stephenson, R. A., submitted. Middle Carboniferous sedimentary evolution of the Donets segment of the Dniepr-Donets basin in the Donbas Foldbelt, Ukraine, *Geological Quarterly*.
- Adamia, S. A., Chkhotua, T., Kekelia, M., Lordkipanidze, M., Shavishvili, I., Zakariadze, G., 1981. Tectonics of the Caucasus and adjoining regions: implications for the evolution of the Tethys ocean, *Journal of Structural Geology*, 3(4), 437-447.
- Aiello, I. W., Hagstrum, J. T., Principi, G., 2008. Peri-equatorial paleolatitudes for Jurassic radiolarian cherts of Greece, *Tectonophysics*, 448, 33-48.
- Alexandre, P., Chalot-Prat, F., Saintot, A., Wijbrans, J., Stephenson, R., Wilson, M., Kitchka, A., Stovba, S., 2004. The $^{40}\text{Ar}/^{39}\text{Ar}$ dating of magmatic activity in the Donbas Fold Belt and the Scythian Platform (East European Craton), *Tectonics*, 23(TC5002), doi:10.1029/2003TC001582.
- Altiner, D., Koçyiğit, A., Farinacci, A., Nicosia, U., Conti, M. A., 1991. Jurassic-lower Cretaceous stratigraphy and paleogeographic evolution of the southern part of north-western Anatolia (Turkey), *Geologica Romana*, 27, 13-80.
- Altiner, D., Yılmaz, I. Ö., Özgül, N., Akçar, N., Bayazitoğlu, M., Gaziulusoy, Z. E., 1999. High-resolution sequence stratigraphic correlation in the Upper Jurassic (Kimmeridgian)-Upper Cretaceous (Cenomanian) peritidal carbonate deposits (Western Taurides, Turkey), *Geological Journal*, 34, 139-158.
- Andrew, T., Robertson, A. H. F., 2002. The Beyşehir-Hoyran-Hadım Nappes: genesis and emplacement of Mesozoic marginal and oceanic units of the northern Neotethys in southern Turkey *Journal of the Geological Society, London*, 159, 529-543.
- Anferova, K. I., 1971. Paleomagnetic directions and pole positions: Data for the USSR, Soviet Geophysical Committee: World data Center-B (Moscow)(1).
- Angiolini, L., Gaetani, M., Muttoni, G., Stephenson, M. H., Zanchi, A., 2007. Tethyan oceanic currents and climate gradients 300 m.y. ago, *Geology*, 35(12), 1071-1074; doi: 10.1130/G24031A.1.
- Arthaud, F., Matte, P., 1977. Late Paleozoic strike-slip faulting in southern Europe and northern Africa: Result of a right-lateral shear zone between the Appalachians and the Urals, *Geological Society of America Bulletin*, 88, 1305-1320.
- Bağcı, U., Parlak, O., 2009. Petrology of the Tekirova (Antalya) ophiolite (Southern Turkey): evidence for diverse magma generations and their tectonic implications during Neotethyan-subduction, *International Journal of Earth Sciences*, DOI 10.1007/s00531-007-0242-7.
- Banks, C. J., Robinson, A. G., 1997. Mesozoic strike-slip back-arc basins of the western Black Sea region, In: A. G. Robinson (Eds.), *Regional and petroleum geology of the Black Sea and surrounding regions*, AAPG Memoir. 68, 53-62.
- Banks, C. J., Robinson, A. G., Williams, M. P., 1997. Structure and Regional Tectonics of the

- Achara-Trialet Fold Belt and the Adjacent Rioni and Kartli Foreland Basins, Republic of Georgia, In: A. G. Robinson (Eds.), *Regional and petroleum geology of the Black Sea and surrounding region*, AAPG Memoir. 68, pp. 331-346.
- Baraboshkin, E., 2003. Early Cretaceous development of the Mountain Crimea, Annual University of Mining and Geology 'St. Ivan Rilski', part 1 Geology and Geophysics, 46, 25-30.
- Barrier, E., Vrielynck, B. 2008. Paleotectonic maps of the Middle East. Paris, Middle East Basins Evolution Programme.
- Bassant, P., van Buchem, F. S. P., Strasser, A., Görür, N., 2005. The stratigraphic architecture and evolution of the Burdigalian carbonate-siliciclastic sedimentary systems of the Mut Basin, Turkey, *Sedimentary Geology*, 173, 187-232.
- Bazhenov, M., Shatsillo, M., 2010. Late Permian palaeomagnetism of Northern Eurasia: data evaluation and a single-plate test of the geocentric axial dipole model, *Geophysical Journal International*, 180, 136-146, doi: 10.1111/j.1365-246X.2009.04379.x.
- Besse, J., Courtillot, V., 2002. Apparent and true polar wander and the geometry of the geomagnetic field in the last 200 million years, *Journal of Geophysical Research*, 107(B11), doi:10.1029/2000JB000050.
- Besse, J., Courtillot, V. E., 1991. Revised and Synthetic Apparent Polar Wander Paths of the African, Eurasian, North American and Indian Plates, and True Polar Wander Since 200 Ma, *Journal of Geophysical Research*, 96, 4029-4050.
- Bilardello, D., Kodama, K. P., 2009. Palaeomagnetism and magnetic anisotropy of Carboniferous red beds from the Maritime Provinces of Canada: evidence for shallow palaeomagnetic inclinations and implications for North American apparent polar wander, *Geophysical Journal International*, doi: 10.1111/j.1365-246X.2009.04457.x.
- Blumstein, A. M., Elmore, R. D., Engel, M. H., Elliot, C., Basu, A., 2004. Paleomagnetic dating of burial diagenesis in Mississippian carbonates, Utah, *Journal of Geophysical Research*, 109, B04101, doi: 10.1029/2003JB002698.
- Bozkurt, E., Holdsworth, B. K., Koçyiğit, A., 1997. Implications of Jurassic chert identified in the Tokat Complex, *Geological Magazine*, 134, 91-97.
- Bozkurt, E., Winchester, J. A., Yiğitbaş, E., Ottley, C. J., 2008. Proterozoic ophiolites and mafic-ultramafic complexes marginal to the İstanbul Block: An exotic terrane of Avalonian affinity in NW Turkey, *Tectonophysics*, 461, 240-251.
- Boztuğ, D., Güney, Ö., Heizler, M., Jonckheere, R. C., Tichomirowa, M., Otlu, N., 2009. ^{207}Pb - ^{206}Pb , ^{40}Ar - ^{39}Ar and Fission-Track Geothermochronology Quantifying Cooling and Exhumation History of the Kaman-Kırşehir Region Intrusions, Central Anatolia, Turkey, *Turkish Journal of Earth Sciences*, 18, 85-108.
- Boztuğ, D., Jonckheere, R. C., 2007. Apatite fission track data from central Anatolian granitoids (Turkey): Constraints on Neo-Tethyan closure, *Tectonics*, 26, TC3011, doi:10.1029/2006TC001988.
- Boztuğ, D., Jonckheere, R. C., Heizler, M., Ratschbacher, L., Harlavan, Y., Tichomirova, M., 2009. Timing of post-obduction granitoids from intrusion through cooling to

- exhumation in central Anatolia, Turkey, *Tectonophysics*, 473, 223-233.
- Brocher, T. M., Fuis, G. S., Fisher, M. A., Plafker, G., Moses, M. J., 1994. Mapping the megathrust beneath the northern Gulf of Alaska using wide-angle seismic data, *Journal of Geophysical Research*, 99(B6), 11,663-11,685.
- Bullard, E., C., Everett, J. E., Smith, A. G., 1965. The fit of the continents around the Atlantic. A symposium on continental drift IV, London.
- Butler, R. F., 1992. Paleomagnetism: Magnetic domains to geologic terranes (Eds.), Boston, Blackwell Scientific Publications, pp. 83-104.
- Carey, S. W., Ed., 1958. A tectonic approach to continental drift. Continental Drift - A symposium, University of Tasmania, 177-363.
- Çelik, Ö. F., Delaloye, M. F., 2003. Origin of metamorphic soles and their post-kinematic mafic dyke swarms in the Antalya and Lycian ophiolites, SW Turkey, *Geological Journal*, 38, 235-256.
- Çelik, Ö. F., Delaloye, M. F., Feraud, G., 2006. Precise ^{40}Ar - ^{39}Ar ages from the metamorphic sole rocks of the Tauride Belt Ophiolites, southern Turkey: implications for the rapid cooling history, *Geological Magazine*, 143, 213-227.
- Channell, J. E. T., Tüysüz, O., Bektaş, O., Şengör, A. M. C., 1996. Jurassic-Cretaceous paleomagnetism and paleogeography of the Pontides (Turkey), *Tectonics*, 15(1), 201-212.
- Chekunov, A. V., Kaluzhnaya, L. T., Ryabchun, L. I., 1993. The Dniepr-Donets paleorift, Ukraine, deep structures and hydrocarbon accumulations, *Journal of Petroleum Geology*, 16, 183-196.
- Chen, F., Siebel, W., Satir, M., Terzioğlu, M. N., Saka, K., 2002. Geochronology of the Karadere basement (NW Turkey) and implications for the geological evolution of the Istanbul zone, *International Journal of Earth Sciences*, 91, 469-481.
- Çiner, A., Karabıyıköğlu, M., Monod, O., Deynoux, M., Tuzcu, S., 2008. Late Cenozoic Sedimentary Evolution of the Antalya Basin, Southern Turkey, *Turkish Journal of Earth Sciences*, 17, 1-41.
- Cloetingh, S., Spadini, G., Van Wees, J. D., Beekman, F., 2003. Thermo-mechanical modelling of Black Sea Basin (de)formation, *Sedimentary Geology*, 156, 169-184.
- Collins, A. S., Robertson, A. H. F., 1998. Processes of Late Cretaceous to Late Miocene episodic thrust-sheet translation in the Lycian Taurides, SW Turkey, *Journal of the Geological Society of London*, 155, 759-772.
- Creer, K. M., 1962. The Dispersion of the Geomagnetic Field Due to Secular Variation and its Determination for Remote Times from Paleomagnetic Data, *Journal of Geophysical Research*, 67(9), 3461-3476.
- Creer, K. M., Irving, E., Nairn, A. E. M., 1959. Paleomagnetism of the Great Whin Sill, *Geophysical Journal of the Royal Astronomical Society*, 2, 306-323.
- Creer, K. M., Irving, E., Runcorn, S. K., 1954. The direction of the geomagnetic field in remote epochs in Great Britain, *Journal of Geomagnetism and Geoelectricity*, 6, 163-168.
- Davydov, V., Wardlaw, B. R., Gradstein, F. M., 2004. The Carboniferous period, In: F. M.

- Gradstein, J. G. Ogg and A. G. Smith (Eds.), *A Geologic Time Scale 2004*, Cambridge University Press, 222-237.
- Davydov, V. I., Crowley, J. L., Schmitz, M. D., Poletaev, V. I., 2010. High-precision U-Pb zircon age calibration of the global Carboniferous time scale and Milankovitch-band cyclicity in the Donets Basin, eastern Ukraine, *Geochemistry, Geophysics, Geosystems*, doi:10.1029/2009GC002736.
- Dean, W. T., Monod, O., 1970. The Lower Palaeozoic stratigraphy and faunas of the Taurus mountains near Beyşehir, Turkey, *Bulletin of the British Museum (Natural History) Geology*, 19(8), 411-426.
- Dean, W. T., Uyeno, T. T., Rickards, R. B., 1999. Ordovician and Silurian stratigraphy and trilobites, Taurus Mountains near Kemer, southwestern Turkey, *Geological Magazine*, 136, 373-393.
- Dercourt, J., Gaetani, M., Vrielynck, B., Barrier, E., Biju-Duval, B., Brunet, M.-F., Cadet, J. P., Crasquin, S., Sandulescu, M., Eds., 2000. *Peri-Tethys Palaeogeographical Atlas*.
- Dercourt, J., Ricou, L. E., Vrielynck, B., Eds., 1993. *Atlas Tethys Palaeoenvironmental Maps*. Beicip-Franlab, Town.
- Derenyuk, N. E., Vanina, M. V., Gerasimov, M. Y., Pirovarov, S. V., 1984. Geological map of the Crimea. Kiev, Geological Ministry of Ukraine (In Russian).
- Deynoux, M., Çiner, A., Monod, O., Karabiyiçođlu, M., Manatschal, G., Tuzcu, S., 2005. Facies architecture and depositional evolution of alluvial fan to fan-delta complexes in the tectonically active Miocene Köprüçay Basin, Isparta Angle, Turkey, *Sedimentary Geology*, 173, 315-343.
- Dietz, R. S., 1961. Continent and ocean basin evolution by spreading of the sea floor, *Nature*, 190, 854-857.
- Dilek, Y., Altunkaynak, S., 2009. Geochemical and temporal evolution of Cenozoic magmatism in western Turkey: mantle response to collision, slab breakoff, and lithospheric tearing in an orogenic belt, In: D. J. J. van Hinsbergen, M. A. Edwards and R. Govers (Eds.), *Geodynamics of collision and collapse at the Africa-Arabia-Eurasia subduction zone: Geological Society of London Special Publication*. 311, pp. 213-234.
- Dilek, Y., Thy, P., Hacker, B. R., Grundvig, S., 1999. Structure and petrology of Tauride ophiolites and mafic dike intrusions (Turkey): Implications for the Neotethyan ocean, *Geological Society of America Bulletin*, 111, 1192-1216.
- Dilek, Y., Whitney, D. L., 1997. Counterclockwise P-T-t trajectory from the metamorphic sole of a Neo-Tethyan ophiolite (Turkey), *Tectonophysics*, 280, 295-310.
- Druschits, V. V., Mikhailova, I. A., Nerodenko, V. M., 1981. Zonal subdivisions of Aptian deposits of Southwest Crimea, *Bulletin Moskovskogo Obshestva Ispytalei Prirody, otd. geol.*, 56(1), 95-103 (In Russian).
- Du Toit, A. L., 1937. *Our Wandering Continents*. Edinburgh, Oliver and Boyd.
- Dumont, J. F., Gutnic, M., Marcoux, J., Monod, O., Poisson, A., 1972. Le Trias des Taurides occidentales (Turquie). Definition du bassin pamphylien: un nouveau domain à ophiolites à la marge externe de la chaîne taurique, *Zeitschrift Deutsche Geologische*

- Gesellschaft, 123, 385-409.
- Egli, R., 2004. Characterization of individual rock magnetic components by analysis of remanence curves. 2. Fundamental properties of coercivity distributions, *Physics and Chemistry of the Earth*, 29(13-14), 851-867.
- Elitok, Ö., Drüppel, K., 2008. Geochemistry and tectonic significance of metamorphic sole rocks beneath the Beyşehir–Hoyran ophiolite (SW-Turkey), *Lithos*, 100, 322-353.
- Elmas, A., Yiğitbaş, E., 2001. Ophiolitic emplacement by strike-slip tectonics between the Pontide Zone and the Sakarya Zone in northwestern Anatolia, Turkey, *International Journal of Earth Sciences*, 90, 257-269.
- Elmore, R. D., Dulin, S., Engel, M. H., Parnell, J., 2006. Remagnetization and fluid flow in the Old Red Sandstone along the Great Glen Fault, Scotland, *Journal of Geochemical Exploration*, 89, 96-99.
- Eris, K. K., Bassant, P., Ülgen, U. B., 2005. Tectono-stratigraphic evolution of an Early Miocene incised valley-fill (Derinçay Formation) in the Mut Basin, Southern Turkey, *Sedimentary Geology*, 173, 151-185.
- Evans, D. A. D., 2003. True polar wander and supercontinents, *Tectonophysics*, 362, 303-320.
- Evans, I., Hall, S. A., Carman, M. F., Senalp, M., Coskun, S., 1982. A paleomagnetic study of the Bilecik Limestone (Jurassic), northwestern Anatolia, *Earth and Planetary Science Letters*, 61, 199-208.
- Evans, M. A., Lewchuk, M. T., Elmore, R. D., 2003. Strain partitioning of deformation mechanisms in limestones: examining the relationship of strain and anisotropy of magnetic susceptibility (AMS), *Journal of Structural Geology*, 25, 1525-1549.
- Eyüboğlu, Y., 2010. Late Cretaceous high-K volcanism in the eastern Pontide orogenic belt: implications for the geodynamic evolution of NE Turkey, *International Geology Review*, 52(2), 142-168.
- Favre, P., Stampfli, G. M., 1992. From rifting to passive margin: the examples of the Red Sea, Central Atlantic and Alpine Tethys, *Tectonophysics*, 215, 69-97.
- Fisher, D. A., 1953. Dispersion on a sphere, *Proc. R. Soc. London, Serie A* 217, 295-305.
- Fleck, R. J., Sutter, J. F., Elliot, D. H., 1977. Interpretation of discordant $^{40}\text{Ar}/^{39}\text{Ar}$ age-spectra of Mesozoic tholeiites from Antarctica *Geochimica et Cosmochimica Acta*, 41, 15-32.
- Flecker, R. M., Robertson, A. H. F., Poisson, A., Müller, C., 1995. Facies and tectonic significance of two contrasting Miocene basins in south coastal Turkey, *Terra Nova*, 7, 221-232.
- Gallet, Y., Besse, J., Krystyn, L., Marcoux, J., 1996. Norian magnetostratigraphy from the Scheiblkogel section, Austria: constraint on the origin of the Antalya Nappes, Turkey, *Earth and Planetary Science Letters*, 140(1-4), 113-122.
- Gallet, Y., Besse, J., Krystyn, L., Marcoux, J., Guex, J., Théveniaut, H., 2000. Magnetostratigraphy of the Kavaalani section (southwestern Turkey): Consequence for the origin of the Antalya Calcareous Nappes (Turkey) and for the Norian (Late Triassic) magnetic polarity timescale, *Geophysical Research Letters*, 27(14), 2033-

2036.

- Gallet, Y., Besse, J., Krystyn, L., Marcoux, J., Théveniaut, H., 1992. Magnetostratigraphy of the Late Triassic Bolucektasi Tepe section (southwestern Turkey): implications for changes in magnetic reversal frequency, *Phys. Earth Planet. Int.*, 73, 85-108.
- Gallet, Y., Besse, J., Krystyn, L., Théveniaut, H., Marcoux, J., 1993. Magnetostratigraphy of the Kavur Tepe section (southwestern Turkey): A magnetic polarity timescale for the Norian, *Earth and Planetary Science Letters*, 117, 443-456.
- Gallet, Y., Besse, J., Krystyn, L., Théveniaut, H., Marcoux, J., 1994. Magnetostratigraphy of the Mayerling section (Austria) and Erenkolu Mezarlik (Turkey) section: Improvement of the Carnian (late Triassic) magnetic polarity time scale, *Earth and Planetary Science Letters*, 125, 173-191.
- Gallet, Y., Krystyn, L., Marcoux, J., Besse, J., 2007. New constraints on the End-Triassic (Upper Norian–Rhaetian) magnetostratigraphy, *Earth and Planetary Science Letters*, 255, 458-470.
- Gautier, P., Bozkurt, E., Bosse, V., Hallot, E., Dirik, K., 2008. Coeval extensional and lateral underflow during Late Cretaceous core complex development in the Niğde Massif, Central Anatolia, Turkey, *Tectonics*, 27, TC1003, doi:10.1029/2006TC002089.
- Gautier, P., Bozkurt, E., Hallot, E., Dirik, K., 2002. Dating the exhumation of a metamorphic dome: geological evidence for pre-Eocene unroofing of the Niğde Massif (Central Anatolia, Turkey) *Geological Magazine*, 139(5), 559-576.
- Genç, S. C., Yılmaz, Y., 1995. Evolution of the Triassic continental margin, northwest Anatolia, *Tectonophysics*, 243, 193-207.
- Gerasimov, M. E., 1994. Deep structure and Evolution of the Southern Margin of the East-European Platform According to Seismostratigraphical Data, and Connection with Oil and Gas Potential. Moscow, VNIGRI: 1-75 (In Russian).
- Gerdjikov, I., 2005. Alpine Metamorphism and Granitoid Magmatism in the Strandja Zone: New Data from the Sakar Unit, SE Bulgaria, *Turkish Journal of Earth Sciences*, 14, 167-183.
- Gessner, K., Collins, A. S., Ring, U., Güngör, T., 2004. Structural and thermal history of poly-orogenic basement: U-Pb geochronology of granitoid rocks in the southern Menderes Massif, Western Turkey, *Journal of the Geological Society of London*, 161, 93-101.
- Glover, C. P., Robertson, A. H. F., 1998. Neotectonic intersection of the Aegean and Cyprus tectonic arcs: extensional and strike-slip faulting in the Isparta Angle, SW Turkey, *Tectonophysics*, 298, 103-132.
- Gold, T., 1955. Instability of the Earth's Axis of Rotation, *Nature*, 175, 526-529.
- Goldreich, P., Toomre, A., 1969. Some Remarks on Polar Wandering, *Journal of Geophysical Research*, 74(10), 2555-2567.
- Gong, Z., Dekkers, M. J., Dinarès-Turell, J., Mullender, T. A. T., 2008. Remagnetization mechanism of Lower Cretaceous rocks from the Organyà Basin (Pyrenees, Spain), *Studia Geophysica et Geodetica*, 52, 187-210.
- Gong, Z., Dekkers, M. J., Heslop, D., Mullender, T. A. T., 2009. End-member modeling of

- isothermal remanent magnetization (IRM) acquisition curves: a novel approach to diagnose remagnetization, *Geophysical Journal International*, 178, 693-701.
- Gong, Z., Langereis, C. G., Mullender, T. A. T., 2008. The rotation of Iberia during the Aptian and the opening of the Bay of Biscay, *Earth and Planetary Science Letters*, 273(1-2), 80-93.
- Gong, Z., van Hinsbergen, D. J. J., Dekkers, M. J., 2009. Diachronous pervasive remagnetization in northern Iberian basins during Cretaceous rotation and extension, *Earth and Planetary Science letters*, 284, 292-301.
- Gorbachev, R., Bogdanova, S., 1993. Frontiers in the Baltic Shield, *Precambrian Research*, 64, 3-21.
- Görür, N., 1988. Timing of opening of the Black Sea basin, *Tectonophysics*, 147(3-4), 247-262.
- Görür, N., 1997. Cretaceous Syn- to Postrift Sedimentation on the Southern Continental Margin of the Western Black Sea Basin, In: A. G. Robinson (Eds.), *Regional and petroleum geology of the Black Sea and surrounding region*, AAPG Memoir. 68, pp. 227-240.
- Görür, N., Oktay, F. Y., Seymen, İ., Şengör, A. M. C., 1984. Paleotectonic evolution of the Tuzgölü Basin Complex, Central Turkey: sedimentary record of a Neo-Tethyan closure, In: J. E. Dixon and A. H. F. Robertson (Eds.), *The Geological Evolution of the Eastern Mediterranean*, London, The Geological Society of London Special Publication. 17, pp. 467-482.
- Gradstein, F. M., Ogg, J. G., Smith, A. G., Agterberg, F. P., Bleeker, W., Cooper, R. A., Davydov, V., Gibbard, P., Hinnov, L. A., House, M. R., Lourens, L., Luterbacher, H. P., McArthur, J., Melchin, M. J., Robb, L. J., Shergold, J., Villeneuve, M., Wardlaw, B. R., Ali, J., Brinkhuis, H., Hilgen, F. J., Hooker, J., Howarth, R. J., Knoll, A. H., Laskar, J., Monechi, S., Plumb, K. A., Powell, J., Raffi, I., Röhl, U., Sadler, P., Sanfilippo, A., Schmitz, B., Shackleton, N. J., Shields, G. A., Strauss, H., Van Dam, J., van Kolfshoten, T., Veizer, J., Wilson, D., 2004. *A New Geologic Time Scale, with special reference to Precambrian and Neogene*, Cambridge University Press.
- Gürsoy, H., Piper, J. D. A., Tatar, O., 2003. Neotectonic deformation in the western sector of tectonic escape in Anatolia: palaeomagnetic study of the Afyon region, central Turkey, *Tectonophysics*, 374, 57-79.
- Gutierrez-Alonso, G., Fernandez-Suarez, J., Weil, A. B., Murphy, J. B., Nance, R. D., Corfu, F., Johnston, S. T., 2008. Self-subduction of the Pangaeian global plate, *Nature Geosciences*, 1, 549-553.
- Gutnic, M., Monod, O., Poisson, A., Dumont, J., 1979. *Géologie des Taurides Occidentales (Turquie)*(Eds.), Société Géologique de France, *Mémoire*. 137, pp. 1-112.
- Gutscher, M.-A., Spakman, W., Bijwaard, H., Engdahl, E. R., 2000. Geodynamics of flat subduction: Seismicity and tomographic constraints from the Andean margin, *Tectonics*, 19(5), 814-833.
- Hayward, A. B., 1984. Sedimentation and basin formation related to ophiolite nappe emplacement, Miocene, SW Turkey, *Sedimentary Geology*, 71, 105-129.

- Heezen, B. C., 1960. The rift in the ocean floor, *Scientific American*, 203, 98-110.
- Hein, C., 2005. Das Konglomerat der mittel- bis spätjurassischen Taphanskaya Formation im Demerdji Gebirge (Südkrim/Ukraine), Steinmann-Institut für Geologie, Mineralogie und Palaeontologie. Bonn, Universität Bonn.
- Heslop, D., Dillon, M., 2007. Unmixing magnetic remanence curves without a priori knowledge, *Geophysical Journal International*, 170, 556-566.
- Heslop, D., McIntosh, G., Dekkers, M. J., 2004. Using time- and temperature-dependent Preisach models to investigate the limitations of modelling isothermal remanent magnetization acquisition curves with cumulative log Gaussian functions, *Geophysical Journal International*, 157, 55-63.
- Heslop, D., Von Dobeneck, T., Höcker, M., 2007. Using non-negative matrix factorization in the "unmixing" of diffuse reflectance spectra, *Marine Geology*, 241(1-4), 63-78.
- Hertzel, R., Reischmann, T., 1996. Intrusion age of Pan-African augen gneisses in the southern Menderes Massif and the age of cooling after Alpine ductile extensional deformation, *Geological Magazine*, 133, 565-572.
- Hippolyte, J.-C., Müller, C., Kaymakci, N., Sangu, E., 2010. Nannoplankton dating in the Black Sea inverted margin of Central Pontides (Turkey) reveals two episodes of rifting, In: M. Sosson, N. Kaymakci, R. A. Stephenson, V. Starostenko and F. Bergerat (Eds.), *Sedimentary basin tectonics from the Black Sea and Caucasus to the Arabian Platform*, London, Geological Society of London, in press.
- Hrouda, F., 1982. Magnetic anisotropy of rocks and its application in geology and geophysics, *Surveys in Geophysics*, 5, 37-82.
- Iosifidi, A. G., Khramov, A. N., 2002. Paleomagnetism of Upper Carboniferous and Lower Permian Deposits of the East European Platform: A key Paleomagnetic Pole and Kinematics of Collision with the Urals, *Izvestiya-Physics of the Solid Earth*, 38(5), 389-403.
- Iosifidi, A. G., Mac Niocaill, C., Khramov, A. N., Dekkers, M. J., Popov, V. V., submitted. Differential inclination shallowing and timing of NRM acquisition in upper Carboniferous and lower Permian variegated sediments from the Donets Basin, Ukraine, *Tectonophysics*.
- Irvine, T. N., Baragar, W. R. A., 1971. Chemical differentiation of the Earth: the relationship between mantle, continental crust and oceanic crust, *Canadian Journal of Earth Sciences*, 8, 523-548.
- Irving, E., 1977. Drift of the major continental blocks since the Devonian, *Nature*, 270, 304-309.
- Isik, V., 2009. The ductile shear zone in granitoid of the Central Anatolian Crystalline Complex, Turkey: Implications for the origins of the Tuzgölü basin during the Late Cretaceous extensional deformation, *Journal of Asian Earth Sciences*, 34, 507-521.
- İşseven, T., Tüysüz, O., 2006. Palaeomagnetically defined rotations of fault-bounded continental blocks in the North Anatolian Shear Zone, North Central Anatolia, *Journal of Asian Earth Sciences*, 28, 469-479.

- Jelinek, V., 1981. Characterization of the magnetic fabric of rocks, *Tectonophysics*, 79(3-4), T63-T67.
- Jelinek, V., 1984. On a mixed quadratic invariant of the magnetic-susceptibility tensor, *Journal of Geophysics - Zeitschrift für Geophysik*, 56(1), 58-60.
- Juteau, T., Nicolas, A., Dubessey, J., Fruchard, J. C., Bouchez, J. L., 1977. Structural relationships in the Antalya Complex, Turkey: possible model for an oceanic ridge, *Geological Society of America Bulletin*, 88, 1740-1748.
- Katz, B., Elmore, R. D., Cogioni, M., Engel, M. H., Ferry, S., 2000. Associations between burial diagenesis of smectite, chemical remagnetization, and magnetite authigenesis in the Vocontian trough, SE France, *Journal of Geophysical Research*, 105, 851-868.
- Katz, B., Elmore, R. D., Cogioni, M., Ferry, S., 1998. Widespread chemical remagnetization: Orogenic fluids or burial diagenesis of clays?, *Geology*, 26, 603-606.
- Kaymakci, N., 2000. Tectono-stratigraphical evolution of the Çankırı Basin (Central Anatolia, Turkey). *Geologica Ultraiectina*, 190, 1-247.
- Kaymakci, N., Duermeijer, C. E., Langereis, C., White, S. H., Van Dijk, P. M., 2003. Palaeomagnetic evolution of the Cankiri Basin (central Anatolia, Turkey): implications for oroclinal bending due to indentation, *Geological Magazine*, 140(3), 343-355.
- Kaymakci, N., Özçelik, Y., White, S. H., Van Dijk, P. M., 2009. Tectono-stratigraphy of the Çankırı Basin: late Cretaceous to early Miocene evolution of the Neotethyan suture zone in Turkey, In: D. J. J. Van Hinsbergen, M. A. Edwards and R. Govers (Eds.), *Collision and Collapse at the Africa-Arabia-Eurasia subduction zone*, London, Geological Society of London. 311, pp. 67-106.
- Kazmin, V. G., Sbornshikov, I. M., Ricou, L.-E., Zonenshain, L. P., Boulin, J., Knipper, A. L., Eds., 1987. Volcanic belt-indicators of the Mesozoic-Cenozoic sctive outskirts of Eurasia. History of the Tethys Ocean. Moscow, Academy of Sciences of the USSR, P.P. Shirshov Institute of Oceanology.
- Kent, D. V., 1985. Thermoviscous remagnetization in some Appalachian limestones, *Geophysical Research Letters*, 12, 805-808.
- Kent, D. V., May, S. R., 1987. Polar Wander and Paleomagnetic Reference Pole Controversies, *Reviews of Geophysics*, 25(5), 961-970.
- Kent, D. V., Smethurst, M. A., 1998. Shallow bias of paleomagnetic inclinations in the Paleozoic and Precambrian, *Earth and Planetary Science Letters*, 160, 391-402.
- Keskin, M., Genç, Ş. C., Tüysüz, O., 2008. Petrology and geochemistry of post-collisional Middle Eocene volcanic units in North-Central Turkey: Evidence for magma generation by slab breakoff following the closure of the Northern Neotethys Ocean, *Lithos*, 104, 267-305.
- Khain, V. Y., 1984. Regionalnaya geotektonika. Alpiysko-Sredizemnomorskiy poyas. (Regional geotectonics. The Alpine-Mediterranean Belt). Moscow.
- Khair, K., Tsokas, G. N., 1999. Nature of the Levantine (eastern Mediterranean) crust from multiple-source Werner deconvolution of Bouguer gravity anomalies, *Journal of Geophysical Research*, 104, 25469-25478.

- Khramov, A. N., Goncharev, G. I., Komissarova, R. A., Pisarevsky, S. A., Pogarskaya, I. A., 1987. Paleomagnetology. Berlin, Springer-Verlag.
- King, R. F., 1955. The remanent magnetism of artificially deposited sediments, *Geophysical Journal International*, 7(s3), 115-134.
- Kirschvink, J. L., 1980. The least-square line and plane and the analysis of paleomagnetic data, *Geophysical journal of the Royal Astronomical Society*, 62, 699-718.
- Kissel, C., Averbuch, O., Frizon de Lamotte, D., Monod, O., Allerton, S., 1993. First paleomagnetic evidence for a post-Eocene clockwise rotation of the Western Taurides thrust belt east of the Isparta reentrant (Southwestern Turkey), *Earth and Planetary Science Letters*, 117, 1-14.
- Kissel, C., Laj, C., Poisson, A., Görür, N., 2003. Paleomagnetic reconstruction of the Cenozoic evolution of the Eastern Mediterranean, *Tectonophysics*, 362, 199-217.
- Kissel, C., Poisson, A., 1986. Etude paléomagnétique préliminaire des formations néogène du bassin d'Antalya (Taurides occidentales-Turquie), *C.R. Acad. Sci. Paris*, 302, Serie II(10), 711-716.
- Kissel, C., Poisson, A., 1987. Etude paléomagnétique préliminaire des formations cénozoïques des Bey Dağları (Taurides occidentales, Turquie), *C.R. Acad. Sci. Paris*, 304, Serie II(8), 343-348.
- Knipper, A. L., Khain, E. V., 1980. Structural position of ophiolites of the Caucasus, *Ophioliti*, 2(Special Issue), 297-314.
- Koçyiğit, A., Kaymakci, N., Rojay, B., Özcan, E., Dirik, K., Özçelik, Y., 1991. Inegöl-Bilecik-Bozüyük arasında kalan alanın jeolojik etüdü, ODTÜ-TPAO Projesi, ODTÜ-TPAO Projesi. 90-03-09-01-05.
- Kodama, K. P., 2009. Simplification of the anisotropy-based inclination correction technique for magnetite- and haematite-bearing rocks: a case study for the Carboniferous Glenshaw and Mauch Chunk Formations, North America, *Geophysical Journal International*, 176, 467-477.
- Köppen, W., Wegener, A., 1924. Die Klimate der geologischen Vorzeit. Berlin, Bornträge.
- Koppers, A. A. P., 2002. ArArCalc software for $^{40}\text{Ar}/^{39}\text{Ar}$ age calculations, *Computational Geosciences*, 28, 605-619.
- Koronovsky, N. V., Mileyev, V. S., 1974. O sootnoshenii otlojenii Tavricheskoi serii i eskiordinkoi svity v doline r. Bodrak (Gornnii Krim) (About the relationships of Tauric series and Eskirda suite in the Bodrak river valley (Mountain Crimea)), *Vestnik Moskovskogo Universiteta Geologiya*, 1, 80-87.
- Kosun, E., Poisson, A., Çiner, A., Wernli, R., Monod, O., 2009. Syn-tectonic sedimentary evolution of the Miocene Çatallar Basin, southwestern Turkey, *Journal of Asian Earth Sciences*, 34, 466-479.
- Krajewski, M., Olszewska, B., 2006. New data about microfacies and stratigraphy of the Late Jurassic Aj-Petri carbonate buildup (SW Crimea Mountains, S Ukraine), *Neues Jahrbuch für Geologie und Paläontologie, Monatshefte*, 5, 298-312.
- Kriachtchvskaia, O., Stovba, S., Stephenson, R., 2010. Cretaceous-Cenozoic evolution of

- the Odessa Shelf and Azov Sea from seismic data and 1-D modelling In: M. Sosson, N. Kaymakci, R. A. Stephenson, V. Starostenko and F. Bergerat (Eds.), *Sedimentary basin tectonics from the Black Sea and Caucasus to the Arabian Platform*, London, Geological Society of London, in press.
- Kröner, A., Şengör, A. M. C., 1990. Archean and Proterozoic ancestry in late Precambrian to early Paleozoic crustal elements of southern Turkey as revealed by single-zircon dating, *Geology*, 18, 1186-1190.
- Kruglov, S. S., Tsytko, A. K., 1988. *Tectonics of the Ukraine*. Moscow, Nedra.
- Kruiver, P. P., Dekkers, M. J., Heslop, D., 2001. Quantification of magnetic coercivity components by the analysis of acquisition curves of isothermal remanent magnetisation, *Earth and Planetary Science Letters*, 189, 269-276.
- Latyshev, A. V., Panov, D. I., 2008. Jurassic magmatic bodies of Mountainous Crimea in the Bodrak River catchment (Southwestern Crimea), *Moscow University Bulletin*, 63(2), 70-78.
- Le Maitre, R. W., Bateman, P., Dudek, A., Keller, J., Lameyre, J., Le Bas, M. J., DSabine, P. A., Schmid, R., Sorenson, H., Streckeisen, A., Woolley, A. R., Zanettin, B., 1989. *A Classification of Igneous Rocks and Glossary of Terms*. Oxford, Blackwell.
- Letavin, A. I., 1980. Basement of the Young Platform of the Southern USSR. Moscow, Nauka: 1-150.
- Loos, S., Reischmann, T., 1999. The evolution of the southern Menderes Massif in SW Turkey as revealed by zircon dating, *Journal of the Geological Society of London*, 156, 1021-1030.
- Lordkipanidze, M. B., Meliksetian, B., Djarbashian, R., Eds., 1989. *Mesozoic-Cenozoic Magmatic Evolution of the Pontian-Crimean-Caucasian Region*. IGCP project n°198: Evolution of the northern margin of Tethys. Paris, Mémoire de la Société Géologique de France, Paris, Nouvelle Série.
- Luterbacher, H. P., Ali, J. R., Brinkhuis, H., Gradstein, F. M., Hooker, J. J., Monechi, S., Ogg, J. G., Powell, J., Röhl, U., Sanfilippo, A., Schmitz, B., 2004. The Paleogene Period, In: F. M. Gradstein, J. G. Ogg and A. G. Smith (Eds.), *A Geologic Time Scale 2004*, Cambridge University Press, 384-408.
- Machel, H. G., Cavell, P. A., 1999. Low-flux, tectonically-induced squeeze fluid flow ("hot flash") into the Rocky Mountain Foreland Basin, *Bulletin of Canadian Petroleum Geology*, 47, 510-533.
- Mackintosh, P. W., Robertson, A. H. E., 2009. Structural and sedimentary evidence from the northern margin of the Tauride platform in south central Turkey used to test alternative models of Tethys during Early Mesozoic time, *Tectonophysics*, 473, 149-172.
- Mazarovich, O. A., Mileev, V. S., 1989. Geological Structure of the Kacha Upland of the Mountain Crimea. Stratigraphy of the Mesozoic. (Eds.), Moscow, 1-168 (in Russian).
- McCabe, C., Elmore, R. D., 1989. The occurrence of Late Paleozoic remagnetization in the sedimentary rocks of North America, *Reviews of Geophysics*, 27, 471-494.

- McCann, T., Chalot-Prat, F., Saintot, A., 2010. The Early Mesozoic evolution of the Western Greater Caucasus (Russia): Triassic-Jurassic sedimentary & magmatic history, In: M. Sosson, N. Kaymakçı, R. Stephenson, F. Bergerat and V. Starostenko (Eds.), *Sedimentary basin tectonics from the Black Sea and Caucasus to the Arabian Platform*, London, Geological Society of London, in press.
- McFadden, P. L., 1998. The fold test as an analytical tool, *Geophysical Journal International*, 135, 329-338.
- McFadden, P. L., Jones, D. L., 1981. The fold test in palaeomagnetism, *Geophysical Journal of the Royal Astronomical Society*, 6, 53-58.
- McFadden, P. L., Lowes, F. J., 1981. The discrimination of mean directions drawn from Fisher distributions, *Geophysical Journal of the Royal Astrological Society*, 67, 19-33.
- McFadden, P. L., McElhinny, L. W., 1988. The combined analysis of remagnetization circles and direct observations in palaeomagnetism, *Earth and Planetary Science Letters*, 87, 161-172.
- McFadden, P. L., McElhinny, M. W., 1990. Classification of the reversal test in palaeomagnetism, *Geophysical Journal International*, 103, 725-729.
- McKenzie, D., 1966. The viscosity of the lower mantle, *Journal of Geophysical Research*, 71, 3995-4010.
- McKenzie, D., Parker, R. L., 1967. The North Pacific: an example of tectonics on a sphere, *Nature*, 216, 1276-1280.
- Meijers, M. J. M., Kaymakçı, N., van Hinsbergen, D.J.J., Langereis, C.G., Stephenson, R.A., Hippolyte, J.-C., 2010 (in review), Late Cretaceous to Paleocene oroclinal bending in the central Pontides (Turkey), *Tectonics*.
- Menning, M., Alekseev, A. S., Chuvashov, B. I., Davydov, V. I., Devuyt, F.-X., Forke, H. C., Grunt, T. A., Hance, L., Heckel, P. H., Izokh, N. G., Jin, Y.-G., Jones, P. J., Kotlyar, G. V., Kozur, H. W., Nemyrovska, T. I., Schneider, J. W., Wang, X.-D., Weddige, K., Weyer, D., Work, D. M., 2006. Global time scale and regional stratigraphic reference scales of Central and West Europe, East Europe, Tethys, South China, and North America as used in the Devonian-Carboniferous-Permian Correlation Chart 2003 (DCP 2003), *Palaeogeography, Palaeoclimatology, Palaeoecology*, 240, 318-372.
- Milanovsky, E. E., 1991. *Geology of the USSR. Part 3*. Moscow, Moscow University Press: 1-272 (In Russian).
- Mileyev, V. S., Baraboshkin, E. Y., Nikitin, M. Y., Rozanov, S. B., Shalimov, I. V., 1996. Evidence that the Upper Jurassic deposits of the Crimean Mountains are allochthons, *Transactions (Doklady) of the Russian Academy of Sciences, Earth Science Sections*, 342(4), 121-124.
- Mileyev, V. S., Rozanov, S. B., Baraboshkin, E. Y., Nikitin, M. Y., Shalimov, I. V., 1995. The position of the Upper Jurassic deposits in the structure of the Mountain Crimea, *Byulleten Moskovskogo Obshestva Ispytatelei Prirody, Geologia*, 70(1), 22-31 (In Russian).
- Mileyev, V. S., Rozanov, S. B., Baraboshkin, E. Y., Shalimov, I. V., Eds., 1997. *The tectonic*

- structure and evolution of the Mountain Crimea. Geological study of Crimea. Moscow, Geological Faculty MSU Publishers (In Russian).
- Moix, P., Beccalotto, L., Kozur, H. W., Hochard, C., Rosselet, F., Stampfli, G. M., 2008. A New Classification of the Turkish Terranes and Sutures and its Implications for the Paleotectonic History of the Region, *Tectonophysics*, 451, 7-39.
- Monod, O., 1977. Recherches géologiques dans le Taurus occidental au sud du Beyşehir (Turquie). Paris, University of Paris-Sud 'Centre d'Orsay'.
- Morel, P., Irving, E., 1981. Paleomagnetism and the Evolution of Pangea, *Journal of Geophysical Research*, 86(B3), 1858-1872.
- Morris, A., Robertson, A. H. F., 1993. Miocene remagnetisation of carbonate platform and Antalya Complex units within the Isparta Angle, SW Turkey, *Tectonophysics*, 220, 243-266.
- Mullender, T. A. T., van Velzen, A. J., Dekkers, M. J., 1993. Continuous drift correction and separate identification of ferromagnetic and paramagnetic contributions in thermomagnetic runs, *Geophysical Journal International*, 114, 663-672.
- Müller, R. D., Royer, J.-Y., Lawver, L. A., 1993. Revised plate motions relative to the hotspots from combined Atlantic and Indian Ocean hotspot tracks, *Geology*, 21(3), 275-278.
- Muratov, M. V., 1960. *Kratkii ocherk geologicheskogo stroeniya Krymskogo poluostrova* (Concise Review of the Geologic Structure of the Crimean Peninsula). Moscow, Gosgeoltekhizdat.
- Muratov, M. V., Ed., 1969. *Geology of the USSR. Volume VIII: Crimea. Part 1: Geology*. Moscow, Nedra.
- Muttoni, G., Erba, E., Kent, D. V., Bachtadse, V., 2005. Mesozoic Alpine facies deposition as a result of past latitudinal plate motion, *Nature*, 434(7029), 59-63.
- Muttoni, G., Gaetani, M., Kent, D. V., Sciunnach, D., Angiolini, L., Berra, F., Garzanti, E., Mattei, M., Zanchi, A., 2009. Opening of the Neo-Tethys Ocean and the Pangea B to Pangea A transformation during the Permian, *GeoArabia*, 14(4), 17-48.
- Muttoni, G., Kent, D. V., Channell, J. E. T., 1996. Evolution of Pangea: paleomagnetic constraints from the southern Alps, Italy, *Earth and Planetary Science letters*, 140, 97-112
- Muttoni, G., Kent, D. V., Garzanti, E., Brack, P., Abrahamsen, N., Gaetani, M., 2003. Early Permian Pangea 'B' to Late Permian Pangea 'A', *Earth and Planetary Science Letters*, 215, 379-394.
- Nikishin, A. M., Alekseev, A. S., Kopaevich, L. F., Yanin, B. T., Baraboshkin, E. J., Yutsis, V. V., 2008. Cretaceous-Eocene sedimentation in the shelf Alma Basin of Cimmerian mobile belt (Crimea): eustatic and tectonic influences. Moscow, Geological Faculty, Moscow State University: 75.
- Nikishin, A. M., Cloetingh, S., Brunet, M.-F., Stephenson, R. A., Bolotov, S. N., Erschov, A., 1998. Scythian Platform, Caucasus and Black Sea region: Mesozoic-Cenozoic tectonic history and dynamics, In: S. Crasquin-Soleau and E. Barrier (Eds.), *Peri-Tethys Memoir 3: Stratigraphy and Evolution of Peri-Tethyan Platforms*, Paris, Mémoires Muséum

national d'Histoire naturelle. 177.

- Nikishin, A. M., Korotaev, M. V., Ershov, A. V., Brunet, M.-F., 2003. The Black Sea basin: tectonic history and Neogene-Quaternary rapid subsidence modelling, *Sedimentary Geology*, 156, 149-168.
- Nikishin, A. M., Ziegler, P. A., Panov, D. I., Nazarevich, B. P., Brunet, M.-F., Stephenson, R. A., Bolotov, S. N., Korotaev, M. V., Tikhomirov, P. L., 2001. Mesozoic and Cainozoic evolution of the Scythian Platform-Black Sea-Caucasus domain, In: P. A. Ziegler, W. Cavazza, A. H. F. Robertson and S. Crasquin-Soleau (Eds.), *Peri-Tethys Memoir 6: Peri-Tethyan Rift/Wrench Basins and Passive Margins*, Paris, Mémoires Muséum national d'Histoire naturelle. 186, pp. 295-346.
- Nikishin, A. M., Ziegler, P. A., Stephenson, R. A., Cloetingh, S. A. P. L., Furne, A. V., Fokin, P. A., Erschov, A. V., Bolotov, S. N., Korotaev, M. V., Alekseev, A. S., Gorbachev, V. I., Shipilov, E. V., Lankreijer, A., Bembinova, E. Y., Shalimov, I. V., 1996. Late Precambrian to Triassic history of the East European Craton: dynamics of sedimentary basin evolution, *Tectonophysics*, 268, 23-63.
- Norton, I. O., 2000. Global hotspot reference frames in plate motion, In: M. A. Richards, R. G. Gordon and R. D. van der Hilst (Eds.), *The history and dynamics of global plate motion*, pp. 339-357.
- O'Brien, V. J., Moreland, K. M., Elmore, R. D., Engel, M. H., Evans, M. A., 2007. Origin of orogenic remagnetizations in Mississippian carbonates, Sawtooth Range, Montana, *Journal of Geophysical Research*, 112, B06103, doi:10.1029/2006JB004699.
- O'Neill, C., Muller, D., Steinberger, B., 2005. On the uncertainties in hot spot reconstructions and the significance of moving hot spot reference frames, *Geochemistry, Geophysics, Geosystems*, 6(4), Q04003, doi:10.1029/2004GC000784.
- Ogg, J. G., 2004. The Jurassic Period, In: F. M. Gradstein, J. G. Ogg and A. G. Smith (Eds.), *A Geologic Time Scale 2004*, Cambridge University Press, 307-343.
- Ogg, J. G., Agterberg, F. P., Gradstein, F. M., 2004. The Cretaceous Period, In: F. M. Gradstein, J. G. Ogg and A. G. Smith (Eds.), *A Geologic Time Scale 2004*, Cambridge University Press, 344-383.
- Ogg, J. G., Ogg, G., Gradstein, F. M., 2008. *The Concise Geologic Time Scale*. Cambridge, Cambridge University Press.
- Okay, A. I., 1984. Distribution and characteristics of the northwest Turkish blueschists, In: J. E. Dixon and A. H. F. Robertson (Eds.), *The Geological Evolution of the Eastern Mediterranean*, London, Geological Society Special Publication. 17, pp. 455-466.
- Okay, A. I., Bozkurt, E., Satır, M., Yigitbaş, E., Crowley, Q. G., Shang, C. K., 2008. Defining the southern margin of Avalonia in the Pontides: Geochronological data from the Late Proterozoic and Ordovician granitoids from NW Turkey, *Tectonophysics*, 461(1-4), 252-264.
- Okay, A. I., Göncüoğlu, C., 2004. The Karakaya complex: A review of data and concepts, *Turkish Journal of Earth Sciences*, 13(2), 77-95.
- Okay, A. I., Monod, O., Monie, P., 2002. Triassic blueschists and eclogites from northwest

- Turkey: vestiges of the Paleo-Tethyan subduction, *Lithos*, 64(3-4), 155-178.
- Okay, A. I., Şahintürk, Ö., 1997. Geology of the Eastern Pontides, In: A. G. Robinson (Eds.), *Regional and petroleum geology of the Black Sea and surrounding region*, AAPG Memoir. 68, pp. 291-311.
- Okay, A. I., Satır, M., Maluski, H., Siyako, M., Monié, P., Metzger, R., Akyüz, S., 1996. Paleo- and Neo-Tethyan events in northwestern Turkey: geologic and geochronologic constraints, In: A. Yin and T. M. Harrison (Eds.), *The tectonic evolution of Asia*, Cambridge, Cambridge University Press, pp. 420-441.
- Okay, A. I., Satır, M., Tüysüz, O., Akyüz, S., Chen, F., 2001. The tectonics of the Strandja Massif: late-Variscan and mid-Mesozoic deformation and metamorphism in the northern Aegean, *International Journal of Earth Sciences*, 90, 217-233.
- Okay, A. I., Sengör, A. M. C., N. G., 1994. Kinematic history of the opening of the Black Sea and its effect on the surrounding regions, *Geology*, 22, 267-270.
- Okay, A. I., Şengör, A. M. C., Görür, N., 1994. Kinematic history of the opening of the Black Sea and its effect on the surrounding regions, *Geology*, 22, 267-270.
- Okay, A. I., Siyako, M., Burkan, K. A., 1991. Geology and tectonic evolution of the Biga peninsula, northwest Turkey, *Bulletin of the Technical University of Istanbul*, 44, 191-256.
- Okay, A. I., Tansel, I., Tüysüz, O., 2001. Obduction, subduction and collision as reflected in the Upper Cretaceous-Lower Eocene sedimentary record of western Turkey, *Geological Magazine*, 138(2), 117-142.
- Okay, A. I., Tüysüz, O., 1999. Tethyan sutures of northern Turkey, In: B. Durand, L. Jolivet, F. Horvath and M. Seranne (Eds.), *The Mediterranean Basins: Tertiary Extension within the Alpine Orogen*, London, Geological Society Special Publication. 156, 475-515.
- Okay, A. I., Tüysüz, O., Satır, M., Özkan-Altınır, S., Altınır, D., Sherlock, S., Eren, R. H., 2006. Cretaceous and Triassic subduction-accretion, HP/LT metamorphism and continental growth in the Central Pontides, Turkey, *Geological Society of America Bulletin*, 118, 1247-1269.
- Opdyke, N. D., Roberts, J., Claoue-Long, J., Irving, E., Jones, P. J., 2000. Base of the Kiaman: Its definition and global stratigraphic significance, *GSA Bulletin*, 112(9), 1315-1341.
- Orbay, N., Bayburdi, A., 1979. Palaeomagnetism of dykes and tuffs from the Mesudiye region and rotation of Turkey, *Geophysical journal of the Royal Astronomical Society*, 59, 437-444.
- Özcan, E., Less, G., Kertész, B., 2007. Late Ypresian to Middle Lutetian Orthophragminid Record from Central and Northern Turkey: Taxonomy and Remarks on Zonal Scheme, *Turkish Journal of Earth Sciences*, 16, 281-318.
- Özer, E., Koç, H., Özsayar, T. Y., 2004. Stratigraphical evidence for the depression of the northern margin of the Menderes–Tauride Block (Turkey) during the Late Cretaceous, *Journal of Asian Earth Sciences*, 22, 401-412.
- Özgül, N., 1976. Some geological aspects of the Taurus orogenic belt (Turkey), *Bulletin of the Geological Society of Turkey*, 19, 65-78 (In Turkish).

- Özgül, N., 1983. Stratigraphy and tectonic evolution of the Central Taurides. International Symposium on Geology of the Taurus Belt.
- Page, F., Wirth, K. R., Dobrovolskaya, T. I., Thole, J. T., 1998. Subduction-related mid-Jurassic magmatism of the Crimean Mountains. Annual Meeting of the Geological Society of America, Toronto, Ontario, Abstracts with Programs, v. 30, p. 378.
- Panek, T., Danisik, M., Hradecky, J., Frisch, W., 2009. Morpho-tectonic evolution of the Crimean mountains (Ukraine) as constrained by apatite fission track data, *Terra Nova*, 21(4), 271-278.
- Payne, J. L., Lehrmann, D. J., Follett, D., Seibel, M., Kump, L. R., Riccardi, A., Altiner, D., Sano, H., Wei, J., 2007. Erosional truncation of uppermost Permian shallow-marine carbonates and implications for Permian-Triassic boundary events, *Geological Society of America Bulletin*, 119(7/8), 771-784, doi: 10.1130/B26091.1.
- Pechersky, D. M., Safonov, V. A., 1993. Paleomagnetic data and palinspastic reconstruction of the Middle Jurassic to Early Cretaceous position of the Crimean mountains, *Geotectonics*, 27, 89-97.
- Pechersky et al., D. M., 1993. Paleomagnetic directions and paleomagnetic pole positions: Data for the former USSR, VNIGRI Institute, St.Petersburg, Russia (unpublished), 8.
- Peynircioğlu, A. A., 2005. Micropaleontological analysis and facies evolution across the Tournaisian - Viséan boundary in Aladağ Unit (central Taurides, Turkey), Department of Geological Engineering. Ankara, Middle East Technical University: 90.
- Pickett, E., Robertson, A. H. F., 2004. Significance of the Volcanogenic Nilufer Unit and Related Components of the Triassic Karakaya Complex for Tethyan Subduction/Accretion Processes in NW Turkey, *Turkish Journal of Earth Sciences*, 13, 97-143.
- Piper, J. D. A., Gursoy, H., Tatar, O., Isseven, T., Kocyigit, A., 2002. Palaeomagnetic evidence for the Gondwanian origin of the Taurides and rotation of the Isparta Angle, southern Turkey, *Geological Journal*, 37, 317-336.
- Poisson, A., Wernli, R., Sagular, E. K., Temiz, H., 2003. New data concerning the age of the Aksu Thrust in the south of the Aksu valley, Isparta Angle (SW Turkey): consequences for the Antalya Basin and the Eastern Mediterranean, *Geological Journal*, 38, 311-327.
- Poisson, A., Yagmurlu, F., Bozcu, M., Sentürk, M., 2003. New insights on the tectonic setting and evolution around the apex of the Isparta Angle (SW Turkey), *Geological Journal*, 38, 257-282.
- Popov, V. S., 1965. The Geological map of pre-Mesozoic sediments of the Ukrainian part of the Great Donbas, Ministry of Geology of USSR.
- Prevot, M., Mattern, E., Camps, P., Daignieres, M., 2000. Evidence for a 20° tilting of the Earth's rotation axis 110 million years ago, *Earth and Planetary Science Letters*, 179, 517-528.
- Rice, S. P., Robertson, A. H. F., Ustaömer, T., 2006. Late-Cretaceous- Early Cenozoic tectonic evolution of the Eurasian active margin in the Central and Eastern Pontides, northern Turkey, In: A. H. F. Robertson and D. Mountrakis (Eds.), *Tectonic Development of the Eastern Mediterranean Region* London, The Geological Society of London. 260, pp. 413-445.

- Richards, M. A., Duncan, R. A., Courtillot, V. E., 1989. Flood basalts and hotspot tracks: plume heads and tails, *Science*, 246, 103-107.
- Ricou, L.-E., Burg, J.-P., Godfriaux, I., Ivanov, Z., 1998. Rhodope and Vardar: the metamorphic and the olistostrome paired belts related to the Cretaceous subduction under Europe, *Geodinamica Acta*, 11(6), 285-309.
- Ricou, L. E., Argyriadis, I., Marcoux, J., 1975. L'axe calcaire du Taurus, un alignement de fenêtres arabo-africaines sous des nappes radiolaritiques, ophiolitiques et métamorphiques, *Bulletin de la Société Géologique de France*, 17, 1024-1043.
- Ricou, L. E., Marcoux, J., Poisson, A., 1979. L'allochtonie des Bey Dağları orientaux. Reconstruction palinspastique des Taurides occidentales, *Bulletin de la Société Géologique de France*, 11, 125-133.
- Roberts, A. P., 1995. Magnetic properties of sedimentary greigite (Fe₃S₄), *Earth and Planetary Science Letters*, 134, 227-236.
- Robertson, A. H. F., Dixon, J. E., 1984. Introduction: aspects of the geological evolution of the Eastern Mediterranean, In: J. E. Dixon and A. H. F. Robertson (Eds.), *The geological evolution of the Eastern Mediterranean*, London, Geological Society Special Publications. 17, pp. 1-74.
- Robertson, A. H. F., Parlak, O., Ustaömer, T., 2009. Melange genesis and ophiolite emplacement related to subduction of the northern margin of the Tauride-Anatolide continent, central and western Turkey, In: D. J. J. Van Hinsbergen, M. A. Edwards and R. Govers (Eds.), *Collision and Collapse at the Africa-Arabia-Eurasia Subduction Zone*, The Geological Society of London. 311, pp. 9-66.
- Robertson, A. H. F., Ustaömer, T., 2004. Tectonic evolution of the Intra-Pontide suture zone in the Armutlu Peninsula, NW Turkey, *Tectonophysics*, 381, 175-209.
- Robertson, A. H. F., Ustaömer, T., Pickett, E. A., Collins, A. S., Andrew, T., Dixon, J. E., 2004. Testing models of Late Palaeozoic-Early Mesozoic orogeny in Western Turkey: support for an evolving open-Tethys model, *Journal of the Geological Society*, London, 161, 501-511.
- Robertson, A. H. F., Woodcock, N. H., 1981. Alakir Çay group, Antalya Complex, SW Turkey: a deformed Mesozoic carbonate margin, *Sedimentary Geology*, 30, 95-131.
- Robinson, A., Spadini, G., Cloetingh, S., Rudat, J., 1995. Stratigraphic evolution of the Black Sea: inferences from basin modelling, *Marine and Petroleum Geology*, 12(8), 821-835.
- Robinson, A. G., 1997. Introduction: Tectonic elements of the Black Sea region, *AAPG Memoir*, 68, 1-6.
- Robinson, A. G., Banks, C. J., Rutherford, M. M., Hirst, J. P. P., 1995. Stratigraphic and structural development of the Eastern Pontides, Turkey, *Journal of the Geological Society*, 152, 861-872.
- Robinson, A. G., Rudat, J. H., Banks, C. J., Wiles, L. F., 1996. Petroleum geology of the Black Sea, *Marine and Petroleum Geology*, 13(2), 195-223.
- Rochette, P., Vandamme, D., 2001. Pangea B: an artifact of incorrect paleomagnetic assumptions?, *Annali di Geofisica*, 44(3), 649-658.

- Rojay, B., 1995. Post-Triassic evolution of the central Pontides: evidence from Amasya region, northern Anatolia, *Geologica Romana*, 31, 329-350.
- Rojay, B., Altiner, D., 1998. Middle Jurassic-lower Cretaceous biostratigraphy in the Central Pontides (Turkey): remarks on paleogeography and tectonic evolution, *Rivista Italiana di Paleontologia e Stratigrafia*, 104(2), 167-179.
- Rolland, Y., Galoyan, G., Bosch, D., Sosson, M., Corsini, M., Fornari, M., Verati, C., 2009. Jurassic back-arc and Cretaceous hot-spot series in the Armenian ophiolites - Implication for the obduction process., *Lithos*, 112, 163-187.
- Rowan, C. J., Roberts, A. P., Broadbent, T., 2009. Reductive diagenesis, magnetite dissolution, greigite growth and paleomagnetic smoothing in marine sediments: A new view, *Earth and Planetary Science Letters*, 277, 223-235.
- Rusakov, O. M., 1971. Paleomagnetic directions and pole positions: Data for the USSR - Issue 1, Soviet Geophysical Committee: World Data Center-B (Moscow).
- Sachsenhofer, R. F., Privalov, V. A., Zhykalyak, M. V., Bueker, C., Panova, E. A., Rainer, T., Shymanovskyy, V. A., Stephenson, R., 2002. The Donets Basin (Ukraine/Russia): coalification and thermal history, *International Journal of Coal Geology*, 49, 33-55.
- Sagnotti, L., Speranza, F., Winkler, A., Mattei, M., Funicello, R., 1998. Magnetic fabric of clay sediments from the external northern Apennines (Italy), *Physics of the Earth and Planetary Interiors*, 105, 73-93.
- Saintot, A., Angelier, J., Chorowicz, J., 1999. Mechanical significance of structural patterns identified by remote sensing studies: a multiscale analysis of tectonic structures in Crimea, *Tectonophysics*, 313(1-2), 187-218.
- Saintot, A., Brunet, M.-F., Yakovlev, F., Sebrier, M., Erschov, A., Chalot-Prat, F., McCann, T., Polino, R., Stephenson, R. A., 2006. The Mesozoic-Cenozoic tectonic evolution of the Greater Caucasus, In: D. Gee and R. A. Stephenson (Eds.), *European Lithosphere Dynamics*, London, Geological Society of London, 277-289.
- Saintot, A., Stephenson, R., Brem, A., Stovba, S., Privalov, V., 2003. Paleostress field reconstruction and revised tectonic history of the Donbas fold and thrust belt (Ukraine and Russia), *Tectonics*, 22(5), 1059.
- Saintot, A., Stephenson, R., Stovba, S., Brunet, M.-F., Yegorova, T., Starostenko, V., 2006. The evolution of the southern margin of eastern Europe (Eastern European and Scythian platforms) from the latest Precambrian-Early Palaeozoic to the Early Cretaceous, In: D. Gee and S. R.A. (Eds.), *European Lithosphere Dynamics*, London, The Geological Society of London. 32, pp. 481-505.
- Saintot, A., Stephenson, R., Stovba, S., Maystrenko, Y., 2003. Structures associated with inversion of the Donbas Foldbelt (Ukraine and Russia), *Tectonophysics*, 373, 181-207.
- Saintot, A., Stephenson, R. A., Chalot-Prat, F., 2007. The position of Crimea and Greater Caucasus along the active margin of Eurasia (from early Jurassic to present). Abstract Volume, International symposium on the Middle east Basins Evolution, Paris, December 4-5, p.c.69.
- Saribudak, M., 1989. New results and a palaeomagnetic overview of the Pontides in northern

- Turkey, *Geophysical Journal International*, 99, 521-531.
- Satir, M., Friedrichsen, H., 1986. The origin and evolution of the Menderes Massif, W-Turkey: a rubidium/strontium and oxygen isotope study, *Geologische Rundschau*, 75(703-714).
- Satolli, S., Besse, J., Calamita, F., 2008. Paleomagnetism of Aptian-Albian sections from the Northern Apennines (Italy): Implications for the 150-100 Ma apparent polar wander of Adria and Africa, *Earth and Planetary Science Letters*, 276, 115-128.
- Satolli, S., Besse, J., Speranza, F., Calamita, F., 2007. The 125-150 Ma high-resolution Apparent Polar Wander Path for Adria from magnetostratigraphic sections in Umbria-Marche (Northern Apennines, Italy): Timing and duration of the global Jurassic-Cretaceous hairpin turn, *Earth and Planetary Science Letters*, 257, 329-342.
- Schaltegger, U., Brack, P., 2007. Crustal-scale magmatic systems during intracontinental strike-slip tectonics: U, Pb and Hf isotopic constraints from Permian magmatic rocks of the Southern Alps, *International Journal of Earth Sciences*, 96, 1131-1151; DOI 10.1007/s00531-006-0165-8.
- Scheepers, P. J. J., Langereis, C. G., 1994. Magnetic fabric of Pleistocene clays from the Tyrrhenian arc: A magnetic lineation induced in the final stage of the middle Pleistocene compressive event, *Tectonics*, 13(5), 1190-1200.
- Şen, C., 2007. Jurassic volcanism in the Eastern Pontides: is it rift related or subduction related?, *Turkish Journal of Earth Sciences*, 16, 523-539.
- Şenel, M., Akdeniz, N., Turhan, N., Konak, N., Ulu, Ü., Türkecan, A., Aksay, A., Uğuz, M. F., Hakyemez, Y., Bilgiç, T., Tarhan, N., Günay, Y., 2001. Geological map of Turkey, 1:500.000. Ankara, Turkey, MTA.
- Şengör, A. M. C., 1984. The Cimmeride orogenic system and the tectonics of Eurasia, *Geological Society of America Special Paper*, 195, 82.
- Şengör, A. M. C., Altınır, D., Cin, A., Ustaömer, T., Hsu, K. J., 1988. Origin and assembly of the Tethyside orogenic collage at the expense of Gondwana Land, In: M. G. Audley-Charles and A. Hallam (Eds.), *Gondwana and Tethys Geological Society Special Publication*. 37, pp. 119-181.
- Şengör, A. M. C., Yilmaz, Y., 1981. Tethyan evolution of Turkey: A plate tectonic approach, *Tectonophysics*, 75(3-4), 181-241.
- Şengör, A. M. C., Yilmaz, Y., Ketin, I., 1980. Remnants of a pre-Late Jurassic ocean in northern Turkey: Fragments of the Permian-Triassic Paleo-Tethys?, *Geological Society of America Bulletin*, 91(10), 599-609.
- Shillington, D. J., White, N., Minshull, T. A., Edwards, G. R. H., Jones, S. M., Edwards, R. A., Scott, C. L., 2008. Cenozoic evolution of the eastern Black Sea: A test of depth-dependent stretching models, *Earth and Planetary Science Letters*, 265, 360-378.
- Shipunov, S. V., 1997. Synfolding magnetization: detection, testing and geological applications, *Geophysical Journal International*, 130(2), 405-410.
- Sinclair, H. D., Juranov, S. G., Georgiev, G., Byrne, P., Mountney, N. P., 1997. The Balkan Thrust Wedge and Foreland Basin of Eastern Bulgaria: Structural and Stratigraphic Development, In: A. G. Robinson (Eds.), *Regional and petroleum geology of the Black*

- Sea and surrounding region. AAPG Memoir 68, pp. 91-114.
- Sosson, M., Rolland, Y., Muller, C., Danelian, T., Melkonyan, R., Kekelia, M., Adamia, S. A., Babazadeh, V., Kangarli, T., Avagyan, A., Galoyan, G., Mosar, J., 2010. Subduction, obduction and collision in the Lesser Caucasus (Armenia, Azerbaijan, Georgia), new insights, In: M. Sosson, N. Kaymakci, R. A. Stephenson, F. Bergerat and V. Starostenko (Eds.), *Sedimentary basin tectonics from the Black Sea and Caucasus to the Arabian Platform*, London, Geological Society of London, in press.
- Spiegel, C., Sachsenhofer, R. F., Privalov, V. A., Zhykalyak, M. V., Panova, E. A., 2004. Thermotectonic evolution of the Ukrainian Donbas Foldbelt: evidence from zircon and apatite fission track data, *Tectonophysics*, 383, 193-215.
- Spiridonov, E. M., Fedorov, T. O., Ryakhovskii, V. M., 1990. Magmatic rocks of the Mountainous Crimea (1), *Bulletin Moskovskogo Obshestva Ispytalelei Prirody, otd. geol.*, 65(4), 119-134.
- Spiridonov, E. M., Fedorov, T. O., Ryakhovskii, V. M., 1990. Magmatic Rocks of the Mountainous Crimea (2), *Bulletin Moskovskogo Obshestva Ispytalelei Prirody, otd. geol.*, 65(6), 102-112.
- Stampfli, G. M., Borel, G. D., 2002. A plate tectonic model for the Paleozoic and Mesozoic constrained by dynamic plate boundaries and restored synthetic oceanic isochrons, *Earth and Planetary Science Letters*, 196(1-2), 17-33.
- Stampfli, G. M., Borel, G. D., 2004. The TRANSMED transects in space and time: Constraints on the paleotectonic evolution of the Mediterranean domain, In: W. Cavazza, F. Roure, W. Spakman, G. M. Stampfli and P. Ziegler (Eds.), *The TRANSMED Atlas: the Mediterranean Region from Crust to Mantle*, Berlin, Springer Verlag, pp. 53-76.
- Stampfli, G. M., Kozur, H. W., 2006. Europe from the Variscan to the Alpine cycles, In: D.G. Gee and R.A. Stephenson (Eds.), *European Lithosphere Dynamics*. London, Memoir of the Geological Society, 57-82.
- Starostenko, V., Buryanov, V., Makarenko, I., Rusakova, O., Stephenson, R., Nikishin, A., Georgiev, G., Gerasimov, M., Dimitrii, R., Legostaeva, O., Pchelarov, V., Sava, C., 2004. Topography of the crust–mantle boundary beneath the Black Sea Basin, *Tectonophysics*, 381, 211-233.
- Steiger, R. H., Jäger, E., 1977. Subcommittee on geochemistry: convention on the use of decay constants in geo- and cosmochemistry, *Earth and Planetary Science Letters*, 36(359-362).
- Steinberger, B., O'Connell, R. J., 1998. Advection of plumes in mantle flow; implications on hotspot motion, mantle viscosity and plume distribution, *Geophysical Journal International*, 132, 412-434.
- Steinberger, B., Torsvik, T. H., 2008. Absolute plate motions and true polar wander in the absence of hotspot tracks, *Nature*, 452, 620-623.
- Steinberger, B., Torsvik, T. H., submitted. Explanation for the present and past locations of the poles, *Geochemistry, Geophysics, Geosystems*.
- Stephenson, R. A., Mart, Y., Okay, A., Robertson, A. H. F., Saintot, A., Stovba, S.,

- Kriachtchevskaia, O., 2004. Transect VIII: Eastern European Craton to Arabian Craton (Red Star to Red Sea), In: W. Cavazza, F. M. Roure, W. Spakman, G. M. Stampfli and P. A. Ziegler (Eds.), *The TRANSMED Atlas – The Mediterranean region from crust to mantle*, Berlin Heidelberg, Springer Verlag.
- Stephenson, R. A., Yegorova, T., Brunet, M.-F., Stovba, S., Wilson, M., Starostenko, V., Saintot, A., Kuznir, N., 2006. Late Palaeozoic intra-cratonic basins on the East European Craton and its margins, In: D. G. Gee and R. A. Stephenson (Eds.), *European Lithosphere Dynamics*, London, The Geological Society of London. 32, pp. 463-479.
- Stovba, S. M., Maystrenko, Y. P., Stephenson, R. A., Kuznir, N. J., 2003. The formation of the south-eastern part of the Dniepr–Donets Basin: 2-D forward and reverse modelling taking into account post-rift redeposition of syn-rift salt, *Sedimentary geology*, 156, 11-33.
- Stovba, S. M., Stephenson, R. A., 1999. The Donbas Foldbelt: its relationships with the uninverted Donets segment of the Dniepr–Donets Basin, Ukraine, *Tectonophysics*, 313(1), 59-83.
- Stovba, S. M., Stephenson, R. A., Kivshik, M., 1996. Structural features and evolution of the Dniepr-Donets basin, Ukraine, from regional seismic reflection profiles, *Tectonophysics*, 268, 127-147.
- Sun, S. S., McDonough, W. F., 1989. Chemical and isotopic systematics of oceanic basalts: implications for mantle composition and processes, In: A. D. DSaudners and M. J. Norry (Eds.), *Magmatism in Ocean Basins*, London, Geological Society Special Publications. 42, pp. 313-345.
- Sysolin, A. I., Pravikova, N. V., 2008. Subvolcanic Bodies of the Bodrak Complex in the Southwestern Crimea: Structure, Composition, and Formation Conditions, *Moscow University Bulletin*, 63(2), 79-85.
- Tan, X., Kodama, K. P., 2003. An analytical solution for correcting paleomagnetic inclination error, *Geophysical Journal International*, 152, 228-236.
- Tatar, O., Gürsoy, H., Piper, J. D. A., 2002. Differential neotectonic rotations in Anatolia and the Tauride Arc: p[alaeomagnetic investigation of the Erenlerdag Volcanic Omplex and Isparta volcanic district, south-central Turkey, *Journal of the Geological Society of London*, 159, 281-294.
- Tauxe, L., Kent, D. V., 1984. Properties of a detrital remanence carried by hematite from study of modern river deposits and laboratory redeposition experiments, *Geophysical Journal of the Royal Astronomical Society*, 76, 543-561.
- Tauxe, L., Kent, D. V., 2004. A simplified statistical model for the geomagnetic field and the detection of shallow bias in paleomagnetic inclinations: Was the ancient magnetic field dipolar?, In: J. E. T. Channell, D. V. Kent, W. Lowrie and J. G. Meert (Eds.), *Timescales of the Paleomagnetic Field*, AGU Geophysical Monograph. 145, pp. 101-115.
- Tauxe, L., Kodama, K. P., Kent, D. V., 2008. Testing corrections for paleomagnetic inclination error in sedimentary rocks: A comparative approach, *Physics of the Earth and*

- Planetary Interiors, 169, 152-165.
- Tauxe, L., Watson, G. S., 1994. The foldtest: an eigen analysis approach, *Earth and Planetary Science Letters*, 122, 331-341.
- Tekeli, O., 1981. Subduction complex of pre-Jurassic age, northern Anatolia, Turkey, *Geology*, 9, 68-72.
- Topuz, G., Altherr, R., 2004. Pervasive rehydration of granulites during exhumation – an example from the Pular complex, Eastern Pontides, Turkey, *Mineralogy and Petrology*, 81, 165-185.
- Topuz, G., Altherr, R., Kalt, A., Satir, M., Werner, O., Schwarz, W. H., 2004. Aluminous granulites from the Pular complex, NE Turkey: a case of partial melting, efficient melt extraction and crystallisation, *Lithos*, 72, 183-207.
- Topuz, G., Altherr, R., Schwarz, W. H., Dokuz, A., Meyer, H.-P., 2007. Variscan amphibolite-facies rocks from the Kurtoglu metamorphic complex (Gümüşhane area, Eastern Pontides, Turkey), *International Journal of Earth Sciences*, 96, 861-873.
- Torçq, F., Besse, J., Vaslet, D., Marcoux, J., Ricou, E., Halawani, M., Basahel, M., 1997. Paleomagnetic results from Saudi Arabia and the Permo-Triassic Pangea configuration, *Earth and Planetary Science letters*, 148, 553-567.
- Torsvik, T. H., Cocks, L. R. M., 2004. Earth geography from 400 to 250 Ma: a paleomagnetic, faunal and facies review, *Journal of the Geological Society*, 161, 555-572.
- Torsvik, T. H., Cocks, L. R. M., 2005. Norway in space and time: A centennial cavalcade, *Norwegian Journal of Geology*, 85, 73-86.
- Torsvik, T. H., Muller, R. D., Van der Voo, R., Steinberger, B., Gaina, C., 2008a. Global plate motion frames: toward a unified model, *Reviews of Geophysics*, 46, RG3004, doi: 10.1029/2007RG000227.
- Torsvik, T. H., Steinberger, B., Cocks, L. R. M., Burke, K., 2008b. Longitude: Linking Earth's ancient surface to its deep interior, *Earth and Planetary Science Letters*, 276, 273-282.
- Torsvik, T. H., Van der Voo, R., 2002. Refining Gondwana and Pangea palaeogeography: estimates of Phanerozoic non-dipole (octupole) fields, *Geophysical Journal International*, 151, 771-794.
- Tüysüz, O., 1990. Tectonic evolution of a part of the Tethyside orogenic collage: The Kargı Massif, northern Turkey, *Tectonics*, 9(1), 141-160.
- Tüysüz, O., 1999. Geology of the Cretaceous sedimentary basins of the Western Pontides, *Geological Journal*, 34, 75-93.
- Tüysüz, O., Tekin, U. K., 2007. Timing of imbrication of an active continental margin facing the northern branch of Neotethys, Kargı Massif, northern Turkey *Cretaceous Research*, 28(5), 854-764.
- Ustaömer, P. A., Mundil, R., Renne, P. R., 2005. U/Pb and Pb/Pb zircon ages for arc-related intrusions of the Bolu Massif (W Pontides, NW Turkey): evidence for Late Precambrian (Cadomian) age, *Terra Nova*, 17, 215-223.
- Ustaömer, T., Robertson, A. H. F., 1997. Tectonic-Sedimentary Evolution of the North Tethyan Margin in the Central Pontides of Northern Turkey, In: A. G. Robinson (Eds.),

- Regional and petroleum geology of the Black Sea and surrounding region, AAPG Memoir. 68, pp. 255-290.
- Ustaömer, T., Robertson, A. H. F., 1993. A Late Paleozoic-Early Mesozoic marginal basin along the active southern continental margin of Eurasia: evidence from the central Pontides (Turkey) and adjacent regions, *Geological Journal*, 28, 219-238.
- van der Meer, D. G., Spakman, W., van Hinsbergen, D. J. J., Amaru, M. L., Torsvik, T. H., 2010. Toward absolute plate motions constrained by lower mantle slab remnants, *Nature Geosciences*, doi:10.1038/ngeo708.
- Van der Voo, R., 1968. Jurassic, Cretaceous and Eocene pole positions from northeastern Turkey, *Tectonophysics*, 6(3), 251-269.
- Van der Voo, R., 1990. The reliability of paleomagnetic data, *Tectonophysics*, 184, 1-9.
- Van der Voo, R., Torsvik, T. H., 2001. Evidence for late Paleozoic and Mesozoic non-dipole fields provides an explanation for the Pangea reconstruction problems, *Earth and Planetary Science Letters*, 187, 71-81.
- Van der Voo, R., Torsvik, T. H., 2004. The quality of the European Permo-Triassic paleopoles and its impact on Pangea reconstructions, In: J. E. T. Channell, D. V. Kent, W. Lowrie and J. G. Meert (Eds.), *Timescales of the Internal Geomagnetic Field*, AGU Geophysical Monograph. 145, pp. 29-42.
- Van der Voo, R., Van der Kleijn, P. H., 1970. The complex NRM of the Permo-Carboniferous Bademli redbeds (Tauride chains, southern Turkey), *Geologie en Mijnbouw*, 49(5), 391-395.
- van Hinsbergen, D. J. J., submitted. A key metamorphic core complex restored: the Menderes Massif of western Turkey, *Earth Science Reviews*.
- van Hinsbergen, D. J. J., Dekkers, M. J., Koç, A., 2010a. Testing Miocene remagnetization of Bey Dağları: Timing and amount of Neogene rotations in SW Turkey, *Turkish Journal of Earth Sciences*, doi:10.3906/yer-0904-1.
- van Hinsbergen, D. J. J., Dekkers, M. J., Bozkurt, E., Koopman, M., 2010b. Exhumation with a twist: paleomagnetic constraints on the evolution of the Menderes metamorphic core complex (western Turkey) *Tectonics*, in press.
- van Hinsbergen, D. J. J., Hafkenscheid, E., Spakman, W., Meulenkamp, J. E., Wortel, R., 2005. Nappe stacking resulting from subduction of oceanic and continental lithosphere below Greece, *Geology*, 33(4), 325-328.
- Van Hoof, A. A. M., Langereis, C. G., 1991. Reversal records in marine marls and delayed acquisition of remanent magnetisation, *Nature*, 351, 223-224.
- van Hunen, J., van den Berg, A. P., Vlaar, N. J., 2002. On the role of subducting oceanic plateaus in the development of shallow flat subduction, *Tectonophysics*, 352, 317-333.
- Van Velzen, A. J., Zijdeveld, J. D. A., 1995. Effects of weathering on single domain magnetite in early Pliocene marls, *Geophysical Journal International*, 121, 267-278.
- Van Wees, J. D., Stephenson, R. A., Stovba, S. M., Shymanovskiy, V. A., 1996. Tectonic variation in the Dniepr-Donets Basin from automated modelling of backstripped subsidence curves, *Tectonophysics*, 268, 257-280.

- Vandamme, D., 1994. A new method to determine paleosecular variation, *Phys. Earth Planet. Int.*, 85, 131-142.
- Vasiliev, I., Franke, C., Meeldijk, J. D., Dekkers, M. J., Langereis, C. G., Krijgsman, W., 2008. Putative greigite magnetofossils from the Pliocene epoch, *Nature Geoscience*, 1, 782-786.
- Vincent, S. J., Allen, M. B., Ismail-Zadeh, A. D., Flecker, R., Foland, K. A., Simmons, M. D., 2005. Insights from the Talysh of Azerbaijan into the Paleogene evolution of the South Caspian region, *GSA Bulletin*, 117(9/10).
- Vine, F. D., Matthews, D. H., 1963. Magnetic anomalies over oceanic ridges, *Nature*, 199, 947-949.
- Voznesensky, A. I., Knipper, A. L., Perfiliev, A. S., Uspenskaya, A. E., Areshin, A. V., 1998. Middle-Late Jurassic history of the Eastern Crimean Mts. Terrane, *Geotektonika*, 1, 27-44.
- Waldhör, M., Appel, E., 2006. Intersections of remanence small circles: new tools to improve data processing and interpretation in palaeomagnetism, *Geophysical Journal International*, 166(1), 33-45.
- Wardlaw, B. R., Davydov, V., Gradstein, F. M., 2004. The Permian Period, In: F. M. Gradstein, J. G. Ogg and A. G. Smith (Eds.), *A Geologic Time Scale 2004*, 249-264.
- Watson, G., 1983. Large sample theory of the Langevin distributions, *Journal of Statistical Planning and Inference*, 8, 245-256.
- Watson, G. S., Enkin, R. J., 1993. The fold test in paleomagnetism as a parameter estimation problem, *Geophysical Research Letters*, 20, 2135-2138.
- Wegener, A. L., 1915. *Die Entstehung der Kontinente und Ozeane*.
- Weltje, G. J., 1997. End-member modeling of compositional data: Numerical-statistical algorithms for solving the explicit mixing problem, *Mathematical Geology*, 29, 503-546.
- Whitney, D. L., Teyssier, C., Dilek, Y., Fayon, A. K., 2001. Metamorphism of the Central Anatolian Crystalline Complex, Turkey: influence of orogen-normal collision vs. wrench-dominated tectonics on P-T-t paths, *Journal of metamorphic Geology*, 19, 411-432.
- Wijbrans, J. R., Pringle, M. S., Koppers, A. A. P., Scheveers, R., 1995. Argon geochronology of small samples using the Vulkan argon laserprobe, *Proc. van de Koninklijke Nederlandse Academie van Wetenschappen*, 98(Ser. B), 185-218.
- Yalınız, K. M., Güncüoğlu, M. C., Özkan-Altın, S., 2000. Formation and emplacement ages of the SSZ-type Neotethyan ophiolites in Central Anatolia, Turkey: palaeotectonic implications, *Geological Journal*, 35, 53-68.
- Yikilmaz, M. B., Okay, A. I., Ozkar, I., 2002. A pelagic Palaeocene sequence in the Biga peninsula northwest Turkey, *Bulletin of the Mineral Research and Exploration*, 123-124, 21-26.
- Yilmaz, C., Kandemir, R., 2006. Sedimentary records of the extensional tectonic regime with temporal cessation: Gumushane Mesozoic Basin (NE Turkey) *Geologica Carpathica*,

- 57(1), 3-13.
- Yılmaz, C., Şen, C., Özgür, A. S., 2003. Sedimentological, paleontological and volcanic records of the earliest volcanic activity in the Eastern Pontide Cretaceous volcanic arc (NE Turkey), *Geologica Carpathica*, 54(6), 377-384.
- Yılmaz, I. Ö., Altıner, D., 2006. Cyclic paleokarst surfaces in Aptian peritidal carbonate successions (Taurides, southwest Turkey): internal structure and response to mid-Aptian sea-level fall, *Cretaceous Research*, 27, 814-827.
- Zijderveld, J. D. A., 1967. A. C. demagnetization of rocks: analysis of results, In: D. W. Collinson, K. M. Creer and S. K. Runcorn (Eds.), *Methods in Palaeomagnetism*, Amsterdam, New York, Elsevier, pp. 254–286.
- Zimmerman, A., Stein, H. J., Hannah, D., Kozelj, D., Bogdanov, K., Berza, T., 2008. Tectonic configuration of the Apuseni–Banat–Timok–Srednogie belt, Balkans-South Carpathians, constrained by high precision Re–Os molybdenite ages, *Mineralium Deposita*, 43, 1-21.
- Zonenshain, L. P., Kuzmin, M. I., Napatov, L. M., Eds., 1990. *Geology of the USSR: a Plate-Tectonic Synthesis Geodynamics Series*, American Geophysical Union.
- Zonenshain, L. P., Le Pichon, X., 1986. Deep basins of the Black Sea and Caspian Sea as remnants of Mesozoic back-arc basins, *Tectonophysics*, 123, 181-211.

Acknowledgements

The last four years have been a crazy mixture of traveling around between fieldworks in Turkey, the Ukraine and Spain and periods in the lab and behind my desks in Utrecht and Amsterdam. And then of course the conferences in Kiev, Veldhoven, Ankara, Vienna, Paris, Veldhoven, San Francisco, Ankara and once again: Ankara. It was great!

This all started with the request from Aline Saintot to Wout Krijgsman in spring 2004. As a post-doc working in Crimea, Dobrogea and the Greater Caucasus, she was interested in paleolatitude reconstructions from these areas. Therefore, she wanted to involve the paleomagnetic lab in Utrecht. An e-mail from Cor Langereis to attract students for trips to Crimea and Dobrogea was answered by Martijn Deenen and me. Two crazy but great weeks in Crimea and two nice weeks in Dobrogea later, we started paleomagnetic measurements at 'The Fort'. The results were very interesting (although quite different after inserting the correct bedding attitudes ;-)) and Cor Langereis was motivated and successful in finding partial funding for a follow-up PhD project on this subject. The results were orally presented in Vienna in 2005. It was probably one of the most nervous days of my life (so far). In the same week, Randell Stephenson and Aline Saintot took me out for lunch, and told me they were willing to fund part of the research proposal I wrote for this PhD on the basis of the results from my MSc research. Thank you all for making this project possible!

I would like to start thanking Cor for his never-ending support throughout the years. Cor, dankje voor de geweldige tijden, met name op veldwerken met slogans als 'Wat een hondenleven hebben we toch' en 'Zonsondergangen, dat kunnen die Turken wel!', de bijna altijd veel te late avonden op balkons (ook gangbaar bij afwezigheid van een balkon), wijn (hoe vies soms ook in bepaalde delen van deze wereld), de ellenlange gesprekken over de meest uiteenlopende zaken en de ontvangsten bij je thuis (zelfs op de laatste zondag voordat dit proefschrift af moest) waarbij ik ontelbare keren gewoon aan tafel kon aanschuiven. Beste Douwe, jij bent onvermoeibaar! Altijd nog even een schepje erbovenop in discussies, altijd nog dingen af weten te krijgen, altijd alles wat ik schreef snel na weten te kijken (eerste versies altijd lekker in rood geveerd). Heel erg bedankt voor je niet-aflatende steun! Ik was de eerste PhD die je begeleidde, en vast niet de eenvoudigste, gezien onze koppigheid en eigenwijsheid die af en toe botste. Maar we kwamen er altijd uit! Ik zal je missen (al zit je natuurlijk al een tijdje in Noorwegen), ook al vermoed ik dat we in de toekomst elkaars onderzoeksgebieden zullen blijven doorkruisen. Randell, it took a while before you managed to kick me to my office in Amsterdam! But I'm very grateful you did: I had great times there! Dankjewel for always answering my questions appropriate and quick. For joining field trips to Crimea and Turkey, and for involving me in the MEBE program. I met many

researchers at the MEBE conferences, and will likely benefit from these connections in the future. Sierd, bedankt voor het mogelijk maken van dit onderzoek bij beide universiteiten.

I would like to thank the reading committee very much for their effort to read this thesis and giving their feedback: Giovanni Muttoni, Aral Okay, Trond Torsvik, Reinoud Vissers and Rinus Wortel.

Thanks also to the other people I collaborated with: Jan Wijbrans, Klaudia Kuiper, Gareth Davies, Liviu Matenco, Mark Dekkers, Demir Altiner, Berend Vrouwe, Françoise Chalot-Prat (thank you for the nice welcome in Nancy), Jean-Claude Hippolyte, Sascha Kitchka and Douwe van der Meer. Tom Mullender, onze technicus op het fort, je weet altijd zo afschuwelijk veel! En Roel van Elzas, voor zijn hulp in het mineraalscheidingslab om monsters te prepareren voor de datering. Bram van der Kooij voor het bekijken van slijpplaatjes. Maartje (Oost-Europa rules!), het was heel leuk om je te begeleiden bij je MSc onderzoek, ik hoop dat je iets aan me had! Succes met jouw PhD en wie weet lopen we ooit weer eens samen in het veld rond.

Dear Nuri, I wouldn't know how to thank you appropriately for all your help during the last 4 years! It took a few weeks or so before I got used to the 'Turkish way' of doing and organizing things, but after I managed to relax, we had great times traveling around everywhere in Turkey (from Kaş to Trabzon and from Bilecik to Ürgüp, from the Black Sea to the Mediterranean), also with Pınar of course! Thank you for the enormous help I had from you from the geological side: you seem to know everything about Turkish geology! We had and still have great discussions. And of course it was good to always come back home in Ankara after one or two weeks in the field to exchange field-assistants/supervisors at the airport. Çok sağolasın both of you for the never-ending support and nice times! I'm looking forward again to this May.

All my fieldworks would not have been possible without the help of many people in the field. Drilling is (luckily) nearly impossible on your own, so I was never alone in the field! Thanks to Ahmet Peynircioğlu, Pınar Ertepinar, Nuri Kaymakçı, Cor Langereis, Ane Wiersma, Ayten Koç, Douwe van Hinsbergen, Mustafa Kaya, Bora Rojay, Yener Eyüboğlu, Aral Okay, Randell Stephenson, Vladimir Bakhmutov, Martijn Deenen, Wout Krijgsman, Iuliana Vasiliev, Aline Saintot, Steve Vincent, Hemmo Abels, Flora Boekhout, Wolter Bosch, Constantin Pechnikov, Maartje Hamers, Sascha Kitchka, Oleg Rusakov, Viktor Yudin, Sergei Yudin, Elena Yudina, Sergey Bolotov, Galina Slivinskaya and Evgeniy Polyachenko.

Martijn, Sjef-de-Pef: we waren de afgelopen 10 jaar zo'n beetje onafscheidelijk. Hoeveel mensen wel niet gespeculeerd hebben over een mogelijke relatie tussen

ons beiden. Haha. Ik zal onze botte en gegarandeerd voor anderen onbegrijpelijke (kantoor)humor missen. Het was vet saai geweest zonder jou..... Uiteraard ben je een van mijn paranimfen. Bedankt ook mijn kamergenoten aan de VU: eerst Karen, later Maarten, Stefan en Suzanne. En natuurlijk Anna, die altijd alles weet te regelen. Ik was er niet zo vaak, maar ik heb zeer goede herinneringen aan de tijd op de VU! Thanks to all people of the Paleomagnetic Lab I haven't mentioned yet: Iuliana (the Queen), Ahmet (I'm looking forward to your defense, and please never scare us again!), Arjan, Fatima, Pinar, Guillaume (thanks for involving me in Himalayan geology, who knows if I ever end-up there), Silja, Zhihong, Gijs, Mariel, Andy, Viktor, Katya, Ksenia, Bora Ü., Lennart, Christine, Marcela, Hayfaa, Roderic, Mark S. and Marius. Thanks for your support, nice lunches and great Friday-borrels during the last 6 (!) years! And not to forget the people from the department across the street! Lots of thanks also to the Tectonics group in Amsterdam and people from other groups at the VU I came across: it was very nice to be there every now and then. I have good memories of the Thursday-borrels!

De eerste drie jaar was de maand juni gereserveerd voor het assisteren van eerstejaars veldwerken in Spanje, eerst twee jaar voor de VU, daarna voor Utrecht (waarbij de cultuurverschillen tussen beide universiteiten aardig aan het licht kwamen ;-)). Het waren zeer goede tijden. Bedankt Kees, Hubert, Geert-Jan, Ronald, Karen, Elco, Ane, Maarten, Frits, Herman, Wout, Martijn, Sietske en Desiree! Ik heb er hele goede contacten aan overgehouden!

Thanks also to Yann Rolland and Marc Sosson for encouraging me to write a research proposal to start working in Armenia and surrounding areas! Great that the proposal is granted, see you in Nice!

Côme, thanks for your endless support and patience during my last year. It was certainly not the easiest year, but it was great, largely because of the good times (also in Turkey!) with you! Thanks also to all my friends and jaargenoten for the necessary support! Speciaal aan Anne, Christien, Annemiek, Mich en uiteraard Sander. Hopelijk zien we elkaar weer wat vaker nu! Hopefully not, but most probably I forgot some people in this long list, so thanks to any of you I forgot!

Pap en mam, super dat ik zo relaxed heb kunnen studeren, en dat jullie me steunden om een PhD te gaan doen, ook al bleef het waarschijnlijk nogal vaag wat ik nu echt deed op een dag! Ik heb het best lang volgehouden voor iemand die vanaf zijn zevende al riep niet meer naar school te willen gaan.... Marijn, allerliefste zus, bedankt voor je interesse! Ik hoop dat je over een jaar ook ongeveer klaar bent met jouw proefschrift! Dankje dat je mijn paramimf wilde zijn! Opa & oma en oma: ik ben eindelijk afgestudeerd!

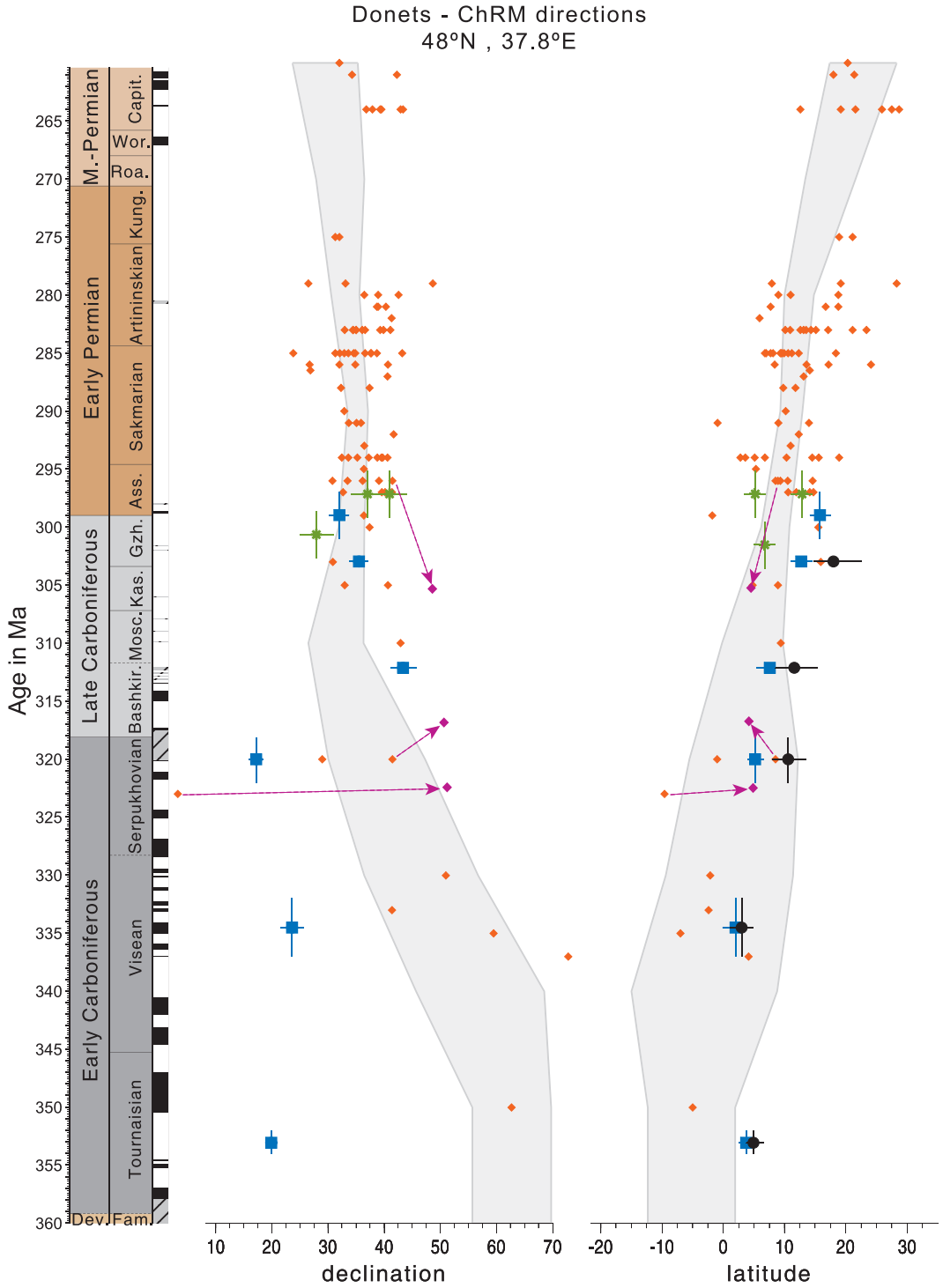
Curriculum vitae

Maud Meijers was born on the 24th of July 1981 in Schinveld (the Netherlands). She passed her pre-university education in 1999 at the Serviam College in Sittard and started her geology studies at Utrecht University the same year. After finishing her Bachelor thesis with Prof. dr. Chris Spiers in the HPT (High Pressure and Temperature) laboratory in 2002, she concentrated more on field work involving research.

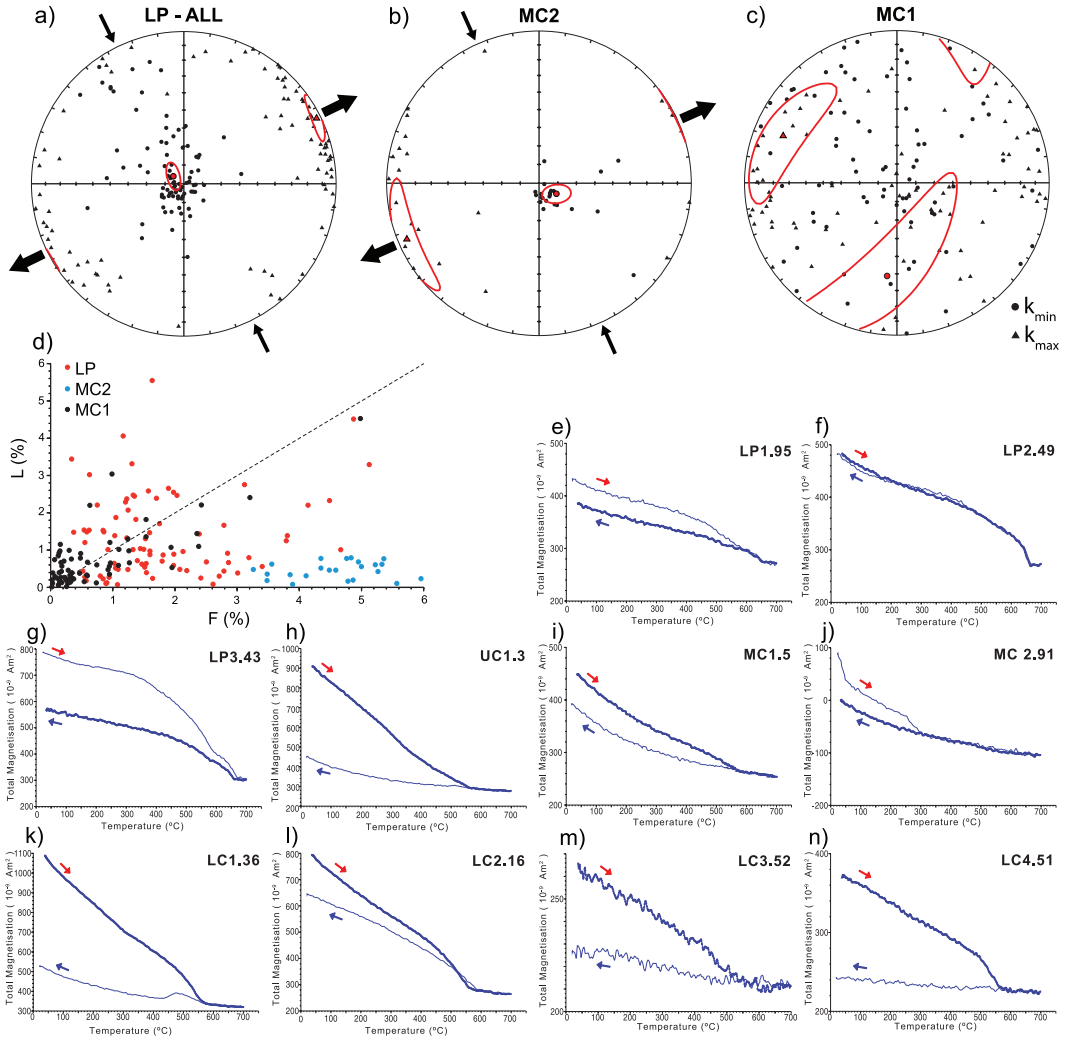
After an e-mail in 2004 from Prof. dr. Cor Langereis who was looking for students that were interested in joining field trips to either Crimea (Ukraine) or Dobrogea (Romania) for their MSc research, she decided to sign up together with Martijn Deenen. To ensure participation in both field works, they requested and received additional funding from the 'Molengraaff Fonds'. The MSc research was carried out in collaboration with dr. Aline Saintot, a post-doc at the VU University Amsterdam at the time, who was interested in the paleolatitude position of the Crimean peninsula and Dobrogea throughout the Mesozoic. After one year of research Maud Meijers finished her MSc thesis entitled 'Mesozoic paleomagnetic data from North Dobrogea (Romania) and Crimea (Ukraine): Cimmerian deformation phases along the southern margin of the East European Platform' and a PhD proposal entitled 'Opening and closure of the Tethys oceans: Mesozoic Cimmerian deformation around the present-day Black Sea'. Joint efforts of the Tectonics Group at the VU University Amsterdam and the Paleomagnetic Laboratory 'Fort Hoofddijk' at Utrecht University ensured financial support for a 4-year PhD study, and Maud Meijers started her PhD research in January 2006. The results of her PhD research are presented in this thesis.

Her research proposal entitled 'Paleomagnetism of the Armenian Block and its foreland: constraints on Tethyan plate reconstructions and oroclinal bending during the Phanerozoic' for the '2010 Henri Poincaré Fellowship' at the Observatoire de la Côte d'Azur in Nice was granted and she will continue doing research as a post-doc in collaboration with Marc Sosson and Yann Rolland.

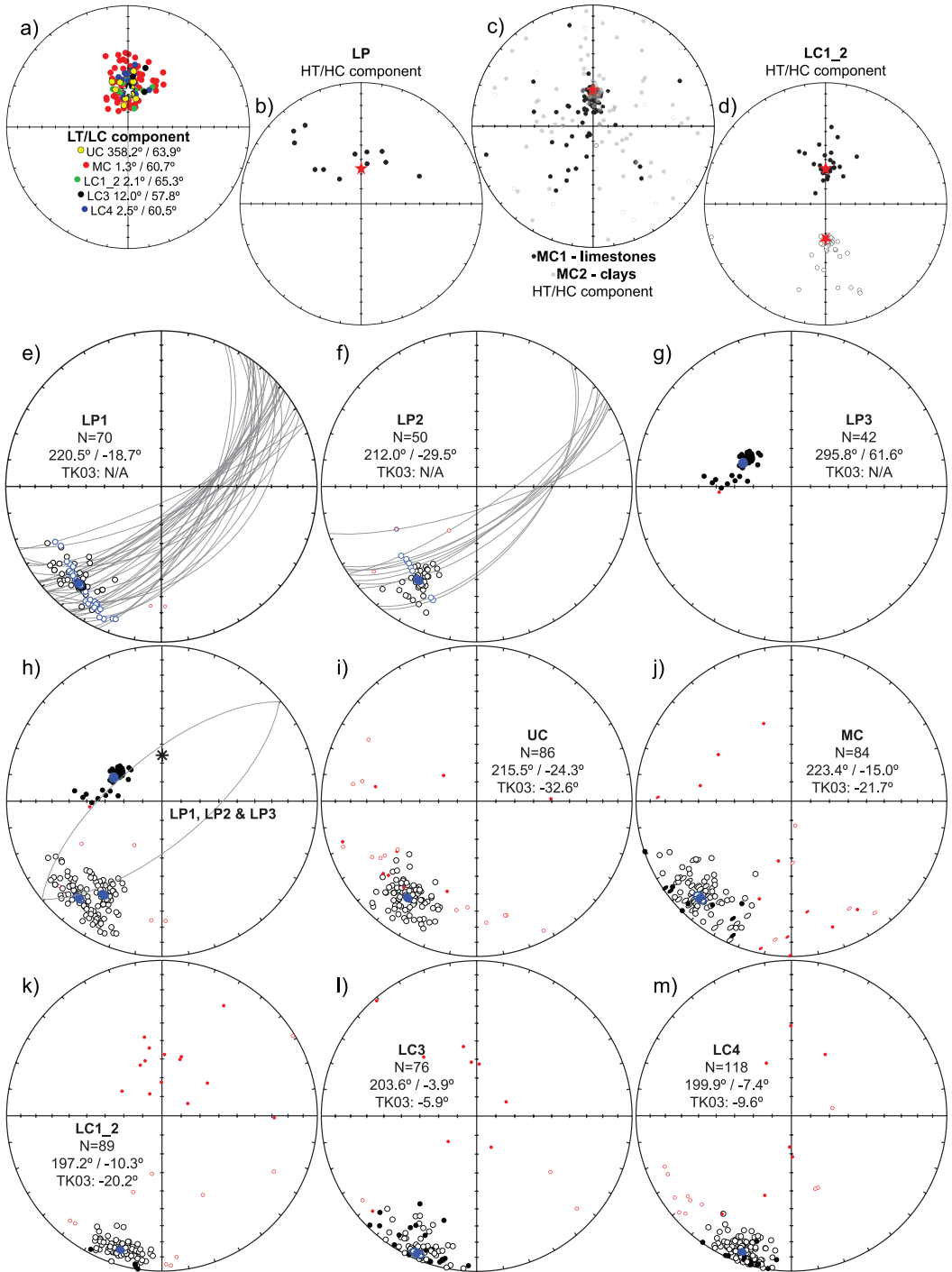
Appendix 1 Chapter 1, Figure 1.3 (p. 31)



Appendix 2 Chapter 1, Fig. 1.4 (p. 35)

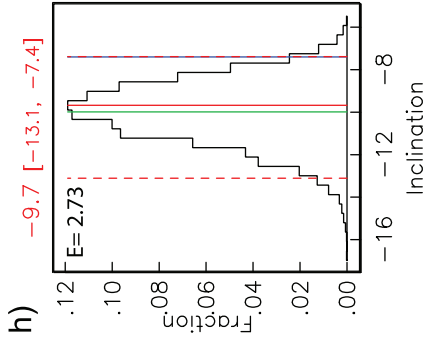
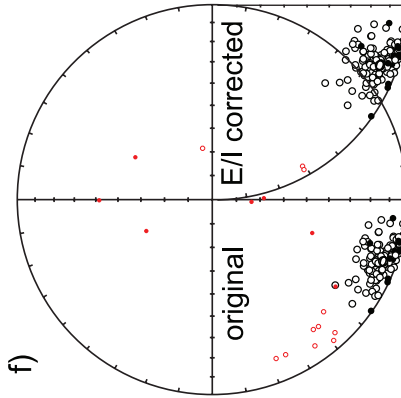
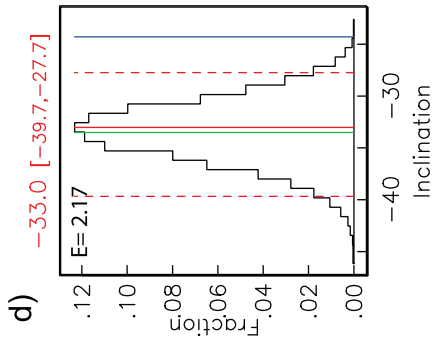
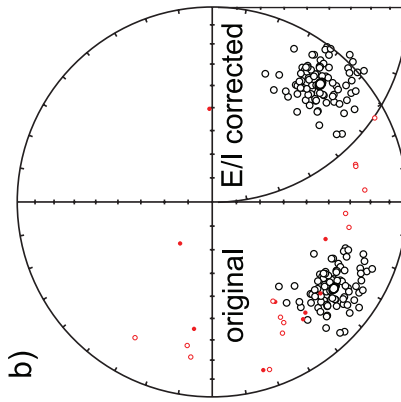
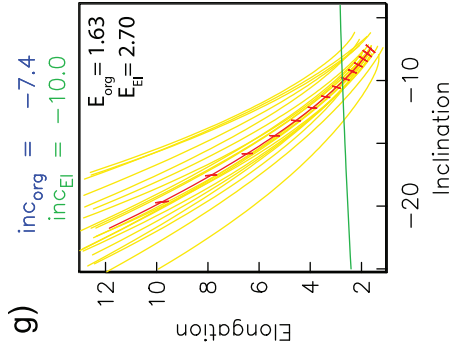
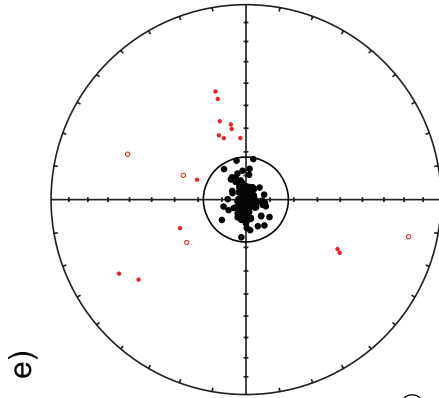
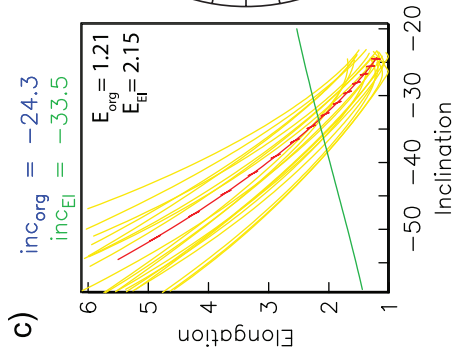
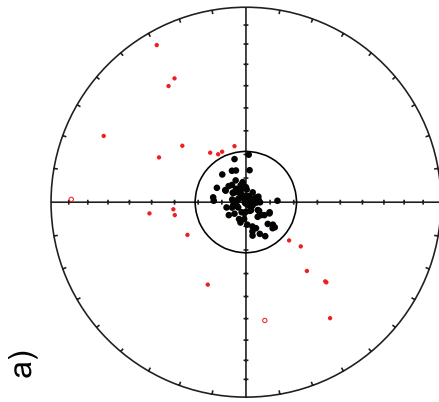


Appendix 3 Chapter 1, Fig. 1.6 (p. 39)



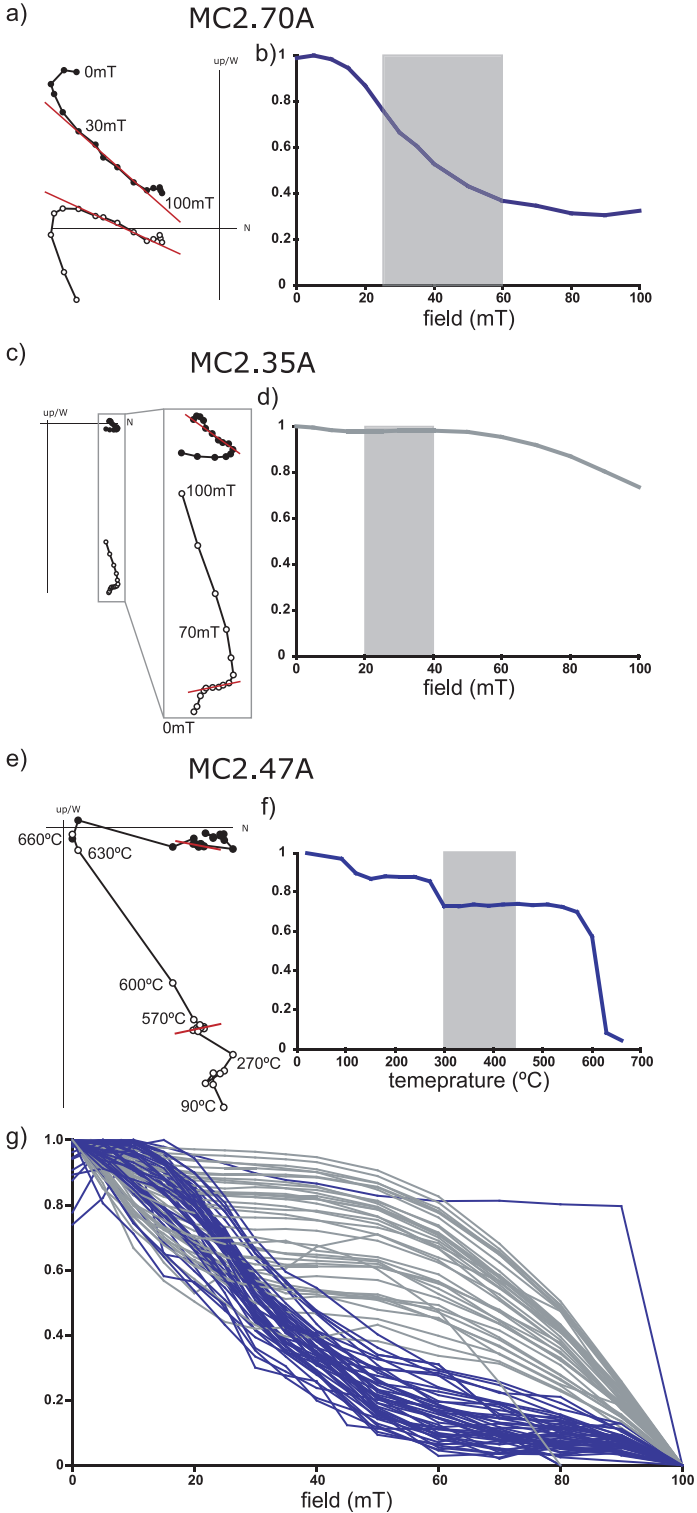
UC

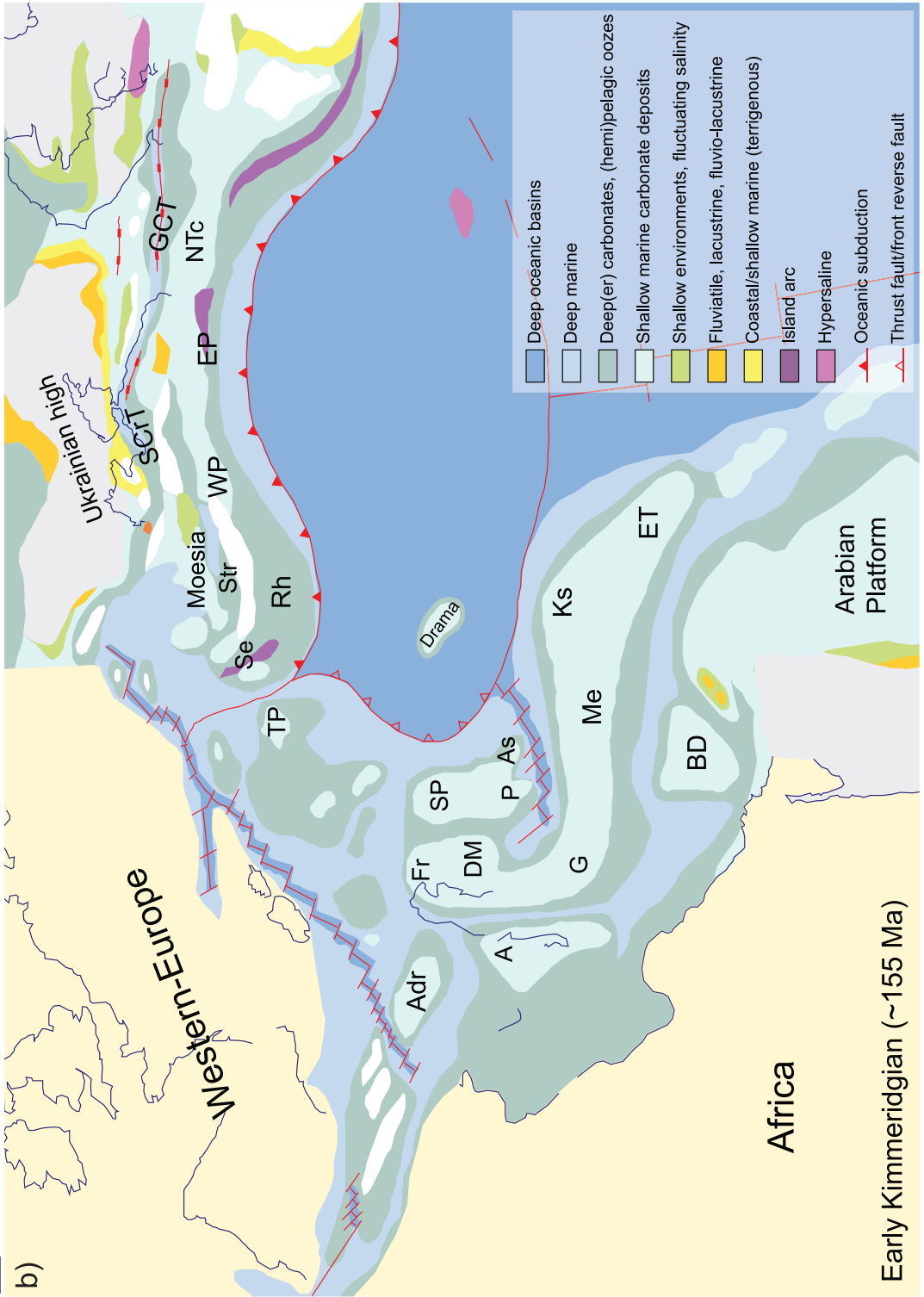
LC4



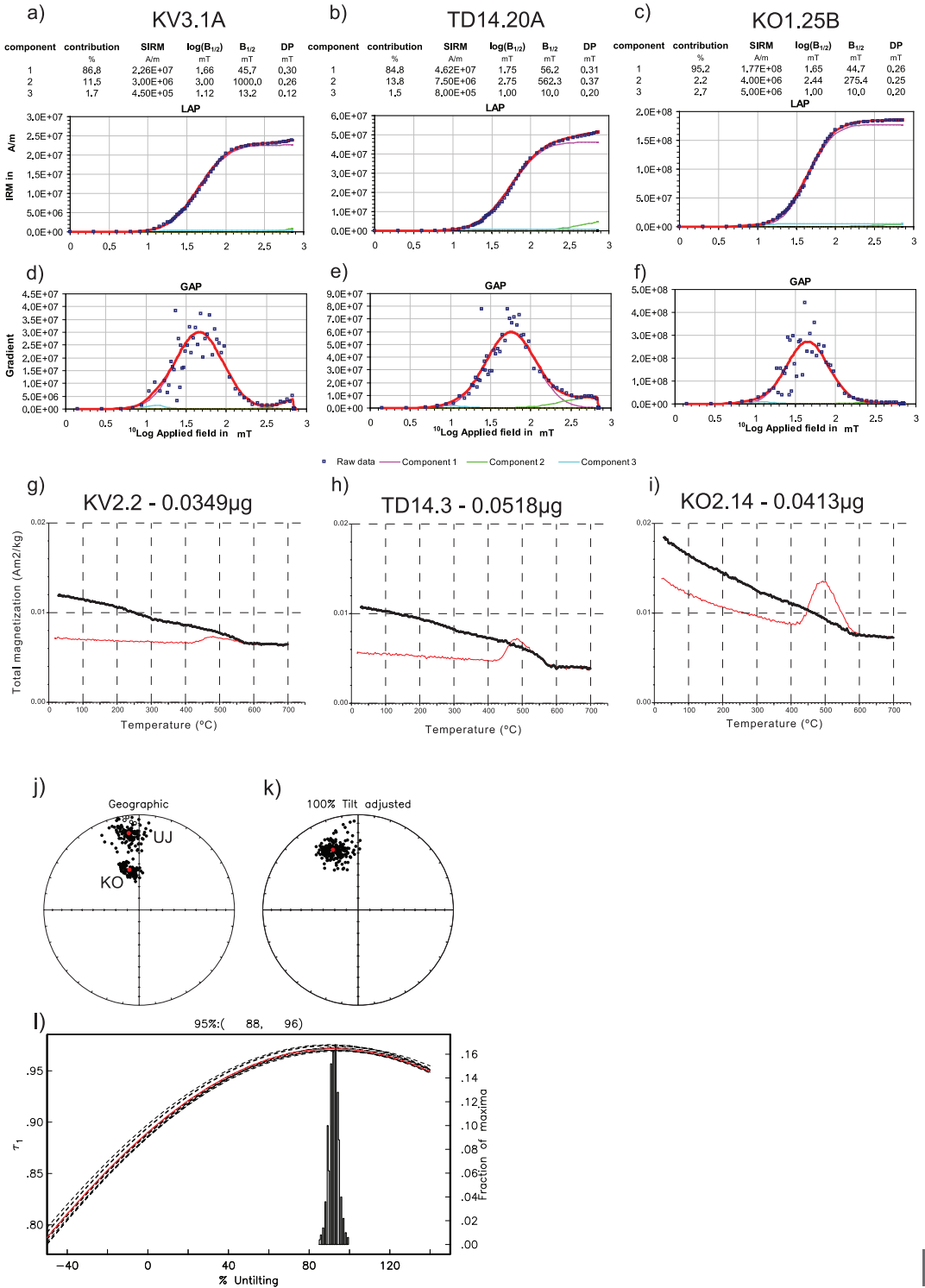
Appendix 4 Chapter 1, Fig. 1.7 (p. 40)

Appendix 5 Chapter 1, Fig. 1.8 (p. 41)

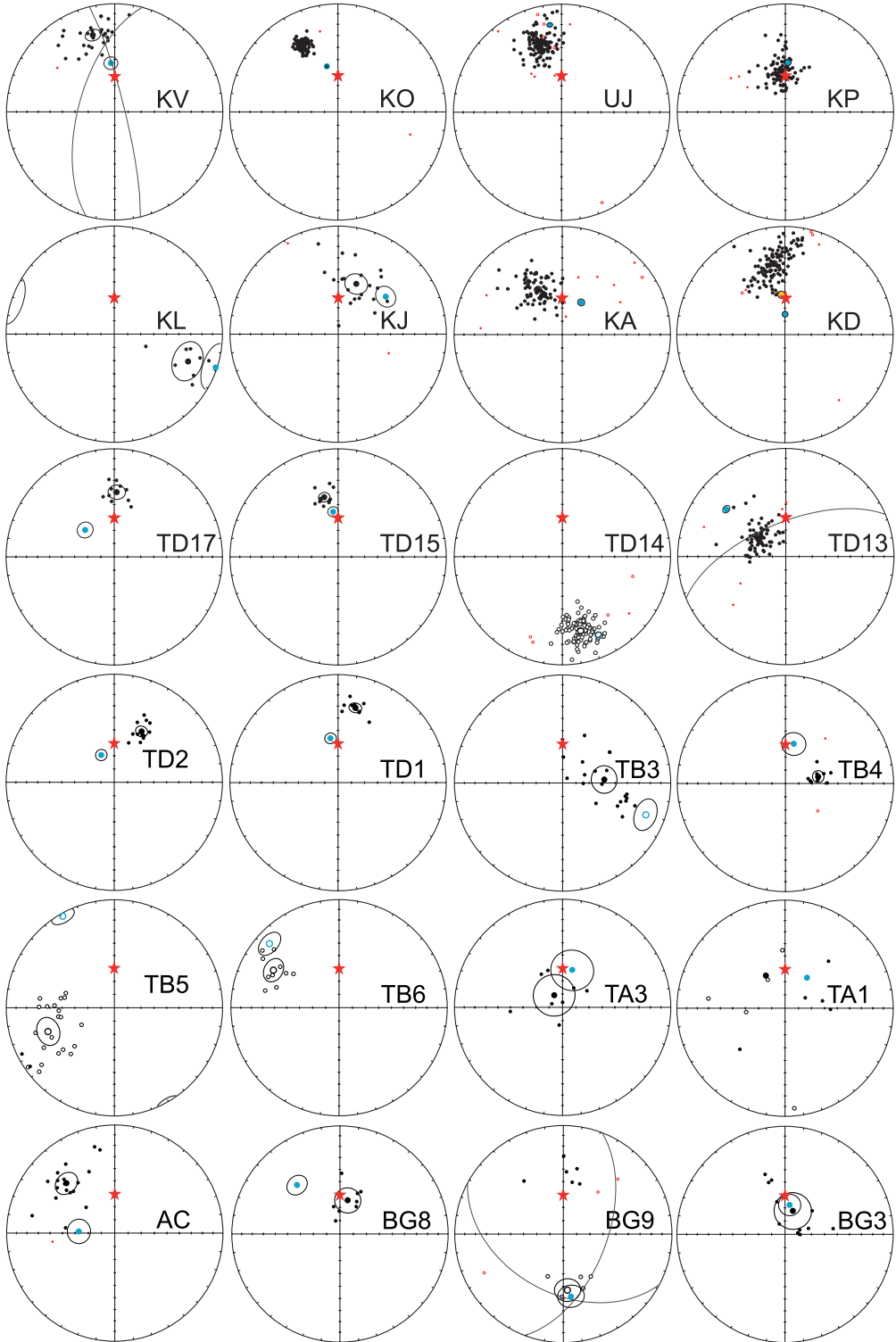




Appendix 7 Chapter 2, Fig. 2.2 (p. 59)

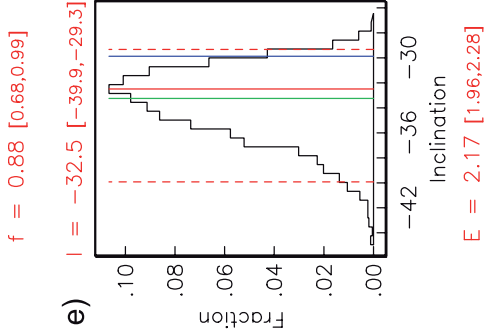
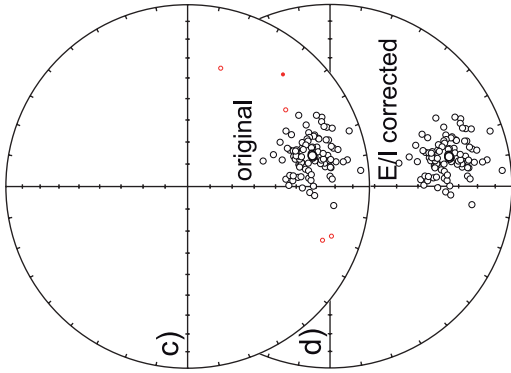
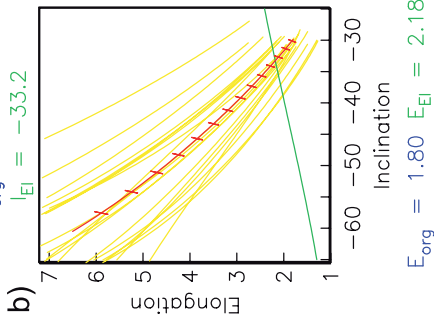
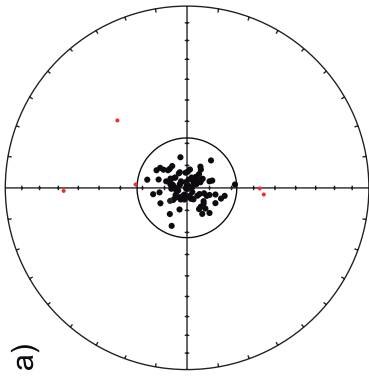


Appendix 8 Chapter 2, Fig. 2.4 (p. 66-67)

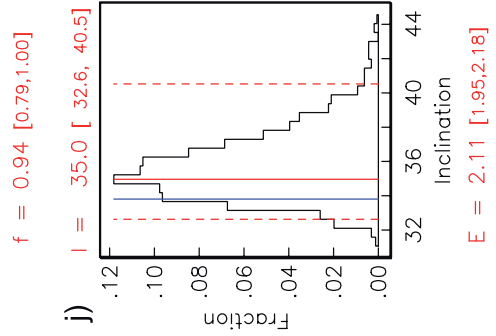
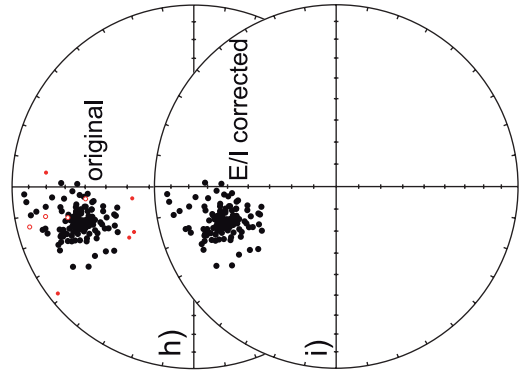
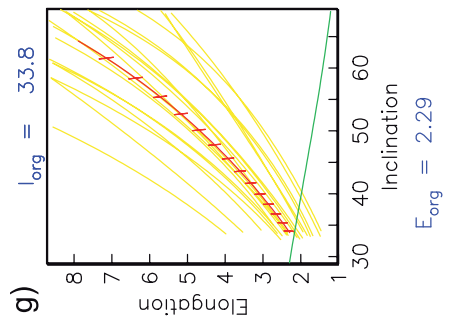
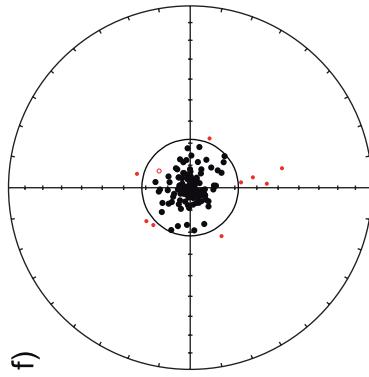


Appendix 9 Chapter 2, Fig. 2.5 (p. 69)

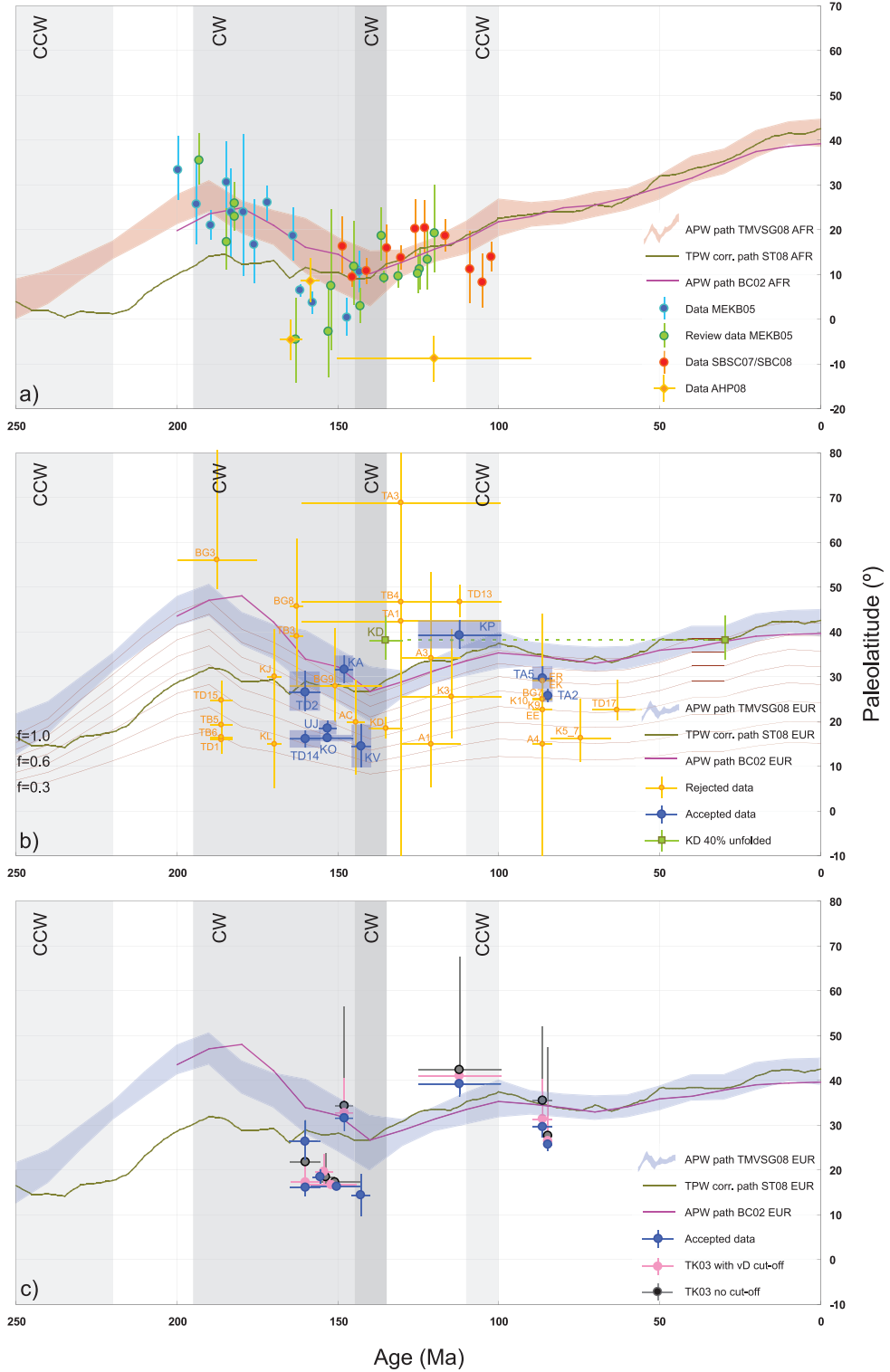
TD 14



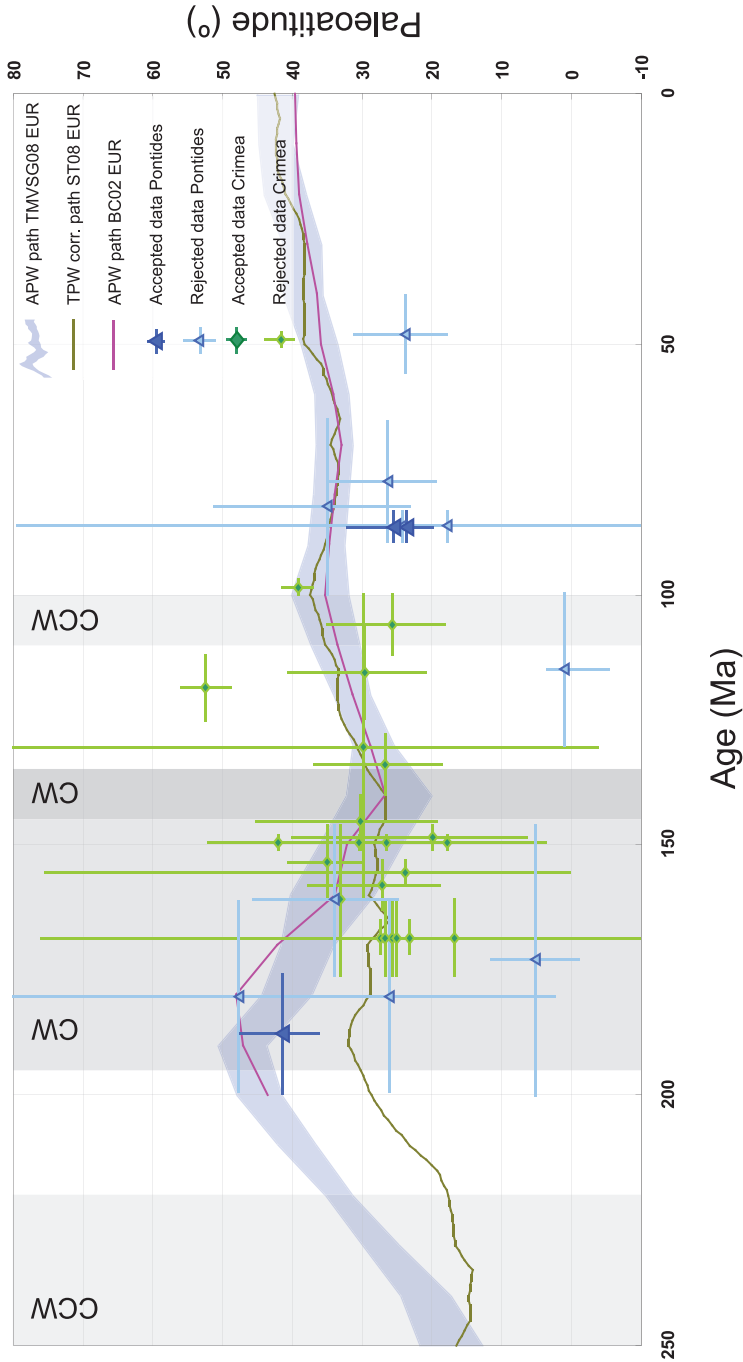
UJ

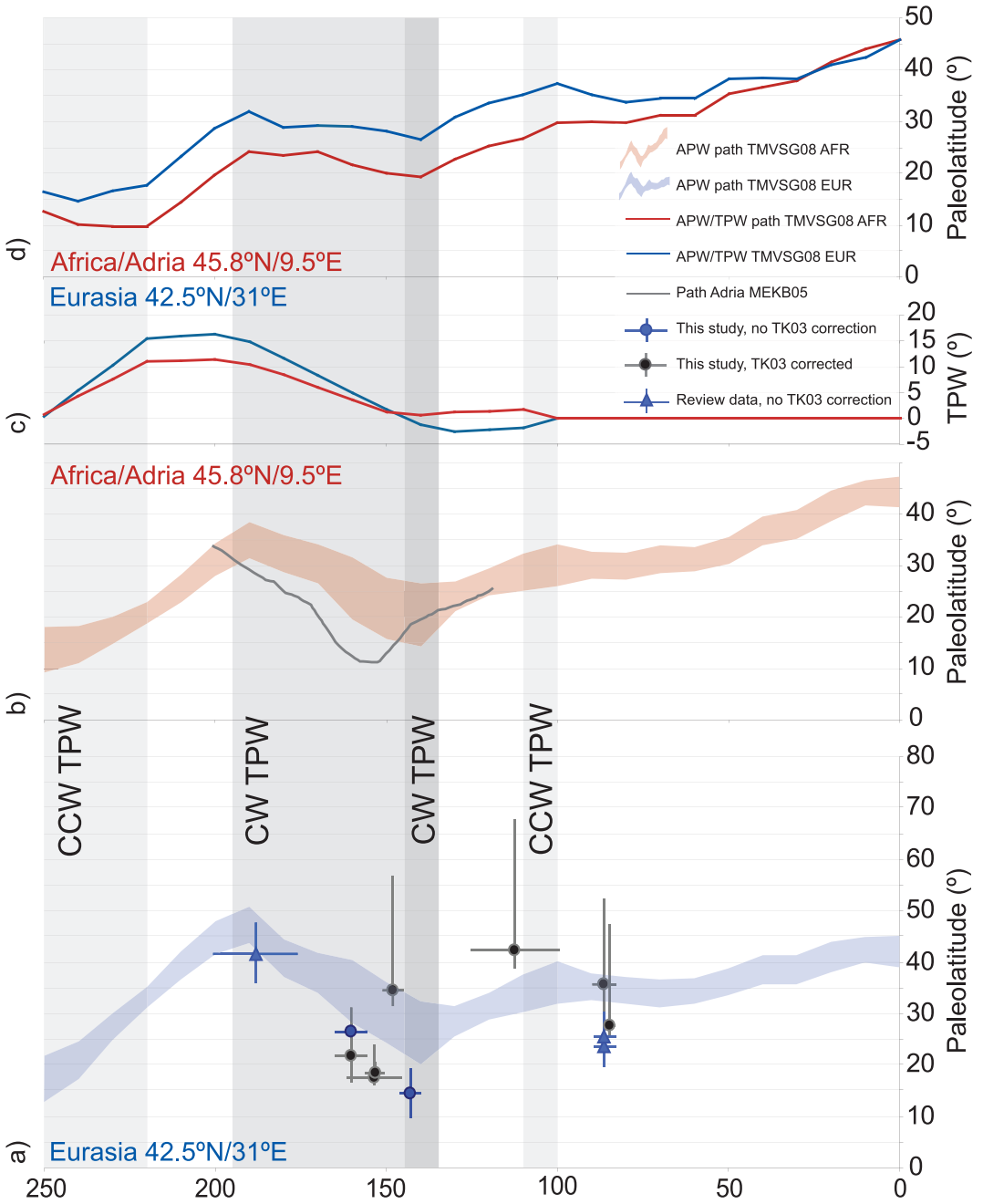


Appendix 10 Chapter 2, Fig. 2.6 (p. 70)

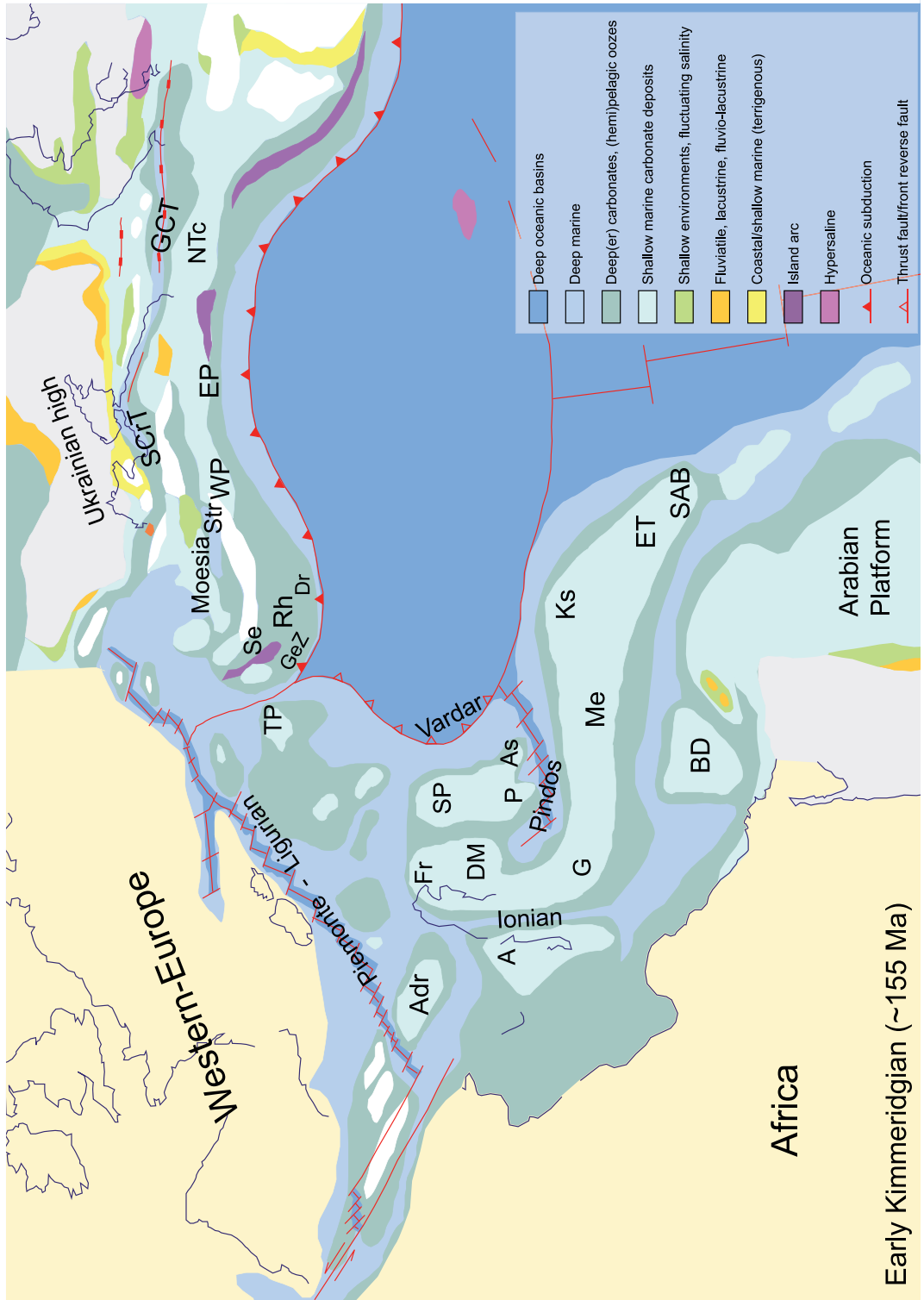


Appendix 11 Chapter 2, Fig. 2.7 (p. 73)



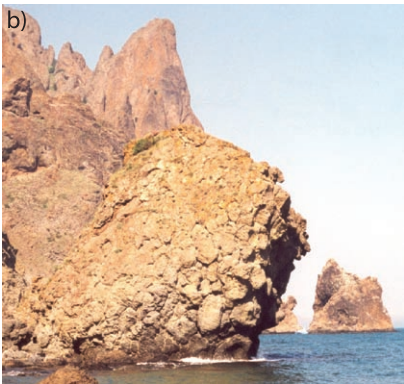
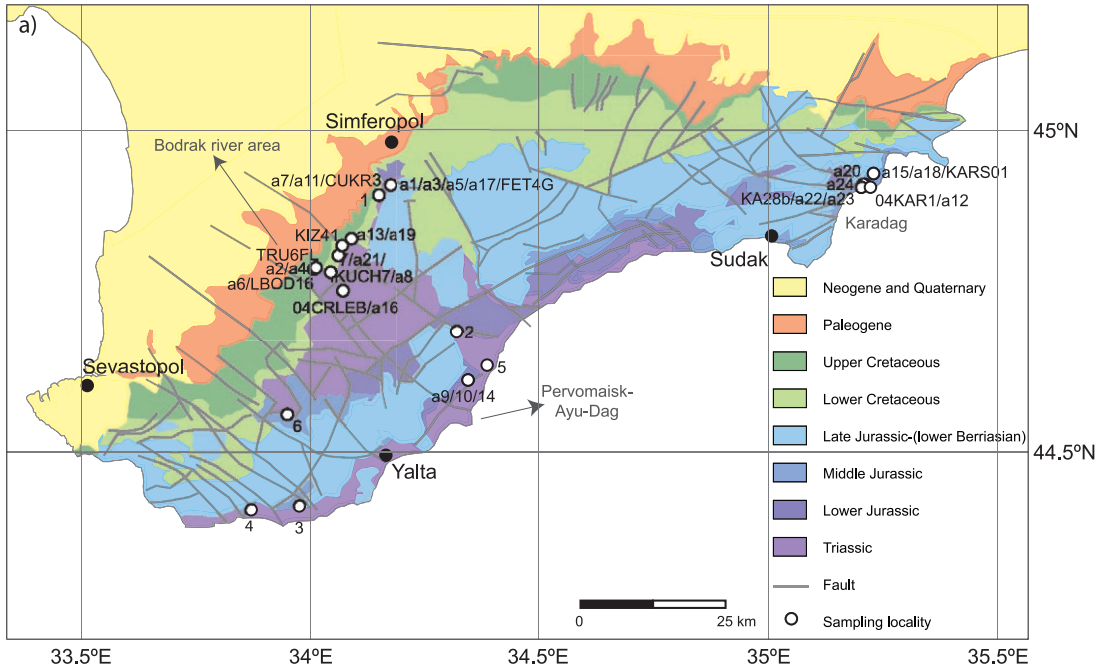


Appendix 13 Chapter 3, Fig. 3.2 (p. 88)

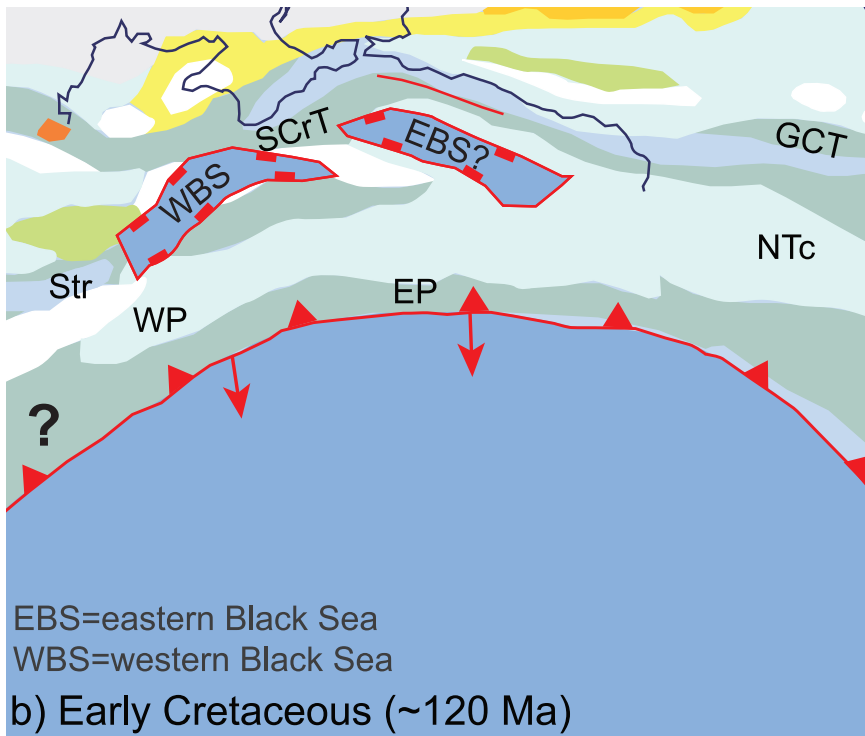
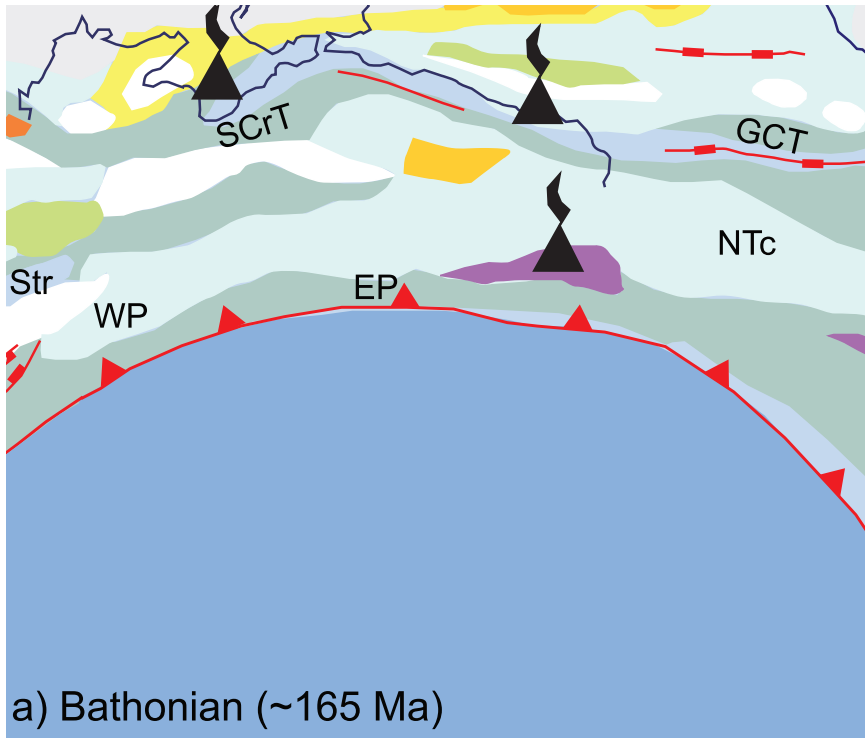


Early Kimmeridgian (~155 Ma)

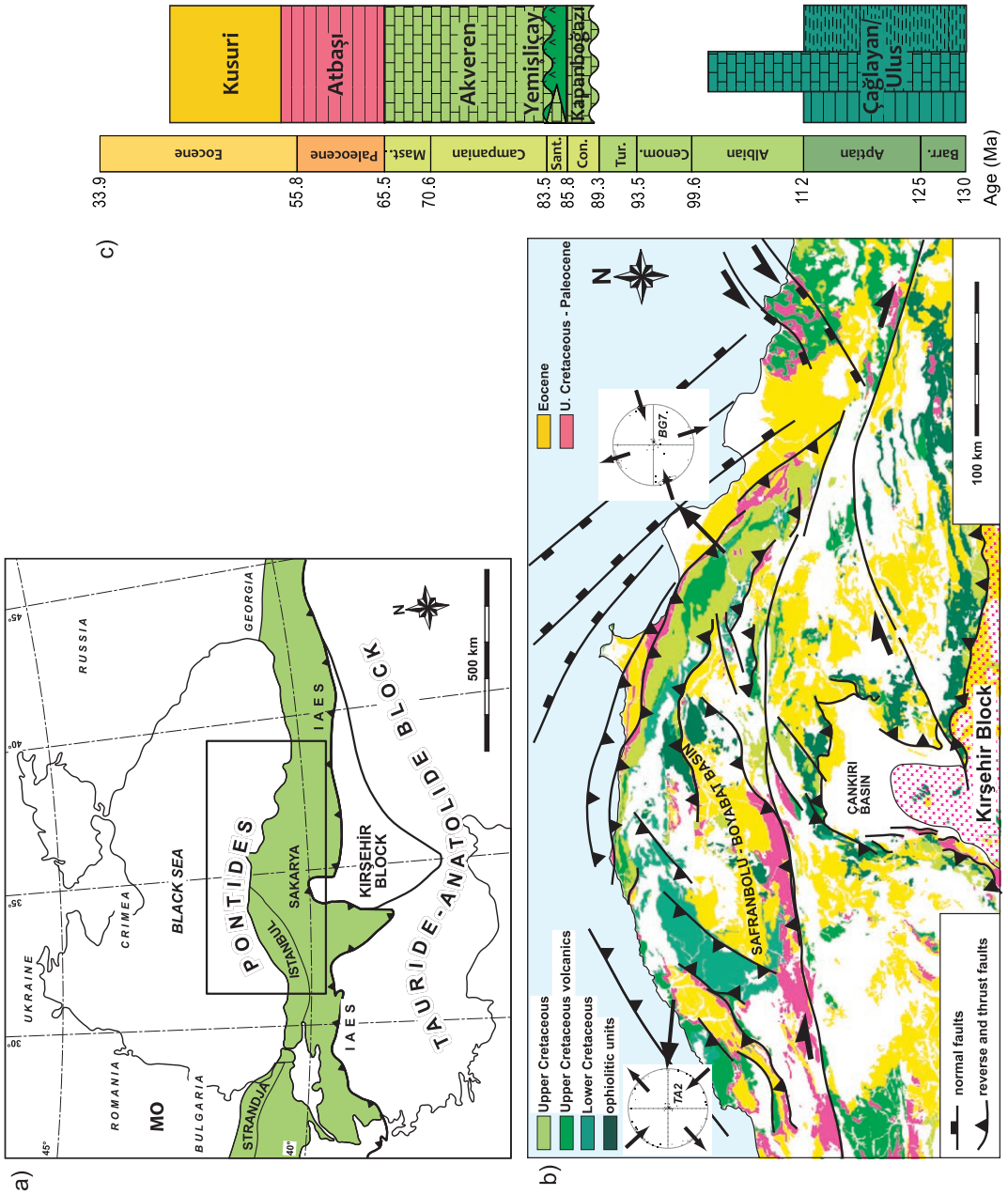
Appendix 14 Chapter 3, Fig. 3.3 (p. 93)



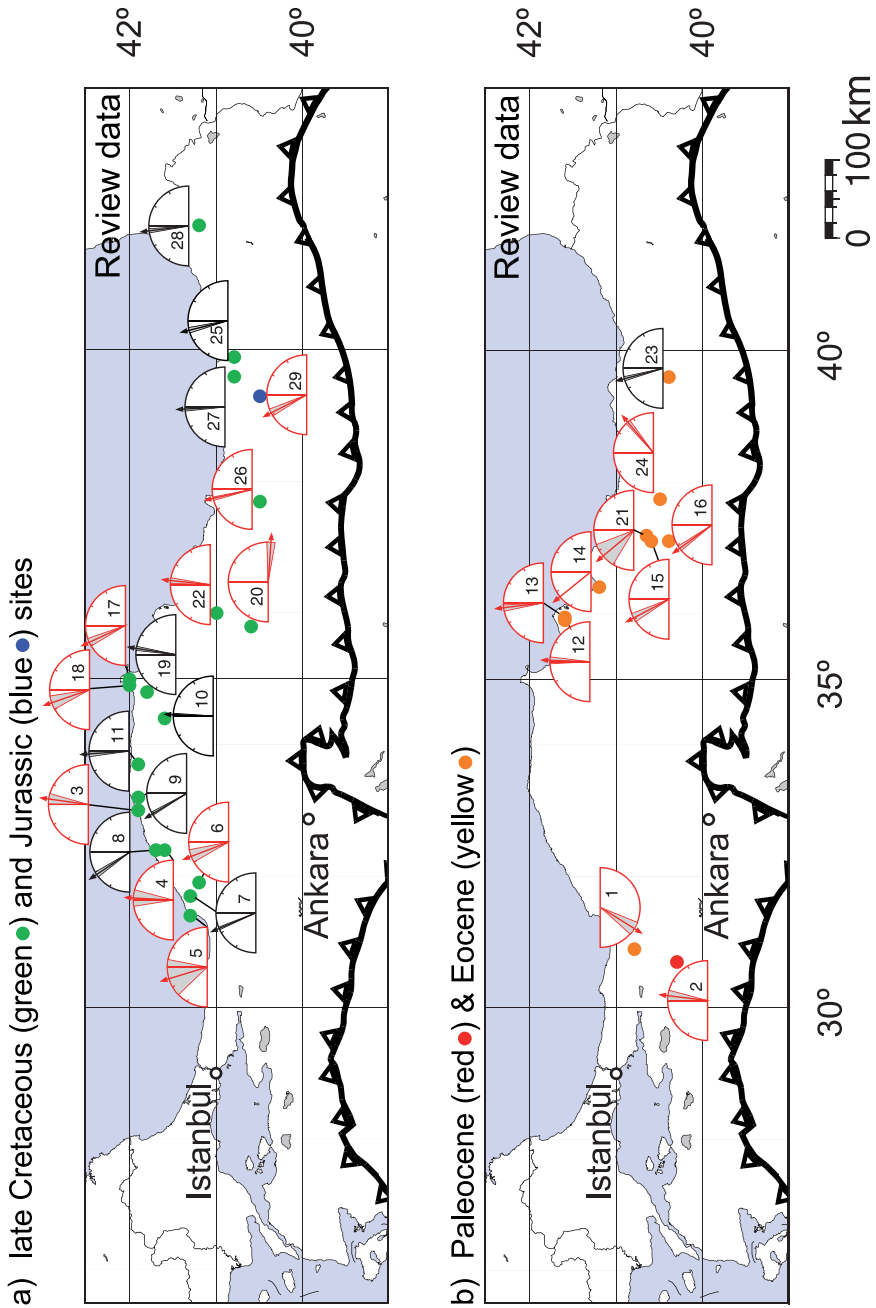
Appendix 15 Chapter 3, Fig. 3.8 (p. 107)



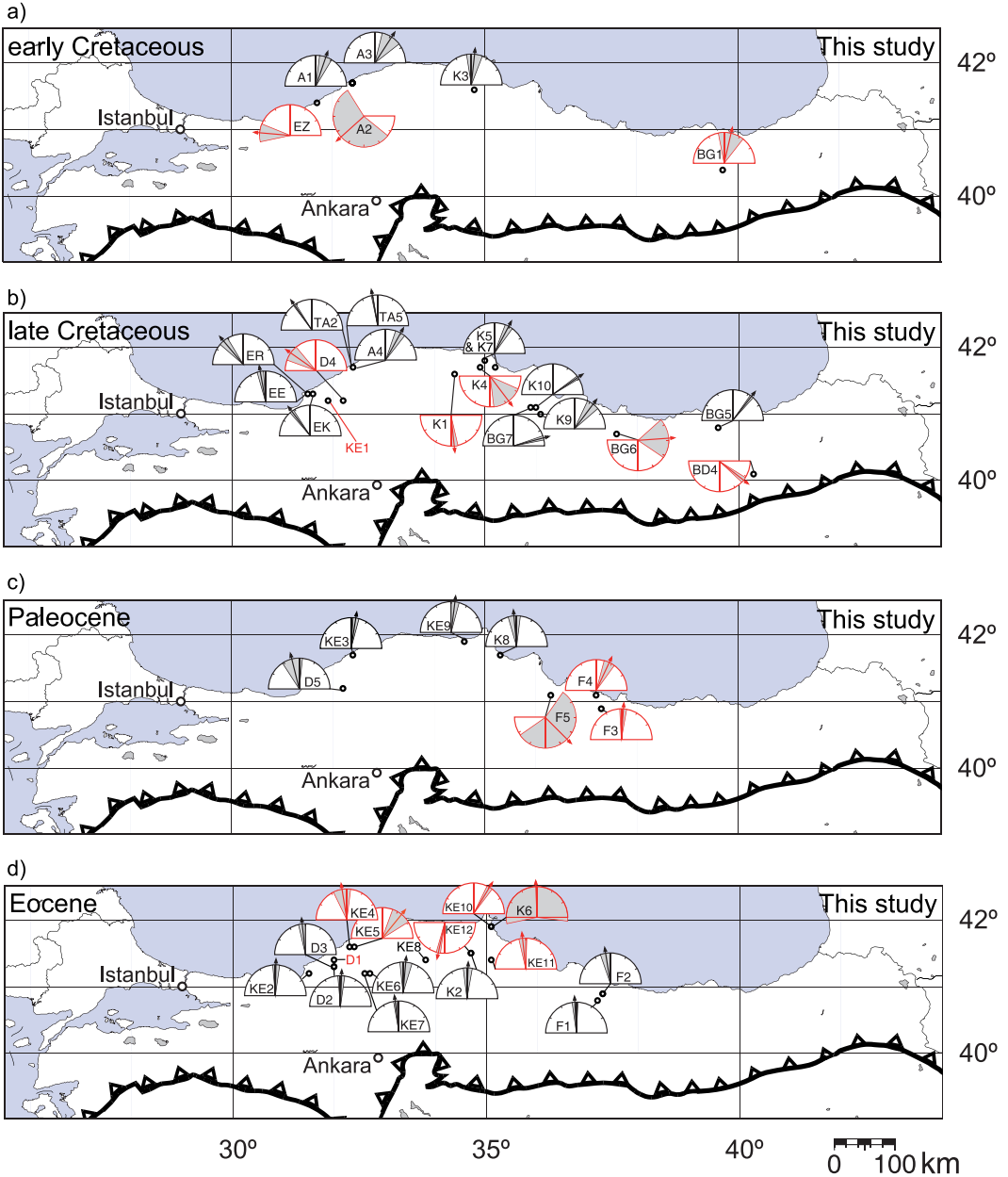
Appendix 16 Chapter 4, Fig. 4.1 (p. 121)



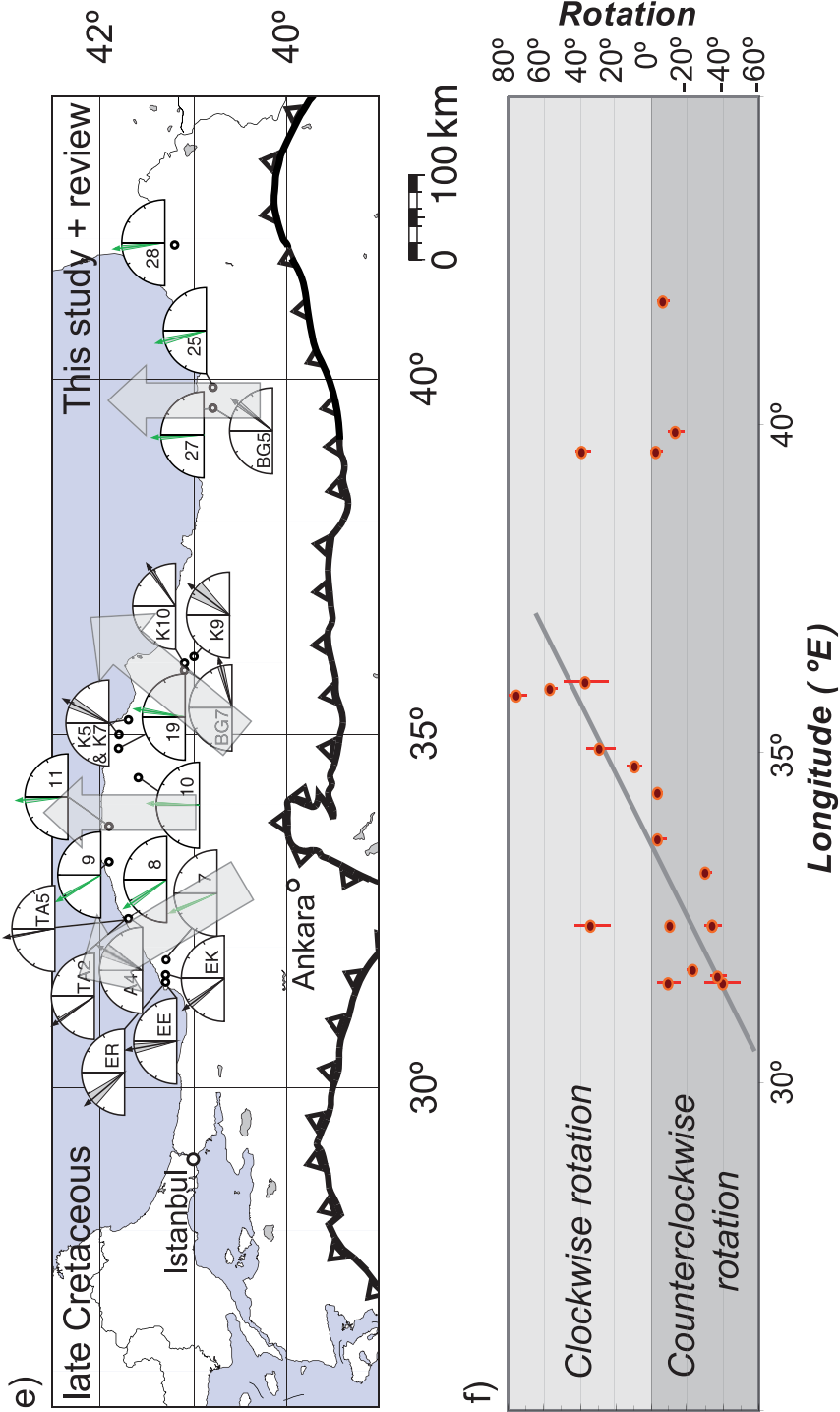
Appendix 17 Chapter 4, Fig. 4.4 (p. 134)

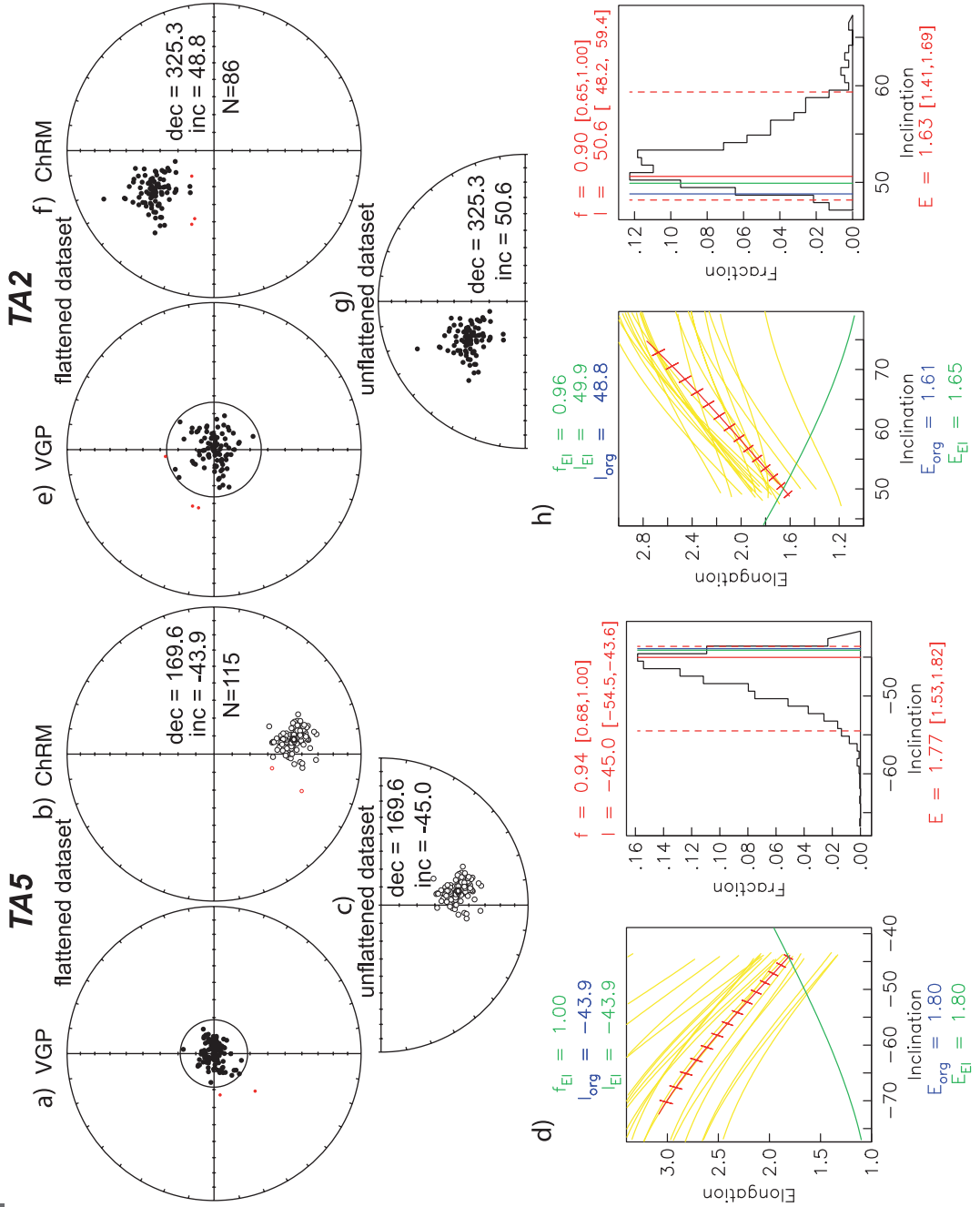


Appendix 18 Chapter 4, Fig. 4.5a-d (p. 135)

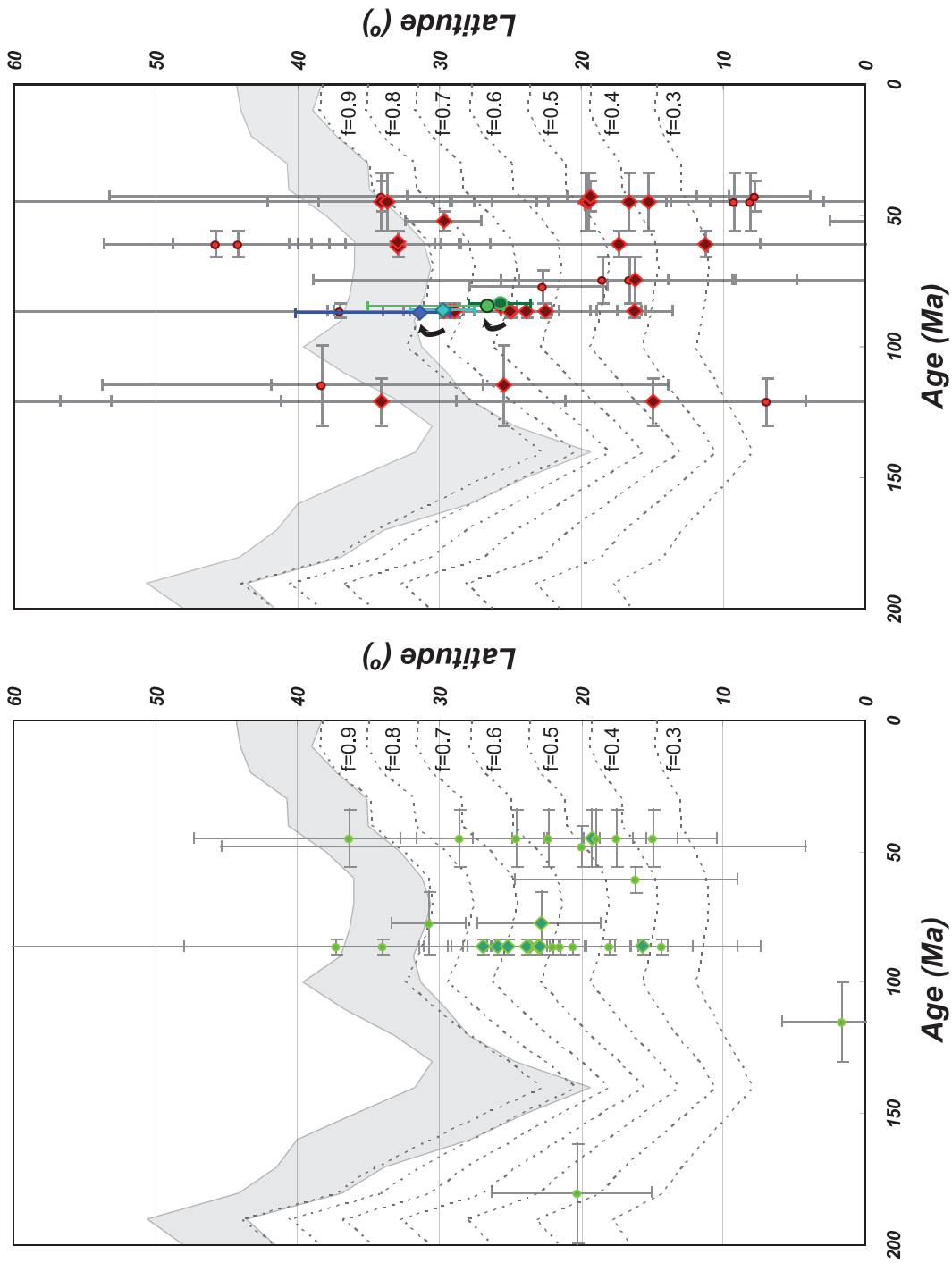


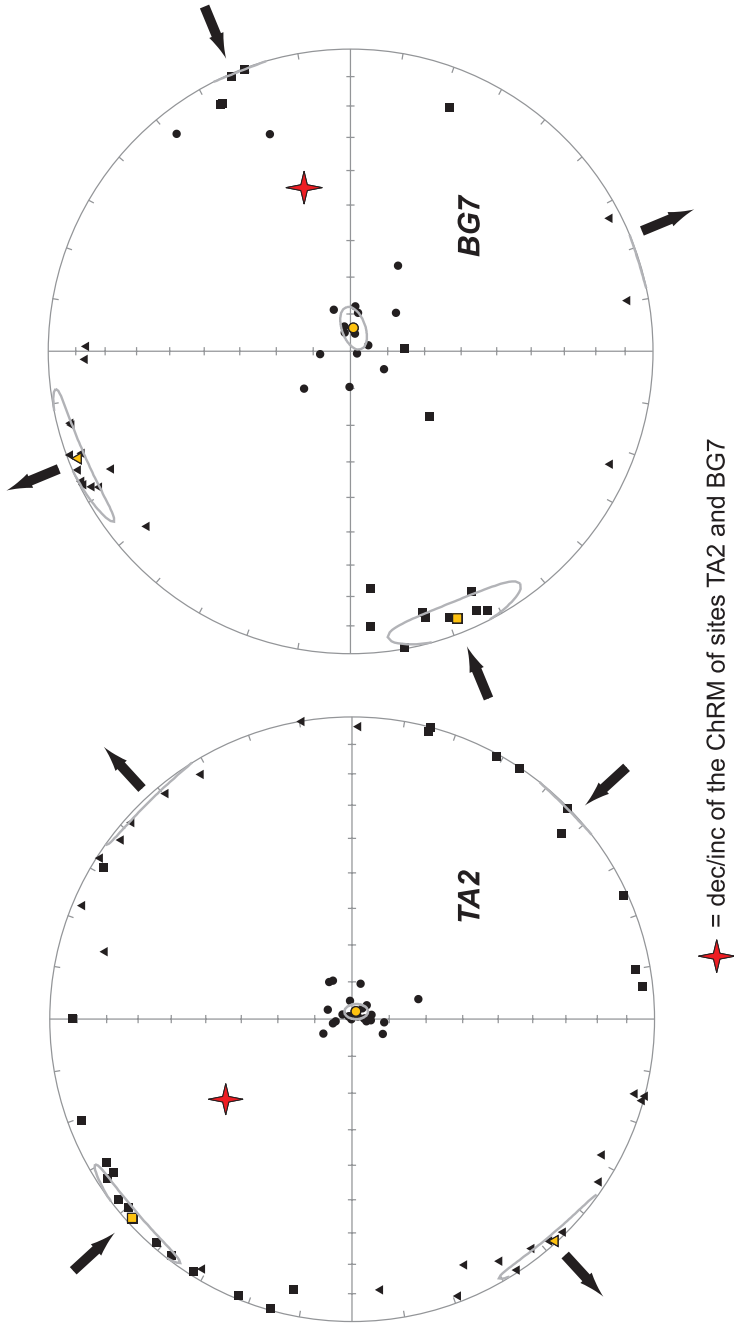
Appendix 19 Chapter 4, Fig. 4.5e-f (p. 136)



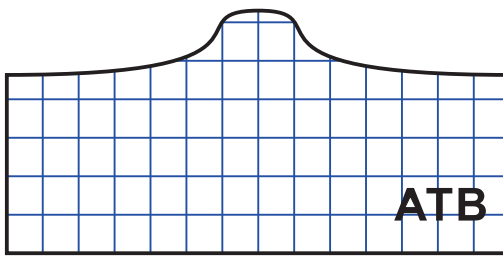
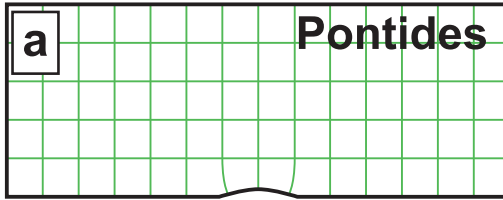


Appendix 21 Chapter 4, Fig. 4.7 (p. 138)

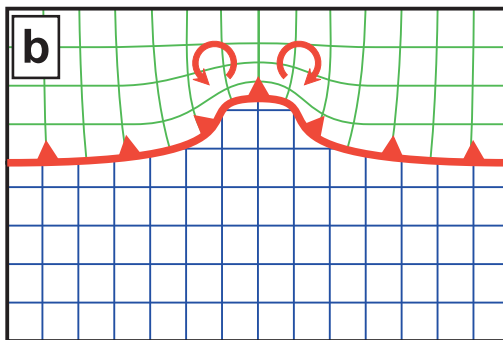




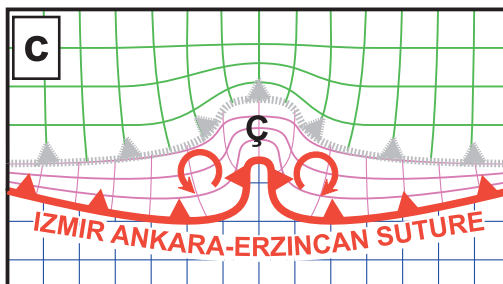
Appendix 23 Chapter 4, Fig. 4.9 (p. 141)
Campanian-Maastrichtian



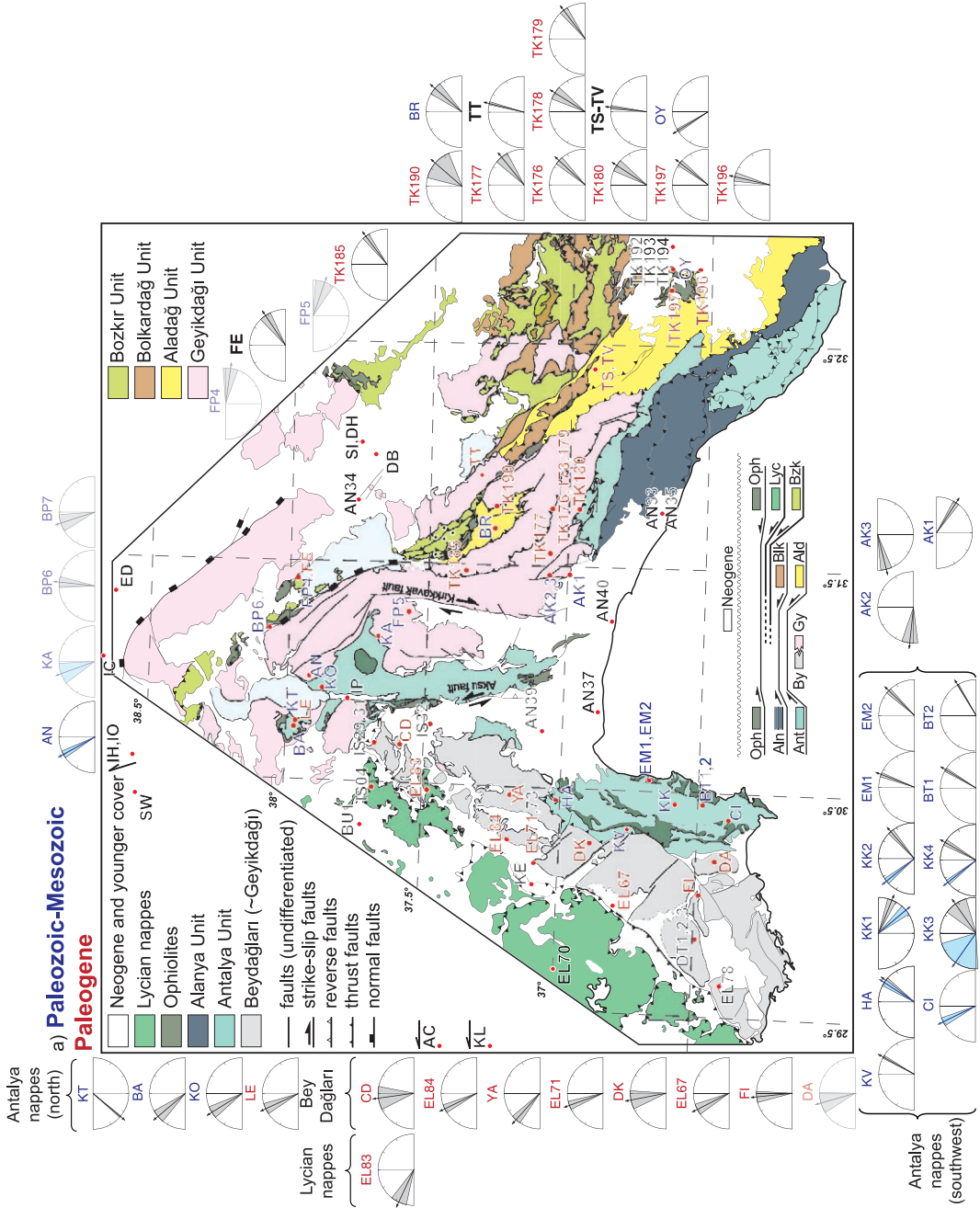
End of Cretaceous



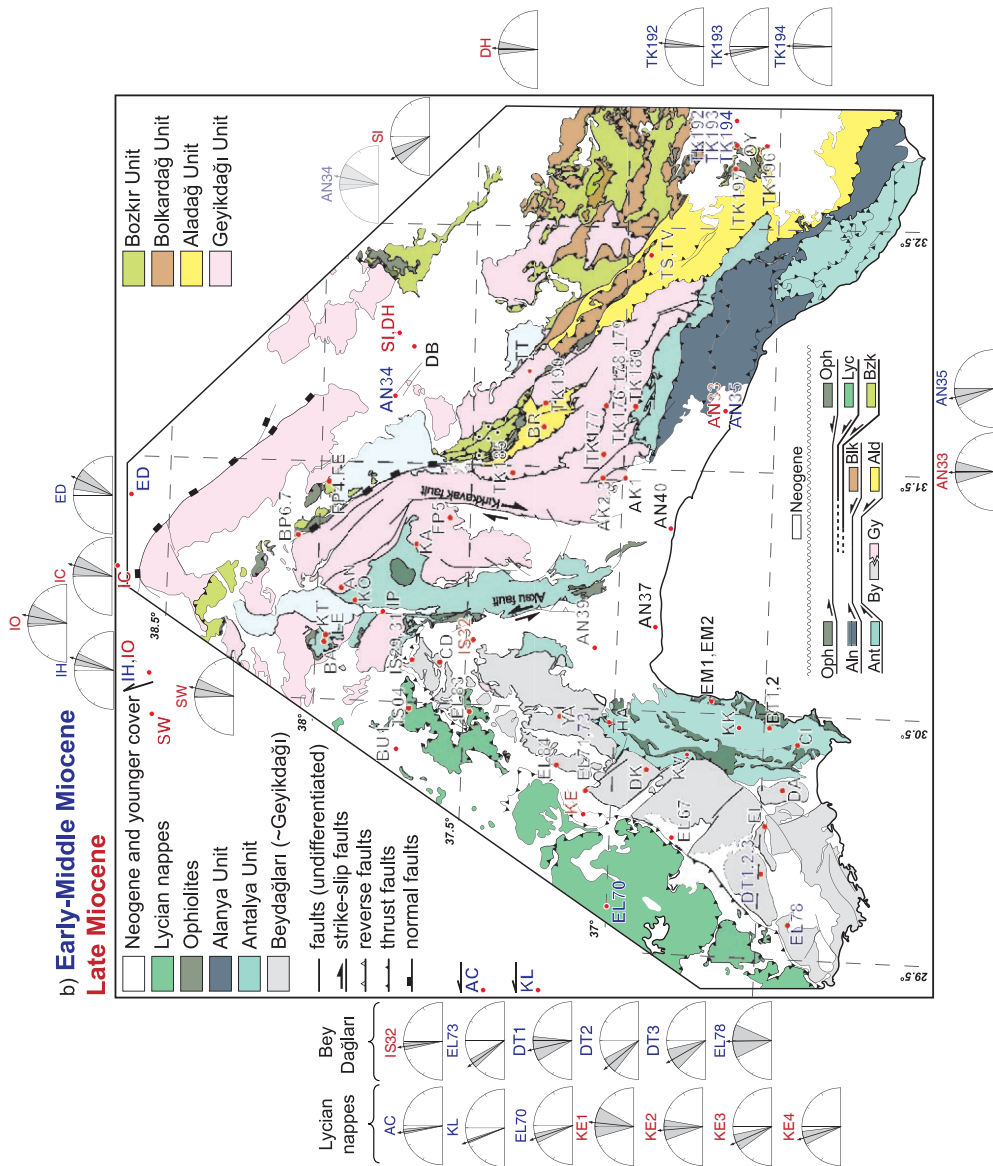
Indentation: rotation of the Pontides
 Eocene-Oligocene



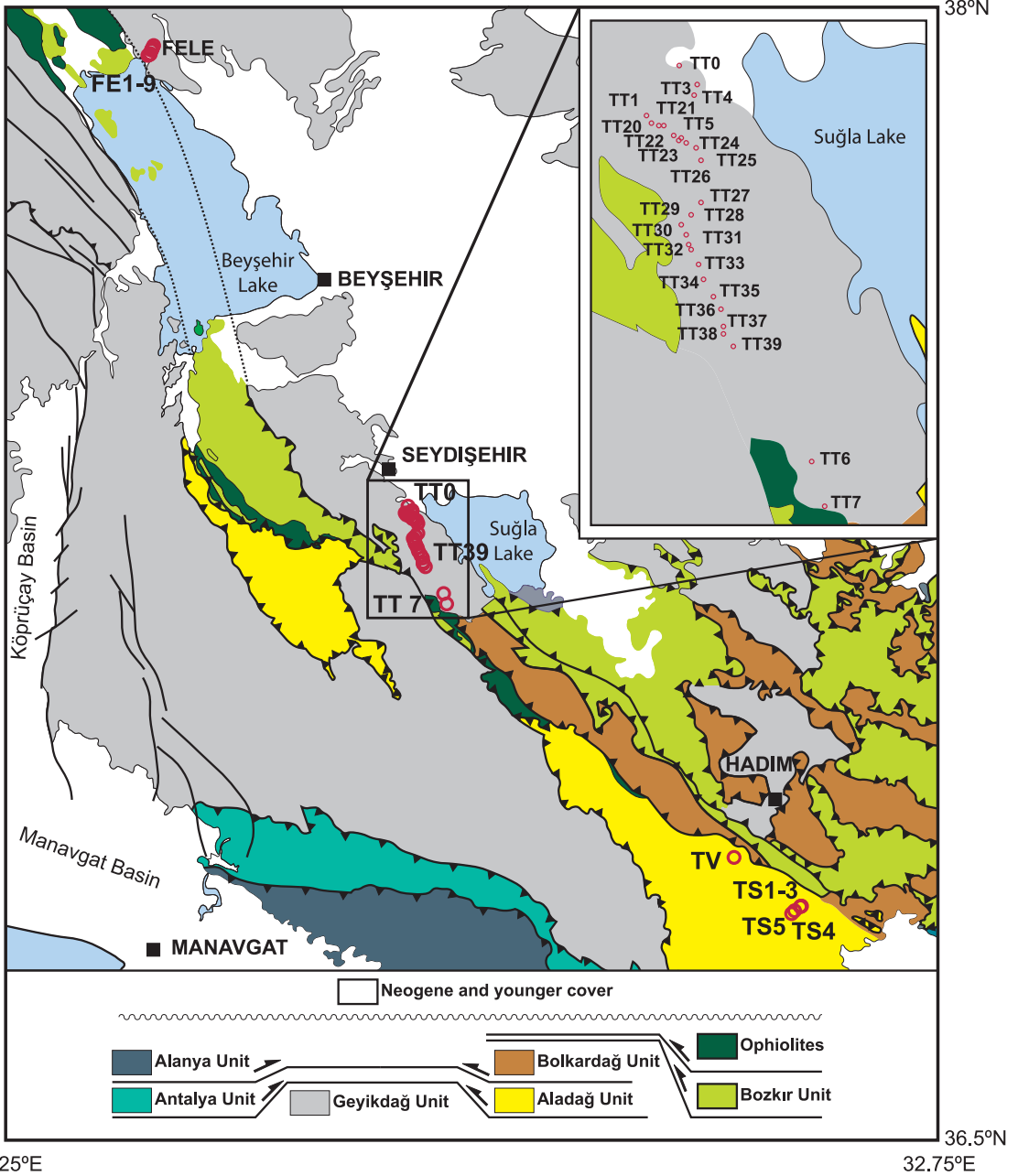
Thin skinned thrusting:
 Thrusting propagates southwards. No Paleogene rotation in the Pontides and main rotations in the Çankırı Basin



Appendix 25 Chapter 5, Fig. 5.2b (p. 152)



Appendix 27 Chapter 5, Fig. 5.3 (p. 156)

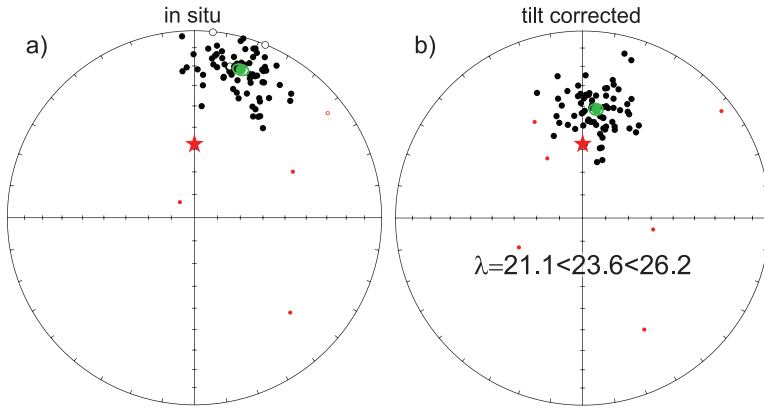


Appendix 28 Chapter 5, Fig. 5.6 (p. 159)

Taşkent (TS-TV) ~345.3-245.0 Ma

N= 75, A95= 2.3 K=50.9
D/I= 17.4/18.2

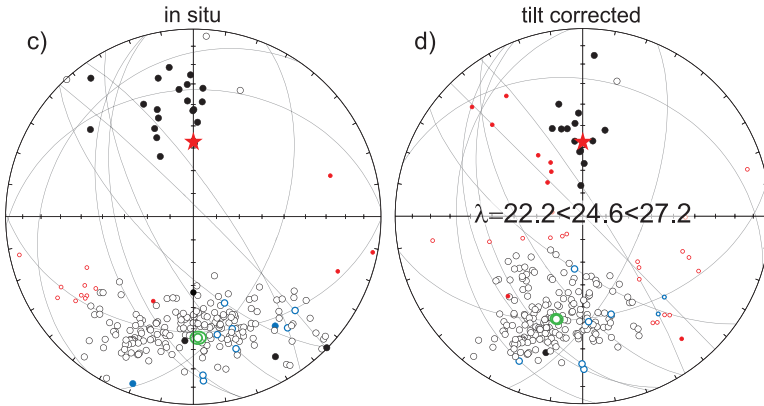
N= 73, A95= 2.6 K= 40.9
D/I= 7.1/41.4



Seydişehir (TT) ~228.0-55.8 Ma

N= 224, A95= 3.0 K= 10.8
D/I= 177.7/-35.5

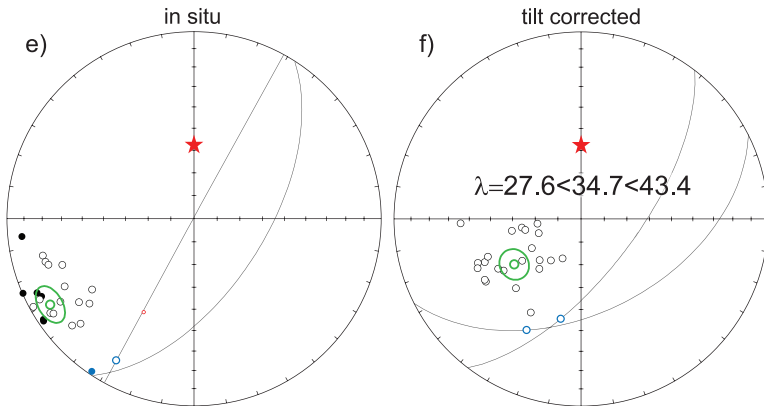
N= 208, A95= 2.5 K= 16.1
D/I= 194.4/-42.5



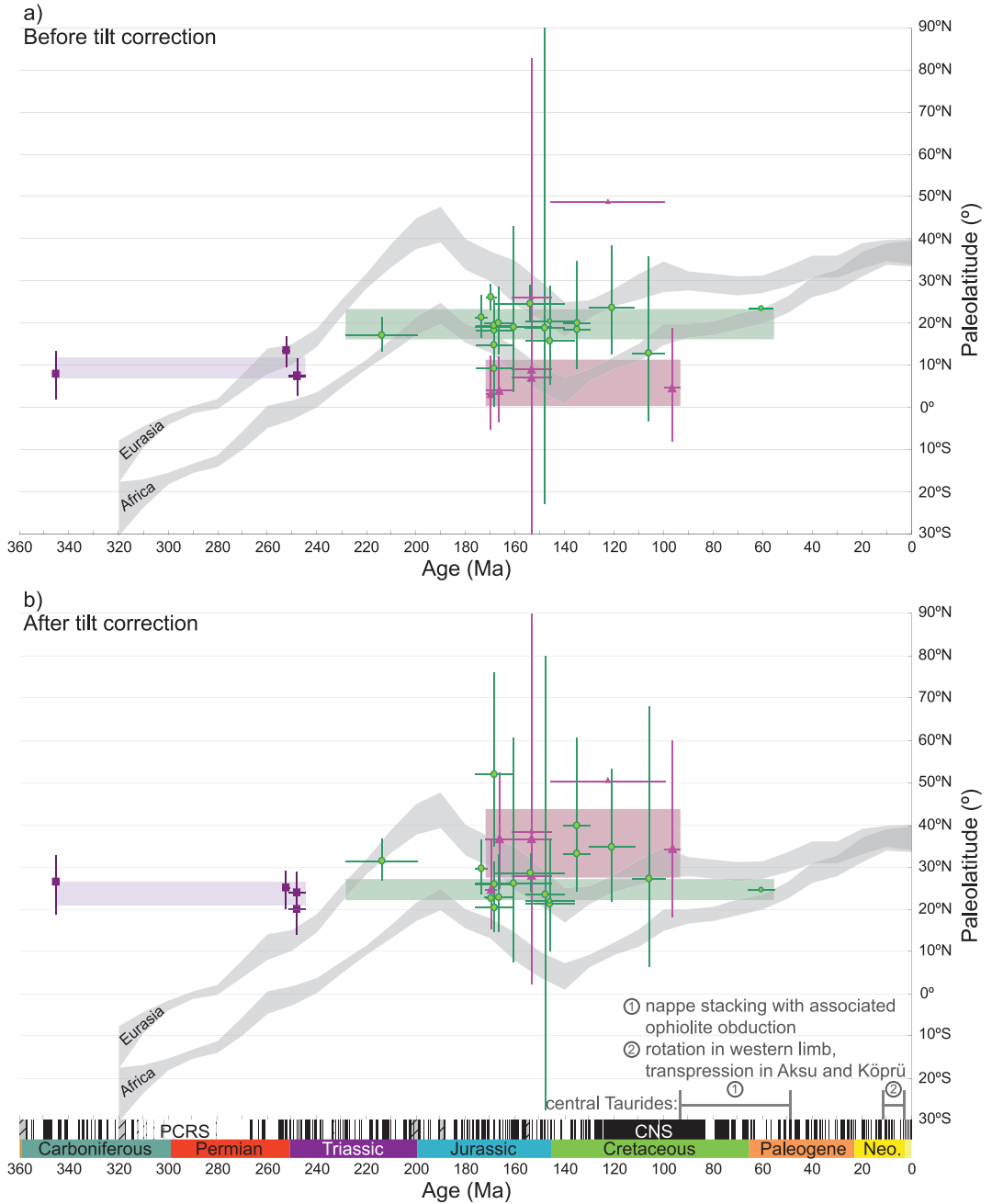
Fele (FE) ~171.6-65.5 Ma

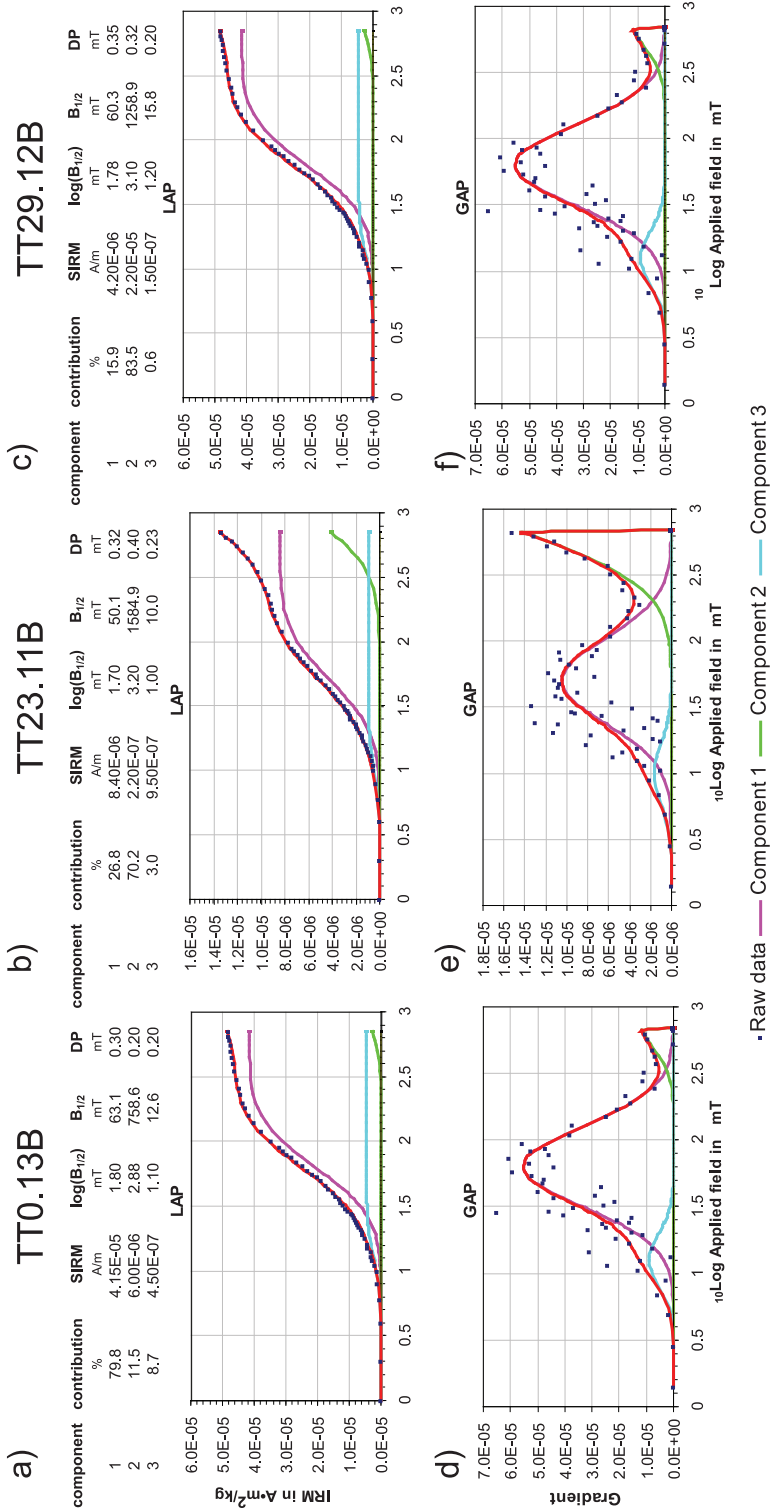
N= 23, A95= 5.4 K= 32.7
D/I= 239.1/-11.2

N= 24, A95= 7.8 K= 15.5
D/I= 235.7/-54.2



Appendix 29 Chapter 5, Fig. 5.7 (p. 165)





Appendix 31 Chapter 5, Fig. 5.10 (p. 176)

